

Light emission, electrochemical reduction and plasma formation during flash sintering of ceramics

Christian Bechteler

Wolfson College

University of Oxford

A thesis presented for the degree of

Doctor of Philosophy

Hilary 2025

Tuesday 24th December 2024

I dedicate this work to my parents - Margot and Otmar - who supported me throughout my whole life.

Thank you for everything.

If I have seen further it is by standing on the

shoulders of Giants.

— Isaac Newton

Abstract

Flash sintering of ceramics uses a combination of high electrical fields and elevated temperatures to achieve (Joule-)heating in the material leading to rapid densification of the material in less time and at significantly lower environmental temperatures compared to conventional sintering. Compared to conventional sintering, flash sintering not only allows considerable time and energy savings, but causes several effects which are not explainable by the rapid heating itself.

The aim of this doctoral thesis is to investigate the (DC-)flash sintering behaviour of various ceramics and understand the phenomena during and post flash sintering which are not solely explainable by heating itself. The materials investigated include transition metal oxides, such as tetragonal and cubic yttria stabilised zirconia (YSZ), yttria stabilised hafnia, as well as semiconducting boron carbide (B_4C), which was rarely investigated in the context of flash sintering and never successfully densified.

Unlike postulated by some researchers, one theory regarding the formation of an avalanche of Frenkel defects as a fundamental mechanism during flash sintering, which causes the emission of electroluminescence or photoemission in a visible spectra between 200 and 1100 nnm, was disproven. This conclusion was drawn after conducting optical spectroscopy under controlled circumstances and, most importantly, considering the significant influence of the experimental setup on the detected spectrum. If the experimental influences are considered the detected spectrum can almost entirely be explained by thermal radiation.

In another substantial piece of this work the electrochemical reduction behaviour of tetragonal and cubic YSZ under (DC-)flash sinter conditions was investigated in controlled atmospheres and varying oxygen partial pressures. It is shown that YSZ under flash sintering conditions behaves differently to what is expected from this material, usually known to be a good ionic conductor. Even from an early flash sintering stage, oxygen from the material itself gets extracted and works as a charge carrying species. The following electrochemical reduction changes the

material´s structure and properties in two stages.

In stage I of electrochemical reduction of the white material changes its appearance towards grey. Greying of the material is a sign for the formation of (Y)$ZrO_{2-\delta}$, which is dominated by the formation of single charged oxygen vacancies compensated by Zr^{3+}-ions. Since the fundamental properties of the material, such as an increase in electrical conductivity, a stronger paramagnetic behaviour, and a change in optical properties, are different to the original tetragonal phase and other known phases (t´ and t´´) it is proposed to label YSZ in stage I of electrochemical reduction as t*. Stage I is reached under moderate DC-flash sinter conditions and AC flash sintering.

Stage II of electrochemical reduction occurs if reduction continues and can be identified by blackening of the material, which is a consequence of the formation of defective FCC rocksalt ZrO phase. Stage II is reached if high currents are conducted through the material or if insufficient oxygen availability is happening during FS. The defective FCC rocksalt ZrO phase formation involves the formation of double charged oxygen vacancies and a fundamental change in bonding structure by delocalisation of electrons between Zr and O, leading to a significant increase in the electronic conductivity, obeying a metallic PTC-behaviour. Dependent on the parent phase, tetragonal or cubic YSZ, the localisation and appearance slightly changes but lattice parameters and properties of the FCC rocksalt ZrO phase are similar. Furthermore, the formation of a defective FCC rocksalt HfO phase was shown in this work. The formation and characterisation of this phase filled the gap of group IV transition metal carbides, nitrides, and monoxides, which show a FCC rocksalt structure.

Each stage of electrochemical reduction can explain some of the phenomena detected during and post flash sintering, which are not explainable by Joule heating alone. The obtained results are also relevant to solid oxide fuel and electrolyser cells as will be discussed in this work.

Unlike oxides, carbides usually require sintering temperatures exceeding 2000 °C and are rarely investigated in the perspective of flash sintering. The combination of high electrical fields and elevated temperatures does also affect other parame-

ters such as a potential atmospheric breakdown. This work shows that a voltage of 50 V in argon at 1500 °C is sufficient to achieve a surface flashover, which leads to an atmospheric breakdown and the formation of a plasma in form of a gas discharge. The plasma in its initial stage is more conductive than the boron carbide (B_4C) sample but transitions into a Joule heating stage after approximately 15 s once the material becomes more conductive due to the reducing effect of the plasma on the boron oxide layer, which also hinders densification of boron carbide by flash sintering.

The process parameters relevant for flash sintering of boron carbide were improved, which includes the addition of carbon, thermal insulation, hold time, power dissipation and sample temperature, as well as the previously mentioned pre-plasma treatment prior to the Joule heating stage. The result of the parameter improvements is the first successful densification of boron carbide at a furnace temperature of 1500 °C within 5 min up to a relative density of 96 %. Characterisation of the flash sintered boron carbide material showed a high degree of twinning in the material, an average grain size of 10 μm and a hardness of 31 GPa (HV1).

Acknowledgements

Personal

First and foremost, I would like to express my deepest gratitude to my supervisor, Professor Richard Todd, for giving me the opportunity to come to Oxford and study under his guidance. His exceptional supervision and extraordinary patience during our discussions, which often extended for hours, have been invaluable. These conversations not only enabled me to make the most of my time but also introduced me to concepts and ideas I had never encountered before. Richard has been the best supervisor I could have imagined. Although we did not always agree on everything, and some of my ideas seemed far-fetched, a few of those are now an integral part of this thesis. His unwavering support carried me through moments of uncertainty, and his direction set me on the right path.

Being part of a group of young researchers has been both inspiring and motivating. Sharing this journey with peers who faced similar challenges enabled us to exchange ideas and support one another. The discussions we had, and the time we spent together outside the lab or department, have been equally significant. I am immensely grateful to have had such fantastic colleagues, many of whom I am proud to call my friends. Thank you all for accompanying me on my DPhil journey; it has been a pleasure.

Among this group, I am especially thankful to Andrew Gibson. From the very beginning, Andrew mentored me, providing an excellent introduction to the field of flash sintering based on his own work and experiences during his DPhil. His guidance prevented me from making countless mistakes and helped me to understand the nuances of flash sintering and the importance of maintaining a balance between work and time away from the lab.

I would also like to acknowledge the support and expertise of several exceptional individuals at Oxford University who contributed significantly to this thesis. My thanks go to Andrew Kirkpatrick for his assistance with optical spectroscopy mea-

surements and to Simone Falco for lending me the high-speed camera equipment and helping with plasma experiment recordings, often late into the evenings. I am grateful to Pedr Charlesworth for conducting some of the XRD measurements, and to Joshua Gibson and Sudarshan Narayanan, whose insights and expertise allowed me to realise, interpret, and understand the XPS measurements, which proved invaluable. I am also indebted to William Myers for his guidance and support with EPR measurements in the Department of Inorganic Chemistry and to Phani Karamched, whose skill with the SEM and willingness to help were greatly appreciated.

I would like to thank Hannes Kühl, who first sparked my interest in ceramics during my studies at the Faculty of Materials Engineering at the Technische Hochschule Nürnberg. His teaching not only gave me a strong foundation in ceramic science but also equipped me with the practical skills necessary to undertake the research presented in this thesis.

I would also like to extend my gratitude to Ralf Girmscheid from Paul Rauschert GmbH & Co. KG, who co-supervised my research during my time at the Technische Hochschule Nürnberg. His mentorship and instruction provided me with foundational knowledge and skills that I have utilised almost every day since.

When I first arrived in Oxford in December 2019, it was a challenging period due to the ongoing pandemic and lockdowns that severely affected much of Europe, especially the UK. Despite these difficulties, I was fortunate to find a second family in the residents of the Annexe at Wolfson College. I am deeply grateful to Ped, Humbi, Lorenzo, Andrew, and Tejo, for the wonderful times we shared, even during those trying days when lockdowns and self-isolation became the new normal.

I would also like to thank all the other incredible people I met during my time at Oxford. Many of them were fellow members of Wolfson College, but others were individuals I encountered through various walks of life. Your companionship and kindness brought joy to my days and made my time in Oxford truly memorable.

Finally, and most importantly, I would like to express my heartfelt gratitude to my family and my partner, Carina, for their unwavering support throughout my DPhil

journey and beyond. Their encouragement, understanding, and love have been an unfailing source of strength. To my family: thank you for being the best family I could ever wish for. To Carina: thank you for standing by my side through every high and low, and for your constant encouragement and love. This achievement would not have been possible without you.

Institutional

I would like to express my sincere gratitude to the Engineering and Physical Sciences Research Council (EPSRC) [EP/T517811/1] for providing the scholarship that enabled me to pursue a DPhil at Oxford.

Furthermore, I am deeply thankful to the Studienstiftung des deutschen Volkes for their generous scholarship support, both during my time as a DPhil student and throughout my previous studies. I would also like to acknowledge the Max Weber Programm for their financial assistance, which greatly supported me during my undergraduate and postgraduate studies.

I am grateful for the characterisation facilities within the David Cockayne Centre for Electron Microscopy at the Department of Materials, University of Oxford, for their technical support. Additionally, I would like to thank the Henry Royce Institute (Grant ref EP/R010145/1) and the Henry Royce Fund for their financial support, which facilitated several key experiments and the results presented in this thesis.

I extend my thanks to Wolfson College, the Department of Materials, and the Institute of Materials, Minerals and Mining (IOM3) for their financial assistance, which enabled me to attend and participate in international conferences.

Research Output

Publications

- C. Bechteler, S. Narayanan, R. I. Todd: Plasma formation during flash sintering of boron carbide - Part II: effect on sintering and optimisation of process variables; *Ceramics International*; vol. 51, November 2024, https://doi.org/10.1016/j.ceramint.2024.11.314.
- C. Bechteler, H. Kuehl, R. Todd: Boron induced abnormal grain growth in alumina; *Open Ceramics*; vol. 19, September 2024, https://doi.org/10.1016/j.oceram.2024.100636.
- C. Bechteler, A. Gibson, S. Falco, A. Kirkpatrick, R. I. Todd: Plasma formation during flash sintering of boron carbide - Part I: plasma characteristics; *Ceramics International*; vol. 50, May 2024, https://doi.org/10.1016/j.ceramint.2024.05.250.
- C. Bechteler, A. Kirkpatrick, R. Todd: Comment on Flash in argon atmosphere yields electronically conducting yttria-stabilized zirconia at ambient temperature; *Journal of the American Ceramic Society*; vol. 107, December 2023, https://doi.org/10.1111/jace.19593.
- C. Bechteler, R. Todd: Lattice modification of $ZrO_{2-\delta}$ and formation of rock-salt structure ZrO and Zr(O,N) after DC electrical loading of 3YSZ; *Journal of the European Ceramic Society*, vol.44, September 2023, https://doi.org/10.1016/j.jeurceramsoc.2023.09.014.
- C. Bechteler, A. Kirkpatrick, R. Todd: Visible light emissions during flash sintering of 3YSZ are thermal radiation; *Scripta Materialia*, vol. 219, May 2022, https://doi.org/10.1016/j.scriptamat.2022.114849.
- C. Bechteler, A. Ruebling, R. Girmscheid, H Kuehl: Development of pressureless sintered and hot-pressed CNT/alumina composites including mechanical characterization; *International Journal of Ceramic Engineering*

and Science, vol. 3, August 2021, https://doi.org/10.1002/ces2.10103.

- C. Bechteler, L. Machuj, K. Hebendanz, A. Ruebling, R. Girmscheid, H Kuehl: Electrical and thermal conductivity of CNT/alumina-nanocomposite ceramics; *International Journal of Ceramic Engineering and Science*, vol. 5, November 2022, https://doi.org/10.1002/ces2.10167.
- C. Bechteler, R. Girmscheid, H. Kuehl: Influence of different alumina powders on thermal decomposition of CNTs during debinding of CNT/Al_2O_3-composite ceramics; *Open Ceramics*, vol. 7, September 2021, https://doi.org/10.1016/j.oceram.2021.100166.
- C. Bechteler, H. Kuehl, R. Girmscheid: Morphology and structure characterization of ceramic granules; *Journal of the European Ceramic Society*, vol. 40, September 2020, https://doi.org/10.1016/j.jeurceramsoc.2020.04.044.

Conferences

- Conference of the European Ceramic Society 2023 - Oral Presentation - Lyon, France
- European Ceramic Society Student Speech Contest UK Heat 2023 - Oral Presentation - Bristol, UK
- Konferenz der Deutschen Keramischen Gesellschaft 2023 - Oral Presentation - Hermsdorf, Germany
- Nano Carbon 2023 - (Opening) Oral Presentation - Würzburg, Germany
- Ceramics in Europe 2022 - Oral Presentation - Krakow, Poland
- Konferenz der Deutschen Keramischen Gesellschaft 2022 - Oral Presentation - Online
- Konferenz der Deutschen Keramischen Gesellschaft 2021 - Oral Presentation - Online

Awards

- Representative of Materials Department at the UK-Heat for Student Speech Contest at ECERS conference in Lyon 2023 - University of Oxford
- Finalist at 2nd year Postgraduate Research Talk 2023 - Department of Materials University of Oxford
- 1st place DCCEM image competition judges´ choice 2022 - Department of Materials University of Oxford
- 1st place DCCEM image competition peoples´ choice 2022 - Department of Materials University of Oxford
- 1st place SEM foto competition 2022 - Young Ceramists Network
- 1st place best oral presentation 2022 - Deutsche Keramische Gesellschaft
- 3rd place Hans-Walter-Hennicke-Wettbewerb 2021 - Deutsche Keramische Gesellschaft

Teaching

- Hochleistungs- und Funktionskeramik (HLFK) course for master students at the Technische Hochschule Nürnberg (online)

Reviewing

- Reviewer for the Journal of the European Ceramic Society

Declaration

I, Christian Bechteler, hereby declare that this thesis entitled "Light emission, electrochemical reduction and plasma formation during flash sintering of ceramics" and the work presented herein is my original and independent research. This thesis has not been previously submitted for any degree or examination at any other institution.

I further declare that:

1. All sources of information and ideas used in this thesis, whether quoted directly or paraphrased, have been duly acknowledged through proper citations and references.

2. Any contributions from other researchers or individuals have been appropriately credited in this thesis.

3. The research presented in this thesis has been conducted with the utmost integrity and in accordance with the ethical guidelines of Department of Materials, University of Oxford.

4. Any assistance received during the course of this research has been acknowledged and attributed.

I am aware that any act of plagiarism, data fabrication, or falsification of results is strictly against the principles of academic integrity and could lead to severe consequences, including the cancellation of my degree.



Christian Bechteler

Table of Contents

1 Introduction **1**

1.1 History of flash sintering 1

1.2 Motivation 4

1.3 Aim and objectives 6

2 Literature Review **10**

2.1 Flash sintering and related subjects 11

2.1.1 Models explaining flash sintering 12

2.1.2 Rapid heating during flash sintering 17

2.1.3 Light emission during flash sintering and its relation to the theory of Frenkel defect formation 18

2.1.4 Defect chemistry in zirconia 22

2.1.4.1 Inclusion of tetravalent cations 23

2.1.4.2 Extrinsic oxygen vacancies 23

2.1.4.3 Intrinsic oxygen vacancies 26

2.1.4.4 Oxidation states and paramagnetic response . . 29

2.1.5 Field-induced crystallographic changes and phase transformation during flash sintering YSZ 31

2.1.6 Electrical conductivity of oxide ceramics 34

2.1.6.1 Electrical conduction in (YS)Z at low temperature and low electrical field strength 34

2.1.6.2 Electrical conduction of oxide ceramics during Flash Sintering 36

2.1.7 Blackening in stabilised zirconia 38

2.1.8 Other athermal effects suggested during and post flash sintering of YSZ 41

2.1.9 Flash sintering of carbides 43

2.2 Plasmas under (flash-) sinter conditions 48

2.2.1 Plasma classification 50

2.2.2 Plasma formation 53

2.2.3 Plasma properties 54

2.2.4 Plasma interactions with solids 55

3 Methodology **57**
3.1 Sample preparation 57
3.1.1 Investigated powders 57
3.1.2 Powder processing 58
3.1.3 Sample processing 60
3.2 Thermal treatment 61
3.2.1 Debinding 61
3.2.2 Conventional sintering 62
3.2.3 Flash sintering and electrical loading 62
3.2.3.1 Flash sinter setup 62
3.2.3.2 Flash sintering conditions 64
3.3 Characterisation 68
3.3.1 Density measurements 68
3.3.2 Grinding and polishing 69
3.3.3 Hardness measurement 69
3.3.4 Etching 70
3.3.5 Grain size measurements 71
3.3.6 Raman Spectroscopy 71
3.3.7 X-Ray Diffraction analysis (XRD) 72
3.3.8 Scanning Electron Microscopy (SEM) 74
3.3.9 Energy Dispersive X-ray Spectroscopy (EDS) 75
3.3.10 Electron Backscatter Diffraction (EBSD) 76
3.3.11 X-ray Photoelectron Spectroscopy (XPS) 77
3.3.12 Electron Paramagnetic Resonance (EPR) Spectroscopy . . 81
3.3.13 Room temperature electrical conductivity 84
3.3.14 Thermogravimetric Analysis 84
3.3.15 Optical spectroscopy 84
3.3.16 High speed video recording 87

4 Light emission during flash sintering **88**
4.1 Light emission during flash sintering of YSZ 88

4.2 Comparison to other previously published results about light emission during flash sintering and electrical loading 96
4.3 Other light emitting phenomena occurring in flash sintering 101
4.4 Discussion 103

5 Flash sintering and the effect of electrical loading on Yttria-stabilised Zirconia 105
5.1 Flash sintering 3YSZ green bodies 108
5.1.1 Flash sintering 3YSZ green body in air 108
5.1.2 Flash sintering 3YSZ green body in other atmospheres . . 109
5.2 Electrical loading of pre-sintered YSZ 112
5.2.1 Arrhenius plot of the electrical resistivity during electrical loading 118
5.2.2 Sample heating and appearance during and after flash sintering and electrical loading in various atmospheres 121
5.3 Characterisation of YSZ after flash sintering and electrical loading 123
5.3.1 SEM and EDS 123
5.3.2 X-Ray Diffraction (XRD) 136
5.3.3 Raman Spectroscopy 142
5.3.4 X-ray Photoelectron Spectroscopy (XPS) 149
5.3.5 Electron Paramagnetic Resonance spectroscopy (EPR) . . 157
5.3.6 Room temperature electrical conductivity 166
5.4 Discussion 167
5.4.1 Electrochemical reduction of (stabilised) zirconia stage I: $ZrO_{2-\delta}$ 167
5.4.1.1 Fundamental (defect) structure 167
5.4.1.2 Effect of electrochemical reduction on the tetragonal YSZ phase 170
5.4.1.3 Change of electrical properties 174
5.4.2 Electrochemical reduction of (stabilised) zirconia Stage IIa: ZrO 176
5.4.2.1 Fundamental structure of the FCC rocksalt transition metal monoxide phases 176

5.4.2.2 Formation and properties of ZrO_xN_{1-x} during electrical loading of (yttria-stabilised) zirconia . 183
5.4.2.3 Change of electrical properties in YSZ reduction stage II 185
5.4.2.4 Stability of ZrO 189
5.4.2.5 Appearance and location of ZrO 192
5.4.2.6 Plastic deformation in YSZ during flash sintering and under electrical load 196
5.4.2.7 Influence of reoxidation on the densification of YSZ during flash sintering 198
5.4.3 General implications for flash sintering 201
5.4.3.1 Predicting the onset of flash sintering 201
5.4.3.2 Rapid densification by flash sintering 202
5.4.4 Electrochemical reduction of YSZ in the perspective of SOFC and SOEC 203
5.4.5 Summary of electrochemical reduction stages in (stabilised) zirconia 206

6 Plasma formation and characteristics during flash sintering of boron carbide 208
6.1 Plasma pre-treatment flash sintering boron carbide at constant power in argon 208
6.2 Electrical characteristics of PPT-FS for boron carbide and silicon carbide 211
6.3 Plasma formation under flash sintering conditions 214
6.4 Plasma properties under flash sintering conditions 215
6.4.1 Optical spectroscopy 215
6.4.2 Plasma conductance 218
6.4.3 Plasma infiltration into powder compacts 218
6.5 Discussion 222
6.5.1 Initial formation of the plasma 222
6.5.2 Classification of the plasma 224
6.5.3 Steady state plasma properties 224

6.5.4 Plasma infiltration of the green body 228
6.5.5 Collapse of the plasma 230
6.5.6 Relevance to plasma formation in other field assisted sintering techniques 232

7 Effect of plasma formation on flash sintering and optimisation of process variables 234
7.1 Constant voltage-constant power tests 234
7.2 Isothermal flash sintering 235
7.2.1 Power dissipation limit 236
7.2.2 C-foil wrapping 236
7.2.3 C-content 238
7.2.4 Heating rate and initial presence of plasma 240
7.2.5 Hold time 241
7.3 Hardness 241
7.4 Microstructure 242
7.4.1 PPT-FS samples 242
7.4.2 Plasma-free samples 243
7.5 Influence of plasma on boron carbide particles 246
7.5.1 Plasma induced change in surface morphology 247
7.5.2 Plasma induced change in surface chemistry 248
7.6 Discussion 254
7.6.1 Boron carbide runaway behaviour at low furnace temperatures 254
7.6.2 Factors affecting sintered density 256
7.6.2.1 Specimen heating: influence of furnace temperature and C-foil insulation 256
7.6.2.2 B_2O_3 I: Effect of heating rate and C additions . 257
7.6.2.3 B_2O_3 II: Effect of plasma 260
7.6.3 Hardness of PPT-FS boron carbide 263

8 Conclusions 265
8.1 Flash sintering and electrical loading of (stabilised) zirconia . . . 265

8.2 Plasma formation during flash sintering of boron carbide 267
8.2.1 Plasma characteristics 267
8.2.2 Effect of plasma on sintering and parameter improvement 268

9 Suggestions for further work 270
9.1 Flash sintering and electrical loading of zirconia and hafnia based ceramics 270
9.2 (Pre-plasma) flash sintering of boron and silicon carbide 272

Appendix A Appendix 274
A.1 Light emission during flash sintering of stabilised zirconia 274
A.2 Flash sintering and electrical loading of stabilised zirconia 275
A.2.1 Resistance test 3YSZ loaded in argon 275
A.2.2 Electrical loading of 8YSZ 276
A.2.3 SEM and EDS 278
A.2.4 XRD 282
A.2.5 Raman Spectroscopy 283
A.2.6 XPS 284
A.2.7 Thermogravimetric Analysis 285
A.2.8 Electrical loading of magnesia stabilised zirconia 287
A.2.9 Calculations 289
A.3 Electrical loading of yttria-doped hafnia 291
A.3.1 Characterisation of electrically loaded yttria-doped hafnia 293
A.3.1.1 Raman Spectroscopy 294
A.3.1.2 XRD 295
A.3.1.3 SEM and EDS 298
A.3.2 Room temperature electrical resistivity 301
A.3.3 Discussion 303
A.3.3.1 Original phase composition 303
A.3.3.2 Local hot spot formation on sample surface . . . 304
A.3.3.3 The FCC rocksalt HfO phase 305
A.4 Plasma formation and characteristics during flash sintering of boron carbide 308

List of Abbreviations

AC ..... Alternating Current

AD ..... Absolute Density

B_4C ..... Boron Carbide

BBR ..... Black Body Radiation

C ..... Carbon

CB ..... Carbon Black

CS ..... Conventional Sintering

DC ..... Direct current

EBSD ..... Electron Backscatter Diffraction

EDS ..... Energy Dispersive Spectroscopy

EPR ..... Electron Paramagnetic Resonance Spectroscopy

ESR ..... Electron Spin Resonance Spectroscopy

FM ..... Ferromagnetism

FS ..... Flash Sintering

FSPS ..... Flash Spark Plasma Sintering

IR ..... Infrared Region

MFP ..... Mean Free Path

MSZ ..... Magnesia Stabilised Zirconia

NIR ..... Near-Infrared Region

NTC ..... Negative Temperature Coefficient

PPT-FS ..... Pre-Plasma Treatment Flash Sintering

PTC ..... Positive Temperature Coefficient

PVA ..... Polyvinylalcohol

PVB . . . . . Polyvinylbutyral

RD . . . . . Relative Density

SEM . . . . . Secondary Electron Microscopy

SiC . . . . . Silicon Carbide

SPS . . . . . Spark Plasma Sintering

TD . . . . . Theoretical Density

TEM . . . . . Transmission Electron Microscopy

TGA . . . . . Thermogravimetric Analysis

XPS . . . . . X-Ray Photoelectron Spectroscopy

XRD . . . . . X-Ray Diffraction

YSZ . . . . . Yttria Stabilised Zirconia

ZTA . . . . . Zirconia Toughened Alumina

1 | Introduction

1.1 History of flash sintering

Ceramics have been known for thousands of years and play an important role in human history. The production of ceramics involves several steps, such as processing the raw materials, forming, thermal treatments, and other potential treatments. The specific processes applied vary greatly depending on the material.

One of the most important steps in the production of ceramics is the thermal treatment, also known as sintering, which defines the final properties of the material. Conventional sintering involves heating the material in a furnace to a certain temperature, sometimes for hours or days, maintaining the maximum temperature for a period of time, and then cooling down the furnace to room temperature. This process not only takes a long time but is also energy-consuming, making the processing and production of ceramics difficult and expensive.

The process of sintering is unfavourable from the perspective of climate change due to the necessity of heating large volumes of gases and solids with high heat capacity to high temperatures, sometimes exceeding 2000 °C. Consequently, alternative sintering methods have been investigated over the last century to achieve faster and more energy-efficient densification. Some alternatives to conventional

sintering use the application of electric fields to heat ceramics more time- and energy-efficiently.

Beside the described development of densification methods, some ceramics, mainly transition metal oxides have been used in various other applications for more than a century. One of the first and most famous practical applications is the Nernst glower [1] which, in its original form, uses a fine platinum wire for heating the actual glower composed of a mixture of zirconium oxide and yttria-erbia oxides to achieve sufficient electrical conductivity. The external heater is needed because the material is "while cold a non-conductor of electricity". [1, 2]

C. Garrard published an article in 1902 in which he proposed a "considerable commercial application and a very useful and prosperous future" for the glower. However, in the same article the behaviour of a Nernst glower over a time of 400 h was investigated and showed an increasing current under constant voltage leading to failure at an average glower lifetime of 380 h. [2]

Even if, against C. Garrard´s proposition, the Nernst glower is usually not used for luminance anymore, various new applications appeared which make use of the same electrical conduction in, or heating of, (yttria-) stabilised zirconia (YSZ) as the fundamental mechanism.

Approximately 100 years ago, in 1922, Alexander L. Duval D´Adrian patented a process under the name *ARTICLE OF FUSED METALLIC OXIDE AND PRO-*

CESS OF PRODUCING THE SAME [3]. The patent describes electrical heating of zirconia from a critical temperature to higher temperatures by resistive heating, leading to the sintering and densification of the material. However, the patented process did not gain much attention.

In 2010, Marco Cologna et al. reported the densification of yttria stabilised zirconia (YSZ) at a furnace temperature of 850 °C in less than 5 s [4]. The process described by Cologna et al. was named *Flash Sintering* and shows great similarity to the process described in the patent by Alexander L. Duval D´Adrian [3] from 1922. The nomenclature introduced by Cologna et al. is still used today, and the published results have attracted significant attention in the scientific community. It remains one of the most investigated topics in the field of ceramic materials science over the past 14 years.

However, as reported for the Nernst glower 120 years ago [2], most of the applications using electrical heating of transition metal oxides are facing major problems. In solid oxide fuel cells (SOFCs) current leakage and lowering of the efficiency is one of the major issues occurring over time. In FS hot-spot formation and inhomogeneous sample heating happen during the process, one of the issues which prevent the process from being applied on an industrial scale. Thus, understanding the fundamental behaviour of transition metal oxides, particularly YSZ, during electrical heating at elevated temperatures is mandatory to solve some of the

reported issues.

1.2 Motivation

After the initial patent in 1922 [3] and the publication in 2010 [4], Flash Sintering (FS) caught great attention in the scientific community and numerous studies and investigations have been published since then. However, some of the fundamental mechanisms, their influence and importance during FS remain unclear.

Several theories about the fundamental mechanisms involved in FS of YSZ, and other materials, have been proposed. However, unambiguous proof is still missing for most of them. Thus, the general question about the fundamental mechanisms during FS of ceramics, particularly YSZ, remains unanswered.

Even though some fundamental mechanisms have not been explained, most researchers agree that the combination of electrical fields and elevated temperatures can lead to changes in defect structure and the fundamental properties of materials. Since FS uses a combination of electrical fields and elevated temperatures, it can be used not only for sustainable densification of ceramics but also to alter material properties. However, the lack of knowledge prevents fully realizing the potential of such processes to produce modified materials that could help overcome future challenges.

Besides FS and field-induced changes in defect structure, the formation of plasmas as another parameter in the processing of ceramics could provide a potential way to produce materials in a more sophisticated way or improve their final properties. For other materials like metals or polymers, plasmas have been commonly used to advantageously change their properties. However, in ceramic processing, plasmas are rather unexplored, and some of the most basic questions remain unanswered. These include the conditions under which a plasma forms, if plasma formation under FS conditions is possible, how a plasma interacts with ceramics, and whether this process can be controlled and used beneficially.

Based on the previously described issues, many possibilities and necessities for further research open up. In this thesis, FS of materials such as YSZ, and boron carbide, was investigated, and subsequent characterisation of the synthesised materials was conducted to understand field-induced changes in the materials. This part of the thesis contributes to the understanding and influence of FS on ceramic materials, oxides as well as non-oxides, whereby the latter ones are significantly less researched.

Furthermore, the formation of plasmas under FS conditions was researched to evaluate if and how plasmas could be involved in the process of producing ceramics and how they can influence it. Such investigations are rare, and the conducted research provides preliminary insights into the potential usage and interaction of

plasmas in the context of ceramic processing.

1.3 Aim and objectives

This Thesis aims to investigate the fundamental mechanisms occurring during FS of ceramics, with a focus on yttria stabilised zirconia (YSZ) as the most investigated oxide ceramics in the perspective of FS and boron carbide (B_4C) a non-oxide ceramics, which was not successfully densified by FS.

Therefore, direct-current flash sintering (DC-FS) is conducted in various atmospheres and under various conditions to achieve different effects such as densification, electrochemical reduction and reoxidation. Subsequently, the material was characterised dependent on the treatment to enable the identification of various parameters on the structure of the material and its properties.

Chapter 2 reviews the most important literature and work conducted on FS of YSZ and carbide ceramics. This includes various observed phenomena reported in the perspective of FS of mainly oxide ceramics. Furthermore, the defect chemistry in YSZ is summarised to enable a better understanding and discussion of some of the results presented in the following chapters. A short section about plasmas, their formation and properties is included due to its importance in this work.

The materials used and the methodology conducted are described in Chapter 3.

This includes the setup used for FS, as well as the powder and green body preparation, but also a short description of the the characterisation methods used.

In Chapter 4, which is the first chapter that includes results, optical spectroscopy was conducted to clarify the origin and kind of light emitted during FS to identify a potential connection and importance of Frenkel defects in FS.

Chapter 5 investigates the field induced changes in the defect structure of YSZ in greater detail to identify the fundamental mechanisms of electrochemical reduction in (YS)Z and its consequences for FS.

The investigation of the circumstances under which a plasma during FS of carbides, such as boron and silicon carbide, forms and its characteristics are aims and objectives of this work described in Chapter 6. Properties of the plasma such as electrical conductivity, optical emission and estimated temperature are investigated.

How a plasma influences and improves the properties and densification of boron carbide during FS is another aim and objective of this work described in Chapter 7, which also includes the optimisation of other parameters important for densification and FS of boron carbide. Relative densities, microstructures and hardness values for the ceramics produced are reported.

In Chapter 8 the results obtained from the different sections will be summarised

and the most important key findings of the chapters are highlighted.

Based on the work conducted in this thesis, potential for future work is described in Chapter 9.

The objectives of this thesis can be summarised as follows:

1. Investigate the fundamental mechanisms active during FS of ceramics under different conditions.
2. Study yttria-stabilized zirconia (YSZ) as a representative oxide ceramic and boron carbide (B_4C) as a challenging non-oxide ceramic for FS.
3. Clarify the origin and mechanism of light emission during FS using optical spectroscopy.
4. Apply DC-FS in various atmospheres to explore densification behavior, electrochemical reduction, and reoxidation phenomena.
5. Explore field-induced changes in defect chemistry of YSZ, focusing on electrochemical reduction mechanisms.
6. Characterise the structure-property relationships of sintered ceramics as a function of FS parameters.
7. Determine the conditions under which plasmas form during FS of non-oxides such as B_4C and SiC, and investigate their properties.

8. Assess how plasma formation influences sintering and mechanical properties (e.g. hardness, density) of B_4C.

9. Derive design strategies and ideal parameters for effective FS of B_4C.

10. Summarise key findings and suggest directions for future research based on the presented results.

2 | Literature Review

To enable a deeper understanding of the results obtained in this work and to summarise the history of some of the processes, the relevant literature will be reviewed in this chapter of the thesis, divided into several sections.

Section I elaborates on FS in general, focusing on related effects observed during and after FS, with an emphasis on YSZ. Insights into work conducted on alumina and boron carbide, the other materials investigated, will also be provided. Furthermore, the defect chemistry in yttria-stabilized zirconia, which is necessary for the discussion of the experimental results is part of this section.

Section II provides a short summary of the most important aspects of plasmas that can be formed under conditions similar to those applied during FS. This includes their classification, formation, properties, and potential interactions with solids.

2.1 Flash sintering and related subjects

FS is a way of sintering ceramics in a very short time and low furnace temperature by applying a sufficiently strong electric field leading to electrical heating of the sample. Usually, a constant electric field is applied to a ceramic green body and the furnace temperature is slowly increased until, at a critical combination of field and furnace temperature, the "flash event" [4, 5, 6, 7, 8] occurs. At the flash event, a term coined in 2013 by Zapata-Solvas et al. [7], Joule heating rapidly increases the specimen temperature above that of the furnace, thermal radiation is emitted [9] in consequence, and the specimen sinters, often in less than a minute.

From the perspective of FS, various materials have been investigated over the past fourteen years, including those that are typically known as insulators, ionic conductors, semiconductors, and conductors.

Furthermore, following the original method of FS (as shown in Figure 3.3), where two electrodes are connected to a sample without any die surrounding it, and no pressure being applied, other techniques of FS and related field assisted sinter techniques have been developed. The most important ones are Flash Spark Plasma Sintering (FSPS) [10, 11], Contactless Flash Sintering (CFS) [12, 13], Flash Microwave Sintering (FMWS) [14, 15, 16], Flash Cold Sintering [17], and Reactive Flash Sintering (RFS) [18, 19].

2.1.1 Models explaining flash sintering

Raj 2012

In 2012, Raj published an investigation about the contribution of Joule heating to the rapid densification observed during FS [20, 21]. In the investigation, data from conventional sintering was used and extrapolated to predict the temperature necessary to achieve densification as rapid as occurs in FS. Equation 2.1 was used to estimate the sample temperature based on equating the electrical power dissipation to the radiative heat loss.

$$T = [{T_0}^4 + \frac{W}{A\sigma}]^{1/4} \tag{2.1}$$

Where:

T_0 = furnace temperature

W = dissipated electrical power

A = surface area of the specimen

σ = Stefan-Boltzmann constant (5.67×10^{-8} W/m^{2}K^4)

The conclusion from this work, and other previous investigations [4, 22], is that Joule heating alone is insufficient to explain FS and the observed rapid densifica-

tion. Thus, the inclusion of an avalanche of defects, such as Frenkel pairs, was proposed [4]. This defect avalanche supposedly enhances the rate of mass transport and enables rapid densification during FS [20]. This theory can be considered the first model attempting to explain FS and the rapid densification.

Since the model solely bases its predictions on values extrapolated from conventional sintering, the fundamental data used to build this model is rather inappropriate because it does not account for other effects on sintering rate under FS conditions other than Frenkel defects, such as a change in heating rate, or electrochemical reduction.

Todd and Luo 2015

Two models explaining the onset conditions of FS were independently proposed around the same time by Todd [5] and Zhang [23] and co-workers in 2015. Although the two models are presented in different mathematic form, they are physically equivalent.

The so-called *flash event* represents the point of thermal runaway of Joule heating [5, 24] in which the flow of current through the sample activates a feedback mechanism that increases the electrical conductivity due to the NTC behavior of most ceramics. This feedback mechanism results in a higher current and an even greater rate of increase in conductivity.

According to the model by Todd et al., the onset of FS, at which the investigated sample undergoes thermal runaway, can be predicted for a critical electric field (E_{crit}) at a furnace temperature (T_0) if radiative heat loss is considered the dominating heat-loss mechanism and the sample conductivity obeys an Arrhenius equation. A mathematical expression by Todd et al. was first proposed for cylindrical samples [5], and later for bar-shaped samples [25]. Since bar-shaped specimens are usually used for FS, the latter is more important and can be expressed by the following equations 2.2 and 2.3:

$$E_{\text{crit}}{}^2 = \frac{4P\epsilon\sigma\rho_0 R}{AQ}(T_0 + \Delta T_{crit})^5 exp[\frac{Q}{R(T_0 + \Delta T_{crit})}] \tag{2.2}$$

$$\Delta T_{crit} \approx \frac{RT_0{}^2}{Q - 5RT_0} \tag{2.3}$$

Where:

E_{crit} = critical electrical field

P = perimeter of the specimen

ϵ = emissivity

σ = Stefan-Boltzmann constant (5.67x10^{-8} W/m^{2}K^4)

ρ_0 = pre-exponential

R = gas constant

A = surface area of the specimen

Q = activation energy

T_0 = furnace temperature

T_{crit} = critical temperature

Based on the previous equation a critical runaway parameter can be calculated by equation 2.4 as follows.

$$1 = \frac{4P\epsilon\sigma\rho_0 R}{AQ}(T_0 + \Delta T_{crit})^5 exp[\frac{Q}{R(T_0 + \Delta T_{crit})}] \cdot \frac{1}{E^2} \tag{2.4}$$

If the critical parameter (equation 2.4) falls below the value of 1, the critical combination of temperature and applied field is reached, and according to the model [25], thermal runaway occurs. This idea is also tested and supported by other researchers [8]. The model is usually applied to ionically conducting materials that exhibit NTC behavior obeying an Arrhenius equation over a wide range of temperature, like YSZ. Furthermore, the runaway mechanism, as proposed, covers the electrical and thermal response of the material under such circumstances, but not the effect of sintering.

However, under many practical conditions of electric field and temperature, ad-

ditional feedback mechanisms occur that modify the precise conditions at which runaway happens. The most straightforward of these mechanisms is the early stages of sintering, which improve the electrical contacts between the powder particles in the green body and increase their cross-sectional area, thereby increasing electrical conductivity in response to Joule heating for oxides as well as carbides [25, 26].

In the specific case of applying direct currents (DC) and electrical fields on YSZ, a further increase in conductivity can occur as a result of electrochemical reduction, due to the difficulty of supplying oxygen (O) ions at a sufficient rate to satisfy the requirements of ionic conduction at the cathode. This reduction causes electrochemical blackening, as well as a bandgap reduction of YSZ, and a significant electronic contribution to the overall conductivity [27, 28, 29, 30].

Effects such as sintering, and electrochemical reduction, lead to deviations of the conductivity from an ideal Arrhenius relation over temperature. If instantaneous values for the activation energy (Q) and conductivity (σ_0) are used, the *flash event* can still be predicted based on these models [5, 24]. However, if these effects are significant, the *flash event*, and the *runaway* is not solely *thermal runaway*. Since it is difficult to separate the various influences directly during the *flash event*, which usually takes a few seconds, separation of these effects by alternative, indirect methods is mandatory to investigate the possibility and significance of their

contribution to the rapid densification happening during FS.

In the following sections, various phenomena detected during and post-FS will be elaborated with a focus on YSZ as the most investigated material in FS and in this work.

2.1.2 Rapid heating during flash sintering

Under certain conditions, the rapidly increasing current in FS leads to an increase in power dissipation and a significant rise in temperature within the material, exceeding the furnace temperature by several hundred degrees.

The investigation into whether rapid heating and high heating rates, without the involvement of an electrical field, enhance the densification of ceramic materials, both oxides and non-oxides, has been studied for several materials [31, 32, 33, 34, 35, 36, 37, 38].

Ji et al. [38] investigated the effect of heating rate on the sintering of 3YSZ with and without an applied electric field, comparing heating using an exothermic self-propagating high-temperature synthesis (SHS) reaction, furnace insertion (FI), and conventional furnace heating (CH). The study, as well as another study about ZnO [23] demonstrated that rapid heating can improve sintering rates by over two orders of magnitude, irrespective of the presence or effect of external fields. This highlights that the primary reason for the rapid densification of 3YSZ during FS

is rapid (Joule) heating, which was not considered in the FS-model presented by Raj and co-workers [20, 21].

However, despite some previous studies suggesting that high heating rates are the primary effects during FS, other effects not explainable by heating on its own have been observed during and after FS, such as the emission of electroluminescence and photoemission [39, 40], as described in the upcoming sections. These effects indicate the involvement of processes in FS beyond just rapid heating, which play a crucial role in this thesis.

2.1.3 Light emission during flash sintering and its relation to the theory of Frenkel defect formation

Several mechanisms which might be responsible for the rapid densification have been discussed in the literature. One of the earliest proposals was that the applied electric field generates an avalanche of Frenkel defects that ionize into highly mobile, charge-neutral vacancies and interstitials and electron-hole pairs [20, 21], as described in section 2.1.1. However, numerous objections have been raised to this proposal. One is that the thermal and electrical characteristics of FS can be completely explained in terms of the thermal runaway of Joule heating [5, 24], elaborated in greater detail in section 2.1.1.

Many papers have now corroborated this [41, 42, 43] so it is not necessary to

invoke avalanches of Frenkel defects to explain this aspect of FS.

Similarly, the rapid densification seems to be primarily a consequence of the rapid heating in FS rather than a direct effect of the electric field [38, 44, 45], as described in the previous section. Again, whatever the detailed mechanism responsible for the effect of rapid heating, it is not consistent with the field-induced generation of Frenkel defects.

More direct evidence against the formation of Frenkel defects as an important mechanism in FS of ionic conductors has been presented by Schie and co-workers, who investigated the field strength necessary for their formation. The conclusion was that field strengths of ≈ 10 GV m^{-1} are necessary for the formation of Frenkel defects in ionic conductors such as zirconia [46], which is six orders of magnitude greater than the fields typically used in flash sintering.

Despite these objections, the Frenkel defect mechanism is still sometimes mentioned as a potential mechanism for FS. A key observation cited in its support and often regarded as a distinctive signature of FS is the fact that specimens emit light during the process [39, 40, 47]. This has been interpreted as electroluminescence resulting from the recombination of the electron-hole pairs created during the ionization and recombination of the Frenkel defects, although other possible mechanisms based on more established defect reactions have also been proposed [9, 48].

There are, however, several unanswered questions concerning these experimental observations. First, although [39] and [40] both concern flash sintering of 3YSZ from the same powder, the primary peaks identified are at markedly different wavelengths (740 nm in [39], 1175 nm in [40]). Secondly, although it is argued that the observed spectra do not conform to the expectation from black body (thermal) radiation, no explanation is given as to why this source of radiation is apparently absent.

A more detailed study of the emission of light during FS of alumina has been published by Biesuz and co-workers [9]. In contrast to Raj and co-workers [39, 40, 47], these authors were able to explain their spectra mainly in terms of thermal emission. Although a few features were identified in the spectrum that were not explained as thermal radiation, they found nothing that could be attributed to electroluminescent phenomena or intrinsic luminescence. [9]

It is important to resolve the apparent contradiction between the reported results and interpretations concerning the emission of light during FS, not just to ascertain the cause of the phenomenon itself but also to test the association of the light emissions with the Frenkel defect theory.

An overview about the published work investigating the light emission during FS or related to it is given in Table 2.1, which includes the experimental setup used to enable an identification of systematic errors in the different experiments and

conclusions drawn from it.

Table 2.1: Summary of the published literature about light emission during flash sintering or related to it including investigated materials, kind of detected light emission assumed by the authors of the specific publications, and spectrometer setup used for the investigation.

Ref.	**Year**	**Material(s)**	**Detected Emission**	**Spectrometer**
[39]	2014	3YSZ	Photoemission	USB4000-UV-VIS (OceanOptics)
[40]	2015	3YSZ	Electroluminescence	AvaSpec-ULS2048 AvaSpec-NIR256-2.5TEC (Avantes)
[49]	2015	8YSZ, SnO2	Unclear but light emission detected when field is applied	Photocell
[47]	2016	SrTiO3, KNbO3	Electroluminescence	No information
[50]	2017	3YSZ, 8YSZ	Electroluminescence	AvaSpec-ULS2048 AvaSpec-NIR256-2.5TEC (Avantes)
[9]	2017	α-alumina, magnesium silicate glass	Thermal radiation, except of low density samples at low current around 680 nm	USB4000-UV-VIS NIR512 (both OceanOptics)
[51]	2020	carbon fiber	Electroluminescence	USB4000-UV-VIS (OceanOptics)
[52]	2022	8YSZ/Al_2O_3	Electroluminescence	No information
[53]	2023	3YSZ	-	-

Some of the work in this thesis investigates the issue using carefully controlled experiments to characterise the effect of the equipment used on the emission spectra and to extend similar analysis methods to those used by Biesuz et al. on alumina [9] to 3YSZ, the ionic conductor most used by Raj and co-workers both to investigate the light emissions [39, 40] and in the justification of the Frenkel defect avalanche hypothesis as an explanation for FS [20].

2.1.4 Defect chemistry in zirconia

Pure zirconia (ZrO_2) is known to undergo various phase transformations, from monoclinic to tetragonal (1173 °C) to cubic (2370 °C) to liquid (2690 °C) with increasing temperature as shown in the Zr-O-Phase diagram in Figure 2.1. These transformations lead to some interesting effects but also cracking of the material during the cooling process in sintering.

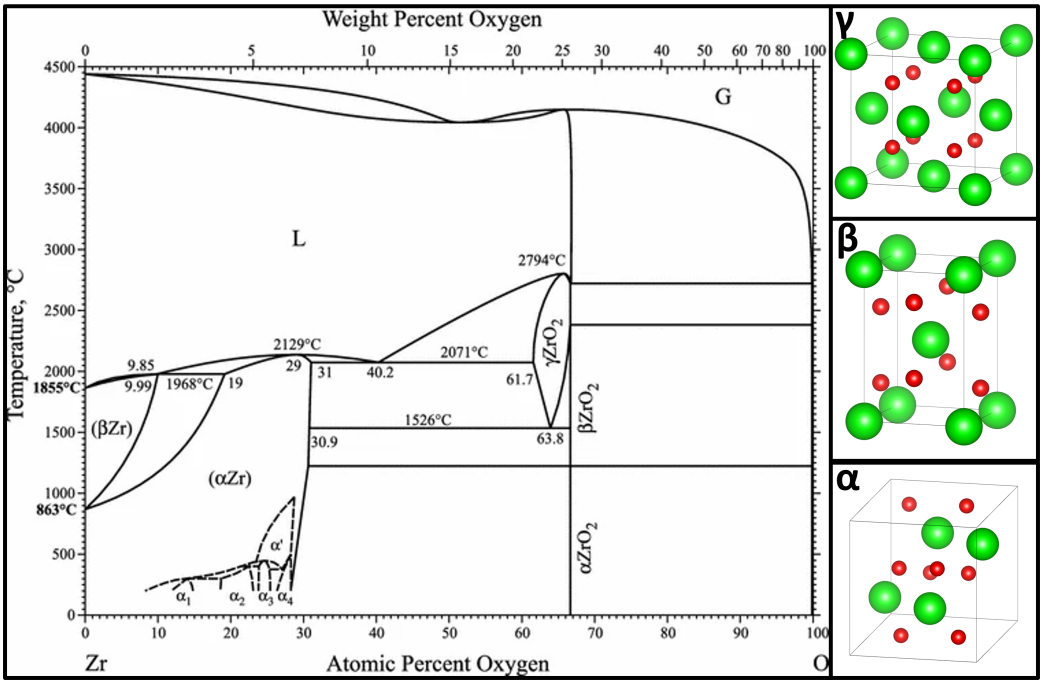


Figure 2.1: Zr-O-Phase diagram according to Okamoto [54], including the crystallographic structure for monoclinic (α), tetragonal (β) and cubic (γ) ZrO_2.

Stabilisation of the tetragonal or cubic zirconia phase at room temperature can be achieved by various mechanisms, such as the inclusion of other di-, tri-, or tetravalent cations, the formation of oxygen vacancies, limiting the grain size,

rapid quenching, or generating (compressive) stress in the material, which could be done by the production of composites like zirconia toughened alumina (ZTA).

2.1.4.1 Inclusion of tetravalent cations

The inclusion of various tetravalent cations, such as Ce^{4+} and Ge^{4+}, can stabilise the tetragonal structure at room temperature due to the reduction of internal strain by dilation of the cation network through the inclusion of oversized Ce^{4+} or scheelite structure formation by undersized Ge^{4+}. The internal strain originates from the small size of the host Zr^{4+} cation which is overcrowded by the oxygen network in an eightfold coordination, also causing a strained cation network. [55]

This size effect can be explained by the cation/anion radius ratio of ≈ 0.6 in ZrO_2. According to the first rule of Pauling, this should lead to a coordination number below 8, which is why the inclusion of larger cations in the cation network favors the eightfold coordination. [56]

2.1.4.2 Extrinsic oxygen vacancies

The inclusion of lower valent elements, such as Mg^{2+} or Y^{3+}, leads to the formation of extrinsic oxygen vacancies and the stabilisation of tetragonal and cubic phase(s). Which phase is being stabilised at room temperature depends on the dopant concentration and the amount of oxygen vacancies created in the material as shown in Equation 2.5 and Figure 2.2 representative for Y-doping.

$$Y_2O_3 \rightarrow 2Y'_{Zr} + 3O^x_O + V^{\bullet\bullet}_O \tag{2.5}$$

Beside the described phase transformation from monoclinic to tetragonal to cubic, further structural changes and phases in YSZ can occur, which depend on the dopant concentration as well as the thermal history. Phase diagrams according to Miller et al. [57] (Figure 2.2 a), Miller and Yashima et al. (Figure 2.2 b), which includes stable-metastable boundary lines, and Viazzi et al. [58] showing the phase formation dependent on the dopant concentration (Figure 2.2 c), have been developed to show the potential phase formations.

Various forms of tetragonal zirconia, *t*-ZrO_2, *t´*-ZrO_2 and *t´´*-ZrO_2, have been identified throughout the last decades. The well-known *t*-ZrO_2, is formed by a diffusional reaction if the high temperature cubic phase is slowly cooled down. The *t´* and *t´´* phases are diffusionlessly formed from the high-temperature cubic phase if it is rapidly quenched and because of that kinetically stabilised.

t´ phase shows oxygen displacement and forms at dopant concentrations around 3-4 mol%. It is characterised by a c/a ratio relatively close to 1. [60]. If *t´* is heated up to high temperature it transforms into high yttria cubic and low yttria tetragonal phases. The cubic phase is then stable at room temperature or forms another tetragonal phase, however the tetragonal phase is transformable and transforms

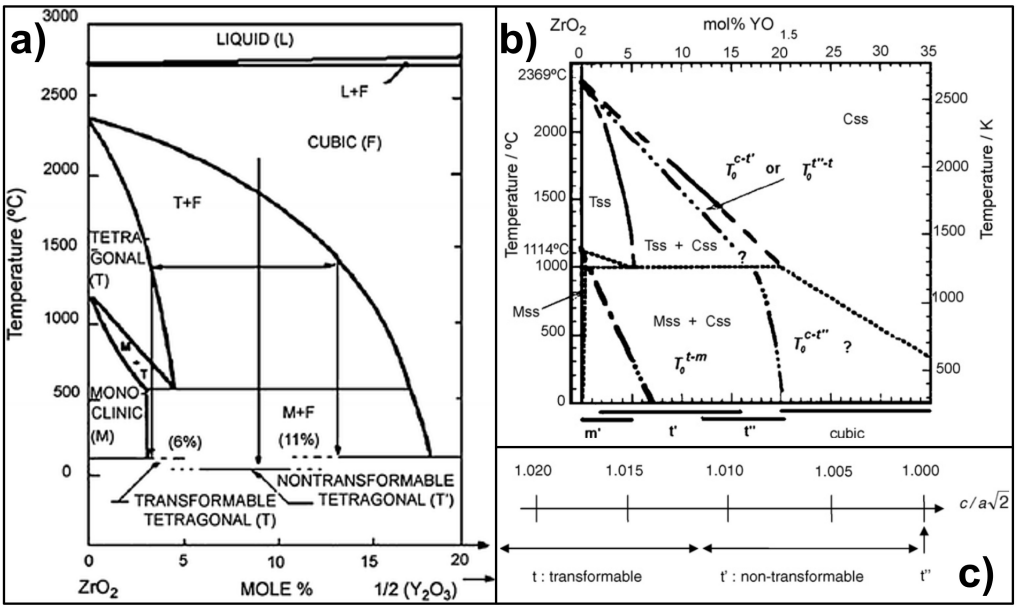


Figure 2.2: ZrO_2-Y_2O_3-Phase diagram according to a) Miller et al. [57], including regions for transformable (t) and non-transformable (t´) tetragonal YSZ; b) according to Miller and Yashima including stable-metastable boundary lines [57, 59]; c) tetragonal forms (t, t´, or t´´) of YSZ dependent on the dopant concentration [58].

to monoclinic phase during cooling if the grain size is sufficiently big or remains tetragonal if the grain size is sufficiently small, the threshold for the transformation toughening effect is usually in the range of 1 μm.[56, 61, 62, 63]

$t´´$ phase shows minimal displacement of oxygen from their ideal position in a cubic structure and forms at yttria concentrations of $\approx$ 5-8 mol%. $t´´$ exhibits an even more cubic-like tetragonal structure, with a c/a ratio very close to 1, or equal to 1. It is difficult to distinguish from the other tetragonal and cubic phases by XRD, which is why it is sometimes described as a cubic phase showing different Raman spectra and neutron scattering patterns compared to the common cubic

YSZ phase described before. [58, 59, 64]

An overview over the various types of tetragonal zirconia phases is provided in Table 2.2, reproduced from [65].

Table 2.2: Summary of the tetragonal zirconia phases and their properties.

Form	**Space group**	**System**	**Oxygen displacement**	Axial ratio (c/a_f)
t	$P4_2/nmc$	Tetragonal	Yes	$c/a > 1$
t´	$P4_2/nmc$	Tetragonal	Yes	$c/a > 1$
t´´	$P4_2/nmc$	Tetragonal	Yes	$c/a = 1$
c	$Fm\bar{3}m$	Cubic	No	$c/a = 1$

2.1.4.3 Intrinsic oxygen vacancies

Unlike extrinsic vacancies, intrinsic vacancies can be generated in zirconia if oxygen is retracted from the lattice without the inclusion of other cations.

The presence of a few intrinsic anionic vacancies at room temperature, reduces the strain in the anionic lattice and leads to a motion of all anions along the tetragonal distortion of the anionic sublattice, which stabilises the tetragonal phase. At higher contents of intrinsic oxygen vacancies the cubic phase can be stabilised because of ordering and clustering of almost all anions in the lattice [66]. This explains the phase transformation in stabilised zirconia by removal of oxygen from the lattice and not the presence of other cations.

The filling of oxygen vacancies by the diffusional penetration of oxygen from water molecules into the material is the explanation for the well-known and re-

searched mechanism of low temperature degradation (LTD) in tetragonal zirconia. LTD is a martensitic phase transformation from tetragonal towards monoclinic zirconia, which happens in humid air or an aqueous environment [67, 68, 69, 70] at room temperature but also slightly higher temperatures around human body (37 °C) or boiling water temperature (100 °C) starting at the grain-atmosphere- and grain-grain-interface, where low coordinated ions tend to be less stable and undergo various interactions and reactions with the environment, even at low temperatures. [69, 71, 72, 73, 74]

To enable an appropriate discussion of various defect structures the most likely defects will be explained and defined in the next paragraphs. Therefore, the nomenclature for point defects in ionic solids and semiconductors proposed by DeSouza and Harrington [75] will be used throughout this work and will be mostly applied to the defects present in (yttria stabilised) zirconia.

Models of tetragonal ZrO_2, one of the most discussed structures in this work, including various defects and oxygen (O)-vacancies, were generated in Vesta [76]. The models are based on an ideal fully oxidised tetragonal ZrO_2 structure as shown in Figure 2.3 a).

Figure 2.3 b) shows the tetragonal structure including an O-vacancy in magenta. In this case the O-vacancy has no real charge and can be described as $V_O{}^0$. In Kröger-Vink notation the relative charge of 2+ is expressed as $V_O{}^{\bullet\bullet}$.

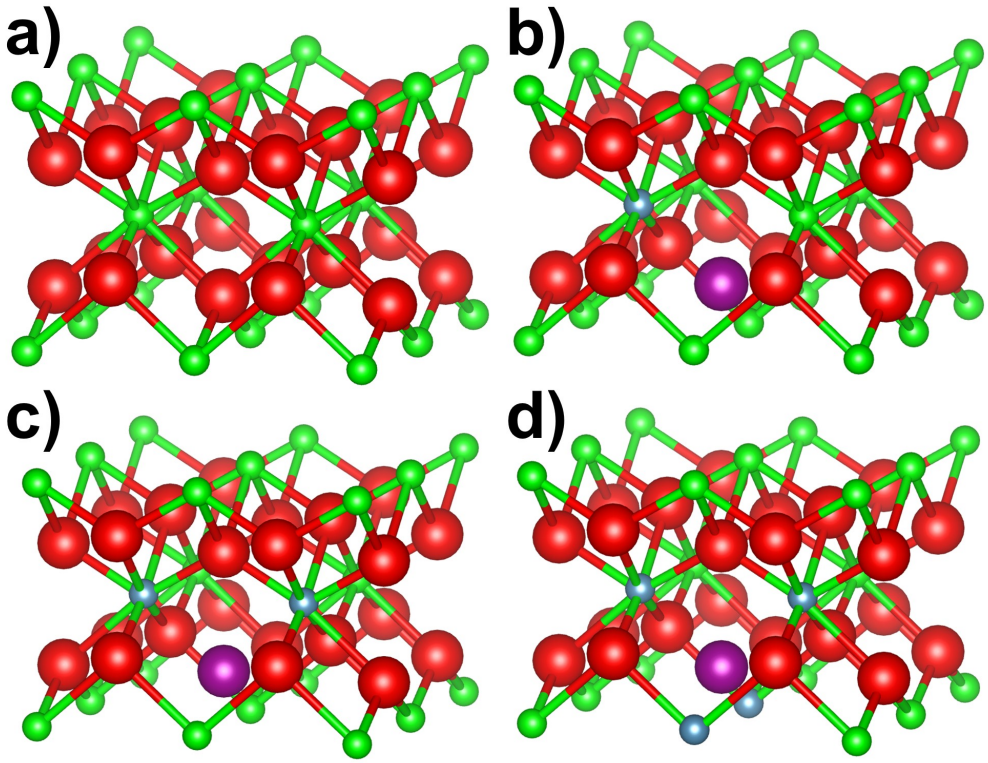


Figure 2.3: a) Ideal and fully oxidised tetragonal ZrO_2 structure showing Zr^{4+} green and O^{2-} red; b) tetragonal structure including an O-vacancy in magenta and one neighbouring Zr^{2+} ion in blue; c) tetragonal structure including O-vacancy and two neighbouring Zr^{3+} ions in blue; d) tetragonal structure including O-vacancy and four neighbouring Zr^{4+} ions in blue.

The charge balance for this kind of defect can happen in three ways:

I) one of the surrounding (Zr^{4+}-)ions lowers its oxidation state by 2, leading to the formation of one Zr^{2+}-ion (Figure 2.3 b). Vacancies filled with one electron are equivalent to removal of an O^{1-}-ion. In this case the O-vacancy can be considered as showing a real charge of 1- shown as $V_O{}^{1-}$, which in terms of Kröger-Vink notation leads to a relative charge of 1+ expressed as $V_O{}^{\bullet}$. Charge balance can happen

if one of the surrounding (Zr^{4+}-)ions lowers its oxidation state by 1, leading to the formation of Zr^{3+}-ions as visualised in Figure 2.3 b) in blue.

II) two of the surrounding (Zr^{4+}-)ions lower their oxidation state by 1, leading to the formation of two Zr^{3+}-ions (Figure 2.3 c).

III) alternatively, a vacancy filled with two electrons is equivalent to the removal of an O-atom. In this case the O-vacancy shows a real charge of 2- described as V_O^{2-} which, in terms of Kröger-Vink notation leads to relative charge of 0 expressed as V_O^X. In this case the charge balance is still working without changing the oxidation state of the surrounding cations. In this case, the surrounding Zr-species will be affected in the same way as shown in Figure 2.3 d), affecting their environment and binding energies (B.E.) compared to the Zr^{4+}-ions surrounded by O-ions.

2.1.4.4 Oxidation states and paramagnetic response

As explained, a change in the oxidation state of the cations surrounding the vacancy is mandatory for charge balance if oxygen is removed, unless the charge balance is maintained as described in Figure 2.3 d).

Table 2.3 shows the known and most important ionic states of zirconium, yttrium and oxygen including their electron configuration, magnetic type and number of unpaired electrons which can occur due to the ongoing charge-balance process.

Since the specific species show different properties, they can be detected by methods such as XPS and EPR, as conducted in this work to define which charge balancing process is most likely and dominant.

Table 2.3: Electron configuration of zirconium (Zr), yttrium (Y) and oxygen (O) based on the noble-gas configuration plus valence electrons; the type of magnetic properties (D = Diamagnetic, P = Paramagnetic) and the number of unpaired electrons.

Ion	Electron Configuration	Magnetic Type	Unpaired Electrons
Zr^{0}	[Kr] $4d^2\ 5s^2$	P	2
Zr^{1+}	[Kr] $4d^2\ 5s^1$	P	3
Zr^{2+}	[Kr] $4d^2$	P	2
Zr^{3+}	[Kr] $4d^1$	P	1
Zr^{4+}	[Kr]	D	0
Y^{0}	[Kr] $4d^1\ 5s^2$	P	1
Y^{1+}	[Kr] $4d^1\ 5s^1$	P	2
Y^{2+}	[Kr] $4d^1$	P	1
Y^{3+}	[Kr]	D	0
O	[He] $2s^2\ 2p^4$	P	2
O^{2-}	[He] $2s^2\ 2p^6$	D	0

The previously described generation of vacancies and oxidation state changes in the material can lead to various changes properties, like the transformation of the crystallographic properties, which will be elaborated in the following section of the literature review.

2.1.5 Field-induced crystallographic changes and phase transformation during flash sintering YSZ

In its early stages of electrochemical reduction, 3YSZ retains the tetragonal structure of the unreduced ceramic. However, in situ synchrotron investigations have shown the appearance of new phases during FS. For short times under electrical loading ($\approx$ 1 min), Lebrun et al. [77] reported an anisotropic residual lattice expansion and a reduction in tetragonality during and after flash sintering. With longer times under electrical load ($\approx$ 5 min) or higher currents, Lebrun et al. [78] reported the appearance of new diffraction peaks, whose positions and intensities correspond closely to those of cubic F, fluorite structure YSZ. These new peaks disappeared over a period of a few minutes when the current was switched off [78].

Similarly, in situ FS-experiments using 8YSZ, which already has the cubic fluorite structure at both room temperature and at sintering temperatures, were conducted by Charalambous et al. [79]. In DC tests, new peaks again arose, this time corresponding to a different cubic F lattice with a smaller lattice parameter of 0.46 nm. Again, the new phase disappeared when the electrical current was switched off. No new peaks were observed when using an AC power supply, suggesting that the new phase was also associated with the electrochemical reduction of the

YSZ. Charalambous et al. suggested that the new phase corresponded to rocksalt structure ZrO, which is not a well-known compound but was reported to exist in the 1950s after oxidising metallic zirconium alloys with steam in the presence of H_2 at temperatures exceeding 700 °C [80].

Recent work on the autoclave (360 °C, 18 MPa, with pure H_2O with 2 ppm LiOH and 1000 ppm boric acid, de-aeration for 34 and 100 days) induced oxidation of zirconium alloys (Zircaloy-4 and ZIRLO), however, concluded that the structure of ZrO was hexagonal [81]. In a further report, ZrO formed by condensation from the vapour phase has been reported to be unstable at high temperature, decomposing by disproportionation to metallic Zr(O) solid solution and $ZrO_{2-\delta}$ [82].

In the above FS investigations, the new phases were not retained on cooling to room temperature, presumably because of reoxidation on removal of the current and subsequent furnace cooling [78, 79]. Morisaki et al. [83], however, reported the formation of zirconium oxynitride $Zr(N_xO_{1-x})$ with $x \approx 0.8$ by applying a controlled DC field to 3YSZ for extended periods of time (250 min) and retained this phase at room temperature in the form of small (< 0.5 mm) regions of golden material where the current had concentrated during prolonged flash sintering [83].

Microanalysis using TEM and EELS confirmed the presence of nitrogen and a diffraction pattern consistent with a rocksalt structure with a lattice constant of 0.46 nm, which corresponds closely to the crystallographic characteristics of ZrN

[84, 85]. It is evident from this that the new phase observed in the in situ investigation of Charalambous et al. [79] probably also contained nitrogen as well as oxygen and is likely $Zr(N_xO_{1-x})$ rather than pure ZrO.

Kathiria et al. [86] transferred samples of 8YSZ from a furnace in which they had been flash sintering, to immersion in liquid nitrogen whilst maintaining the electrical current. When the current was switched off, the specimens were rapidly quenched. The resulting materials had a metallic appearance and conduction characteristics, but no attempt to identify the crystal structure was made.

A better understanding of these phenomena under FS-conditions is essential not only for an accurate determination of the electrical properties of ceramics during FS but also to understand the microstructural development and post-FS properties. There may also be opportunities to synthesise new phases by electrochemical reduction. In order to understand the microstructural developments, some of the work conducted in this thesis focuses on this question and brings together some of the above observations.

In addition to the field-induced crystallographic changes other phenomena, which are not explainable by Joule heating on its own, are discussed in the following paragraphs.

2.1.6 Electrical conductivity of oxide ceramics

2.1.6.1 Electrical conduction in (YS)Z at low temperature and low electrical field strength

The electrical conductivity in stabilised zirconia is usually explained based on oxygen vacancies ($V_O^{\bullet\bullet}$), formed by the inclusion of lower-valent cation additives, which provide the pathway for ionic conduction.

A maximum in conductivity in YSZ is measured at a stabiliser concentration of around 8-10 mol.%, where the formation of the cubic fluorite (FCC) YSZ structure happens due to the overall lattice distortion, formation of (vacancy) clusters and ordering of the structure, originating from the presence of a high amount of oxygen vacancies [66, 87, 88, 89, 90, 91]. If the electrical conductivity at an even higher amount of dopants is investigated, the conductivity does not increase further even if theoretically more vacancies should be formed by increasing the amount of dopants [92, 93, 94]. Based on this observation, it can be assumed that the maximum conductivity is directly associated with the formation of the fluorite structure and reaches its peak around 8-10 mol.% dopant concentration.

However, the complexity of the defect structure in stabilised zirconia, described in the previous sections of the Literature Review, and deviating processing methods are shown in various investigations, which also report the occurrence of differ-

ent activation energies of the electrical conductivity in stabilised zirconia [95]. Furthermore, complications about the unified concept of dopant induced oxygen vacancies as responsible charge transfer mechanism were mentioned in the past [96, 97]. The complications include that electronic conduction in YSZ occurs even under the influence of a low DC-Voltage of < 15 V [98] or 4 V in air [99] due to a change in the defect structure of the material, which changes the activation energies measured [96, 97]. Even if the voltages applied are rather low, the field strength in [99] for instance is in the range of 40 GV/m.

Another influence on the electrical conductivity of YSZ is the presence of low-ordered lattice, grain boundary, and interface structures, as discussed in the context of LTD, which can change the electrical conduction measured in (mostly) polycrystalline YSZ [100, 101, 102, 103].

Since many applications, such as solid oxide fuel cells (SOFCs) and solid oxide electrolyser cells (SOECs) rely on a pure ionic conduction over a long period of time, the understanding of the fundamental conduction, particularly under an electrical load at elevated temperature, is highly important and part of the investigations in this thesis.

2.1.6.2 Electrical conduction of oxide ceramics during Flash Sintering

Unlike many other procedures used for characterising or densifying ceramics, FS combines high electrical fields with elevated temperatures. These unique conditions significantly influence the electrical conductivity of materials like YSZ, typically recognised for their good ionic conductivity. However, many reports indicate that the electrical conductivity of YSZ does not adhere to ideal Arrhenius behavior under these conditions and deviates from typical ionic conduction as described in the previous section. Some studies suggest ongoing electrochemical reduction during FS as a potential explanation for this deviation.

Grimley and Biesuz et al. [27, 30] highlighted indicators of electrochemical reduction. Grimley et al. [27] noted that, according to the calculations and theory proposed by Mitterdorfer and Gauckler [104, 105], the intake of atmospheric oxygen as a charge carrier is severely restricted by the FS-conditions applied and the fundamental defect structure of (8)YSZ. According to the proposed theory and calculations [27, 104, 105], a current level of 0.07 A/cm^2 at 900 °C and 0.18 A/cm^2 at 1200 °C can be maintained in 8YSZ, if it would be purely oxygen-ion based conduction through oxygen vacancies. However, the current levels observed during DC-FS of YSZ typically range in the magnitude of a few A/cm^2,several orders of magnitudes higher than theoretically proposed, indicating that electrical conduction during FS cannot be solely attributed to ionic currents.

Further indication supporting the doubt of a pure ionic conduction during FS of YSZ can be found in theoretical calculations, conducted by the author of this thesis, on the volume of air that would need to be "consumed" per second to maintain specific current levels purely based on atmospheric O-ions. Figure 2.4 illustrates theoretical calculations for various currents at different temperatures at atmospheric pressure and an oxygen content of 21 % in air.

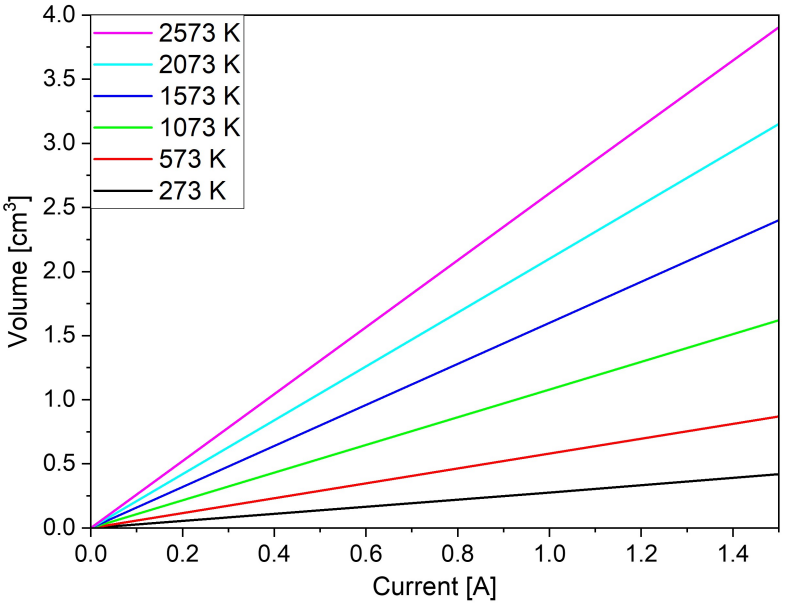


Figure 2.4: Necessary air volume which needs to be consumed per second to maintain various current levels purely based on O-ions extracted from the atmosphere at various temperatures.

In FS, bar- or dog-bone-shaped samples with Pt-paste applied on both ends are typically used. These experimental conditions create a scenario where the area available for atmospheric oxygen to potentially incorporate into the material and function as ionic charge carriers is extremely limited. This limitation supports the

assumption that the intake of oxygen is insufficient to sustain the currents required for FS solely based on O-ions in materials like YSZ. One effect that can occur under such circumstances is blackening of YSZ as described in greater detail in the upcoming section.

2.1.7 Blackening in stabilised zirconia

Various investigations about electrochemical reduction and particularly current-induced blackening in YSZ [106, 107, 108, 109, 110, 111, 112, 113] were published about 30 years prior to the 1999 publication by Janek and Korte [29] which investigates the same phenomenon in greater detail and is often used as a reference, not only in the perspective of FS.

Particularly relevant to this thesis are investigations which were published around 1970 by Thorp, Casselton, Wright and other researchers who reported and investigated current induced blackening in YSZ [108, 109, 110, 111, 112, 113]. In their investigation blackening and a change in the optical absorption were reported. Interestingly, the researchers around that time also used methods such as EPR for the investigation of the fundamental changes in the material, which nowadays is rarely used in this context.

According to the EPR study conducted [94, 95, 106, 107, 109, 112, 114], various effects were seen but no strong changes were detected due to blackening and only

weak new signals were detected which were associated with the ongoing blackening as will be discussed later.

According to their, and the interpretation by some other researchers [94, 95, 106, 107, 109, 112, 114], electrons are injected into the material from the cathode. This electron injection leads to the formation of defect centres, blackening and the lower resistance of the material which moves the virtual cathode across the material. In a first stage electrons are trapped by vacancies and later aggregates might be formed but no clear evidence is given. Potentially this could lead to the formation of colloidal zirconium metal particles, as was suggested by Wright et al. in 1973 [111], even if there was no evidence for the formation of such particles up to ten years after this postulation.

Moghadam et al. investigated the blackened region in scandia stabilised zirconia by TEM and found a primitive cubic grain boundary phase consisting partly of non-stoichiometric $ZrO_{2-\delta}$ with a size between 10 and 20 nm [113], however no change in lattice parameter compared to the cubic fluorite (FCC) parent lattice was observed in this investigation as well as other investigations which also reported no change in elastic constants [108].

Blackening of ceria stabilised zirconia was also reported in the past [115, 116], which indicates that the blackening mechanism seems to be independent of the kind of additive but the fundamental structural change in the blackened region

was not fully explainable for these materials.

Like briefly mentioned, a lot of the work about electrochemical reduction from around the 1970s was picked up by various researchers who reported the phenomenon of current-induced blackening alongside other athermal effects in the context of FS [28, 29, 30, 117], however, often the connection between results published around the 1970s and the more recently published results about FS is missing.

The most recent and still valid explanation for the blackening phenomenon was proposed by Janek and Korte and their visualised explanation can be seen in Figure 2.5. It is shown that on the cathode side electrons get injected into the material and extraction of oxygen on the anode side, where oxygen vacancies get injected to maintain the charge balance. At the reaction front between the blackened and white/grey material an internal reduction process happens. According to the conclusion in [29], the blackened material exhibits a higher electronic conductivity than the overall conductivity of the less reduced material, leading to a high transport coefficient of oxygen, whereby grain boundaries are seen as barriers for oxygen transport because blackening in polycrystalline samples is rather slow compared to singly crystalline specimens under similar conditions.

The reconsideration of literature about electrochemical reduction in YSZ and its blackening shows that the reported fundamental mechanisms are not consistent

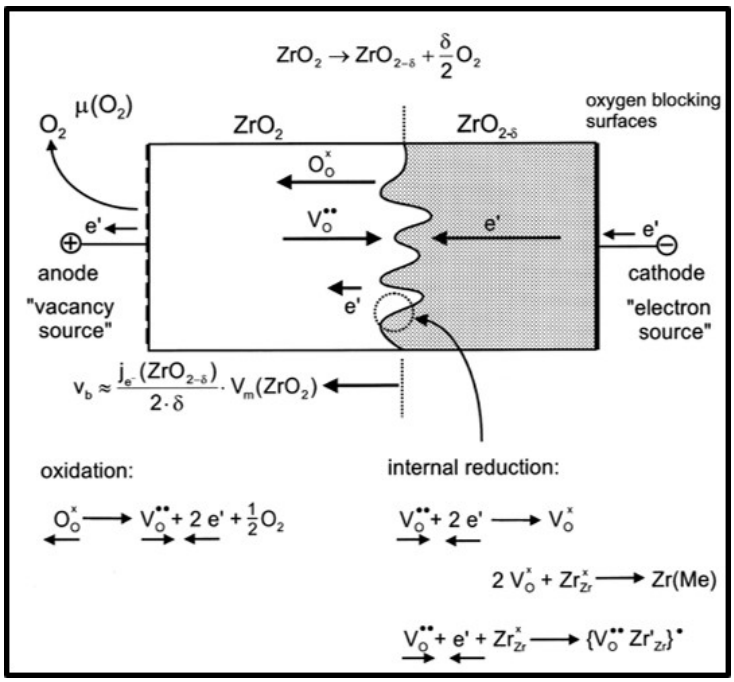


Figure 2.5: Electrochemical reduction of zirconia and local potential variation for an ideally oxygen ion blocking cathode according to Janek and Korte, reproduced from [29].

throughout the literature. The effect of electrochemical reduction and blackening of YSZ under FS conditions will be addressed in this work.

2.1.8 Other athermal effects suggested during and post flash sintering of YSZ

One of these other effects is post-FS luminescence in YSZ under UV-radiation, which was also found in other materials [118, 119, 120, 121, 122]. The UV activated post-FS luminescence intensity, mainly in the blue region around 440 nm, strongly increased after AC and DC isothermal flashing, which is most likely

linked to a changed defect structure.

Enhanced or even abnormal grain growth of YSZ is another of the observed effects [123, 124] detected in the centre of the cross section of the samples. Abnormal grain growth was also reported for flash sintered corundum, however the orientation and location of the abnormally grown grains in corundum is different to the results reported for YSZ, in a way that in corundum the abnormal grains are located in a blackened region of the sample which is not in the centre of the cross section but rather close to the surface [125].

Aligned growth of single-crystalline ZnO structures was observed during FS of Bi_2O_3-doped ZnO in the anode direction at high current densities [24]. Unlike the AGG described before, these structures grew on the cracked surface of the sample, where usually no or only a small current should flow, which is why the classical Joule heating can not explain this phenomenon on its own, even if a liquid phase forms during the process.

Another effect is an enhanced plastic deformation [126, 127, 128, 129, 130] reported at high currents/fields or atmospheres with low oxygen partial pressures. According to the researchers the dominant mechanism of plastic deformation in 8YSZ is grain boundary sliding [129, 130].

Accelerated crack healing in 8YSZ polycrystals under an electrical load (DC) was reported at 800 °C furnace temperature after applying 100 V in the voltage-

controlled stage and a constant power dissipation of > 100 mW/mm^3 is another athermal effect linked to an increased diffusion. [131, 132]

If, where and which athermal effects appear, depends on the FS-conditions applied for YSZ but also other materials, which are mostly transition metal oxides. Since the effects do not show any direct relation to each other, the question about their potential connection arises and therefore the defect structure of, in this case, (yttria-stabilised) zirconia needs to be revisited.

2.1.9 Flash sintering of carbides

Pressureless flash sintering

Only a few publications about FS of semiconducting materials such as carbide ceramics have been published up to now. A preliminary investigation about FS of SiC was published by Zapata-Solvas et al. in 2013, who used a modified hot-press setup [7]. This investigation is important since it shows that FS of covalent ceramics up to 88 % RD is possible at 1170 °C environmental temperature under 50 V/cm and a 15 A current. A continuation of this work was published by Gibson et al. [26] who managed to FS SiC up to 95 % density in a conventional alumina tube furnace at 1500 °C. The influence of various additives on FS of SiC was investigated by Candelario et al. who reported an increase in RD by increasing the additive-content [133], showing the importance of the right additives and power

specifications for FS.

Rosenberger et al. investigated pressureless FS of B_4C by applying fields up to $\approx$ 280 V/cm at environmental temperatures of > 600 °C and a power dissipation of 100 W. They reported a localised densified area within the samples due to current concentration but no further investigation was reported since [134]. Compared to the work about SiC the environmental temperature is significantly lower and the power is in the range of 20 % compared to [26], which could suggest potential parameter adjustments to improve the densification of B_4C by FS.

Flash Spark Plasma Sintering

Other investigations followed but most of them used pressure-assisted FS described as flash spark plasma sintering (FSPS). In an investigation by Grasso et al. FSPS of α- and β-SiC up to 96 % RD in 16 s [10, 135] was reported by conducting a current of > 1 kA through the material. Comparable work was also conducted by Olevsky [136] Demirskyi [137] and Sharma et al. [138].

FSPS of B_4C was reported by Niu and Wu et al. [139, 140] who managed to densify B_4C in less than 1 min up to > 99 % RD by running a current between 1.4 and 2 kA through the material which showed limited grain growth (< 3.5 μm), supposedly caused by short sinter time and plastic deformation.

FSPS WC up to 95 % RD in less than 10 s under AC (50 Hz) 2.8-4.5 kA/cm^2 and

an applied field of up to 9 V/cm was reported by Mazo and co-workers [141, 142, 143, 144].

FSPS of $Zr_{1-X}Ti_XC$ was conducted by Li et al. who achieved RD of 98.6 % and hardness of > 20 GPa in a solid solution composition of $Zr_{0.4}Ti_{0.6}C$ [145].

Comparison and conclusions from FS(PS) of carbides

All the reports show that the NTC behaviour, known from oxides such as YSZ, is not mandatory to achieve FS and a more rapid densification compared to conventional sintering. However for some high temperature semiconducting materials such as B_4C feasibility of pressureless FS remains unclear.

The reports about FS(PS) of carbides show fundamental differences such as possible densification with and without pressure, whereby limitation in sample geometry and cost of equipment are significant drawbacks in FSPS. Furthermore, applied conditions are different in a way that in FS currents of tens of amps are applied, whereas in FSPS currents in the range of kA are applied.

Since carbide sintering temperatures in CS, FS as well as FSPS are in the range of $\approx$ 2000 °C $\pm$ 200 °C, which is $\approx$ 400 °C below the melting temperature for B_4C and $\approx$ 700 °C for SiC, it can be concluded that in some investigations, which are falsely described as FSPS, most of the current, which is 100-1000 times higher than in FS, does not flow through the material itself if its conductivity does not

change by several orders of magnitude. If it would, power dissipation and the following Joule heating of the material in FSPS would lead to serious degradation which becomes clear if it is considered that the current flow contributes by the power of 2 to the power dissipation at a constant resistance ($P = R \cdot I^2$).

An indicator for this assumption can be found by the comparison of the detected resistance of 2.7 Ω during pressureless FS of SiC [26] and 0.01 Ω in FSPS [10] of SiC. In the latter a C-felt is wrapped around the SiC disk shaped sample which most likely conducts most current and should not be described as FSPS. Furthermore, the measured resistance drop which is two orders of magnitude during FS due to an ongoing densification [26] and only $\approx$ 50 % during FSPS [10]. Based on that FS can be seen as direct Joule heating, whereas FSPS in the case of [10] is rather indirect heating and more comparable to pressure assisted UHS or simply SPS rather than FS.

Due to the high sinter temperatures ($\approx$ 2000 °C), the potential for energy and time savings by FS semiconducting carbides compared to conventional sintering is even bigger than it is for oxide ceramics. Due to that part of this work is to investigate the densification of B_4C by pressureless FS. The comparison to the previously described oxide materials enables the cross comparison of the obtained results.

Since high temperatures in the range of 2000 °C, electrical fields and currents in

the range of kA are present during (F)SPS of carbides, other phenomena, such as atmospheric breakdown and the following plasma formation could happen under such a combination of process parameters. The inclusion plasmas in processes such as (F)SPS and FS is often proposed, however without actual evidence for or against it. Because of that, a potential plasma formation/involvement in processes such as FS will be addressed in this work and a the following section of the Literature Review.

2.2 Plasmas under (flash-) sinter conditions

The involvement of plasmas in the processing of polymers and metals is quite common and often used for several processes such as etching, cleaning, activation, sputtering, etc. However, this is not the case in ceramics processing.

Since FS combines high electric fields and elevated temperatures, some researchers have proposed that formation of plasmas may also be important and one potential mechanism which may be responsible for the rapid heating and densification during FS [146, 147, 148, 149, 150].

It is known that plasmas can be used to achieve rapid heating (10^3 K/min [151]) and densification of metal [151, 152, 153] and TiO_2 nanopowders, which were sintered up to 98 % in a DC plasma [151]. 3YSZ has also been densified using Joule heating of the compact by a current supplied using a cold plasma [13]. Although the conditions in these investigations are far from those normally used for FS, it can be concluded that plasmas provide a potential source of heating that can be useful to densify (ceramic) powder compacts.

In addition, improved microstructures have been demonstrated for carbide and oxide ceramics if a plasma treatment is applied to ceramic powders prior to conventional sintering, [154, 155, 156]. Such plasma pre-treatments can also change the surface chemistry of alumina powders, leading to more stable water suspen-

sions used for shaping of the green body [157, 158], leading in turn to improved final microstructure in the sintered ceramics.

The inclusion of plasmas as a mechanism which improves densification is also often discussed in the context of Spark Plasma Sintering (SPS). Various experimental investigations have concluded that no plasma is formed under the usual conditions [159, 160, 161, 162]. However, plasma has been reported if SPS is conducted at elevated temperatures (> 1150 °C) [159] or using conductive powers without the surrounding graphite die at an applied voltage of 50 V (500 V/cm) [160], i.e. in conditions more similar to FS.

Various investigations of FS of oxide ceramics have suggested that atmospheric breakdown followed by plasma or arc formation is possible, even at room temperature. Plasma formation during FS occurs if the applied voltage and electrical field is sufficiently high, usually in the range of several kV/cm, especially if the sample shows an increased moisture content, or at decreased atmospheric pressure [13, 146, 147, 148, 149, 161, 162, 163]. In some of these investigations a *gas-discharge induced FS* process was investigated [161, 162, 163, 164], which enabled heating of the powder compact by the surrounding plasma until the conductivity of the sample exceeded the conductivity of the plasma, leading to a transition towards the conventional FS in which Joule heating by passage of current through the sample dominates. Furthermore, it is suggested that the plasma for-

mation is based on surface flashover which happens within a few microseconds.

Although these previous studies demonstrate that a plasma or arc can heat the material by several hundred degrees, the mechanisms involved have not been explored in detail. Also, potential influences of the surrounding plasma on the material and its sintering other than heating, and whether the plasma can enter the powder compact have not yet been studied. Furthermore, only oxide ceramics have been investigated which opens the question about potential plasma formation and its effects during FS of non-oxide ceramics. The potential formation of plasmas at the lower voltages normally applied in FS also remains unexplored.

2.2.1 Plasma classification

Therefore the most basic aspects of plasmas, their formation and properties will be summarised. Figure 2.6 shows the four fundamental states of matter including an illustration for cold and thermal plasmas, whereby thermal plasmas are higher in (kinetic) energy and charged particle motion.

Beside the plasmas which can be formed in a laboratory environment, a variety of plasmas occur under more extreme conditions as they appear in the universe. An overview shows some different types of plasmas is shown in Figure 2.7, where the rather low energy side is the more interesting one, particularly Arcs and Glow Discharges are relevant in this work.

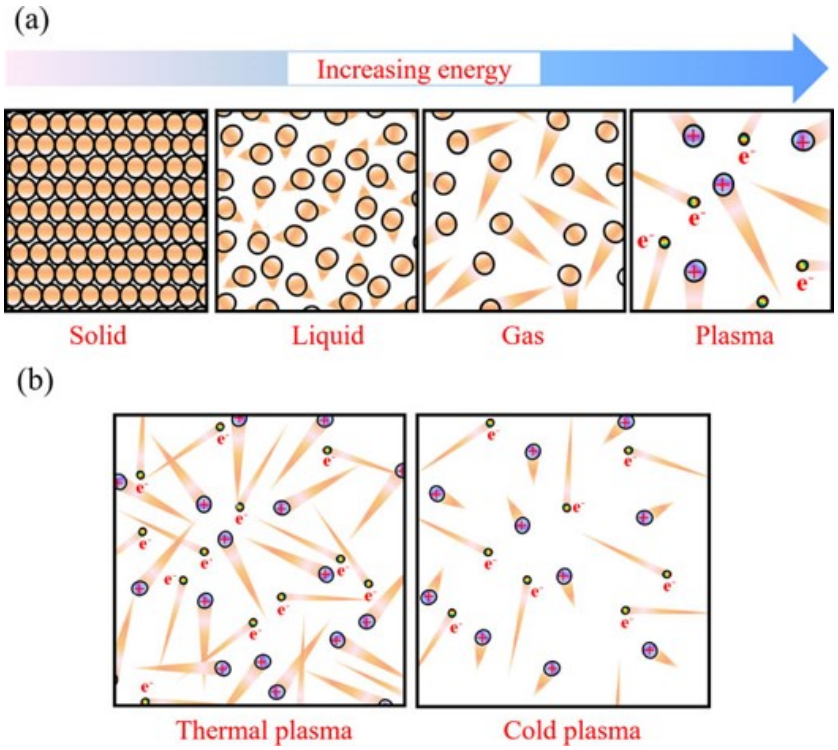


Figure 2.6: a) visualisation of the four fundamental states of matter; b) schematic illustration of thermal and cold plasmas. Triangles represent the thermal motion strength of the particles which are either charged ions or electrons, but no neutral atoms are shown. Image reproduced from [165].

Since most of these plasmas are not very interesting in the perspective of materials science and their practical application, another definition is more interesting and can be made dependent on the applied electrical field and current flowing through the plasma as shown in Figure 2.8, which applies to DC discharge. As in Figure 2.7, Figure 2.8 Arc and Glow Discharge regions are described based on the voltage applied and current flowing.

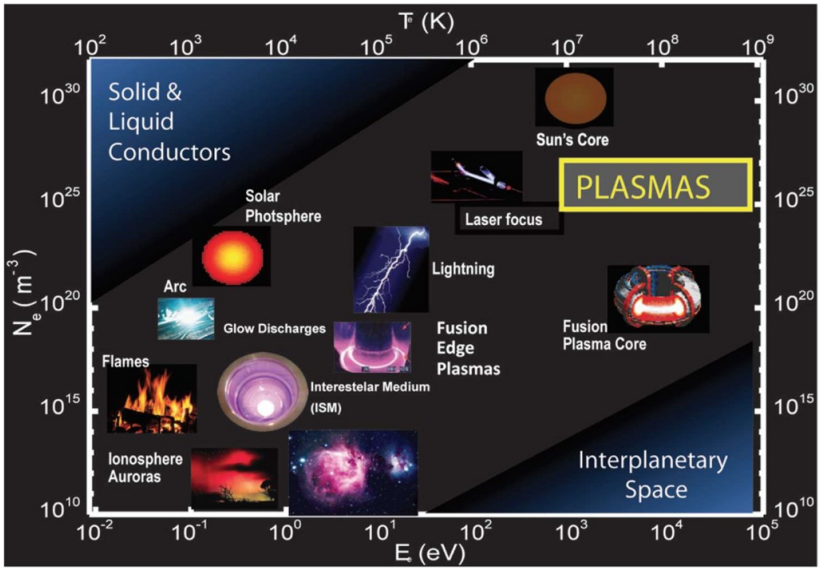


Figure 2.7: Plasma overview dependent on the electron energy and density. Reproduced from [166].

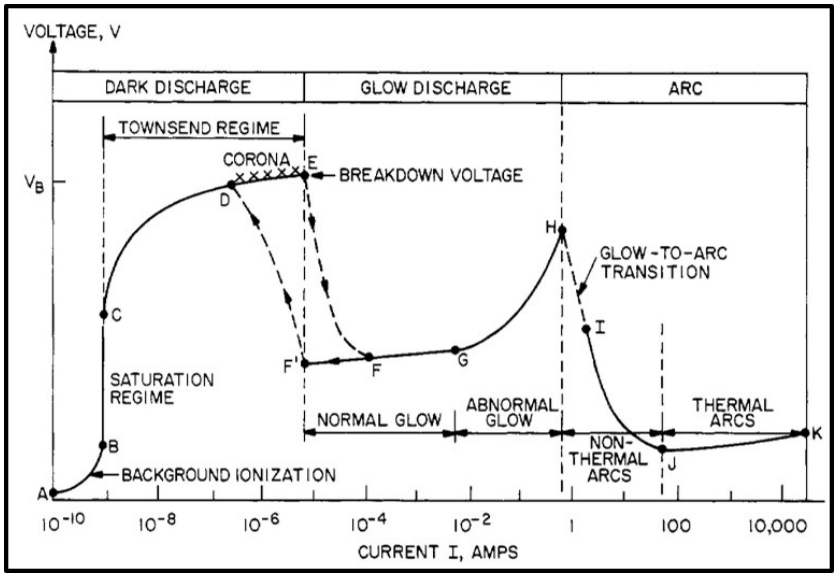


Figure 2.8: Definition of various types of DC-discharges dependent on their characteristic voltage-current behaviour, reproduced from [167].

2.2.2 Plasma formation

Regarding the formation of plasmas certain requirements have to be met. [167, 168, 169]

I) The voltage needs to exceed a certain voltage, usually described as breakdown voltage (v_B). This voltage depends on various factors such as type of particles, particle density, which itself is dependent on the pressure and temperature, and distance between the electrodes.

II) Other mechanisms such as (surface) flashover can lower the necessary v_B due to charge transport processes along the gas-solid interface, which needs to be considered as soon as any solid material is located within the electric field.

III) Sufficient charge carriers must be present or formed to sustain the plasma for a certain time because otherwise the plasma collapses after its formation. Charge carriers can be supplied by effects such as thermionic emission of electrons from the cathode.

Since all requirements are possibly met during FS or SPS, the potential for plasma formation is investigated in this work, its involvement in such processes is often speculated about.

2.2.3 Plasma properties

Debye length

One important parameter in plasmas is the Debye layer which describes the thickness of the shield of particles with an opposite charge which form a layer around an electrically charged or conducting object inside a plasma, and can also be described as a sheath. The Debye length describes the shortest possible distance over which a charge separation can occur. [167, 169]

Mean Free Path

The mean free path (MFP) is considered as the average distance through which a particle travels before it collides with another particle. This can lead to a change in direction of travel, energy transfer or other interactions.

Electrical conductivity

Since electrons and nuclei are separated, both can be used for electrical charge transfer leading to a certain level of electrical conductivity, which depends on several factors such as ionisation degree as well as applied voltage, electron and ion temperature, and the kinetic energy and length scale over which the charges are transferred. Dependent on the conditions, the electrical conductivity of plasmas can exceed the conductivity of solid materials. However this strongly depends on

the type of plasma and the applied circumstances.

2.2.4 Plasma interactions with solids

Various interactions between plasmas and solid surfaces can happen dependent on the material and the kind of plasma. This involves, cleaning or activation, thermal diffusion treatments, ion-beam implantation, plasma ion implantation, sputter deposition of thin films and plasma chemical vapor deposition as well as plasma etching [167].

Cleaning, for instance, can be divided into passive and active cleaning, whereby passive cleaning happens when the solid work piece is affected by the plasma but does not work as an electrode, as is the case in active cleaning. Usually, thin layers up to 1 μm are affected by such cleaning processes.

Important parameters for passive cleaning are gas type and pressure, dissipated power, gas flow rate and geometry, voltage and frequency of operation, discharge geometry, electrode characteristics and magnetic induction. [167]

Beside cleaning, etching of solid surfaces is another interaction which is used in the field of microelectronics, which usually uses RF or microwave glow discharge plasmas providing the active species necessary for etching in form of energetic ions. Furthermore, masks are often used to define the section of the workpiece which requires etching as shown in Figure 2.9, however, if no mask is used the

material is etched everywhere where the plasma can interact with the solid. Microelectronics, metal surface treatment or processing polymers are only a few of the broad range of practical applications of plasmas in current usage.

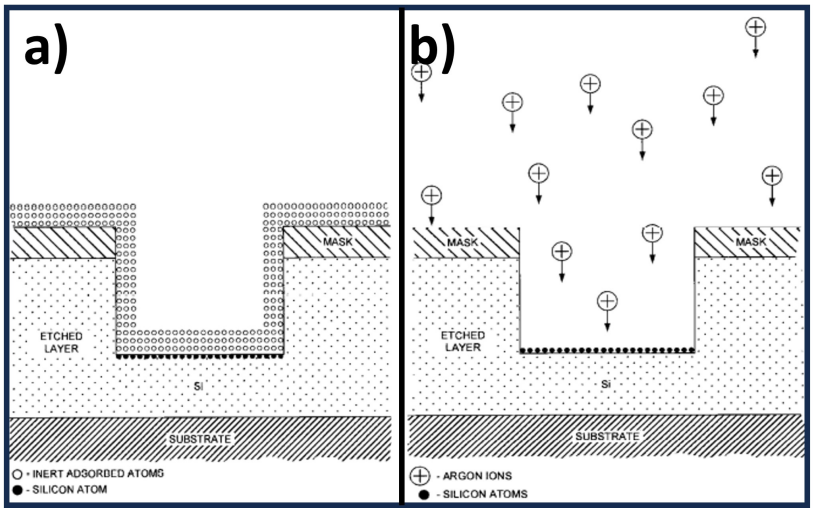


Figure 2.9: a) partially etched trench before plasma etching with adsorbed inert monolayers; b) impingement of energetic (Ar-)ions on solid surface after removal of adsorbed monolayers. Reproduced from [167].

In this thesis some of the work conducted investigates the formation of plasmas and potential interactions between plasmas occurring under (flash) sintering conditions and (boron) carbide ceramics before and during the rapid densification.

3 | Methodology

3.1 Sample preparation

3.1.1 Investigated powders

Zirconia powders

The FS-behaviour of various compositions of stabilised zirconia (ZrO_2), shown in Table 3.1, was investigated with a focus on 3YSZ and 8YSZ. Some of the powders include *binder* highlighted with a B, others are *easy to sinter* and include 0.25 wt.% Al_2O_3 labeled with an E, in the name of the powder.

Most of the powders are commercially available, however, some of the compositions mentioned in the Appendix (TZ-1.5YB and TZ-10YB) were prototypes provided by Tosoh Corp. Japan, results are shown in the Appendix. Magnesia stabilised powder was provided by Daiichi Corp.

All powders include impurities, mainly HfO_2 (< 5 wt.%), but also SiO_2, Al_2O_3 and Fe_2O_3 summing up to an impurity amount of approx. 0.4 wt.%.

Table 3.1: Investigated (stabilised) zirconia powders with specifications from product data sheets.

Name	Manufacturer	Stabiliser	Stab. Ratio [mol%]	D_{50} [μm]
TZ-3YB	Tosoh Corp.	Y	3	0.04
TZ-8YB	Tosoh Corp.	Y	8	0.04
M8SZ	Daiichi Corp.	Mg	8	0.04

Carbide powders

Boron carbide (B_4C) and silicon carbide (SiC) powders were used in this research.

Table 3.2 shows the specific parameters for the carbide powders investigated.

Table 3.2: Investigated carbide powders with specifications from product data sheets.

Material	Name	Manufacturer	D_{50} [μm]	Surface area [m^2/g]	B:C ratio
B_4C	HD 20	Höganäs	0.3 - 0.6	22.0 - 27.0	3.7 - 3.9
SiC	Starceram	Höganäs	0.65	23.0 - 26.0	-

3.1.2 Powder processing

Additives

Additives used in this work are listed in Table 3.3. Some of the additives were used as organic binders, others were used as binder and for C-sources for the reduction of the oxide layer during production of carbides.

PVA was mainly used as a binder for oxide ceramics because of its solubility in water. A binder content of 1 wt.% of the weight of the powder was used to enable

appropriate uniaxial pressing of the powders. PVB was mainly used as binder for carbide ceramics with ethanol as a solvent to prevent unnecessary oxidation of the carbide particles.

The effect of additional carbon between 0 and 6 wt.% on the densification of B_4C via FS was investigated.

Table 3.3: Additives with specific parameters according to the specific product data sheet.

Material	Manufacturer	Kind of Additive	Other Function
Polyvinyl alcohol (PVA)	Sigma Aldrich	Binder	-
Polyvinyl butyral (PVB)	Sigma Aldrich	Binder	C-source
Monarch 700 (CB)	Cabot	Carbon black	C-source

Dispersion of powders

To achieve a homogeneous binder and carbon distribution in the materials investigated, the liquid solvent was heated up to 60 °C under constant magnetic stirring and the binder was slowly added into the heated solvent and homogenised for at least 15 min while stirring.

For oxides, the ceramic powders were added to the binder-containing solvent and magnetic stirring was conducted for at least 30 min.

For carbides, the CB and 15 min later the B_4C-powder, were added into the solvent and the stirring was maintained for another 30 min.

The slurries produced were ultrasonicated 5 times for 1 min to avoid overheating. For some powders subsequent ball milling in a Nalgene bottle was conducted for 24 h.

As the next step the homogenised slurry was dried in a rotary evaporator for at least 2 h under vacuum at a water bath temperature of 55 °C. The powder was sieved to 150 μm to generate appropriately sized particles for further processing.

3.1.3 Sample processing

For FS the (prepared) powders were pressed into bar-shaped samples by filling them into a stainless steel die (Figure 3.1) and subsequently pressing uniaxially at 100 MPa.

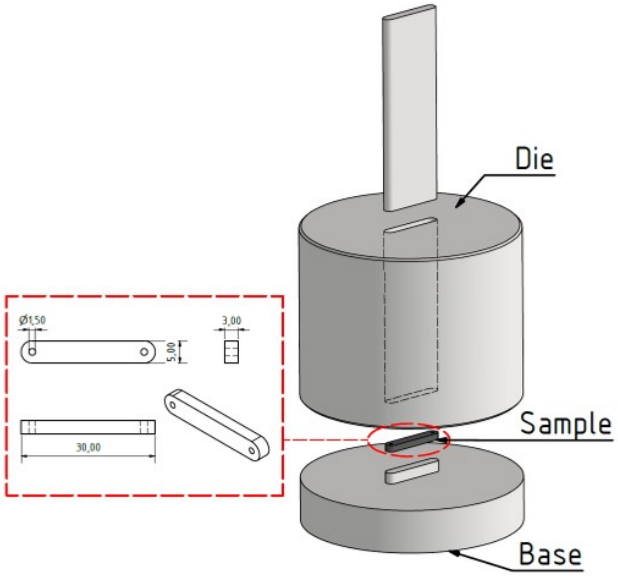


Figure 3.1: Stainless steel die for uniaxial pressing of bar-shaped samples.

After uniaxial pressing, samples were wrapped into vacuum film and heat-sealed under vacuum for cold isostatic pressing (CIP) under a pressure of 200 MPa as shown in Figure 3.2.



Figure 3.2: Wrapped and heat-sealed sample in vacuum film for cold isostatic pressing in oil/water-emulsion. Sample is approx. 30x5x3 mm^3 in size.

Afterwards, holes were manually drilled at both ends of the sample using a 1.0 or 1.5 mm drill. The holes were used for connecting the metal wire electrodes, necessary for FS, to the samples.

3.2 Thermal treatment

3.2.1 Debinding

Debinding oxide ceramic green bodies was conducted at 600 °C for 1-2 h in air in a furnace heated with a rate of 300 °C/h.

Debinding carbides was conducted in argon (Ar), with otherwise equal settings. Debinding in Ar led to some residual carbon, confirmed by Raman spectroscopy, which is why the added binder (PVB) can be seen as an additional carbon source.

3.2.2 Conventional sintering

Conventional sintering was usually conducted either in an alumina tube furnace, which can be atmosphere controlled, or in a box furnace in air. If not stated otherwise, heating rates of 300 °C/h up to 1400 °C were applied and held for 2 h at maximum temperature to sinter samples either as reference materials or before electrical loading.

3.2.3 Flash sintering and electrical loading

3.2.3.1 Flash sinter setup

FS and electrical loading of debinded samples was executed in a horizontal alumina tube furnace with a tube of 120 cm length and an inner diameter of 7 cm, which was calibrated with at least one external thermocouple prior to the experiments.

The overall furnace setup, including electrodes and sample, is depicted in Figure 3.3. A smaller alumina tube was used to hold the metal electrodes in place, which were bent around another alumina insert. This setup enabled an appropriate po-

sitioning of the sample in the center of the main tube where the hot region of the furnace is.

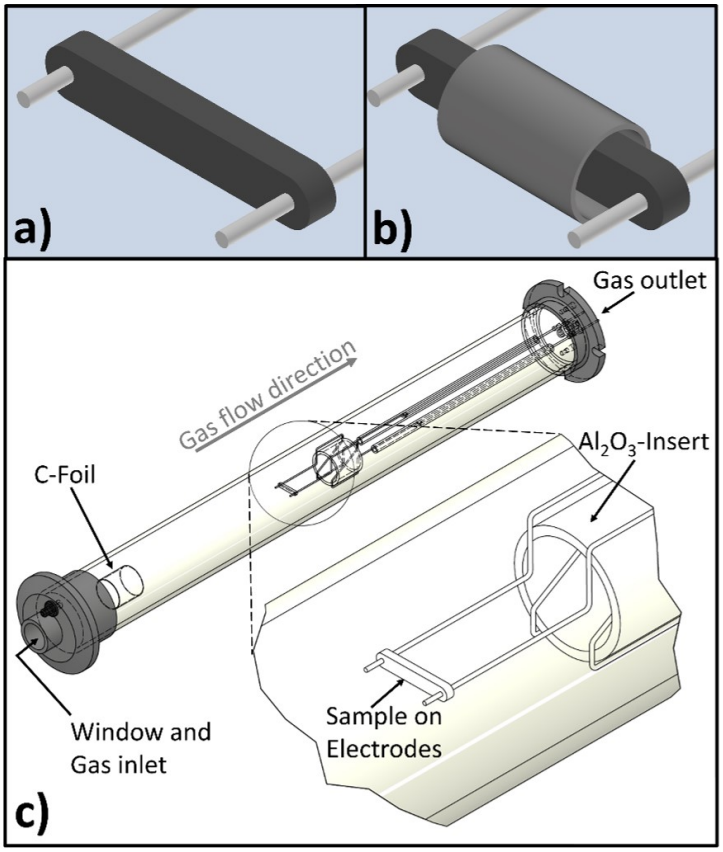


Figure 3.3: Schematic diagram of a sample mounted on tungsten (W) electrodes, a) without and b) with C-foil loosely wrapped around the sample for thermal insulation. Cathode (-) is on the right and the anode (+) on the left side of the sample; c) flash sinter setup including horizontal tube furnace, bent electrodes, alumina insert, gas in- and outlet, window and (if applicable) graphite-foil.

A gas inlet was installed on the left of Figure 3.3, the corresponding outlet being installed on the right of the furnace where the electrode wires also entered the furnace. Prior to furnace heating, both ends were sealed to make the setup gas-tight and enable atmosphere control and change during electrical loading using

the connected compressed gas cylinders. A window was installed on the left end of the furnace to record the FS-process with a standard video camera.

For FS oxide ceramics, platinum (Pt) or nickel (Ni) wires were used as electrodes. To reduce contact resistance between the metal wires and the sample, Pt-paste was applied on both ends of the sample. In the case of FS carbides, tungsten (W) wires were used and carbon paste was applied to reduce contact resistance. An additional piece of graphite foil was placed near the gas inlet to reduce the oxygen partial pressure in the atmosphere.

LabVIEW software was used to control the DC-power supply (EA-PSI 9750-60; EA Elektro-Automatik GmbH & Co. KG, Germany) and to record the electrical data.

3.2.3.2 Flash sintering conditions

Yttria stabilised zirconia and hafnia

FS of yttria-stabilised zirconia and hafnia was conducted by heating the furnace up to 800 °C and ramping up the field in steps of 10 V/30 s at a constant furnace temperature. Ramping up the field was conducted until a rapid increase in current and the onset of FS were detected. An experiment-dependent power limit was set and after the change from voltage- to power-control power dissipation was held for a certain time between a few seconds and several hours.

For some experiments atmospheres were changed during an ongoing power dissipation. This was done by closing and opening the valves of the connected gas cylinders. The duration between opening the valve, and the detection of an effect in the electrically loaded material, was a few seconds ($\approx$ 5 s).

Carbides - constant voltage-constant power tests

Preliminary investigations of the electrical and thermal response of B_4C without added CB were conducted by applying constant electrical fields between 50 and 200 V/cm while heating the furnace with a heating rate of 600 °C/h from room temperature in Ar atmosphere. The field was applied from room temperature and a maximum power dissipation of up to 500 W (1.1 W/mm^3) was defined in the power-controlled stage after the transition from voltage to power control and held for 60 s before turning off the electrical field and furnace cool-down.

Carbides - isothermal flash sintering of carbides

If not stated otherwise, the electric field was applied in one step in Ar as soon as the furnace reached the defined temperature. Also for these default conditions, 4 wt.% CB-containing B_4C-samples with C-foil thermal insulation were used at a furnace temperature of 1500 °C and a power of 700 W was dissipated for 5 min after initially applying 700 V ($\approx$ 350 V/cm). For all experiments results shown in this work the cathode (-) was located on the right and anode (+) on the left side of the sample.

Departures from these standard isothermal pre-plasma treatment flash sintering (PPT-FS) conditions were used to investigate the effects of various parameters including power limit, the presence or absence of carbon foil around the sample for thermal insulation, carbon additive content, heating rate, suppression of plasma formation by changing atmospheric gas or electrical conditions, and hold time, as described in greater detail in the next paragraphs.

Power limits between 500 W (1.1 W/mm^3) and 800 W (1.8 W/mm^3) were used for the power-controlled stage, which affects the sample temperature during the Joule heating stage of (PPT-)FS.

Carbon foil (C-Foil, 0.25 mm thick, 99.8% (metals basis), Thermo Scientific Chemicals) was loosely wrapped around some samples to reduce heat loss by radiation from the sample surface and to improve heat distribution, shown in Figure 3.3 b).

The effect of between 0 and 6 wt. % *additional CB* was investigated, to enable carbothermal reduction of the B_2O_3-layer on the surface of the powder particles.

The influence of *heating rate* and *plasma formation* were investigated by various approaches:

I) PPT-FS, where maximum power was applied from the very beginning of the experiment, conducted in argon (Ar). This led to plasma formation with the fields

used.

II) Ramped FS in Ar, where power dissipation was increased stepwise at a rate of 50 W every 30 s up to the defined power limit.

III) FS in helium (FS-He), where the power limit is set to the maximum value from the beginning, but no plasma formation happened due to the higher breakdown resistance of He compared to Ar, enabling high heating rates without plasma formation to separate the influence of heating rate and plasma.

Hold times between 30 s and 30 min were applied from the point at which the maximum power dissipation in the power-controlled stage was reached. The plasma stage in PPT-FS, is included in the applied hold times.

The sample temperature during FS and electrical loading was estimated according to the black body radiation (BBR) model using the formula 2.1 shown in the Literature Review. For (yttria stabilised) zirconia 0.7 [170], was assumed as a constant emissivity. For boron carbide 0.85 was used [171].

3.3 Characterisation

3.3.1 Density measurements

Density measurements were performed based on Archimedes' principle at room temperature. The method involved weighing of the sample in air (m_1), immersing the sample in water with a temperature dependent known density and measuring the apparent weight loss under water. If the sample showed open porosity, the sample was immersed in water for 2 h prior to the weighing under water (m_2). Subsequently, the sample was dried on its surface and weighed in air again (m_3). The buoyant force acting on the sample was calculated, and the true volume of the sample was determined.

Equation 3.1 and 0.99821 g/cm^3 (ρ_w), which equals water density at 20 °C, was used for density calculations.

$$\rho = \frac{m_1}{m_2 - m_3} \cdot \rho_w \tag{3.1}$$

Where:

m_1 = sample weight in air

m_2 = immersed sample weight in water

m_3 = immersed sample weight in air

ρ_w = water density at 20 °C

3.3.2 Grinding and polishing

Grinding and polishing of the materials was performed with a Buehler grinding machine initially using diamond abrasives. The final polishing step was performed with colloidal silica. The duration and the steps of the procedure depended on the materials.

3.3.3 Hardness measurement

Hardness measurements were performed at room temperature using a Future-Tech Corp. FV-110 Vickers hardness (HV) tester. The indenter was pressed into the polished sample surface with a known load, typically 9.8 N, for a fixed duration of 10 s.

Samples were prepared following standard procedure including sectioning and mounting in epoxy resin to create ground and polished surfaces to achieve a smooth and flat surface without any scratches or defects.

The Vickers hardness indentation impressions were observed using an optical mi-

croscope with a calibrated measuring eyepiece or by SEM investigation for a more detailed analysis. The diagonal lengths of the indentation were measured, and the hardness values were calculated using equation 3.2:

$$HV = 1.854 \cdot F/d^2 \tag{3.2}$$

Where:

HV = Vickers hardness

F = applied load

d = mean diagonal length of the indentation

The hardness values were obtained from multiple indentations (> 3) on each sample to ensure statistical significance and accuracy. The average hardness value and standard deviation were calculated for each sample.

3.3.4 Etching

Thermal etching of polished samples was conducted for 15 - 30 min at $\approx$ 80 % of the absolute specimen sinter temperature, in air or inert atmosphere, depending on the sample.

Etching of the sintered B_4C-specimens was done via electrochemical etching (10 V for 30 s in 2.5 M NaOH solution).

3.3.5 Grain size measurements

Measurement of grain sizes was performed based on SEM images of etched materials using the linear intercept method on etched SEM images or EBSD pattern quality maps on more than 100 intercepts [172], which are not subject to the corrections involved in grain orientation software. Errors are calculated as deviations of grain size calculated for each line and the overall average calculated.

3.3.6 Raman Spectroscopy

Raman spectroscopy was used to study the molecular and crystal structures of materials based on their Raman scattering at room temperature using a Renishaw (UK) Raman microscope System 1000. Samples were prepared in bulk-form and care was taken to ensure sample homogeneity and minimise any potential artifacts during Raman measurements. This included a reference measurement and comparison on pure silicon (Si) prior to every session.

Samples were placed on a microscope stage, focused by using an optical microscope with magnifications between 5 and 100 and the incident laser beam was focused on the sample surface to induce Raman scattering. A 632.8 nm red line

of a 50 mW He-Ne laser was used to excite the fluorescence of the investigated material. The scattered light was collected and analyzed using a high-resolution spectrometer and a sensitive detector.

The collected Raman spectra were analysed using Origin and compared to other detected spectra or literature.

3.3.7 X-Ray Diffraction analysis (XRD)

XRD was used for the structural analysis and was performed using an Empyrean diffractometer from Malvern Panalytical GmbH, Germany, using Cu Kα (0.154 nm) radiation, operating at a voltage of 40 kV and a current of 40 mA at room temperature.

For the characterisation, mainly bar- or disk-shaped samples were investigated after electrical loading. Both, untreated or ground and polished surfaces were investigated. Prior to the measurement both ends of the FSed samples, where Pt-paste was applied, were removed to prevent contamination of the spectra. In the case of flash sintered or electrically loaded samples, the characterised region of the sample was half-way between cathode and anode.

If necessary, measurements were performed without the surface contacting air for more than 5 s, by preparing samples in an argon-filled glovebox where they were mounted on an air-tight sample holder which was then directly loaded into the

machine. The various sample holders are shown in Figure 3.4.

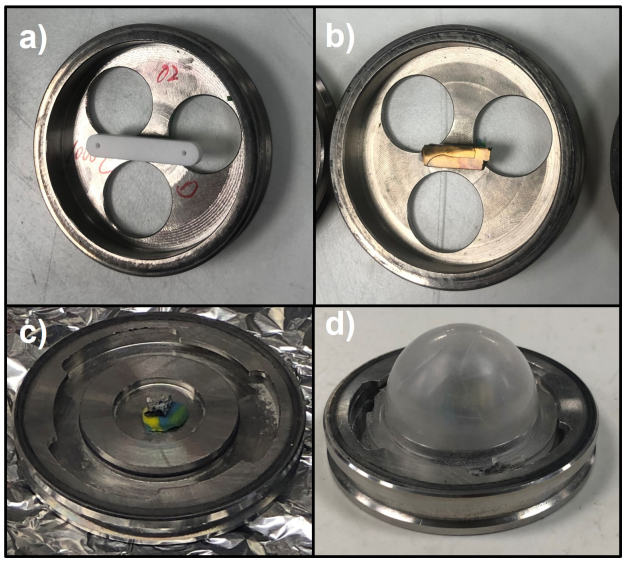


Figure 3.4: XRD sample holder with a) conventionally sintered 3YSZ sample; b) electrochemically reduced 3YSZ sample; c) air-tight XRD sample holder without cap in Ar-filled glove box and d) air-tight, X-ray transparent XRD sample holder with air-tight cap outside Ar-filled glovebox.

XRD patterns were recorded in the 2Θ range of 10 or 20 to 120 ° with a step size of 0.02° 2Θ and an acquisition time of 1 s/step. The incident X-ray beam was monochromated to remove the Kα2 and other unwanted frequencies.

The XRD data were analysed using Vesta [76], Profex [173] and Origin. The raw diffraction patterns were processed, and the background subtracted to enhance peak intensities. The diffraction peaks were indexed, and the crystallographic phases present in the samples were identified using the predicted model and confirmed with relevant literature, if available. For some spectra, Rietveld refinement was conducted within Profex and predicted diffraction patterns were calculated

within Vesta. The lattice parameters as well as the full-width at half-maximum (FWHM) of the peaks/spectra were determined based on the refined fit of the spectrum.

3.3.8 Scanning Electron Microscopy (SEM)

SEM was performed using a Merlin field emission gun (FEG) microscope from Zeiss, Germany, operating at an accelerating voltage between 1 and 10 kV. The investigated bulk samples were prepared by sectioning, grinding and polishing, sometimes etching, mounting on aluminium stubs, and sputter-coating with a thin layer ($\approx$ 4 nm) of conductive material (e.g. carbon, platinum or chromium) to enhance the surface conductivity and minimize charging effects. For some characterisations pristine or fractured surfaces, as well as powder samples were investigated.

Samples were placed on a nine stub holder in the SEM chamber, and the electron beam was focused on the sample surface to obtain high-resolution images. Secondary electron (SE) and backscattered electron (BSE) signals were collected to generate topographic, compositional, surface morphology and microstructure information, respectively. The acquired SEM images were processed and analysed to measure features such as grain size, etc.

3.3.9 Energy Dispersive X-ray Spectroscopy (EDS)

EDS was performed using the FEG-SEM mentioned before to determine the elemental composition of materials based on the characteristic X-rays emitted during electron beam-sample interactions.

X-rays were detected by the EDS detector (Bruker FlatQuad EDS detector) shown in Figure 3.5 a) and b), and their energies were analysed to identify the elements and their distribution in the sample.

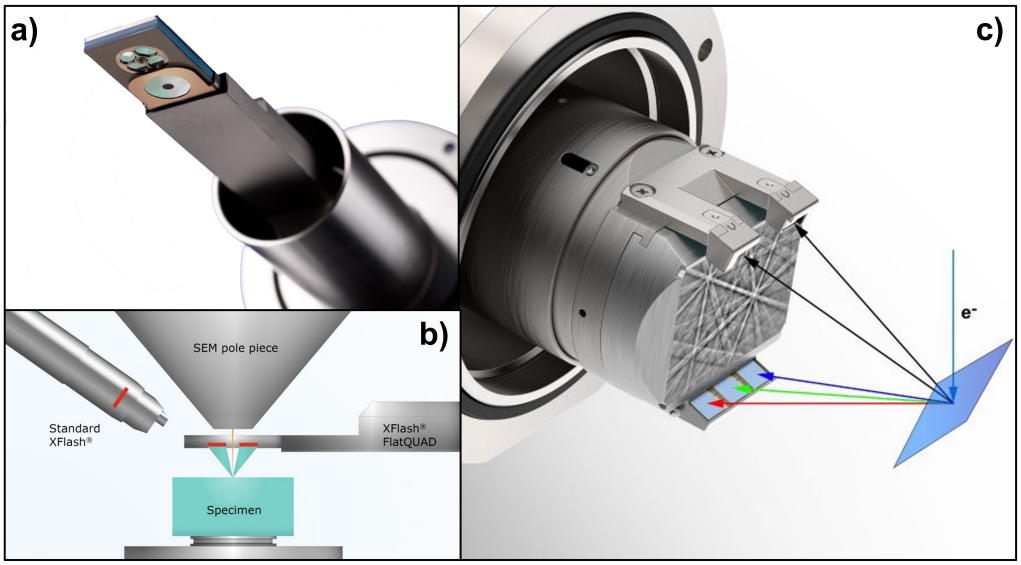


Figure 3.5: a) FlatQuad EDS-detector, b) EDS setup including FlatQuad EDS-detector compared to standard EDS-detector, sample stage and electron source, c) Bruker QUANTAX EBSD detector including phosphorus screen used for EBSD data aquisition as well as three silicon diodes used for forescattered electron imaging. Images taken from Bruker website.

Spectra were acquired from specific regions of interest (ROI). The data were processed and analysed using Bruker Esprit 2.3 software. The detected X-rays were

matched against known reference spectra to confirm the presence of specific elements and quantify their relative concentrations. The detected elements and their relative concentrations were correlated with the material´s expected composition or any specific variations, for instance due to electrochemical reduction.

3.3.10 Electron Backscatter Diffraction (EBSD)

Electron Backscatter Diffraction (EBSD) is used to study the crystallographic orientation and microstructural properties of crystalline materials at the sub-micrometer scale. Prior to EBSD analysis, performed with the previously mentioned FEG-SEM and a Bruker QUANTAX EBSD-detector (Figure 3.5 c), careful sample preparation is essential to ensure accurate and meaningful results. The samples were prepared as follows:

Sectioning and Mounting: Specimens were sectioned from bulk materials using precision cutting techniques and mechanically ground and polished to remove any surface damage and achieve a mirror-like finish.

Surface Cleaning: Samples were ultrasonically cleaned prior to ion polishing (4 keV for 4 h) to remove any contaminants.

Initial Imaging: A low-magnification SEM image of the sample surface was acquired to identify regions of interest and to ensure proper alignment.

Data Collection: High-resolution EBSD maps were collected from ROIs using 20 - 30 kV accelerating voltage, beam current of 10 nA, sample-dependent step size, and specific exposure time. The electron beam was rastered across the region of interest, and the backscattered and diffracted electrons were detected to determine crystallographic orientation. The data collection took between 30 min and 8 h.

Forescattered imaging was conducted on polished sample surfaces using three silicon diodes located below the phosphorus screen with otherwise comparable parameters.

Data Processing: Bruker ESPRIT was used for data processing and analysis.

3.3.11 X-ray Photoelectron Spectroscopy (XPS)

X-ray Photoelectron Spectroscopy (XPS) characterisation of the investigated samples, mainly electrochemically reduced (yttria stabilised) zirconia, as well as plasma treated boron carbide, was performed on the sample surfaces at room temperature using a PHIVersaprobe III XPS system generating focused, monochromatic Al Kα X-rays at 1486.6 eV, under ultrahigh vacuum (UHV) conditions with the main chamber maintained at pressures between 10^{-7} - 10^{-6} Pa.

The X-ray monochromator was operated at a power of 25 W and an electron beam voltage of 15 kV. The instrument was equipped with dual beamcharge neutralisation capabilities, a low-energy BaO electron source (beam diameter $\approx$ 5 mm) and

a low-energy Ar^+-ion source. The device as well as the mounted samples is shown in Figure 3.6.

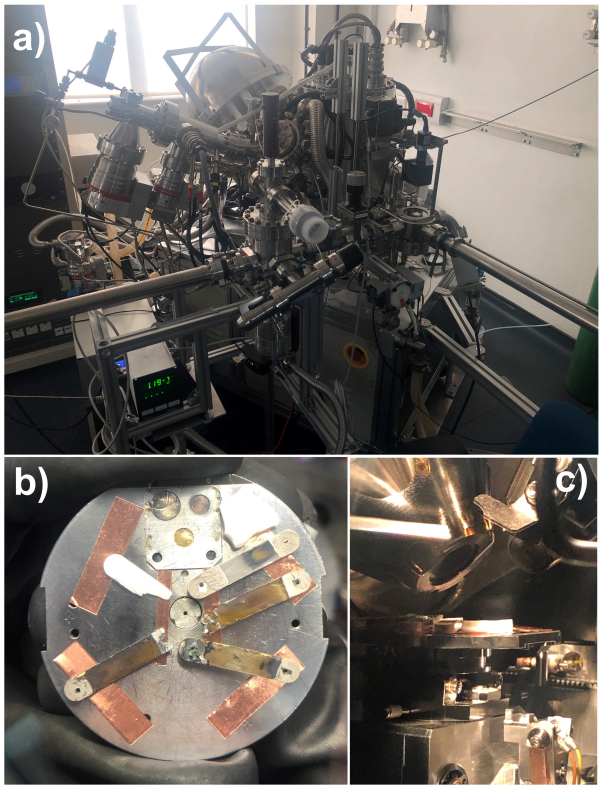


Figure 3.6: a) PHIVersaprobe III XPS system, b) YSZ-samples mounted on sample carrier, c) sample carrier in measurement chamber.

Pristine or electrically loaded YSZ samples were transferred from a glovebox into the XPS chamber using a vacuum transfer vessel to avoid contamination and any ambient exposures. Spectra from insulating YSZ samples were charge corrected by shifting all peaks to the adventitious C 1s spectral component (C-C, C-H) BE set to 284.8 eV.

Since some of the boron carbide samples, investigated by XPS, contained addi-

tional C and others did not, the C 1s signal, usually used as reference value in XPS, was not used. Instead, the B1s XPS-signal at 192.9 eV, referring to boron (B) in B_2O_3 [174], was used as reference value for all spectra, and the results verified using the corresponding O1s signal, located at a binding energy (BE) 139.3 eV higher than the B 1s signal for B_2O_3.

Treatments conducted and compared by XPS are:

I) green body made from pristine powder without any treatment (referred to in the Results section as P),

II) pure B_4C green body heat treated at 1500 °C in Ar for 5 min (P-1500 °C),

III) same heat treatment for B_4C green body containing 4 wt.% of additional C (P-C-1500 °C),

IV) 4 wt.% C-containing green body subjected to Ar plasma treatment for 30 min in a low pressure plasma (cleaning) system/chamber (Tetra22 - Bell, Diener electronic GmbH Co. KG, Germany), which is contained in an Ar-filled glove box at room temperature (P-C-PlCh),

V) surface of a 4 wt.% C-containing B_4C powder compact, pre-plasma treated at 1500 °C (700 W) and stopped before the Ar plasma collapsed (P-C-PPT-Su),

VI) cross section of condition V) (P-C-PPT-CS),

VII) surface of a sample as for V) but after densification by PPT-FS conducted at

a furnace temperature of 1500 °C, power limit 700 W, hold time 5 min with C-foil wrapping (D-PPT-FS-Su), and

VIII) cross section of condition VII) (D-PPT-FS-CS).

If powder compacts (P) were investigated, fractured cross sections (CS) were used. For dense, sintered (D) samples, ground and polished CS were characterised. A summary of the samples investigated by XPS can also be found in Table 7.2 in Chapter 7.5.2.

To reduce the potential influence of reoxidation or other atmospheric reactions, the samples (YSZ and B_4C) produced were transferred into an air-tight Ar-filled glove box (MB Braun, MB 200B) with O_2 and H_2O concentrations below 0.1 ppm, where all further preparation and mounting of the samples on the XPS sample holder was conducted.

Transfer into the XPS without contact with air was possible.

The emitted photoelectrons were detected and analysed using an energy analyser in the XPS instrument. The kinetic energy (KE) of the photoelectrons was measured, and their BE were determined relative to the incident X-ray energy. The BE information allowed the identification of the chemical states and oxidation states of the elements present in the sample.

Gaussian-Lorentzian and Voigt lineshapes were used to fit the spectra after ap-

plying a linear background for YSZ and a Shirley background for boron carbide samples, within the CasaXPS software. Peak asymmetry due to charging of insulating samples was detected by fitting an asymmetric peak to the adventitious C 1s peak and using the asymmetric peak shape for all other peaks and species of the sample.

To identify the present oxidation states, particularly of the transition metal oxides in YSZ, some constraints, summarised in Table 3.4, were used to achieve correct and accurate fitting.

Table 3.4: Applied constraints for fitting Y and Zr 3d XPS-spectra.

Orbital	Area	FWHM [eV]	Position [eV]
Y 3d5/2	A	B	C
Y 3d3/2	A*2/3	B	C+2.05
Zr 3d5/2	X	Y	Z
Zr 3d3/2	X*2/3	Y	Z+2.4

3.3.12 Electron Paramagnetic Resonance (EPR) Spectroscopy

EPR, also known as Electron Spin Resonance (ESR), is used to study materials with unpaired electrons or paramagnetic centres such as some of the oxidation states of transition metals, but also oxygen vacancies and other defects.

EPR measurements were performed using a Bruker EPR spectrometer, operating in the X-Band at a frequency of ≈ 9.8 GHz and a magnetic field strength between 1000 and 6000 Gauss.

Samples were prepared by carefully breaking the material with a pestle and mortar between two layers of Parafilm to prevent impurities in the material. Subsequently, the fractured particles were filled into a quartz tube with an inner diameter of 2 mm. To prevent reoxidation of the materials after FS or electrical loading, samples were crushed and loaded in an Ar-glovebox. The quartz tube was sealed in the glovebox and transferred to the measurement device without air-contact.

EPR spectra were collected at room temperature (293 K) and 100 K, cooled down by liquid (N_2). Samples were placed in a resonant cavity, and microwave radiation was focused on the sample to induce EPR transitions. The magnetic field was swept around the expected resonance condition while monitoring the changes in microwave absorption.

Origin was used to analyse the spectra and extract the g-factor (*g)* and linewidth (ΔHpp) of the resonance peaks. The derivative of the EPR spectrum measured was fitted using a blend of Lorentzian and Gaussian functions. Figure 3.7 shows the fundamental principle of EPR, which is based on the Zeeman effect.

To extract the concentration and contribution of various paramagnetic defects to the EPR spectrum, the spectrum was integrated and the calculated area was used as a representative value. For the FS/electrically loaded 3YSZ samples, the detected areas were compared to conventionally sintered 3YSZ to calculate the change in paramagnetic defects formed during the process.

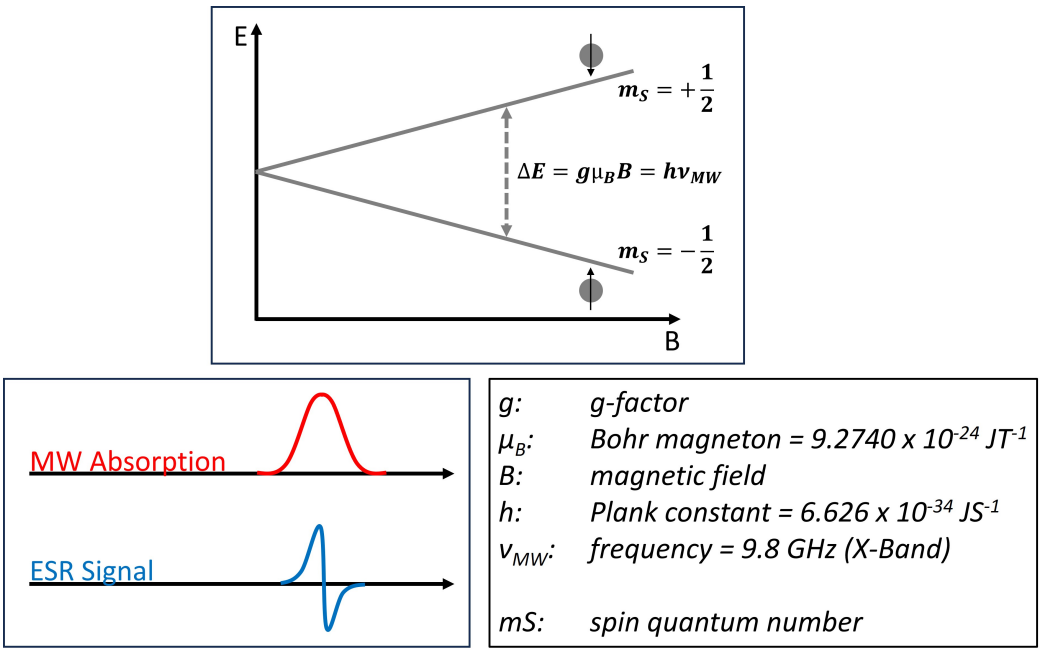


Figure 3.7: Fundamental principle of EPR characterisation.

The EPR results revealed the presence of paramagnetic defects in the investigated YSZ samples. The g-value and linewidth provided information about the electron spin state and relaxation behavior which enabled an appropriate identification of the contributing defects. The obtained data were compared to theoretical models and known references to confirm the identity and properties of the paramagnetic species.

Compared to other methods such as Raman, EDS or XPS, EPR enables the sensitive and quantitative characterisation of bulk materials rather than surfaces, which is particularly interesting in reactive materials which reoxidise or react with the atmosphere. It also gives complementary information to the other methods.

3.3.13 Room temperature electrical conductivity

The approximate electrical conductance of the samples was measured with a hand-held digital multimeter (BEHA-Amprobe 5XPA Hand Digital Multimeter) at room temperature after electrical loading. The electrical conductivity was calculated based on this result and the sample dimensions.

3.3.14 Thermogravimetric Analysis

Thermogravimetric Analysis (TGA) was performed using a Netzsch STA 449F3 device with alumina crucibles in air with a heating rate of 600 K/h.

3.3.15 Optical spectroscopy

Optical Spectroscopy was used to investigate the light emission during FS of green bodies made of YSZ and boron carbide, sample heating under electrical fields as well as a variety of plasmas and sparks.

Light from the furnace and sample was collected by a 2´´ fused silica achromatic doublet lens (f=280mm) which imaged the sample to a fibre coupled spectrometer. The components were aligned to focus 400 - 550 nm light on the fibre, which is below the wavelengths at which most light was emitted during the experiments. The fibre couple acted as a spatial filter to remove the out of focus thermal radiation

preventing damage to the fibre and reducing the influence of the collection system on the relative intensity at higher wavelengths. Most of the experiments used a QP400-2-VIS-BX fibre but a QP400-2-SR-BX fibre was also used to investigate the effect of the fibre on the spectra obtained. The recorded spectra were evaluated using OceanView software. An integration time of 6 ms was used throughout. Figure 3.8 systematically shows the described setup for these experiments.

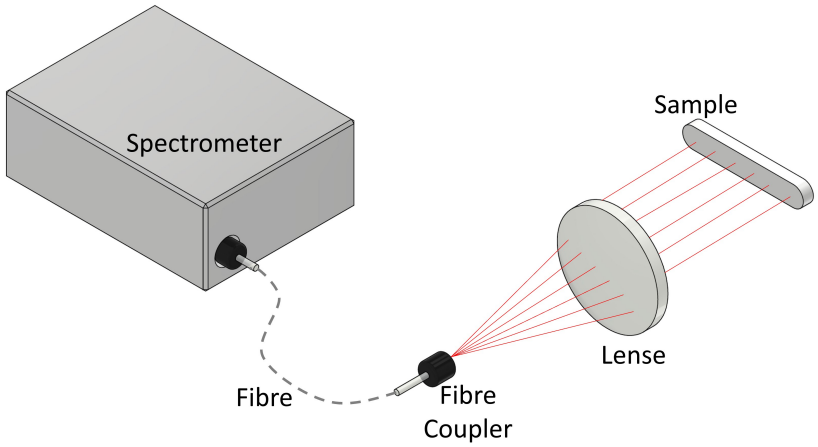


Figure 3.8: Spectrometer setup for optical spectroscopy including spectrometer, optical fibre, fibre coupler, lense and sample.

Two lasers with wavelengths of 520 nm and 532 nm were used to check the wavelength calibration of the spectrometer (OceanOptics HDX, range 200 - 1120 nm). This showed the measurement of the wavelength was accurate to within 0.6 nm. The detection efficiency of the spectrometer was determined using a known light source (Sylvania Satin 40W 240V) with a colour temperature of 2700 K, without the fused silica lens and fibre.

Theoretical black body spectra were calculated for comparison with the experimental results using Planck´s and Wien´s Law as shown in equation 3.3 and 3.4.

$$B(\lambda, T) = \frac{2hc^2}{\lambda^5} \cdot \frac{1}{e^{\frac{hc}{\lambda k_B T}} - 1} \tag{3.3}$$

$$\lambda_{\text{max}} = \frac{b}{T} \tag{3.4}$$

Where:

$B(\lambda, T)$ is the spectral radiance

λ is the wavelength

λ_{max} is the peak wavelength

T is the absolute temperature

h is Planck´s constant (6.626×10^{-34} Js)

c is the speed of light in vacuum (3×10^8 m/s)

k_B is Boltzmann´s constant (1.381×10^{-23} J/K)

b is Wien´s displacement constant (b = 2.897 $\times 10^{-3}$ mK)

Experiments, which simulate a black body, were conducted to determine the influence of the complete spectroscopic measurement system (fused silica lens, fibre, spectrometer) on the detected spectra. These experiments were executed by covering the inside of the alumina tube in the furnace with carbon foil and inserting a piece of graphite in the hot region of the furnace.

3.3.16 High speed video recording

High Speed Camera Video Recording was conducted at the early stage of the plasma formation during pre-plasma FS of carbides as well as the formation of plasma around an insulting material, such as alumina.

A Phantom high speed camera with a frame rate of 30,000 fps was used. The camera was placed on the windowed-side of the furnace and recording was manually stopped shortly after the plasma formation.

4 | Light emission during flash sintering

This chapter of the thesis describes the work conducted on the detection of emitted light during FS and electrical loading of yttria-stabilised zirconia (3YSZ, TZ-3YB-E) and the comparison to spectra emitted from other materials such as graphite or alumina.

Theoretical black body spectra were calculated for comparison with the experimental results using Planck′s Law. These are referred to as "calculated" spectra in the following sections.

4.1 Light emission during flash sintering of YSZ

Figure 4.1 compares the experimentally measured raw spectra emitted by 3YSZ during FS and the *graphite*-furnace measurement for a nominal temperature of 1473 K. The temperature was estimated using the black body model of the FS sample temperature for the 3YSZ and the thermocouple reading of the furnace for the simulated black body. Both spectra were normalised to 1 at their maximum intensity.

It is evident that the spectra are very similar and there are no additional emission peaks in the YSZ although the spectra are not exactly overlapping at all

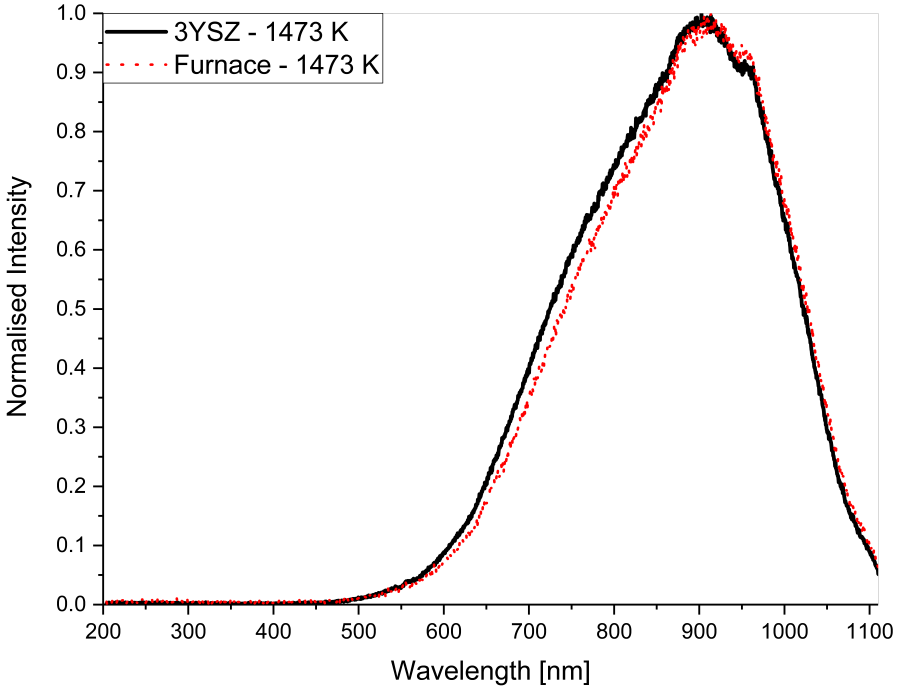


Figure 4.1: Measured spectrum of the 1473 K graphite-furnace and the spectrum of 3YSZ in the constant current/power stage of FS at an estimated temperature of 1473 K.

wavelengths. Furthermore, both spectra display a dip at $\approx$ 950 nm and the maximum intensity is located at $\approx$ 900 nm in both cases, whereas according to Wien′s displacement law (equation 3.4), the maximum black-body intensity at 1473 K should be at approximately 1970 nm. To explore possible explanations for the shape and the origin of the spectra, further measurements and calculations were conducted.

To determine the influence of the spectrometer itself, without the focusing lens and fibre, the spectrum of the 2700 K lamp was measured and compared with

the calculated spectrum for the same temperature (Figure 4.2), normalising the spectra with respect to the maximum intensity as above.

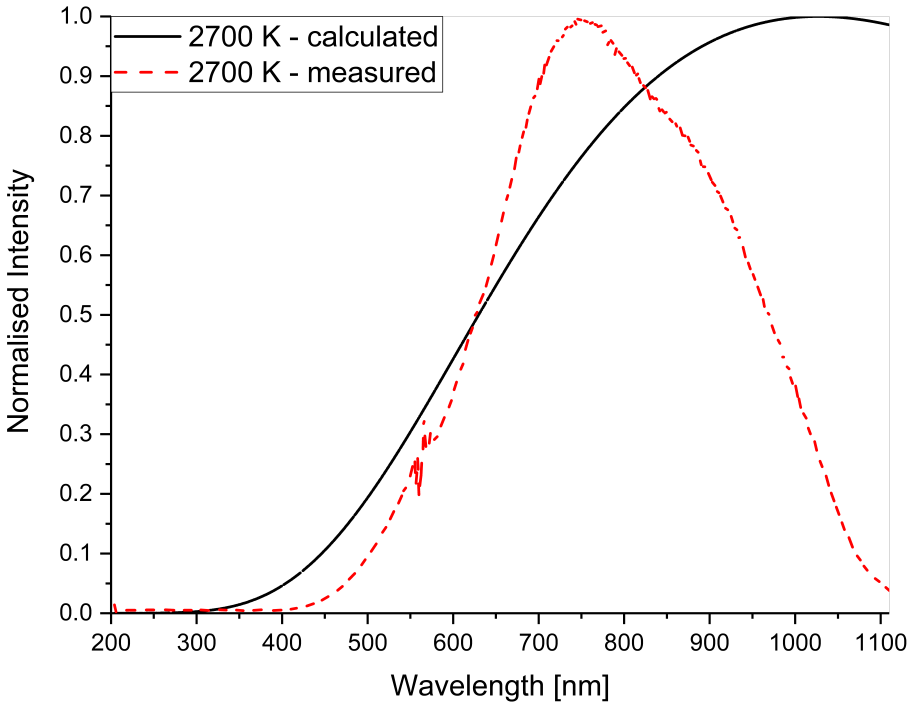


Figure 4.2: Measured spectrum of the 2700 K lamp without additional lens or fibre and the calculated spectrum referring to Planck′s law at the same temperature.

As in Figure 4.1, the experimental curve shows a strongly decreasing intensity at higher wavelengths, well before the calculated maximum intensity ($\approx$ 1050 nm). Furthermore, there is an abnormal deviation of the expected behaviour at approximately 550 nm. Based on Figure 4.2 it can be assumed that the spectrometer causes two main issues. First, strongly decreasing detection efficiency at higher wavelengths which leads to a shifted peak intensity. Second, an artefact around 550 nm, which causes a local oscillation in intensity. This is not noticeable in the

results because most of the intensity is at higher wavelengths owing to the lower temperature involved.

Figure 4.3 shows *graphite*-furnace spectra at 1273 K measured with two different fibres. The dip at 950 nm detected in Figure 4.1 is evident for both fibres but is in the form of a very strong minimum for the QP400-2-SR-BX fibre, to the extent that it leads to apparent peaks in intensity on either side of it. The higher attenuation of the QP400-2-SR-BX fibre compared to the QP400-2-VIS-BX, at around 950 nm is evident in the manufacturer′s specification, as shown in Figure A.1 in the Appendix. Absorption at this wavelength is associated with OH^- ions in the fibre [175].

It is emphasised that Figure 4.3 is the result from the *graphite*-furnace alone. Inspection of the "peaks" identified previously in the emission spectra of FS 3YSZ [24, 41] shows that they can also be interpreted as being a consequence of minima superimposed on a broader spectrum representing black body radiation (BBR), truncated at higher wavelengths in the case of reference [24] and the present work by the reduction in efficiency of the spectrometer. The electroluminescence "peak" identified in [39] is immediately below the minimum, at 740 nm whereas the corresponding feature in Figure 4.3 is at 920 nm; there is no fluctuation in the spectrum around 740 nm in this work. It seems highly probable that the significantly different positions of the "peaks" in [39, 40] and the present work arise

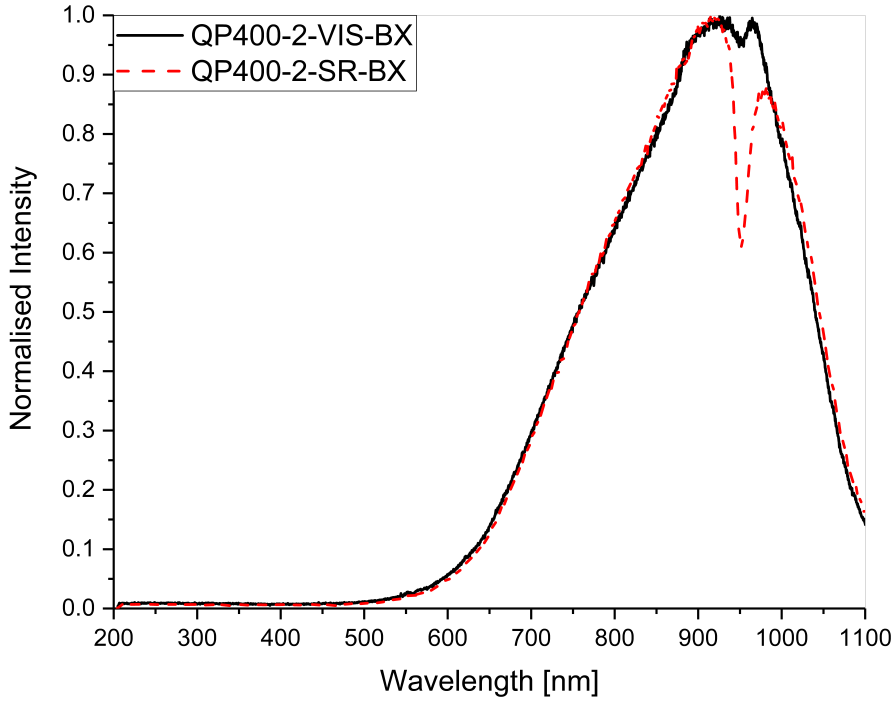


Figure 4.3: Graphite (covered) furnace spectrum measured with two different fibres under same conditions and without any other changes.

because they are an artefact of the collection system (spectrometer and collection optics), which was different in the three papers [24, 39, 40] compared to the experimental setup used in this work. No control experiments without the FS specimen are reported in [39, 40] and the wavelength limit of our system prevents direct comparison with the results in [40].

In order finally to rule out any significant electroemission in the wavelength range investigated, we now return to the small discrepancies between the spectra of the graphite-(covered)-furnace and the FS 3YSZ specimen in Figure 4.1. In order to investigate these, the ratio between the calculated BBR intensity and the result

from the graphite-furnace, which can be seen as an approximation to a black body, was calculated for three different experimental temperatures (1273, 1473 and 1773 K). These ratios are shown as a function of wavelength in Figure 4.4. All ratios were normalised to 1 at 1100 nm. The results show that the ratio is independent of temperature. Figure 4.4 can therefore be used in conjunction with Planck′s law to predict the spectrum that would be measured experimentally for any temperature.

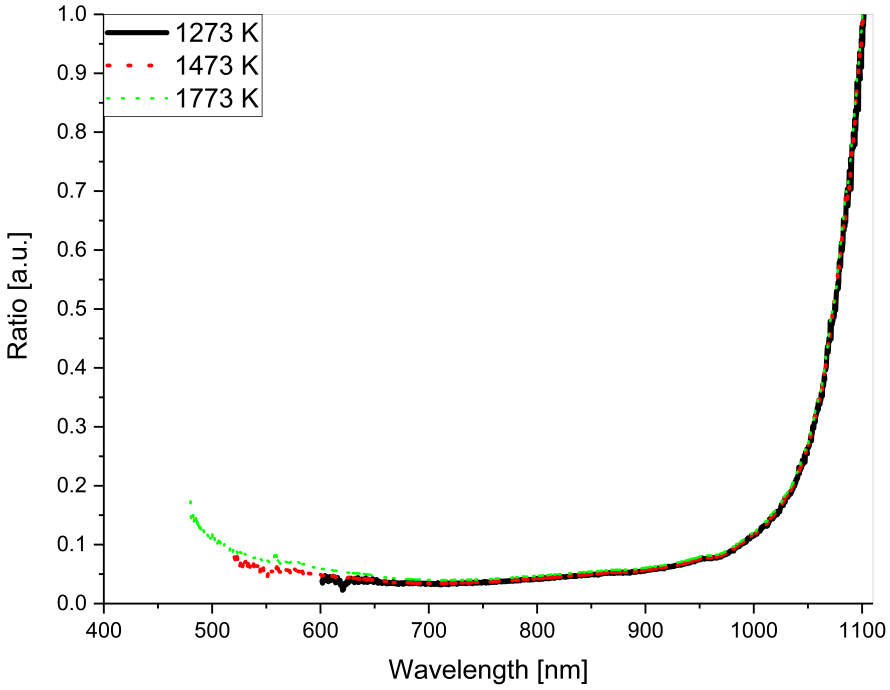


Figure 4.4: Calculated ratio between calculated BBR and the measured spectrum at varying temperatures. The undulations at low wavelengths are noise due to the low intensity.

The following section is used to demonstrate that the minor discrepancies in Figure 4.1 can be explained as a consequence of the non-uniformity of the temperature in and around the FS specimen. There are two main sources of non-

uniformity. The first is that although the black body model used to estimate the specimen temperature assumes a uniform surface temperature, in reality the temperature is non-uniform, being hotter towards the centre-line of the specimen [25]. Recent modelling shows that the maximum surface temperature for similar specimens may exceed the mean surface temperature by $\approx$ 70 K [176]. The second source of non-uniformity is that although BBR from the FS 3YSZ specimen is much more intense than that from the furnace at 1073 K, it accounts for only a small fraction of the area sampled by the spectrometer ($\approx$ 10 % of the furnace cross section) so the contribution of the furnace to the total intensity may not be negligible. These factors can change the form of the spectrum.

A full calculation of the effects of the non-uniform temperature would require detailed modelling of the specimen surface temperature and would also be susceptible to the uncertainty in emissivity for such specimens (which is itself a function of wavelength [177]). However, the simple approximation of combining the extremes of the temperature distribution in ratios appropriate to their cross-sections demonstrates that the range of temperatures present provides a convincing explanation of the experimental temperature distribution during FS in Figure 4.1. Figure 4.5 shows the response predicted using Planck′s law and the measuring system response curve in Figure 4.4 for a simulated experiment consisting of a specimen at a temperature of 1543 K (i.e. a maximum surface temperature 70

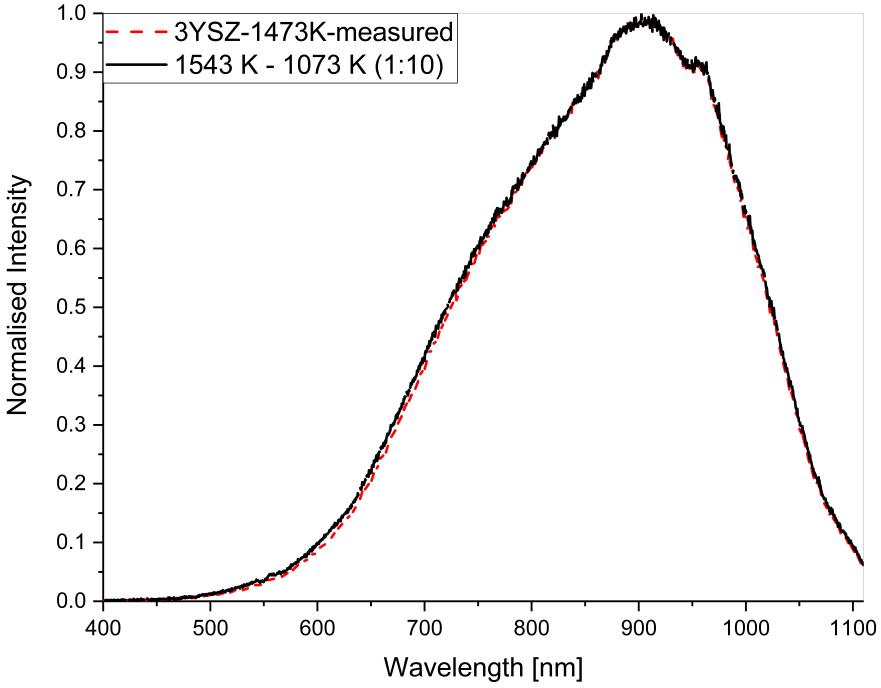


Figure 4.5: Measured 3YSZ spectrum and recalculated spectrum for a (sample-) temperature of 1543 K including background radiation at 1073 K at an estimated ratio of 1:10.

K hotter than the uniform temperature estimate of 1473 K in Figure 4.1) plus a furnace background at 1073 K, the latter contribution being added in at 10 times the former to account for the larger area of the furnace background compared with the specimen. It can be seen that the predicted response matches the experimental FS spectrum almost perfectly.

4.2 Comparison to other previously published results about light emission during flash sintering and electrical loading

Beside the previously investigated light emission during FS and electrical loading of YSZ, similar results regarding electroluminescence and photoemission from other materials were presented in the literature [39, 40, 47, 49, 50, 51, 52, 53].

Like the procedure used for the interpretation of our own results, this section only includes experimental results from investigations by other researchers alongside the theoretically expected light emission according to Planck′s and Wien′s law. If available, temperature measurements were taken from the same publication as the spectra discussed. The conversion from results published in the form of diagrams in various publications into useful data sets was conducted by using WebPlotDigitizer (available online).

Figure 4.6 shows the procedure used for results published by Neto et al. [51] reporting the light emitted by electrically loaded amorphous carbon (C) fibres at various current levels which lead to various temperatures (Figure 4.6 a).

In this case the highest current (150 A/mm^{-2}), leading to a temperature of 2088 K [51], was used and converted into usable data (Figure 4.6 b). Figure 4.6 c)

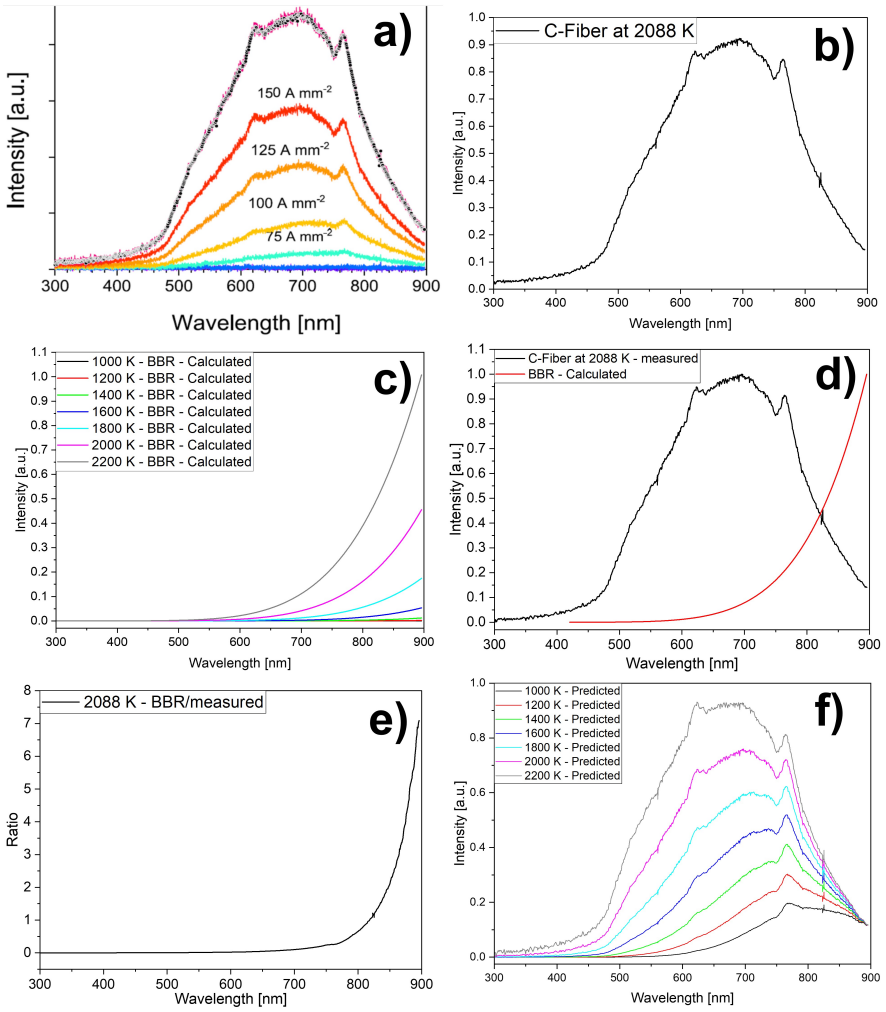


Figure 4.6: a) Measured light emission during electrical loading of carbon fibres published by Neto et al. [51] including the detected data points in form of black circles which are converted by WebPlotDigitizer; b) reproduced data of the emitted light from C-fiber at 2088 K; c) calculated light emission according to Planck and Wien; d) comparison between b) and the calculated light according to Planck and Wien for the same temperature; e) calculated ratio between the expected calculated spectrum and the spectrum shown in b); f) predicted spectra for various temperatures after multiplying the ratio shown in e) and the calculated spectrum shown in c).

shows the calculated light emission in the considered wavelength range according

to Planck and Wien, compared to the experimentally detected C-fiber spectrum at

the same temperature (Figure 4.6 d).

The two spectra compared (Figure 4.6 d) are used to calculate the ratio between calculated and measured spectrum shown in Figure 4.6 e). The calculated ratio based on these results is comparable to the previously shown ratio (Figure 4.4) based on the results obtained in this work, except for the lower wavelength range. The deviation in the lower wavelength range can be explained in terms of temperature difference. Based on the ratio and the calculated light emission it is possible to predict spectra dependent on the temperature for this experimental setup. The predicted spectra for various temperatures are shown in Figure 4.6 f), which shows that based on the calculated ratio and the expected BBR the emitted spectra can be calculated without a significant contribution from any non-thermal effects.

Since the results shown in Figure 4.6 are all from the same material or based on theoretical calculations, it could still be possible that mechanisms, other than thermal radiation, are the origin of the light emission in this particular material. Thus, a comparison between the predicted temperature-dependent spectra shown in Figure 4.6 f) and spectra obtained from other materials ($SrTiO_3$ [47] and 3YSZ [39]) is shown in Figure 4.7. For both materials, $SrTiO_3$ as well as 3YSZ, a good agreement between the predicted and the reported spectrum can be seen without any significant deviations.

As a final consideration the reported spectra obtained from $SrTiO_3$ at 1399 K [47]

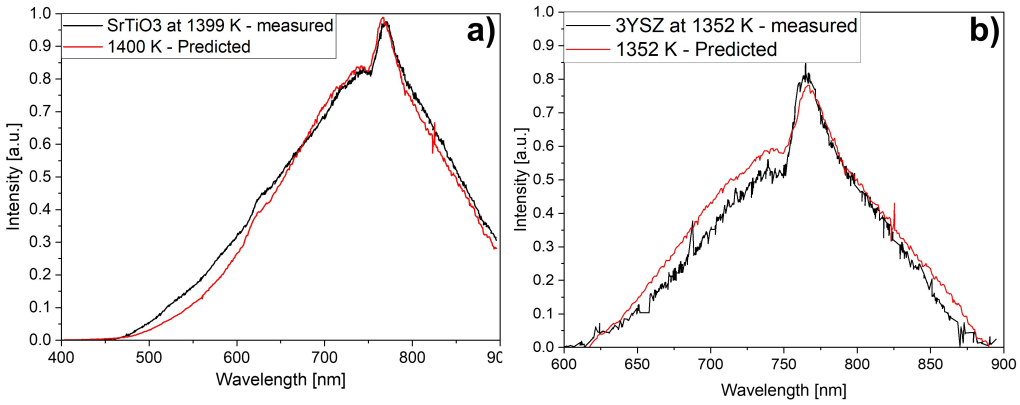


Figure 4.7: Detected light emission during flash sintering of a) $SrTiO_3$ at 1399 K published by Naik et al. [47] and b) 3YSZ at 1352 K published by Lebrun et al. [39] converted by WebPlotDigitizer (black) and predicted spectrum based on the ratio obtained from the emitted light of C-fibers at 2088 K shown in Figure 4.6 e-f).

were multiplied with the ratio shown in Figure 4.6 e) to demonstrate explicitly that the spectrum agrees on the theoretical prediction for an ideal black body radiator at the same temperature. The result is shown in Figure 4.8 and shows excellent agreement.

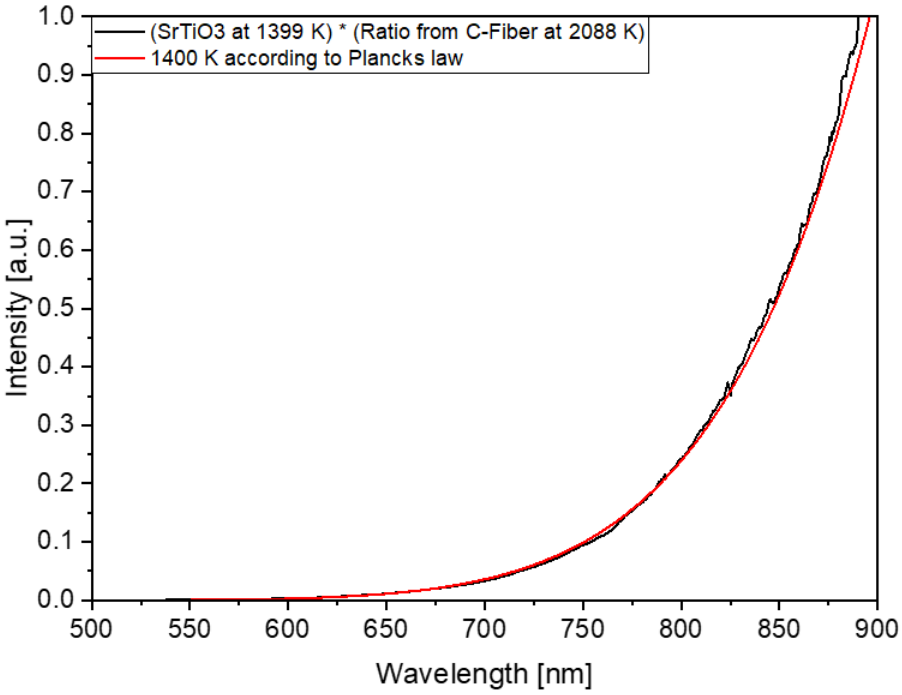


Figure 4.8: Red) calculated spectrum according to Planck and Wien for an ideal BBR at 1400 K; black) spectrum obtained after multiplication of the reproduced $SrTiO_3$ spectrum (Figure 4.7 a) with the ratio calculated based on C-fiber at 2088 K (Figure 4.6 e).

4.3 Other light emitting phenomena occurring in flash sintering

In addition to the thermal radiation described, emitted during FS of various materials, other phenomena were detected by optical spectroscopy, as shown in Figure 4.9.

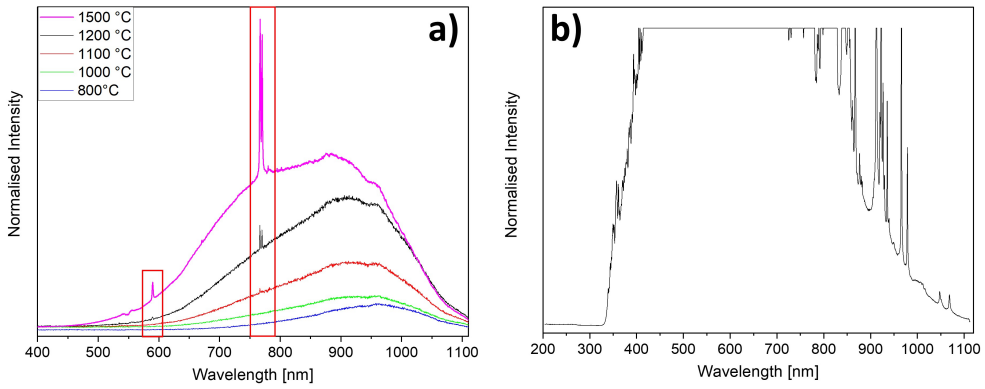


Figure 4.9: Emitted spectra from a) horizontal alumina tube furnace at various temperatures between 800 and 1500 °C; b) sparking during a failed FS experiment where an alumina sample was mounted between the electrodes.

Figure 4.9 a) shows the spectra emitted from the horizontal alumina tube furnace at various temperatures between 800 and 1500 °C. Above 1200 °C three sharp peaks appear and increasing intensity can be detected at increasing temperature.

Figure 4.9 b) visualises the spectrum emitted from a spark which formed during a failed FS experiment in argon at 1500 °C with an alumina sample mounted between the electrodes. The spectrum shows several sharp peaks and an intense

broad background, leading to saturation of the detector.

Both of the phenomena shown in Figure 4.9 show distinctive sharp peaks, not detected during FS and electrical loading of YSZ and other materials.

4.4 Discussion

Based on the results presented it can be concluded that the observed spectrum of FS 3YSZ specimens, as well as other materials presented in the literature, in the range 400-1100 nm, which includes the vast majority of the visible spectrum, can be completely explained in terms of BBR and the influence of the experimental detection system. Apparent peaks in the visible spectrum reported previously are artefacts of the experimental equipment such as absorption by the optical fibre.

As in alumina [43], there is no evidence to support the existence of electroluminescence in the visible spectrum during FS of 3YSZ from electron-hole pair recombination due to Frenkel defect formation or any other source.

In closing, we note that this does not rule out emissions from 3YSZ in other regions of the spectrum nor from other ceramics in the visible part of the spectrum. Indeed, it would not be surprising if such emissions do exist, particularly in YSZ.

Departures from black-body behaviour in the infrared spectrum of the zirconia-based Nernst glower were noted by Coblentz as early as 1908 [178], but also more recently by Terauds et al. [40]. However the departures [40, 178] do not agree with each other and the deviation from BBR at higher wavelengths (> 1100 nm) can also not be explained based on the results shown in this thesis. A potential explanation could be wavelength-dependent absorption of YSZ but requires more

investigation.

It should be noted that YSZ is also well known to luminesce under a variety of conditions such as ion irradiation [179] or mechanical stresses [180]. Ion irradiation and mechanical stresses are not relevant in this work, which is why the reported kind of emission in [179, 180] is not observed here. However, the formation of colour centres (F^+-type and T-centres) was detected as potential origin of the radiation in [179]. The formation of such defects can not be excluded during FS, as shown later in this work, but the thermal radiation emitted during electrical heating outweighs the defect-induced luminescence.

Most relevantly, FSed 3YSZ exhibits blue photoluminescence at room temperature that does not occur with conventionally sintered material [118]. However, these emissions are weak compared with the very bright visible emissions during FS of 3YSZ, which this work has shown to be BBR. This is the consequence of the high specimen temperature caused by Joule heating during FS. Nevertheless, the blue photoluminescence in 3YSZ after FS [118] is interesting and is discussed in the following chapter as a consequence of electrochemical reduction and changed defect structure.

5 | Flash sintering and the effect of electrical loading on Yttria-stabilised Zirconia

Transition metal oxides, particularly yttria-stabilised zirconia (YSZ), are the most investigated materials in the perspective of FS. However, some of the fundamental observations are still not fully explainable.

Beside FS, transition metal oxides are also used in various other applications where the material is exposed to elevated temperatures, high electric fields and (sometimes) reducing atmosphere, like in solid oxide fuel cells (SOFC), solid electrolyser cells (SOEC), etc. Thus, the mechanisms investigated here are not solely limited to FS but should be seen in the general context of the behaviour of transition metal oxides at elevated temperatures under the influence of electrical fields.

In this section electrochemical reduction in YSZ, as one potential mechanism in FS but also other applications, is researched. Therefore, YSZ with various Y-contents between 1.5 and 10 mol.%, and also Mg-stabilised zirconia (MSZ), were investigated with a focus on tetragonal 3YSZ and cubic 8YSZ, which are the most investigated materials in FS and other applications. Yttria-stabilised hafnia is also investigated in the same way and the results are shown in the Appendix in section

A.3.

A distinction is made between FS, conducted on green bodies, and electrical loading of fully dense (> 99 %) pre-sintered samples. All samples investigated, including their electrical treatment, are summarised in the following Table 5.1, excluding conventionally sintered samples. If samples are shown in the Results section, the corresponding Figure number is also referenced in the table.

Table 5.1: YSZ samples, classified by the procedure conducted, Flash Sintering (FS) or Electrical Loading (EL). If power dissipation was maintained during furnace cool down from 800 °C furnace temperature, hold time is labelled as CD, otherwise the hold time in seconds in the atmosphere maintained during cool down is mentioned. If atmospheres were changed during electrical loading the atmospheric order is mentioned accordingly.

Material		FS/Loading	Hold time	Atmosphere	Figure
3YSZ	Green Body	FS	60 s	Air	-
3YSZ	Green Body	FS	60 s	O_2	-
3YSZ	Green Body	FS	60 s	N_2	-
3YSZ	Green Body	FS	CD	Air	5.1 b)
3YSZ	Green Body	FS	CD	O_2	5.7 d)
3YSZ	Green Body	FS	CD	N_2	5.7 e)
3YSZ	Green Body	FS	CD	Ar	5.7 f)
3YSZ	Dense	EL	CD	Air	5.5 c)
3YSZ	Dense	EL	CD	O_2	5.7 g)
3YSZ	Dense	EL	CD	N_2	5.7 h)
3YSZ	Dense	EL	CD	Ar	5.7 i)
3YSZ	Dense	EL	30 s	O_2, Air, Ar	5.5 e)
3YSZ	Dense	EL	CD	O_2, Air, Ar	5.5 h)
8YSZ	Dense	EL	CD	Ar	-
MSZ	Dense	EL	CD	Ar	5.24
MSZ	Dense	EL	CD	N_2	-

Based on the different procedures, the samples in this work are described by

a nomenclature as follows: 3YSZ-FS-60s-Air, which describes the first sample listed in the table. Another example is 8YSZ-EL-CD-Ar, representative for an 8YSZ sample, which was electrically loaded (EL) during furnace cool down (CD) in Ar (Ar).

The following results section starts with FS of green bodies in different atmospheres and hold times before electrical loading on pre-sintered samples in various atmospheres is described, which is followed by the characterisation of the samples prepared by FS or electrical loading. A discussion of the results follows.

5.1 Flash sintering 3YSZ green bodies

5.1.1 Flash sintering 3YSZ green body in air

DC-FS of a 3YSZ green body was conducted under a stepwise increased voltage (U) of 400 V (150 V/cm) in air at 800 °C furnace temperature (T_f). The onset of FS happened a few seconds after applying 400 V leading to a power-controlled stage where 30 W was set as the constant power limit, which led to a current flow of 0.45 A at 73.2 V (Figure 5.1 c).

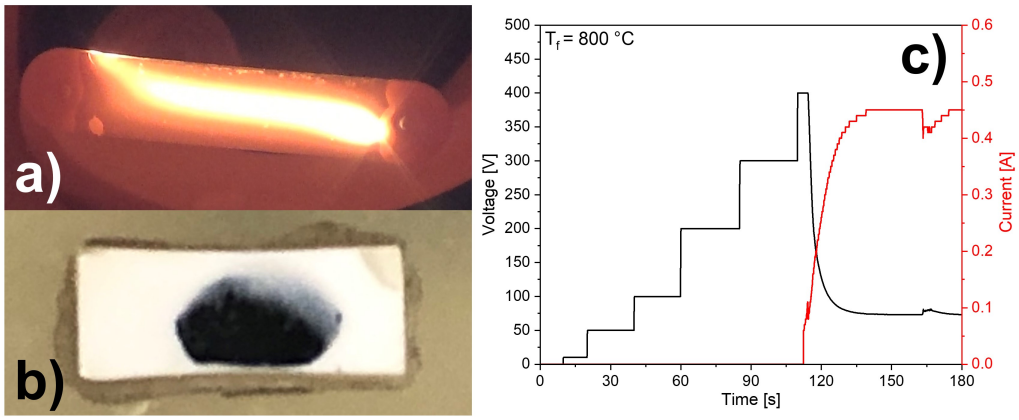


Figure 5.1: 3YSZ a) during FS and b) cross section of the sample after dissipating power during furnace cool-down and quenching; c) shows the stepwise increased voltage and current during FS at a furnace temperature of 800 °C.

The power dissipation was maintained for 60 s before, and during the furnace cool-down. As soon as T_f dropped below 100 °C the field was turned off and the sample was quenched which limited reoxidation to a minimum and enabled investigation of the material at room temperature. Usually, power dissipation is

stopped at T_f of several hundred degrees which causes reoxidation and makes characterisation of the material before reoxidation impossible.

During the experiment current and heat strongly concentrated in the centre of the sample cross section leading to inhomogeneous densification (Figure 5.1 a), as is usually the case in FS of YSZ.

After quenching, the sample surface was white, however, the centre of the sample cross section, where current concentrated, showed blackening (Figure 5.1 b). Since blackening is known to be an indicator of electrochemical reduction in YSZ [111, 112], this experiment reveals that during FS of (3)YSZ an electrochemical reduction happens where current and heat concentrate.

5.1.2 Flash sintering 3YSZ green body in other atmospheres

In addition to the experiment in air, similar experiments were conducted in O_2, N_2 and Ar (comparable results to N_2 but not shown).

A rapid increase in current under comparable circumstances with and without atmospheric O_2 was observed. During FS in N_2 a rapid increase in current happened after a slightly shorter incubation time compared to experiments conducted in O_2-containing atmospheres as shown in Figure 5.2. For both experiments the applied field required for a rapid increase in current is lower compared to the same experiment in air.

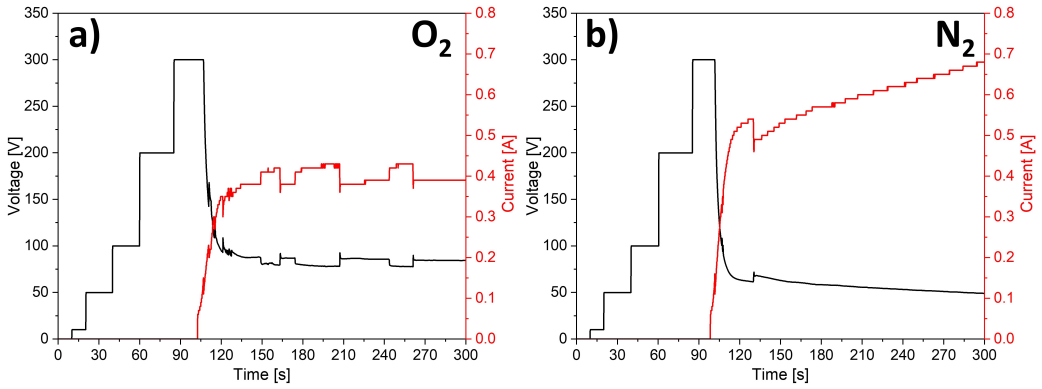


Figure 5.2: Applied Voltage and Current during FS of 3YSZ green bodies in a) O_2 and b) N_2.

As well as the more rapid increase in current, 26 mA/s in N_2 compared to 16 mA/s in O_2 (Figure 5.3 a), the final amount of current flowing through the sample in N_2 after 300 s is almost twice the current flowing in O_2 or air and does not plateau, but continues to increase, even if the same power was dissipated in all three experiments.

Furthermore, the calculated conductance (I/U, U is voltage) in the power-controlled stage in N_2 (Figure 5.3 b) shows a more than twice as rapid increase as the same experiment in O_2 within the first 5, 10 and 15 s. It can be concluded that under FS-conditions no external O_2 is necessary to achieve high current flows in (3)YSZ, as reported before [181]. Actually, higher O_2 partial pressures impede the rapid current increase and lead to plateauing of the current, whereas in inert atmosphere it takes significantly longer to reach a constant state with a constant current and voltage level, if it is reached at all.

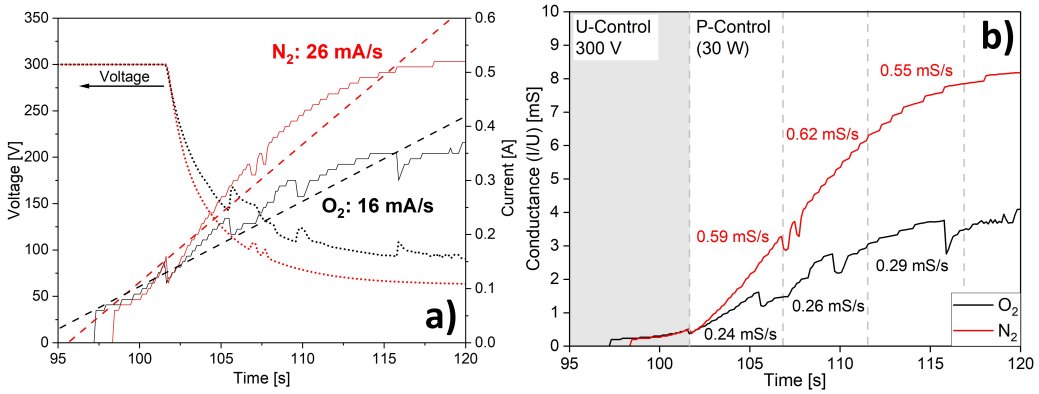


Figure 5.3: a) Applied Voltage and Current during FS of 3YSZ green bodies in O_2 (black) and N_2 (red) time normalised including linear fit for visualisation of the ratio of current increase over time (dashed lines); b) Conductance (I/U) calculated based on the data shown in a) including the increase in conductivity during the first 5, 10 and 15 s of the power-controlled stage highlighted with vertical grey dashed lines.

5.2 Electrical loading of pre-sintered YSZ

Electrical loading of 3YSZ was conducted to investigate the electrochemical reduction process, to eliminate the complication introduced by densification. Similar T_f of 800 °C as for FS of 3YSZ was used and change of atmosphere was conducted by closing/opening the connected (high pressure) gas cylinders, leading to an exchange of atmosphere.

For the experiments where atmosphere was changed from O_2 to air to Ar or N_2, the Pt-paste applied at the electrodes was applied in a way that the electrodes were closer on one side, leading to an increased field on this side, which is facing the windowed side of the furnace, as shown in Figure 5.5 a).

Electrical loading in oxygen including atmospheric change to air

During the first voltage-controlled (50 V) stage in O_2 a rather slow increase in current (Figure 5.4 a) happens before the increase accelerates and slows down again, leading to a constant current flow of 0.26 A after 550 s without reaching the defined power limit of 25 W.

The atmospheric change from O_2 to air, after 700 s, causes a current drop by less than 10 % down to 0.24 A ($\approx$ 2.5 A/cm^2) shown in Figure 5.4 b). Up to this stage the sample shows homogeneous heating (Figure 5.5 b). According to the

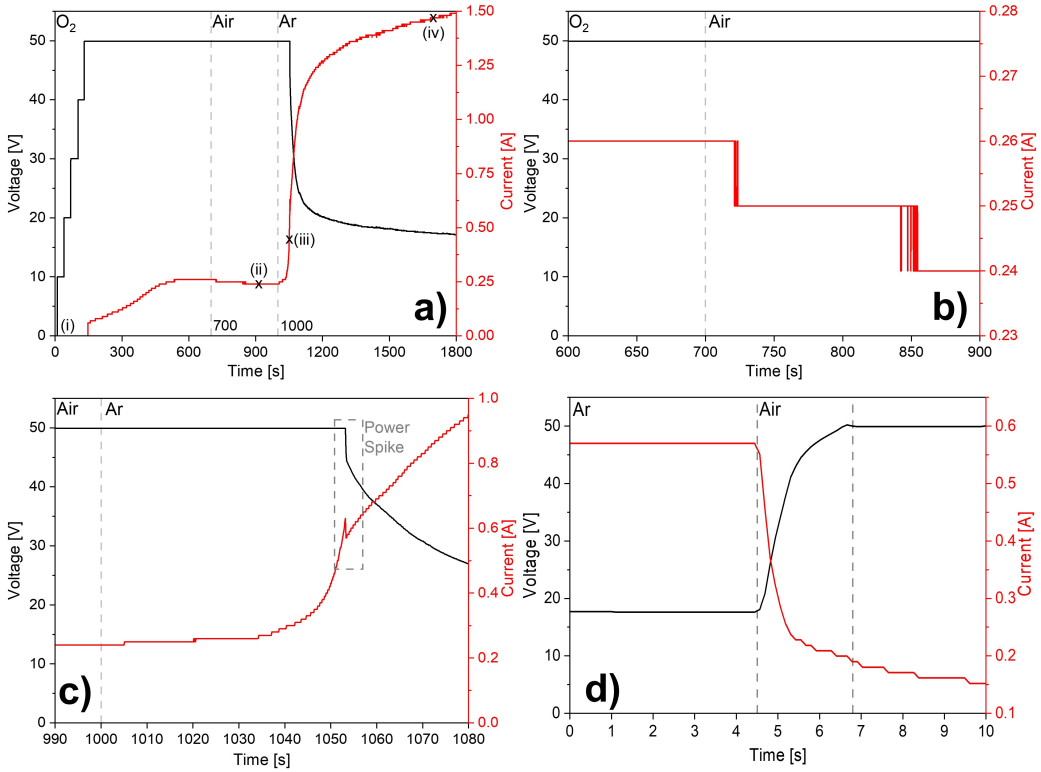


Figure 5.4: Electrical parameters during electrical loading of pre-sintered 3YSZ in various oxygen partial pressures, changing from pure O_2 to air to Ar. The transition from O_2 to air happened after 700 s, the second change from air to Ar after 1000 s. a) V and I, b) V and I during the change from O_2 to air; c) during the change from air to Ar; d) V and I during change from Ar to air conducted in a separate experiment which shows a transition from the power- back to the voltage-controlled stage.

black body radiation (BBR) model [5, 25] the sample in this stage is heated up by 175 °C to ≈ 975 °C. If power dissipation is stopped at this point, and the sample is cooled down in inert atmosphere, a homogeneous grey colouring can be seen (Figure 5.5 c).

Sometimes, locally heated points across the sample surface can be seen. In Figure 5.5 b) such a point, highlighted with a black dashed line, is located about half way

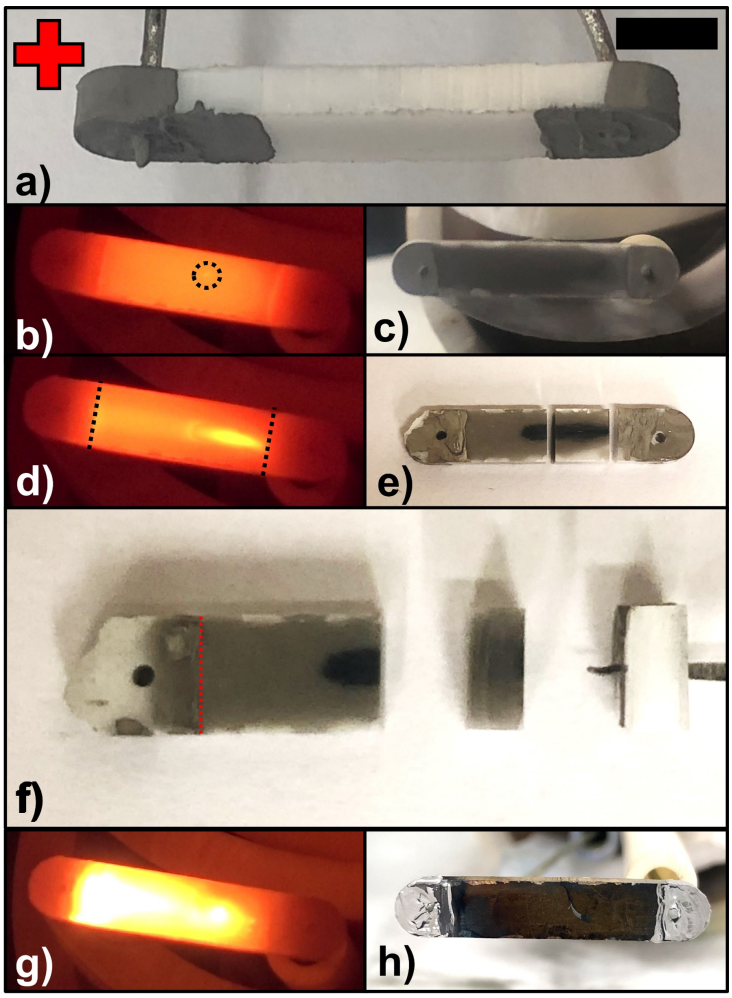


Figure 5.5: Pre-sintered 3YSZ sample mounted on metal electrodes including applied Pt-paste before electrical loading with the anode (+) on the left and cathode on the right (-); b) during electrical loading in air (ii); c) after electrical loading in air; d) during electrical loading a few seconds after atmospheric change from air to Ar (iii); e) after electrical loading for a few seconds after atmospheric change from air to Ar and cooled-down in Ar; f) surface of the sample shown in e) after removal of Pt-paste from the electrodes, the Pt-covered area is highlighted in form of a red dashed line, the right two parts show the cross section originally located on the anode-side of the cut sample after turning the cut pieces (shown in e) by 90 °; g) after electrical loading for a few hours in Ar (iv); h) after electrical loading for a few hours in Ar and cooled-down in Ar.

between the electrodes. Similar behviour is observed during electrical loading of yttria-stabilised hafnia, shown in the Appendix in section A.3.

Electrical loading during atmospheric change from air to Ar

Approximately 30 s after atmospheric change from air to Ar (1000 s) (or N_2), the current starts increasing rapidly (Figure 5.4 a) and c). This second increase in current is significantly faster than the first one. Furthermore, strong current concentration happens with the consequence of inhomogeneous sample heating (Figure 5.5 d), especially near the cathode.

The characteristics of this second increase in current and heat concentration are comparable to the process of FS a 3YSZ green body reported above (Figure 5.1 c).

If the power dissipation in the sample is stopped after $\approx$ 1050 s and cooled down in Ar (or N_2), strong blackening can be seen on the surface where current concentrated (Figure 5.5 e). The centre of the sample cross section did not show blackening at this stage (Figure 5.5 f). Also, the material on the cathode side, originally covered by Pt-paste, did not show any greying or blackening after scratching off the paste. However, the material close to the anode, originally covered by Pt-paste, (Figure 5.5 e) showed greying to the point where the metal wire, acting as electrode, was inserted into the sample (Figure 5.5 f).

Current concentration and blackening of the sample starts on the cathode (right) side of the sample as was reported previously [30, 111, 112] and propagates along the pre-sintered sample surface (Figure 5.5 e) with a speed of $\approx$ 1.5 mm/s.

After 1053 s a transition from voltage- to power-control happens and a power spike occurs, exceeding the defined power-limit of 25 W for $\approx$ 2.5 seconds before stabilising. At this point the blackened region propagated across the sample connecting cathode and anode (Figure 5.4 c), which marks the end of electrochemical reduction induced runaway.

Electrical loading and continuous reduction in Ar

If the power dissipation is continued the overall conductivity increases and sample heating shifts towards the anode (Figure 5.5 g). After maintaining the power dissipation during furnace cool-down the sample shows a metallic shining golden/brown colour (Figure 5.5 h).

Reoxidation after atmospheric change from Ar to air

The reoxidation process was investigated by changing the atmosphere from Ar back to air after dissipating 10 W for 30 s in a pre-sintered sample in Ar.

The electrical parameters (Figure 5.4 d) show transition from power- back to voltage-control within 2-3 s due to an increase in voltage up to the defined voltage

limit, caused by a significantly lower conductivity of the material after reoxidation, suggesting that reoxidation also happens almost immediately after current is turned off at elevated T_f as usually done in FS. It should be mentioned, that in this experiment the reduction mainly happens on the surface, whereas during conventional FS, reduction is according to the previous results, located mainly in the centre.

Additionally, a 3YSZ green body previously FSed in He and a conventionally sintered 3YSZ sample, which is fully oxidised, were used for thermogravimetrical analysis (TGA), showing a strong increase in weight by 1.25 % for the in He FSed sample at temperatures exceeding 50 °C, shown in the Appendix in Figure A.10.

5.2.1 Arrhenius plot of the electrical resistivity during electrical loading

The electrical parameters presented (Figure 5.4) do not consider sample heating during electrical loading.

To interpret and identify ongoing fundamental changes in the material and its conduction mechanisms an Arrhenius plot of the electrical resistivity over inverse sample temperature is shown in Figure 5.6. Sample temperature is estimated according to the black body models presented by others [20, 25, 182], with the assumption and restriction of the power dissipation being homogeneous. Furthermore, activation energies (Q) are calculated for each stage, dependent on the atmosphere applied (O_2, air, or Ar).

The inverse Arrhenius plot shows that during the increase in power dissipation in O_2, the estimated sample temperature increases (Figure 5.5 b) and the resistance decreases non-linearly (Figure 5.6). A reduction of the activation energy (Q) from the very beginning of process is suggested by the decreasing slope.

Even if one single Q-value is insufficient to fully represent the O_2-stage, 106 kJ/mol is the representative Q-value calculated for this O_2-stage, where sample heating is homogeneous, which will be used for comparing the different stages.

If the atmosphere is changed from O_2 to air (ii) the current drops by $\approx$ 10 %

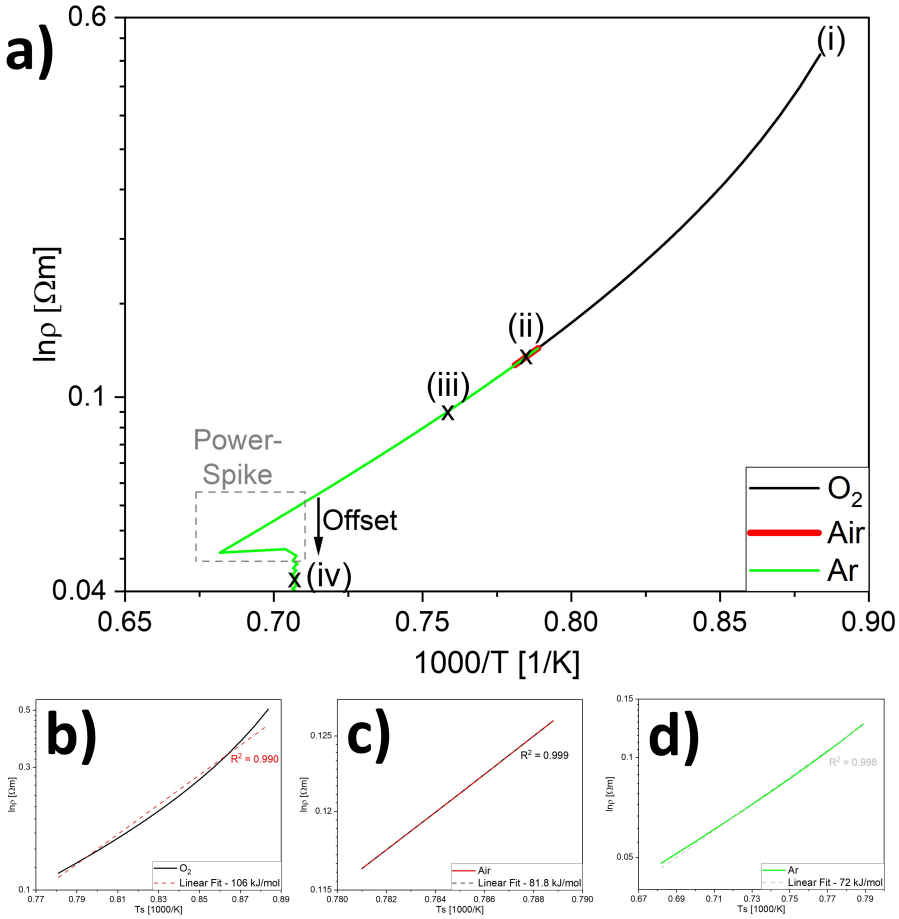


Figure 5.6: a) Inverse Arrhenius plot of the electrical resistance over estimated sample temperature during electrical loading of pre-sintered 3YSZ at 800 °C under an applied voltage of 50 V (25 V/cm) based on parameters shown in Figure 5.4 including an atmospheric change from O_2 to air to Ar, transition from voltage- to power control and (i)-(iv) indicators to visualise the connection to Figure 5.4 a). b) to e) show the calculated activation energies for the different stages dependent on the atmosphere applied.

leading to a reduction in estimated sample temperature and increase in resistivity.

Even if the current drops and the sample heating is still homogeneous, the Q-value in this stage decreased to 81.8 kJ/mol (Figure 5.6 c) $\approx$ 25 % below the representative Q-value in O_2 at the exact same (estimated) temperature range.

During atmospheric change from air to Ar (iii) the power spikes, the supply changes from voltage- to power-control, and subsequently reduces the power dissipation to the defined limit of 25 W, resulting in an estimated sample temperature of 1140 °C ($\approx$ 0.71 1000/K). Furthermore, at two points during this stage, shortly before and after the power spike, the same (estimated) temperature is calculated, however, the resistivity at these two points shows a 20 % resistivity offset.

Based on the data recorded during voltage-control (before the power spike) the representative Q-value for the Ar-stage decreased even further down to 72 kJ/mol (Figure 5.6 d). However, in this stage sample heating is inhomogeneous, which means that the Q-value calculated is not really representative.

If power dissipation is maintained in Ar at the defined power-limit and constant furnace temperature, the resistance drops continuously visualised by the vertical green line (iv).

5.2.2 Sample heating and appearance during and after flash sintering and electrical loading in various atmospheres

A comparison between the appearance of samples with FS and electrical loading of 3YSZ in various atmospheres, with the power dissipation maintained during furnace cool-down, is shown in Figure 5.7. For all samples Pt-paste on all sides was applied equally, leading to a rather homogeneous electrical field.

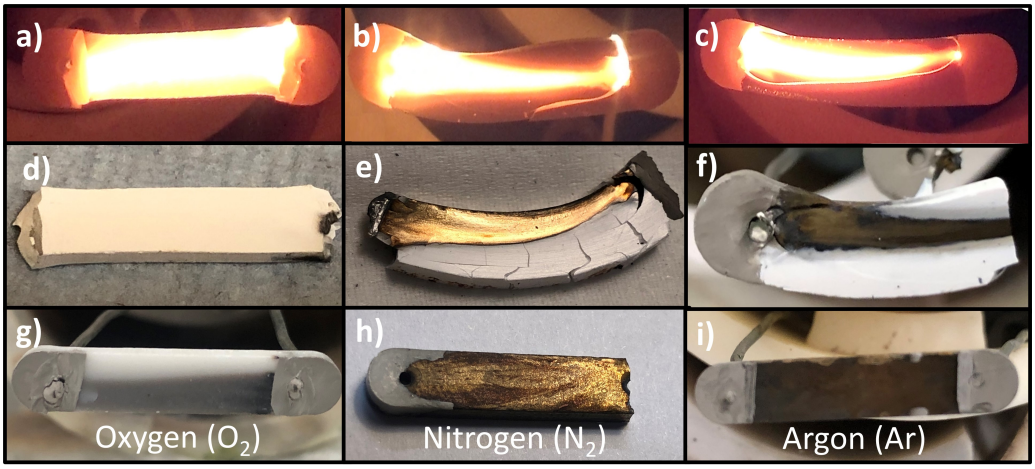


Figure 5.7: 3YSZ during and after FS of green bodies and pre-sintered samples in O_2 (a, d, g), N_2 (b, e, h) and Ar (c, f, i). The power limits were 25 W for green bodies and 40 W for pre-sintered samples, which were maintained during furnace cool-down. For all samples the cathode (-) side is on the right and the anode (+) on the left.

If FS or electrical loading was conducted in O_2, sample heating was rather homogeneous for both processes (Figure 5.7 a). After FS almost no blackening was detected on the sample surface (Figure 5.7 d). However, the pre-sintered sample showed greying on the bottom half of the sample after electrical loading (Figure

5.7 g).

FS in N_2 showed inhomogeneous sample-heating, spreading out from cathode to anode (Figure 5.7 b) and golden coloured material in the heated region after FS (Figure 5.7 e). The pre-sintered sample showed the same characteristic golden colour with a more even distribution and with some finger shaped regions ranging from cathode towards anode (Figure 5.5 h). This resembles the morphology of electrochemical blackening of YSZ reported by Janek and Korte [29].

FS in Ar caused inhomogeneous sample heating (Figure 5.7 c) and post-heating colour change (Figure 5.7 f) as described for N_2. However, the colour was more brown/grey than gold and was more evenly distributed in the pre-sintered sample (Figure 5.7 i).

In all samples, except the FS green body in O_2 (Figure 5.7 a), an inhomogeneous colouring of the sample surface can be seen which clearly points towards an inhomogeneous structural change of the material.

5.3 Characterisation of YSZ after flash sintering and electrical loading

The previous results revealed fundamental changes in the materials´ structure during FS or electrical loading.

The effects and influence of the electrical loading on YSZ are investigated by the following characterisation techniques: *SEM, EDS, Raman spectroscopy, XRD, XPS, EPR* and *room temperature electrical conductivity measurements*.

5.3.1 SEM and EDS

3YSZ flash sintered in air - including cool down

SEM images of 3YSZ-FS-CD-air (Figure 5.1), were taken from the cross section in the white and black areas shown in Figure 5.8. In the white section of the cross section, intergranular fracture occurred and a grain size of $\approx$ 400 nm was measured, whereas the black centre shows transgranular fracture of most larger grains, hundreds of nm in size, as well as the formation of separate small crystals, smaller than 100 nm.

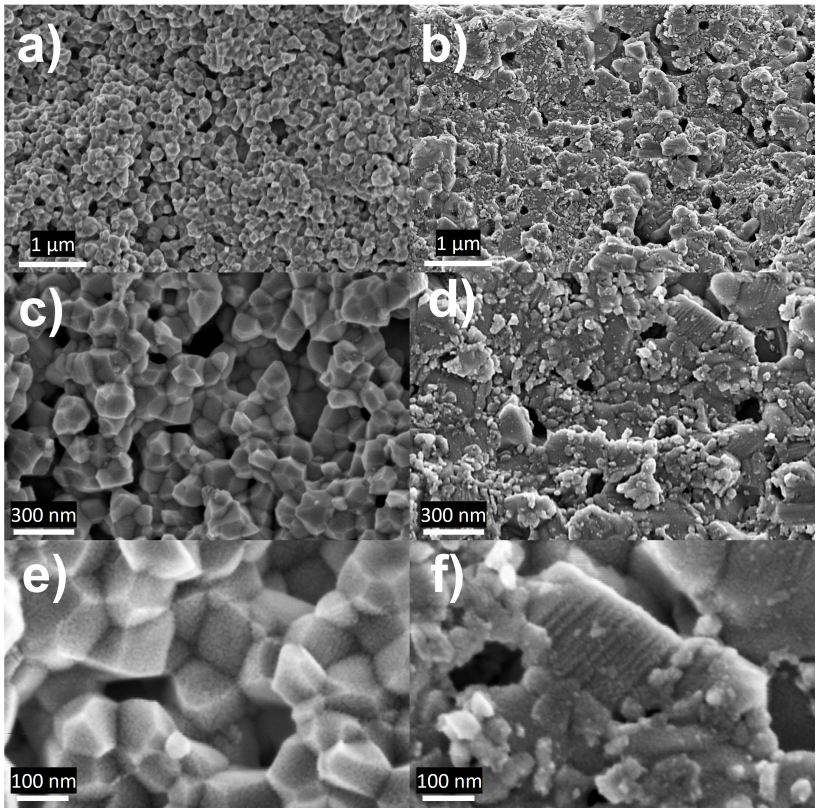


Figure 5.8: SEM images taken from a fractured cross section of a 3YSZ green body flash sintered in air with power dissipation maintained during furnace cool-down as shown in Figure 5.1 and fractured half way between the electrodes. a), c) and e) show the fractured white part of the cross section close to the surface of the sample; b), d) and f) show the fractured black centre of the sample cross section.

3YSZ electrically loaded in Ar - 30 s

The early stage of the ongoing electrical loading in an inert atmosphere (Ar) for a few seconds was characterised by EDS investigating the cross section of the 3YSZ-EL-30s-O_2, air, Ar sample, also shown in Figure 5.5 d), e) and f).

Figure 5.9 shows the blackened region of the polished cross section of the sample, located half way between anode and electrode. The elemental distribution

on the left side of the sample shown in Figure 5.9 d) shows an O depleted region close to the surface which is approximately 0.5 μm in depth, a clear sign of electrochemical reduction. In this region the Zr signal is stronger due to the lack of O.

The very surface of the sample is not depleted in O, which, most likely, happened due to reoxidation of the reduced material during sample preparation. However, point spectra taken from the oxygen depleted region and the less reduced inner section of the sample (normalised for Zr) visualised in Figure 5.9 e) show that the O-content in the reduced region is almost exactly half of the O-content in the less reduced region, suggesting the electrochemically induced formation of ZrO.

3YSZ electrically loaded in Ar - including cool down

If electrical loading is continued and maintained during furnace cool down, the near-surface cross sections of two samples after electrical loading in Ar (3YSZ-EL-CD-Ar) and N_2 (3YSZ-EL-CD-N_2) show an O depleted surface layer, relative to the bulk, being $\approx$ 1 μm thick in the Ar sample (Fig. 5.10 d) and $\approx$ 10 μm thick in the N_2 sample (Fig. 5.10 j). Furthermore, the 3YSZ-EL-CD-N_2 sample shows a strong N signal in the reduced region (Fig. 5.10 n), whereas the sample loaded in Ar shows a weaker N signal in the reduced region (Fig. 5.10 h). In both cases a sharp transition from the unreduced bulk to a clearly reduced surface region can

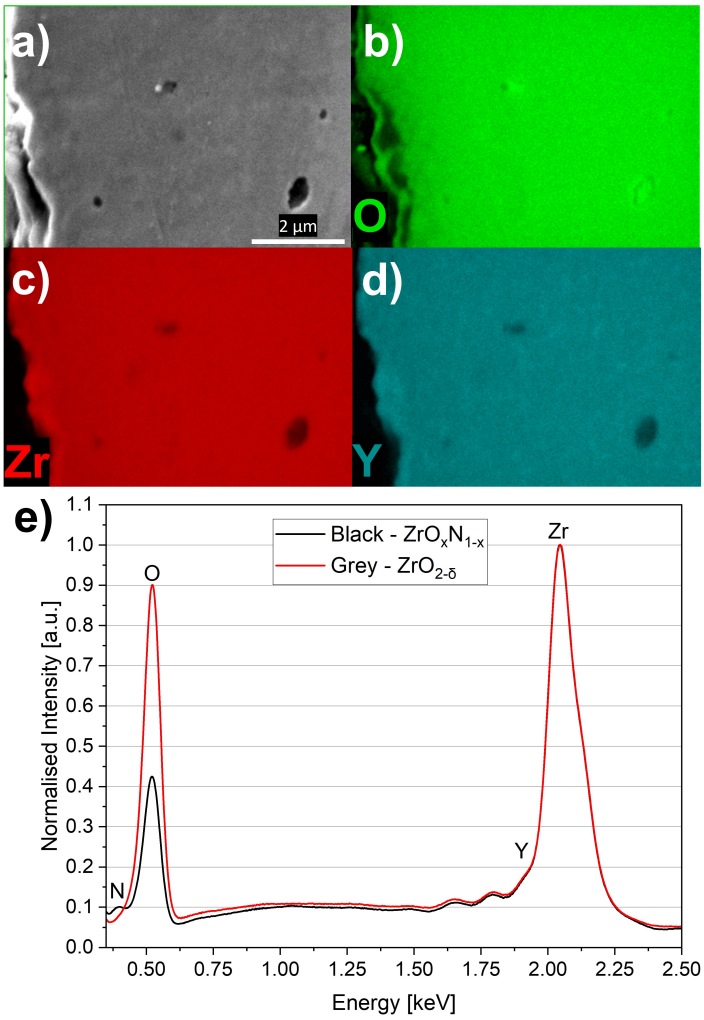


Figure 5.9: SEM and EDS of the blackened side of the cross section near the surface of 3YSZ electrically loaded in Ar for a few seconds after loading in air as is shown in Figure 5.5 e) and f). Elemental distribution in the partially reduced region of the sample is shown as follows: b) O green, c) Zr red, d) Y light blue. e) EDS point spectra taken from the oxygen depleted region close to the surface (black) and the less reduced inner section of the sample (red), both spectra are normalised for Zr.

be seen in the elemental distribution.

The N signal in the reduced region in the 3YSZ-EL-CD-Ar sample (Fig. 5.10

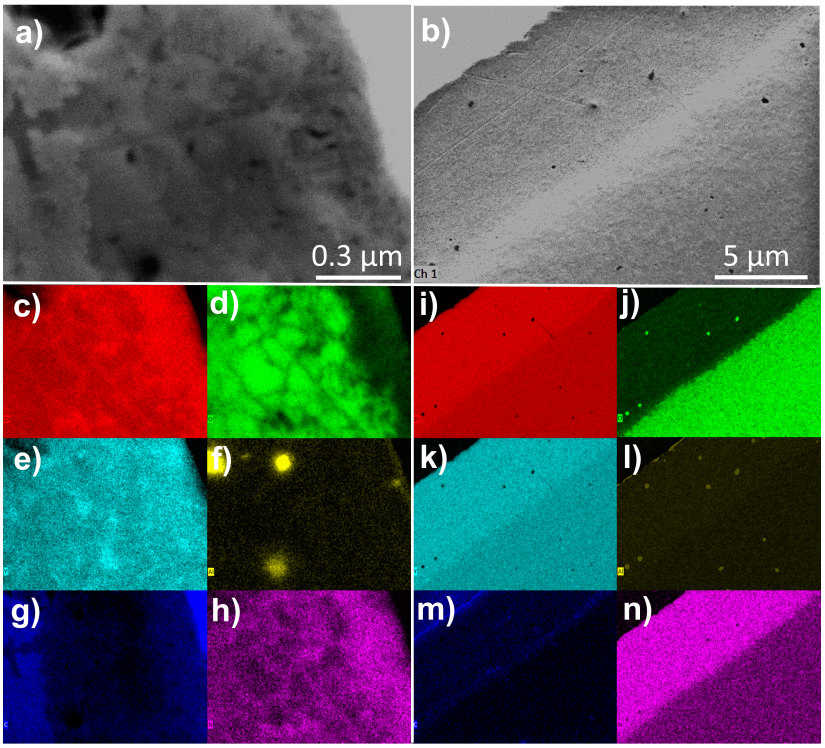


Figure 5.10: SEM and EDS of cross section near the surface of 3YSZ electrically loaded in Ar (fracture surface, a, c-h) and in N_2 (polished section, b, i-n). Elemental distribution in the partially reduced region of the sample is shown as follows: Zr red, O green, Y light blue, Al yellow, C dark blue and N magenta.

h) can most likely be explained by a reaction between the reduced region of the sample and the atmosphere because the time between electrical loading and SEM/EDS-characterisation was in the range of 2 days. During electrical loading itself (almost) no N was available in the atmosphere since the furnace was filled with Ar, which was constantly flowing into the furnace preventing air or N getting into the furnace.

Figure 5.11 a) shows the fractured cross section of the 3YSZ-EL-CD-Ar sample close to the surface where a lack of O was detected. A fundamental change in the

grain structure and fracture mode can be seen about 10 μm from the surface, which is a little way beyond the right hand boundary of the micrograph. The grains of around 250 nm diameter and intergranular fracture in the specimen interior are replaced near the surface by a finer structure with some transgranular fracture (Figure 5.11 b)-e).

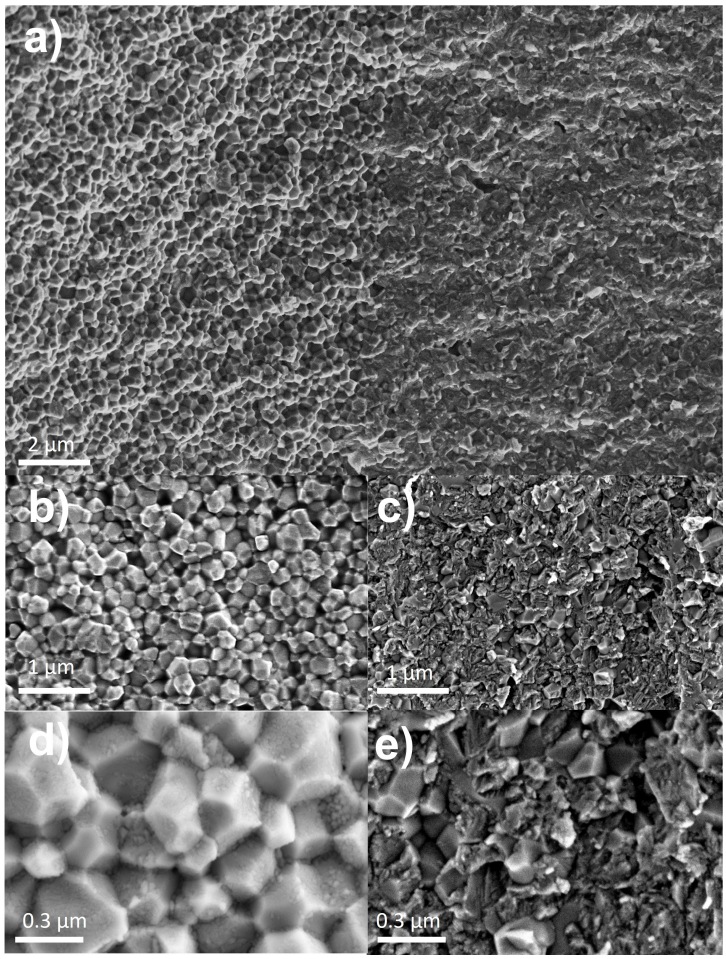


Figure 5.11: SEM of a fractured cross section of a 3YSZ sample after electrical loading in Ar (40 W). a) shows the transition zone between (to the left) inter- and (to the right) trans-granular fracture. b) and d) show the less reduced region with inter-granular fracture at higher magnifications. c) and e) show the reduced and transformed region of the sample with transgranular fracture.

Figure 5.12 shows the surface of the 3YSZ-EL-CD-Ar sample in three different regions with three different stages of reduction from just slightly reduced grey (Figure 5.12 a)-c) to more reduced black (Figure 5.12 d)-f) to the most reduced bronze region (Figure 5.12 g)-i). It can be seen that with the ongoing reduction the original grains transform into the previously mentioned significantly smaller grains which are in the range of tens of nanometres in size.

SEM images and EDS maps with a focus on the alumina additives, which were added by the powder manufacturer, are shown in the Appendix in Figure A.4 showing a change in the shape and distribution of Al in, or close to, the blackened regions where a lack of O was detected. In O-rich regions, well-defined alumina grains can be seen, whereas these show a rather blurred boundary in the reduced regions.

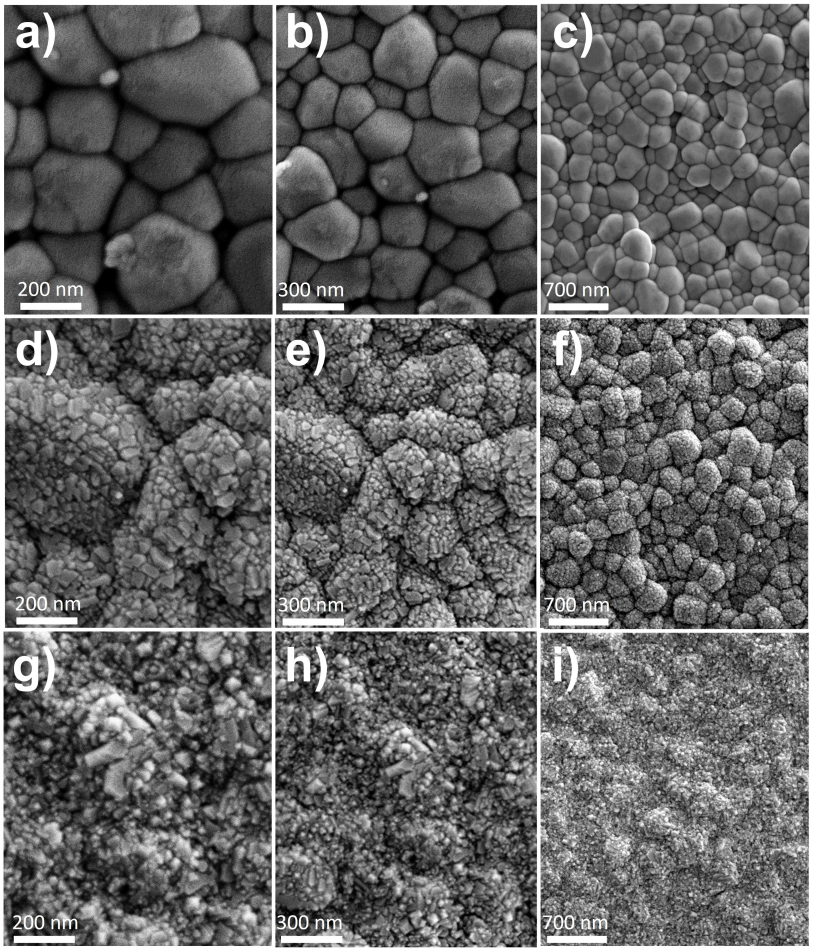


Figure 5.12: SEM of the surface of 3YSZ sample in different regions of the sample after electrical loading in Ar. a)-c) show the mostly unreduced (light) grey surface of the sample; d)-f) show the blackened region of the surface and g)-i) show the heavily reduced bronze section of the sample surface.

8YSZ electrically loaded in Ar - including cool down

In addition to the previously described results about 3YSZ, the behaviour of 8YSZ (8YSZ-EL-CD-Ar) was also investigated by SEM and EDS of electrically loaded samples, to investigate the potential electrochemical reduction in Ar.

EDS point spectra and maps taken from a lightly polished surface of a reduced 8YSZ sample are shown in Figure 5.13. It is evident that the surface is inhomogeneous in appearance. The positions of the point spectra are highlighted in Figure 5.13 a). Spectra were normalised to 1 for Zr and are shown in Figure 5.13 b). Figure 5.13 c) shows the O-region of the EDS spectra revealing significant differences of up to 40 % as can also be seen in Figure 5.13 f). Furthermore, the EDS-spectra (Figure 5.13 d) and the EDS-maps (Figure 5.13 g) show that these regions contain less, or even no, Y compared to the surrounding matrix.

SEM images of another polished 8YSZ-EL-CD-Ar sample are shown in Figure 5.14. The regions where a lack of O was detected, as shown in Figure 5.13, are visible as bright areas, potentially due to their higher relative Zr-concentration.

Figure 5.15 shows SEM images from a fractured 8YSZ cross section at various magnifications. In general the fracture behaviour is comparable to electrically loaded 3YSZ with the difference that smaller precipitates are visible along the grain boundaries, and also within the grains.

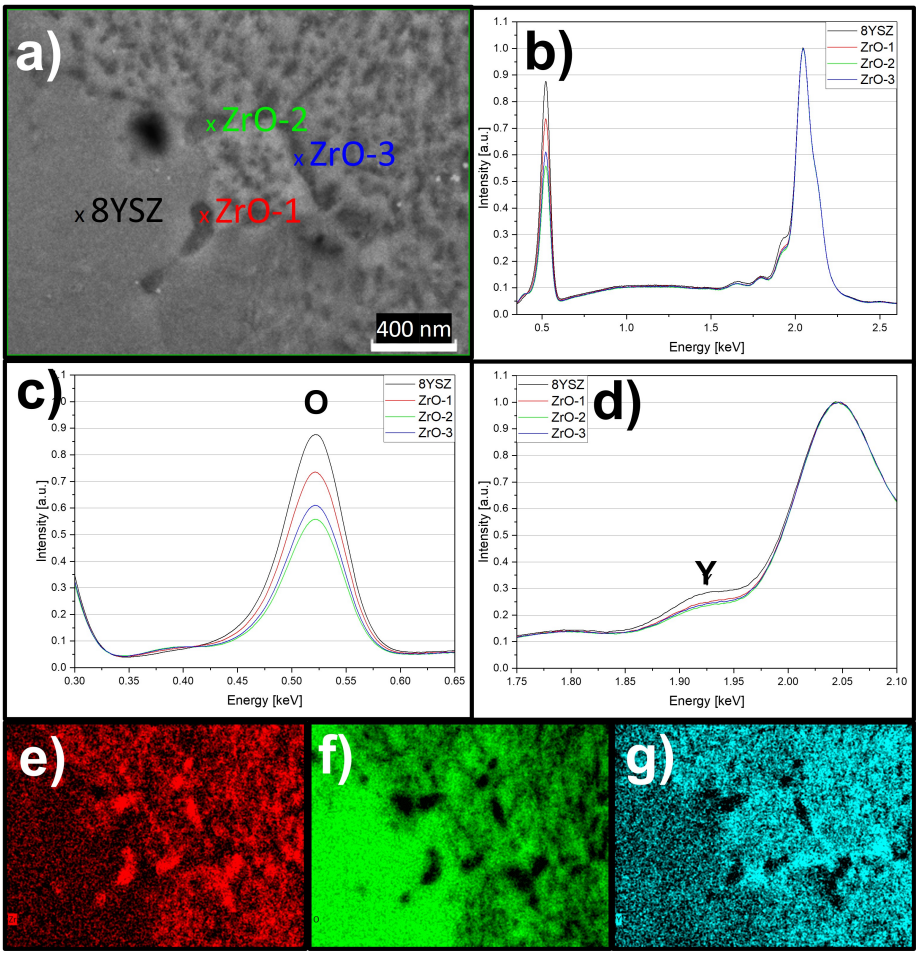


Figure 5.13: SEM and EDS point spectra and maps of the surface of an 8YSZ sample electrically loaded in Ar. a) shows the SEM image including the location of point spectra; b) detected point spectra normalised to 1 for Zr; c) O-region of the EDS spectrum; d) Y-region of the EDS spectrum; e) Zr EDS map; f) O EDS map; g)Y EDS map.

SEM images of the surface of an 8YSZ-EL-CD-Ar sample, shown in Figure A.5 in the Appendix, reveal small crystals comparable to those on the surface of 3YSZ after electrical loading (Figure 5.12).

Figure 5.16 shows the SEM image and the elemental distribution in an electro-

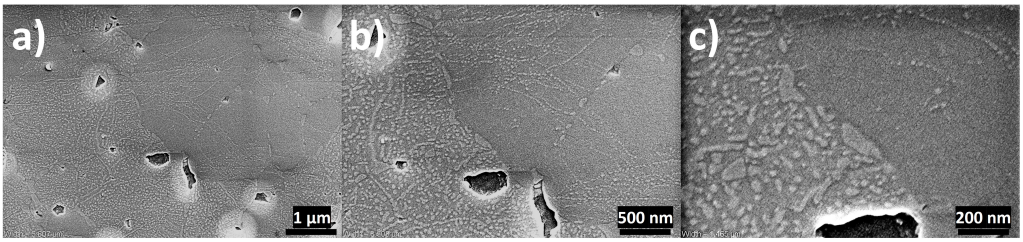


Figure 5.14: SEM of polished surface of pre-sintered 8YSZ electrically loaded in Ar at various magnifications.

chemically reduced and fractured 8YSZ region. The EDS map shows that in the precipitates a lack of O and Y is apparent which is accompanied by an increased Zr signal. This is particularly visible at the grain boundary where more precipitates are formed.

A similar behaviour as for 3YSZ and 8YSZ was observed vor yttria-stabilised hafnia, which also forms small grains < 50 nm in size, shown before and after electrical loading in the Appendix in Figure A.19, A.22 and A.21.

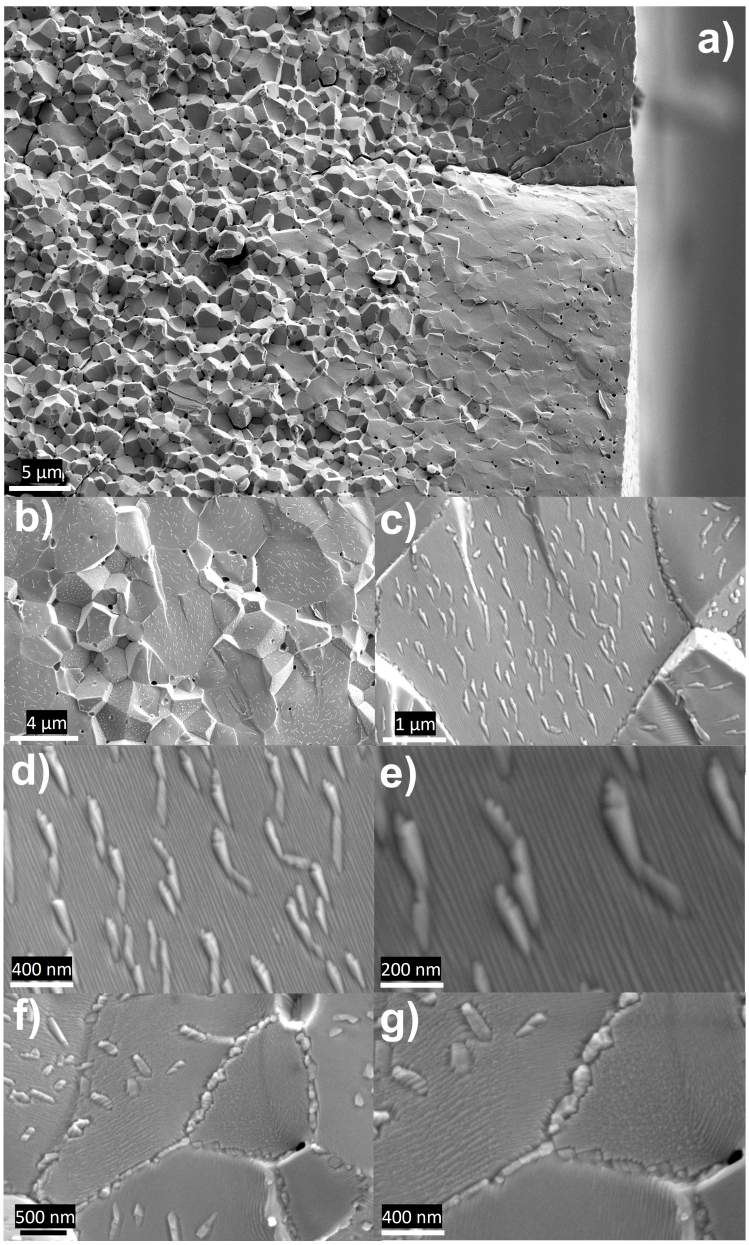


Figure 5.15: SEM of cross section of a near surface fractured pre-sintered 8YSZ sample electrically loaded in Ar at various magnifications. a) shows the transition zone between (to the left) inter- and (to the right) trans-granular fracture. b)-g) show the trans-granular fractured region at various magnifications.

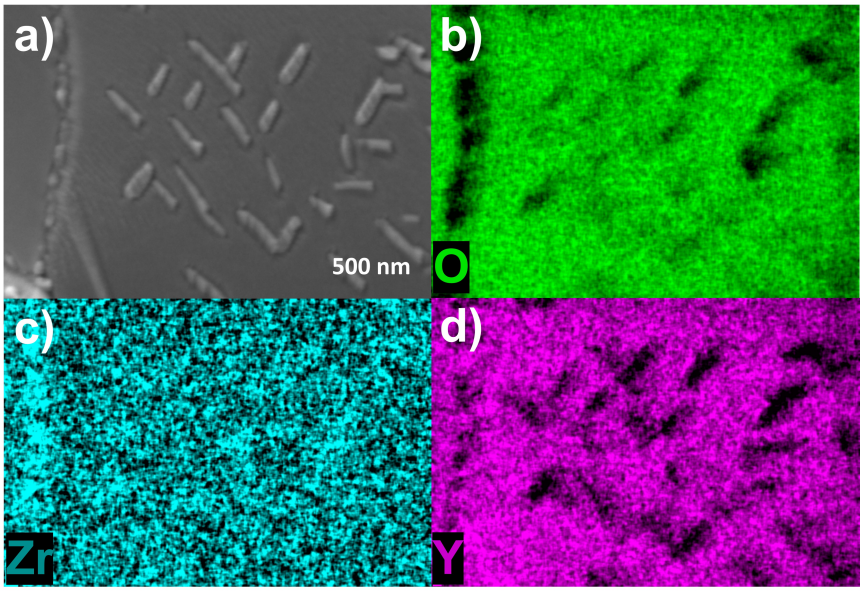


Figure 5.16: SEM and EDS of a more central cross section of 8YSZ electrically loaded in Ar. Elemental distribution is shown as follows: Zr light blue, O green and Y magenta.

5.3.2 X-Ray Diffraction (XRD)

Figure 5.17 a) and b) show the background-corrected XRD spectra between 20 and 120 ° for conventionally sintered unloaded and electrically loaded (40 W) a) 3YSZ-EL-CD-Ar and b) 3YSZ-EL-CD-N_2.

After electrical loading, new peaks appear and the experimental peak positions and intensities are consistent with the predictions for FCC rocksalt ZrO in both atmospheres (Figure 5.17 a) and b). The peak positions were predicted using VESTA [76] software.

Figure 5.17 c) and d) show the slow-scanned spectra between 33 and 36 °, where the {002} and {110} tetragonal peaks for 3YSZ are expected [60]. Conventionally sintered 3YSZ shows the expected tetragonal crystal structure where the {002} and {110} tetragonal peaks are separated by approximately 0.6 ° at around 35 °. However, broadening and loss of clear separation of the tetragonal peaks in the {002} and {110} peak region (Figure 5.17 c) and d) were observed in the case of in N_2 electrically loaded samples, where the tetragonal {112} and {200} peaks merge into a single broad peak. If electrically loaded in Ar, the same trend is visible from 0 to 25 and from 25 to 40 W, however the trend is not continued if the power is further increased from 40 to 60 W (Figure 5.17 c) and e). In this region changes were also reported in investigations conducted by other researchers [78].

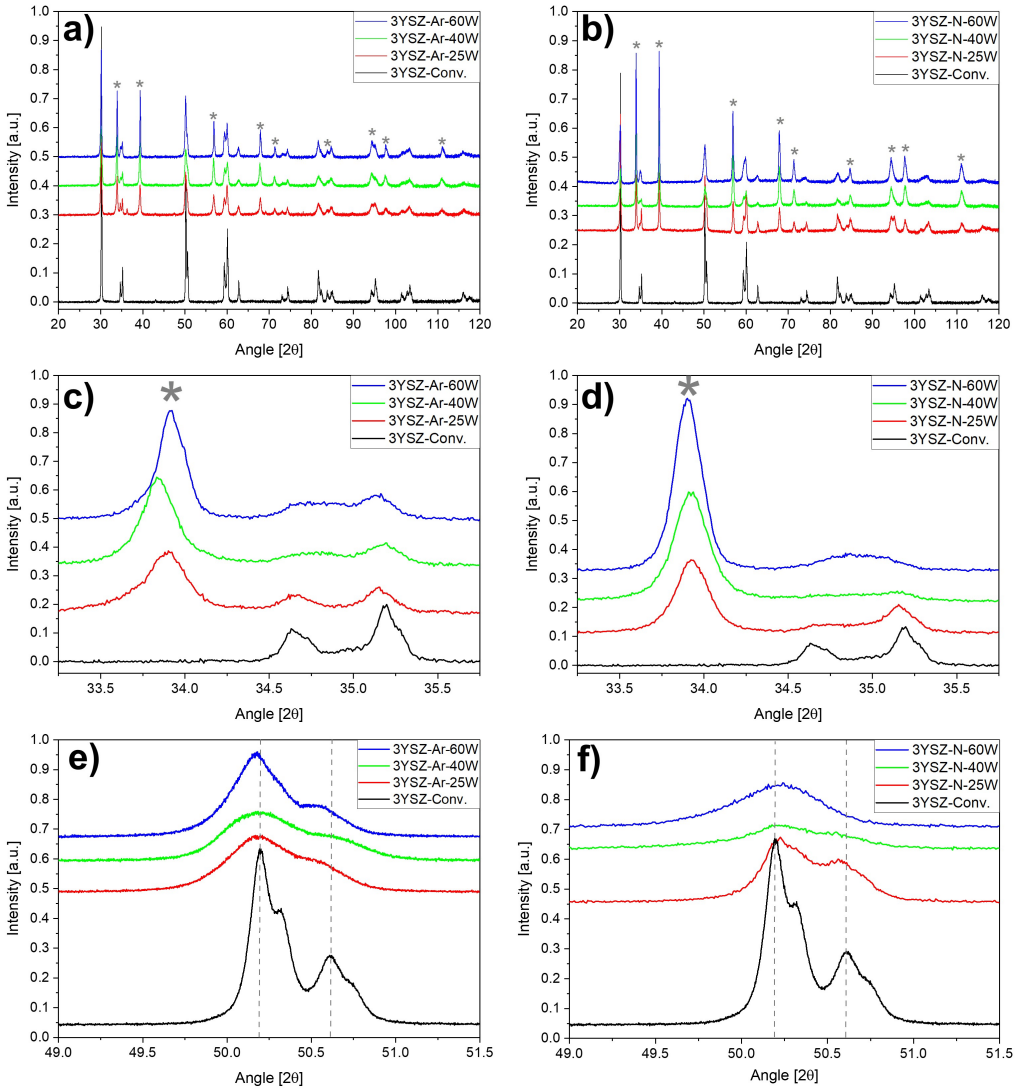


Figure 5.17: Phase evolution during electrical loading of pre-sintered 3YSZ in Ar (a, c, e) and N_2 (b, d, f) with varying power dissipation (25, 40 or 60 W). The codes in the legend denote starting composition - atmosphere - limiting power (conv. = conventional sintering). Stars (*) on top of some peaks highlight the rocksalt ZrO(N) peaks.

Furthermore, Figure 5.17 e) and f) show the range between 49 and 51.5 ° where the {112} and {200} peaks of tetragonal YSZ phase are located [60].

In the case of electrical loading in N_2 it is assumed that the new phase is Zr(O,N)

with some O from the original ZrO_2 lattice but also incorporating a significant amount of N_2 from the atmosphere, as was reported previously by Morisaki et al. [83] and presumably Charalambous et al. [79]. However, during electrical loading in Ar the incorporation of N must be negligible, leaving ZrO as the only possible rocksalt phase, which also agrees with the ZrO giving a slightly better refined fit in both atmospheres. The detected Zr(O,N) phase and the ZrO phase show comparable refined lattice parameters of 0.4577 nm and 0.4580 nm, respectively.

The refined phase compositions are shown in Figure 5.18 a) and b). For both atmospheres the amount of ZrO(N) formed after electrically loading the sample with 40 W is highest, and the amount of Zr(O,N) formed at higher power in N_2 is significantly higher than the amount of ZrO formed in Ar. The rocksalt structures formed mainly at the expense of the tetragonal phase in N_2, where approximately 65 wt.% of the volume sampled at 40 W consisted of Zr(O,N). Furthermore, the FWHM of the Zr(O,N) {111} peak reduced as the power was increased, by up to 50 % (Figure 5.18 e).

In Figure 5.18 f) an example Rietveld refinement of 3YSZ-N-60W is shown from 28 to 41 °, which includes 52 wt.% of Zr(O,N), showing the good fit of this rocksalt phase. The 60 W sample shows a significantly lower amount of Zr(O,N) (52 wt.%) compared to the sample loaded with 40 W (65 wt.%), which is contrary to the expected behavior. This result could potentially be explained by the inhomo-

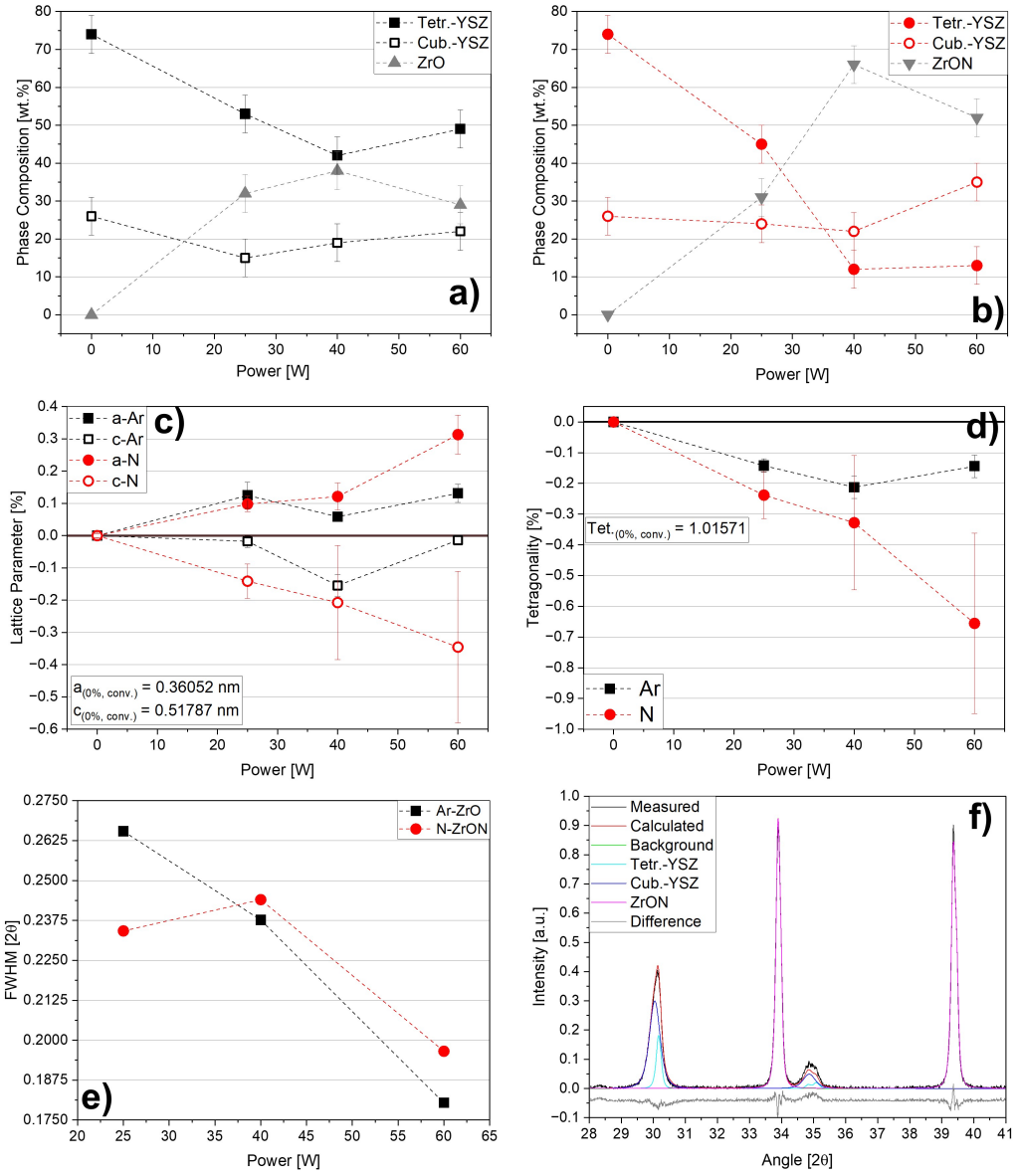


Figure 5.18: Refined phase composition before (0 W) and after electrical loading in a) Ar and b) N_2; c) lattice parameters and d) tetragonality of the tetragonal phase. e) 111 FWHM for Zr(O,N) after electrical loading. f) Rietveld refinement of 3YSZ-N-60 W.

geneous sample composition, and the rather local XRD characterisation, or the power dissipation of 40 W is ideal for the ongoing reduction and phase transfor-

mation, which could be related to the electrical conductivity.

Figure 5.19 a) shows the XRD results and the corresponding Rietveld refinement for for a 3YSZ-Ar-60W sample including one cubic and tetragonal YSZ phase as well as the FCC rocksalt ZrO phase. The FCC rocksalt ZrO phase shows a very good agreement in position and intensity between the measured XRD spectrum and the refined model, as mentioned before and shown in Figure 5.19 b) where the cubic and tetragonal YSZ phases are not included.

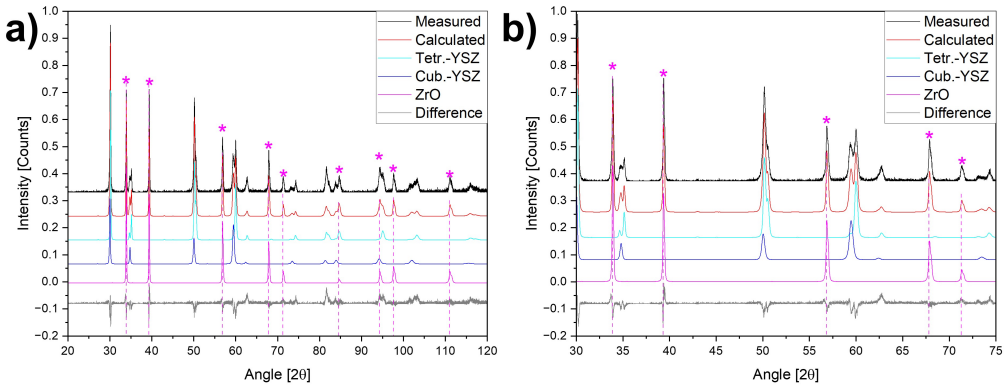


Figure 5.19: a) XRD pattern including Rietveld refinement results for a 3YSZ sample loaded in Ar with a power dissipation of 60 W; b) detailed results with the Rietveld refinement of the FCC rocksalt ZrO phase, including vertical dashed lines where peaks for FCC rocksalt ZrO with a lattice parameter of 0.4580 nm would be located.

The lattice parameter a of the tetragonal phase increased with electrical loading, whereas c decreased (Figure 5.18 c). A consequence of these changes in lattice parameters is a decreasing tetragonality $\frac{c}{a\sqrt{2}}$ with power (Figure 5.18 d). Most of the results showed a net increase in unit cell volume but those at 40 W showed

little change.

In addition to the detailed XRD-analysis of 3YSZ, XRD spectra taken from originally cubic 8YSZ which was also electrically loaded and electrochemically reduced are shown in the Appendix in Figure A.7. 8YSZ shows, like 3YSZ, the formation of ZrO after electrical loading in He or Ar as well as the formation of Zr(O,N) after loading in N_2 with a similar lattice parameter.

Besides stabilised zirconia, stabilised hafnia was investigated after electrical loading. New peaks, most likely related to the formation of FCC rocksalt HfO were detected, with a lattice parameter of 0.4527 nm, shown in the Appendix in Figure A.17, Figure A.18 and Table A.3.

5.3.3 Raman Spectroscopy

3YSZ flash sintered in air - including cool down

Raman point spectra of a 3YSZ-FS-CD-air sample, were taken from the cross section, which showed a white surface/shell and a blackened core, shown in Figure 5.20.

Compared to the reference spectrum, taken from a conventionally sintered 3YSZ sample in air, which is fully explainable by a tetragonal (3)YSZ spectrum [58], with the peaks being located at 147, 260, 320, 465, and 642 cm^{-1}, the spectrum from the white surface shows identical peaks. However, the peaks are less visible due to a stronger background signal and a generally lower peak intensity.

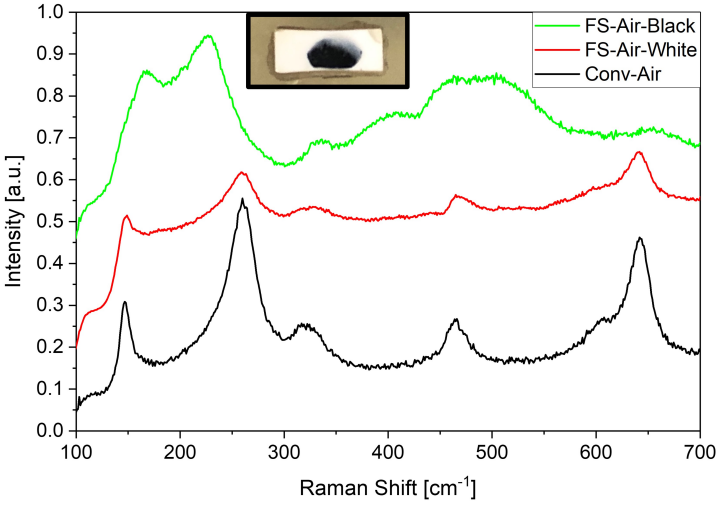


Figure 5.20: Raman point spectra taken from the white (red) and black (green) part of a cross section of a flash sintered 3YSZ sample, with power dissipation being maintained during furnace cool-down, as shown in the small insert. Raman spectrum of a conventionally sintered 3YSZ sample in air is also shown (black).

The signal taken from the blackened core region of the sample shows a different Raman spectrum with two new peaks being located at 165 and 225 cm^{-1} and a broader peak around 500 cm^{-1}.

The measured signal in the blackened region is comparable to Raman spectra obtained from ZrO_xN_{1-x}-films reported by other researchers [183].

A line scan across the cross section of the same sample was taken and the spectra collected for each point are shown in Figure 5.21. Whereby more intense spectra show high background intensities without any clear peak(s).

Figure 5.21 b) shows the lower-intensity scans revealing that the fundamentally changed structure is located in the blackened cross section of the sample, as shown in Figure 5.20.

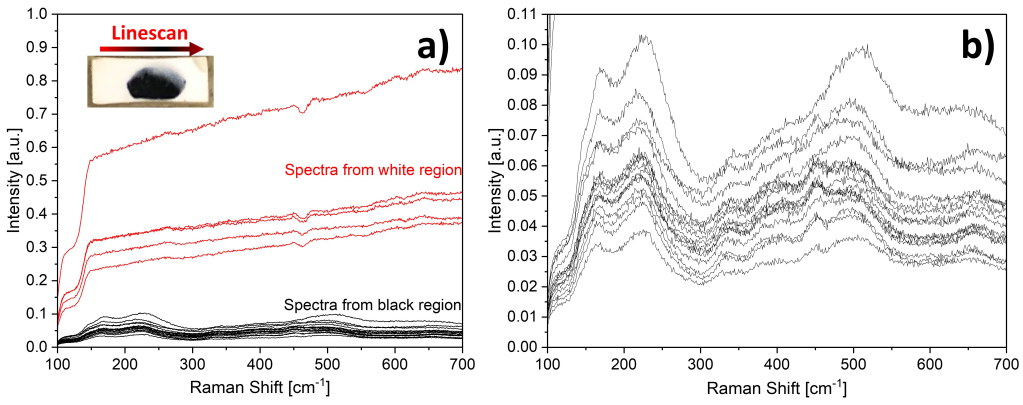


Figure 5.21: Raman line scan on the cross section of a flash sintered 3YSZ sample in air, with power dissipation during furnace cool-down shown in the small insert in a). a) shows the overall normalised intensity; b) visualises the low-intensity spectra collected from the phase transformed blackened region of the sample.

3YSZ electrically loaded in Ar - 30 s

Raman spectra from the 3YSZ-EL-30s-O_2, air, Ar, which was cooled down in Ar with no power dissipation being maintained, are taken from the white (near the edge) and grey surface regions. Raman spectra from these regions are fully explainable by the spectrum of a tetragonal 3YSZ structure [58] and except for minor deviations at higher Raman shifts these spectra coincide completely (Figure 5.22 a).

The blackened cross-section of the sample (Figure 5.22 a), showed significantly different and more intense Raman spectra as was also observed in the blackened cross section of a FSed sample (Figure 5.20 and 5.21), which is comparable to the Raman spectra expected for FCC rocksalt structured ZrON [183, 184, 185, 186].

Due to the presence of alumina (Al_2O_3) as an additive in the powders used, the characteristic alumina Raman signal can be detected at higher Raman shifts exceeding 1200 cm^{-1}, as is also shown in Figure 5.22 c). Particularly, at frequency shifts of 1400 cm^{-1} the characteristic Cr^{3+} R_1 and R_2 peaks [187, 188] are detected in the white mostly unreduced tetragonal YSZ and the slightly reduced grey ((Y)$ZrO_{2-\delta}$) sample regions.

In the blackened region, the Cr^{3+} R_1 and R_2 peaks at $\approx$ 1400 cm^{-1}, as well as the rest of the alumina signal, visible between 1600 and 2000 cm^{-1}, are almost com-

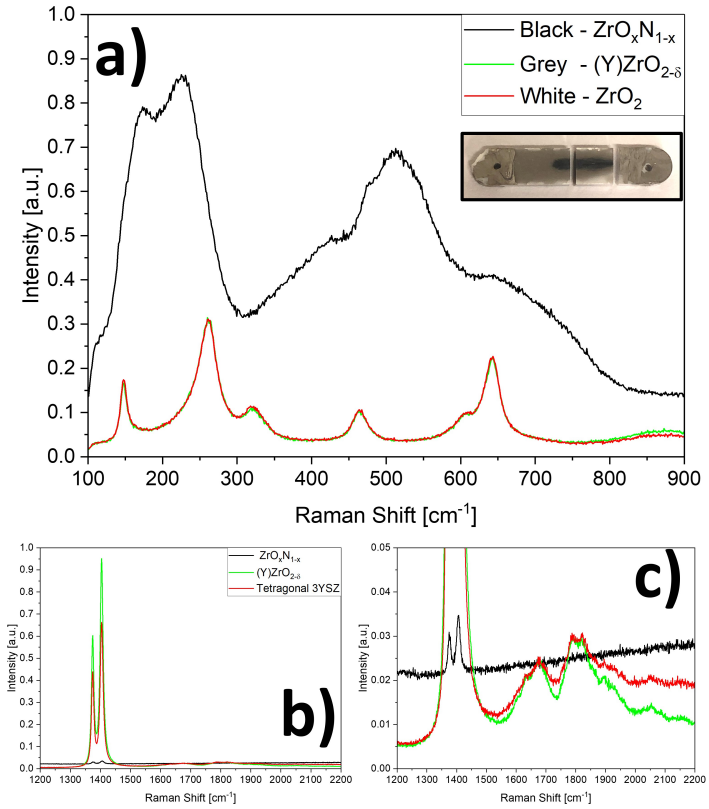


Figure 5.22: Raman point spectra taken from the black, grey and white surface area of an electrically loaded 3YSZ sample loaded in changing atmospheres (O_2, air and Ar) and cooled down in Ar; b) the Cr^{3+} R_1 and R_2 peaks at Raman shifts of $\approx$ 1400 cm^{-1} are detectable in the white and grey region, but not the blackened part of the sample; c) detailed Raman spectrum exceeding shifts of 1200 cm^{-1}, where the alumina signal would be expected.

pletely absent (Figure 5.22 b and c), indicating a fundamental change in alumina if the surrounding YSZ changes its structure during electrical loading.

3YSZ electrically loaded in Ar/N_2 - including during cool down

Raman spectra from 3YSZ-EL-CD-Ar and 3YSZ-EL-CD-N_2 are shown in Figure 5.23.

The Raman spectrum taken from 3YSZ-EL-CD-Ar shows a spectrum with two distinctive peaks around 165 and 225 cm^{-1}, a broader peak around 500 cm^{-1} and a separate peak around 600 cm^{-1}.

Even if the spectrum taken from a 3YSZ sample loaded in N_2 is mostly similar to the spectrum taken from the in Ar loaded sample, the peak around 600 cm^{-1} is absent after loading in N_2.

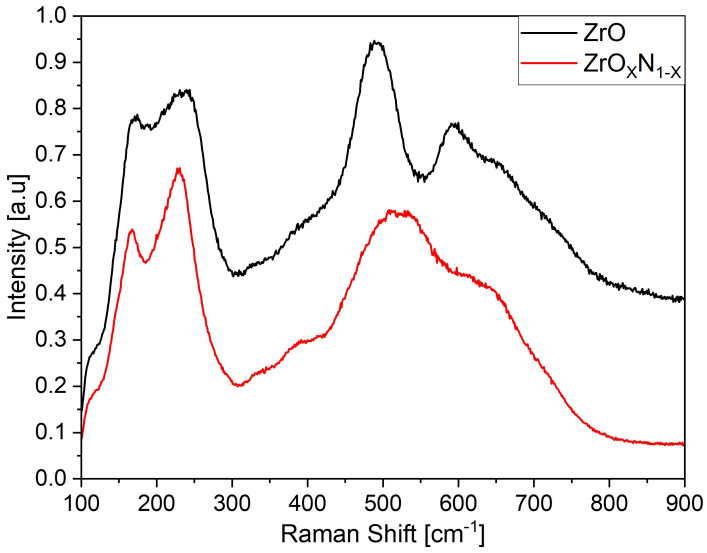


Figure 5.23: Raman point spectra taken from pre-sintered 3YSZ samples electrically loaded in Ar (black) or N_2 (red) with the power dissipation being maintained during furnace cool down.

Besides the mostly investigated 3YSZ and 8YSZ samples, 1.5YSZ and 10 YSZ samples were also investigated by Raman spectroscopy and showed comparable results as shown in Appendix Figure A.8.

Based on these results it can be concluded that the observed fundamental change

in the materials´ structure is not restricted to a certain Y-concentration or initial crystal structure.

MSZ electrically loaded in Ar - including cool down

Raman spectroscopy was conducted on a Mg-stabilised zirconia (MSZ) sample before (MSZ) and after electrical loading (Figure 5.24).

The results show that after electrical loading of MSZ in Ar, labelled as ZrO, or for N_2, labelled as ZrO_XN_{1-X}, with the power dissipation being maintained during furnace cool down, the same spectra as YSZ after electrical loading in Ar or N_2 were observed.

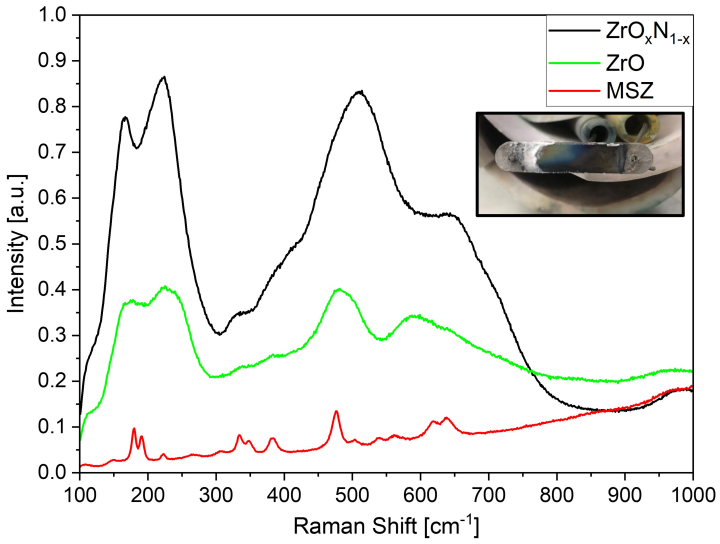


Figure 5.24: Raman point spectra taken from pre-sintered MSZ sample unloaded and electrically loaded in Ar, labelled as ZrO, or N_2, labelled as ZrO_XN_{1-X}, with the power dissipation being maintained during furnace cool down. The small insert shows the MSZ sample after electrical loading in Ar.

These results indicate that the change in the fundamental structure is independent of the kind of dopant.

Based on the Raman spectra obtained from the reduced samples investigated, which are comparable to the Raman spectrum expected for FCC rocksalt Zr(O,N), it should be mentioned that FCC rocksalt structures should not be allowed for first-order Raman scattering. However, it is known that even in stoichiometric transition metal FCC rocksalt structures sublattice defects like vacancies or anti-site defects on the cationic and anionic sites occur [183, 184, 185, 186]. Thus, the detected Raman spectra suggest a defective FCC rocksalt structure including a certain degree of defects or disordering.

Similar behaviour and comparable Raman spectra were obtained from electrically loaded yttria-stabilised hafnia, shown in the Appendix in Figure A.16.

5.3.4 X-ray Photoelectron Spectroscopy (XPS)

XPS was conducted on the surface of pre-sintered 3YSZ samples before and after electrical loading in air, Ar, N_2 and an 8YSZ sample after electrical loading in Ar.

As will be discussed in the Discussion section of this thesis, the investigated samples were labelled according to their state before ((Y)ZrO_2) or after electrical loading, whereby (Y)$ZrO_{2-\delta}$ refers to a sample loaded in air, ZrO refers to a sample loaded in Ar, ZrO_xN_{1-x} represents a sample loaded in N_2 and the ZrO(8Y) refers to 8YSZ loaded in Ar.

For all deconvoluted spectra the element-specific constraints, mentioned in the Methodology section in Table 3.4, are applied.

Survey scans and general trends

Figure 5.25 a) shows the survey scans of the samples between a binding energy (BE) of 0 and 1050 eV with significant differences in some regions. The regions of interest (ROI) are Zr 3d (Figure 5.25 b), Y 3d (Figure 5.25 c) and O 1s (Figure 5.25 d), shown in a normalised way to visualise the overall trends.

The BE-region including C 1s, which was used for correcting the spectra and setting the C 1s signal to a BE-value of 248.8 eV, as well as Y $3p_{3/2}$ at 299 eV, is shown in the Appendix in Figure A.9.

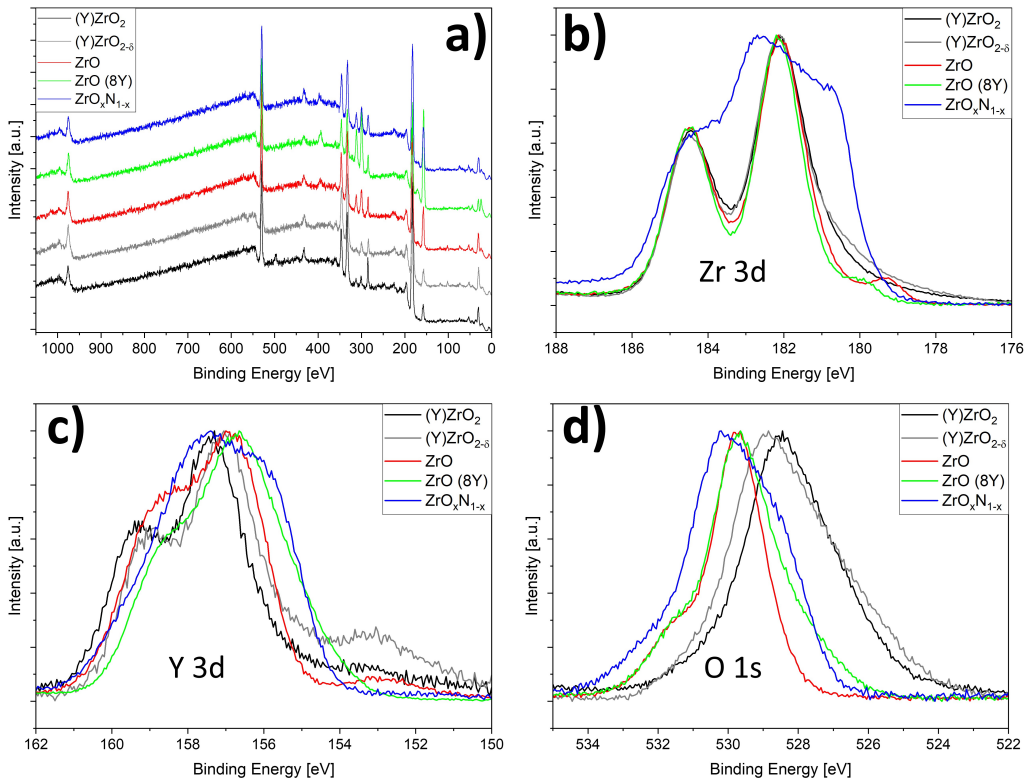


Figure 5.25: a) XPS Survey; b) Zr 3d; c) Y 3d and d) O 1s region of the XPS signal of various YSZ samples before and after electrical loading in Ar or N_2.

In the Zr 3d spectra (Figure 5.25 b) two distinct peaks, Zr $3d_{3/2}$ (184.48 eV) and Zr $3d_{5/2}$ (182.05 eV) peaks of Zr^{4+}-ions in tetragonal ZrO_2 [189], can be seen for the unloaded, as well as the samples loaded in air or Ar. The sample after loading in N_2 shows a significantly different shape of XPS spectrum, where the two Zr $3d_{3/2}$ and Zr $3d_{5/2}$ peaks are not as obvious as for the other samples. In addition to the expected Zr^{4+} peaks another peak can be seen at lower BE for the samples loaded in Ar.

In the Y 3d region (Figure 5.25 c) two overlapping peaks, representing Y $3d_{3/2}$

(159.38 eV) and Y $3d_{5/2}$ (157.33 eV) peaks of Y^{3+}-ions in a tetragonal YSZ environment [190], can be seen. As for the Zr 3d signal, the Y 3d peak position changes dependent on the electrical loading procedure and the atmosphere present. After loading in N_2, the Y 3d signal shows a general shift towards lower BEs and the original Y $3d_{3/2}$ and Y $3d_{5/2}$ peaks are not as clear as they have been in conventionally sintered 3YSZ.

Peaks at 153 eV in Figure 5.25 c) are representative of Si 2s [191], present as an impurity in the material, and not related to the Y 3d species, however a potential overlap with the Y 3d-signal needs to be considered during analysis of the XPS spectra.

The O 1s spectra (Figure 5.25 d) show a trend of increasing BE with ongoing electrical loading. Furthermore, the width of the spectrum narrows for samples loaded in Ar compared to the other samples investigated. Again, the sample loaded in N_2 (ZrO_xN_{1-x}) is different and compared to the O 1s spectrum from a sample loaded in Ar (ZrO) the O 1s spectrum shows a wider signal and a maximum at higher BE.

Deconvolution of the Zr-Spectra

Deconvolution of the XPS spectra was conducted for Zr 3d, Y 3d and O 1s signals to reveal the presence of the different atomic species and environments.

The deconvolution of the O 1s signal is difficult because of the vast amount of

possible O-containing species in the samples investigated, which makes it almost impossible to define the influence of each of them and due to that it should be seen as a rough trend rather than a quantitatively reliable analysis. Nevertheless, deconvolution of Zr 3d and Y 3d signals obey some constraints (Methodology section Table 3.4), which allows a reliable and quantitative deconvolution and interpretation.

The first column in Figure 5.26 shows the deconvoluted Zr 3d spectra of the samples dependent on the electrical loading procedure conducted. The spectrum of the conventionally sintered 3YSZ sample ((Y)ZrO_2) can be explained by only fitting Zr 3d peaks representing Zr^{4+}-ion in tetragonal ZrO_2 [192].

If the sample is electrically loaded in air and shows greying, additional peaks at lower BE are necessary to fit the spectrum indicating the presence of Zr^{3+}-ions.

Another peak doublet is necessary to fit the spectra from a sample loaded in Ar (Figure 5.26 g). This additional peak doublet shows one clearly separated Zr $3d_{5/2}$ peak at 179.3 eV accompanied by a 2.4 eV-shifted Zr $3d_{3/2}$ peak, signifying the presence of another Zr species, labelled as Zr^0. Compared to other XPS-investigations the BE-gap between fully oxidised Zr^{4+} and metallic Zr^0 should be $\approx$ 4.6 eV [193, 194]. In this work the BE-gap between the (fully oxidised) Zr^{4+} peak and the new peaks is $\approx$ 2.8 eV, which is significantly lower and rules out the formation of purely metallic Zr^0. Furthermore, the detected BE-gap is also

not consistent with the idea of Zr being present as Zr^{2+} as was reported during the reoxidation of metallic zirconium [193]. However, the fit of the additional peak doublet at 179.3 and 181.7 eV requires a 40 % lower peak-width (FWHM), which indicates a Zr species with a rather metallic character [195].

Compared to the samples loaded in air or Ar, the sample loaded in N_2 shows another shape and peak location due to the incorporation of N in the transformed material in addition to the (Y)ZrO_2 Zr^{4+}-peaks, leading to the formation of Zr^{3+} species in form of Zr-N-(O) bonds, whereby the Zr^{3+}-species which are close or bonded to N show a slightly different BE [196, 197]. It should be considered that a potential local difference in N-content could change the BE of cations in this region. This local difference can hardly be deconvoluted, which is why the fitted peaks are seen as representative for these species and provide the best deconvolution possible.

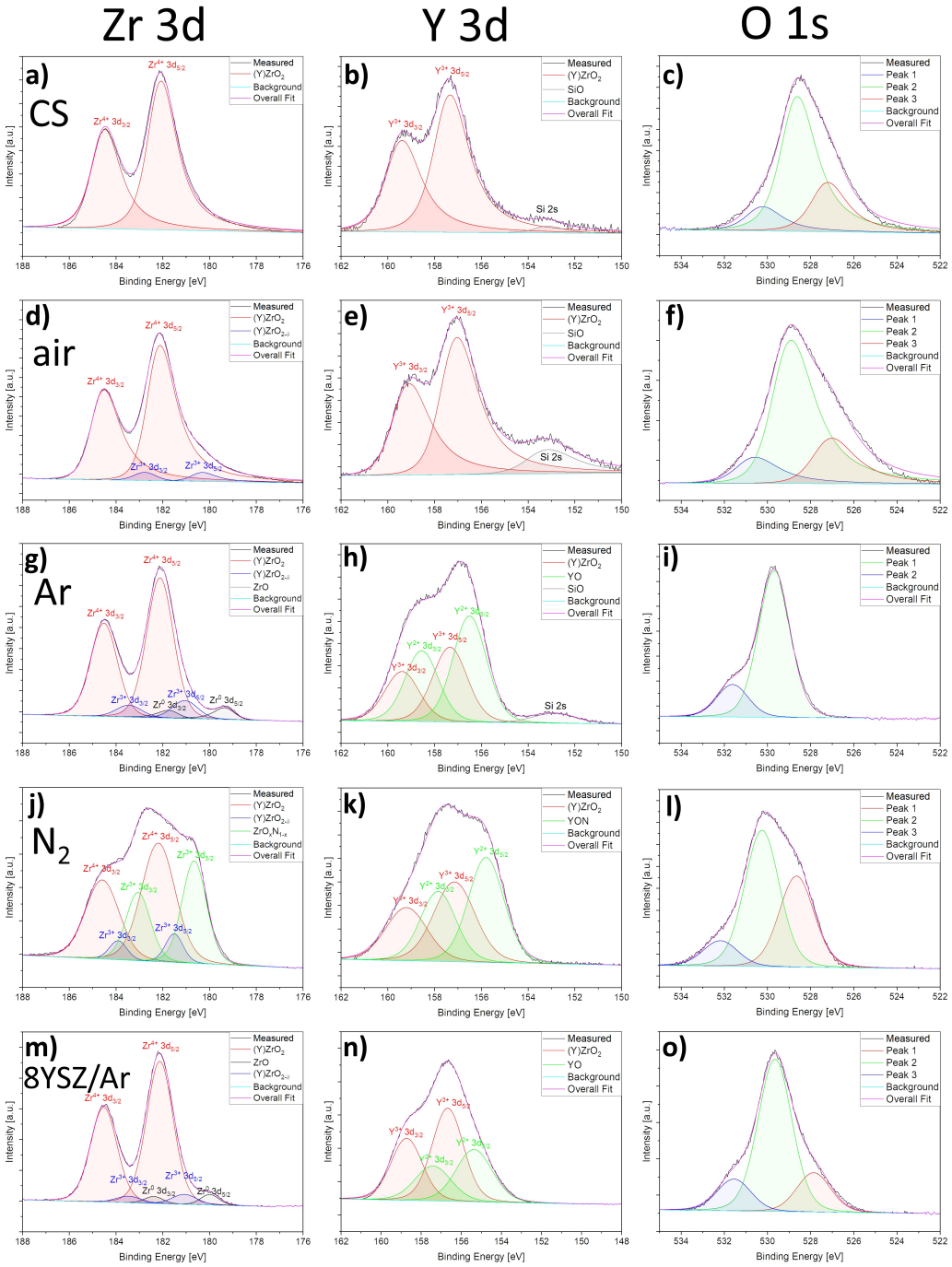


Figure 5.26: Deconvoluted Zr 3d (a, d, g, j, m), Y 3d (b, e, h, k, n) and O 1s (c, f, i, l, o) region of the XPS signal of conventionally sintered 3YSZ (a, b, c); electrically loaded in air (d, e, f); Ar (g, h, i); N_2 (j, k, l) and 8YSZ electrically loaded in Ar (m, n, o).

Deconvolution of the Y-Spectra

The second column in Figure 5.26 shows the deconvoluted Y 3d spectra, including the Si 2s region. The Y 3d spectra of the unloaded (Figure 5.26 b) and the sample loaded in air (Figure 5.26 e) can be explained by only one peak doublet associated with the presence of Y^{3+}-ions in the YSZ environment [192].

After loading 3YSZ or 8YSZ in Ar, an additional peak doublet at lower BE points towards Y-species with a lower oxidation state or a changed environment (Figure 5.26 h) and n). One potential explanation, agreeing with a FWHM comparable to the FWHM of the Y^{3+}-ions, is the formation of Y^{2+}-ions with a rather ionic character.

The sample loaded in N_2 shows two peak doublets, but their maxima are located at different BE values compared to the previous samples, which points towards the formation of Y-N-O bonds. The results obey the same behaviour as previously discussed for Zr-N-O bonds and environments.

Deconvolution of the detected O-Spectra

As mentioned the deconvolution of the O 1s spectra is difficult and the peaks fitted are one potential way of deconvolution, but no assignment of peaks to bonds or environments was conducted due to the high uncertainty. However, the presence of an O-species at 527 eV completely disappears if the 3YSZ sample is loaded in

Ar (Figure 5.26 i) and after reduction the O 1s-peaks shift to higher BE indicating a higher oxidation state or changed environment of the O-species.

Detection of Nitrogen

Since the 3YSZ sample loaded in N_2 shows significantly different spectra, the presence of N in the sample was investigated and the N 1s region of the XPS spectra of the samples can be seen in Figure 5.27 which shows that only the sample loaded in N_2 shows a peak located at a BE of 398 eV representative for N.

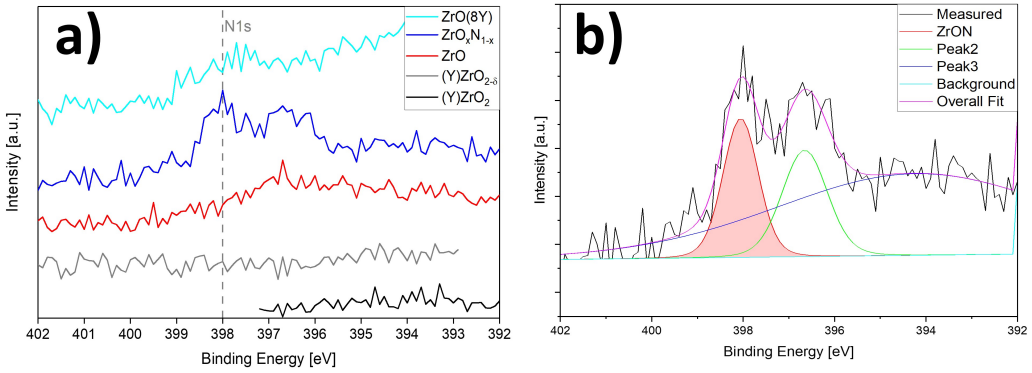


Figure 5.27: N 1s region of the XPS spectrum, a) overview and b) deconvoluted region for fully reduced 3YSZ in N_2.

The deconvoluted spectrum can be seen in Figure 5.27 b) showing the presence of a significant amount of N in the form of Zr-N-(O) bonds [196, 197] with two different energies, suggesting two different kinds of N-bonds, which are not specified further. The deconvoluted broad yttrium peak represents the Y 3s BE [198].

5.3.5 Electron Paramagnetic Resonance spectroscopy (EPR)

EPR-characterisations of untreated monoclinic ZrO_2 powder, conventionally sintered 3YSZ ((3Y)ZrO_2) and 8YSZ ((8Y)ZrO_2), before and after electrical loading, were conducted including specification of the paramagnetic defects by calculating their g-factor by differentiation and deconvolution of the spectra. The meaning and origin of the g-factor is explained in the Methodology section in Figure 3.7.

Conventional(-ly sintered) materials

As shown in the first column of Figure 5.28, all conventionally sintered samples show an EPR-signal at a field strength between 1500 and 1700 Gauss (Figure 5.28 c) revealing the presence of Fe^{3+}, with spin S=5/2 and an orbital angular moment L=0, as an impurity, as is well-known in such materials [199, 200, 201, 202].

Since all graphs in Figure 5.28 are shown for similar absolute y-axis values, comparison of the samples is possible. The results show a significantly stronger EPR signal occurs between 2000 and 5000 Gauss as shown in Figure 5.28 e), whereby tetragonal 3YSZ shows a stronger response than the pure monoclinic ZrO_2 powder. Cubic 8YSZ, however, shows almost no signal except for a weak signal at 3407 Gauss, also detected in undoped monoclinic ZrO_2. The decreasing signal from 3YSZ to 8YSZ agrees with previous work [200, 203] reporting a decreasing EPR signal and paramagnetic defect concentration at Y-contents > 5 mol.%.

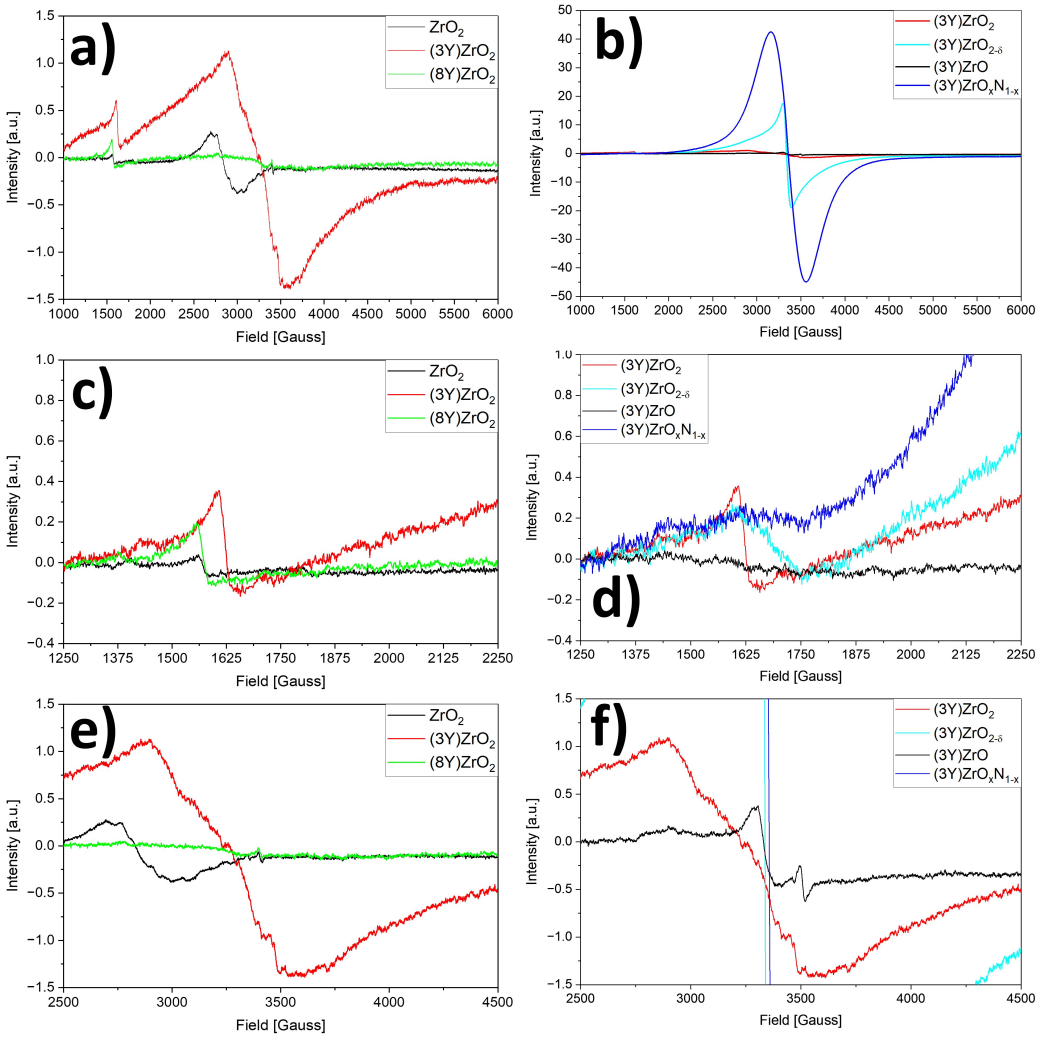


Figure 5.28: EPR spectrum of untreated undoped monoclinic ZrO_2 powder as well as pre-sintered 3YSZ and 8YSZ (a, c, e) and electrically loaded 3YSZ in comparison to the conventionally sintered 3YSZ (b, d, f); a) and b) show the overall spectra; c) and d) the detailed spectra at lower fields showing the Fe^{3+} signal; e) and f) show the spectra at the zirconia / yttria defect region.

Furthermore, undoped monoclinic ZrO_2 also showed a signal between 2000 and 5000 Gauss, which is why Y-ions of any kind can be ruled out as the origin of the EPR signals in this range. Since Zr^{4+}-ions are diamagnetic and would not respond

to EPR, the signal must be caused by the presence of not fully oxidised paramagnetic Zr^{3+}-ions, which agrees with suggestions made by other researchers who reported that g-values in this range originate by a change in the oxidation state and environment of the Zr species [200, 203, 204, 205].

Electrically loaded materials

EPR spectra obtained from electrically loaded pre-sintered 3YSZ compared to the spectrum from conventionally sintered 3YSZ ($(3Y)ZrO_2$) are shown in Figure 5.28 b).

The integrated spectra (Figure 5.29) visualise the concentration of paramagnetic defects relative to the amount of paramagnetic defects formed in 3YSZ ($(3Y)ZrO_2$). The most intense signal, 15x stronger than conventionally sintered 3YSZ, is obtained from 3YSZ loaded in N_2 ($(3Y)ZrO_xN_{1-x}$) showing a strong signal between 2000 and 4500 Gauss (Figure 5.29). At 1600 Gauss the Fe^{3+}-signal of this material is detected (Figure 5.28 d), which, however, is weaker and differently shaped compared to unreduced $(3Y)ZrO_2$.

The signal from the sample loaded in N_2 is followed in intensity by the signal of the partly reduced sample loaded in air ($(3Y)ZrO_{2-\delta}$). An EPR-signal $\approx$ 5x the reference signal was obtained from this sample and shows a significantly different shape compared to $(3Y)ZrO_xN_{1-x}$. The Fe^{3+}-signal intensity at 1600 Gauss (Figure

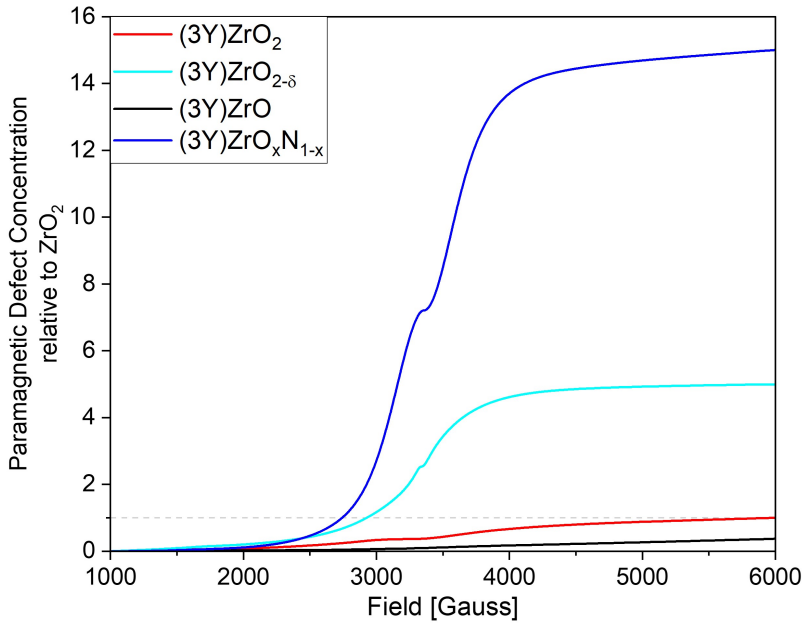


Figure 5.29: Concentration of paramagnetic defects in conventionally sintered unloaded 3YSZ (red), electrically loaded in air (light blue), Ar (black) or N_2 (blue) calculated by integration of the detected EPR spectra. The concentration of paramagnetic defects in conventionally sintered 3YSZ was used as a reference value normalised to 1, visualised by the horizontal dashed line.

5.28 d) is somewhere between $(3Y)ZrO_xN_{1-x}$ and $(3Y)ZrO_2$.

The weakest response of all samples across the whole field strength range, 0.37x the defect concentration in $(3Y)ZrO_2$, was obtained from the ZrO-containing sample electrically loaded in Ar, which includes the Fe^{3+}-signal as well as the Zr-related signal around 3500 Gauss, shown in Figure 5.28 f).

Since the overall concentration of the paramagnetic defects in (3Y)ZrO is significantly lower compared to all of the other investigated samples (Figure 5.28 and 5.29), it can be assumed that the most common oxidation state of zirconium in

this sample is Zr^{4+}, because any other oxidation state would lead to the formation of unpaired electrons, as shown in Table 2.3 in the Literature Review, which then would induce an EPR signal at least as strong as the one for slightly reduced (3Y)$ZrO_{2-\delta}$.

Low temperature EPR spectroscopy

The temperature-dependent behaviour of the paramagnetic defects in electrically loaded samples was investigated by conducting EPR-measurements at 100 K. Conducting EPR at various temperatures changes the behaviour of the paramagnetic and electronic defects in the material, whereby, paramagnetic defects related to ions are more affected by the temperature compared to electronic defects, which are not as sensitive to temperature changes [206].

Figure 5.30 a) and b) show the result for (3Y)$ZrO_{2-\delta}$ indicating a decreasing signal with decreasing temperature as well as a shift towards lower field strengths. The deconvoluted spectrum of partially reduced 3YSZ shows two overlapping peaks with g-factors of 2.08 and 2.07 (Figure 5.31 a). If the overall g-factor is considered, a shift from 2.079 to 2.062 is caused by decreasing temperature (Figure 5.31 b).

EPR-spectra taken from the (3Y)ZrO-containing sample also showed a slight shift towards lower fields, but only some parts of the signal show a decreasing intensity,

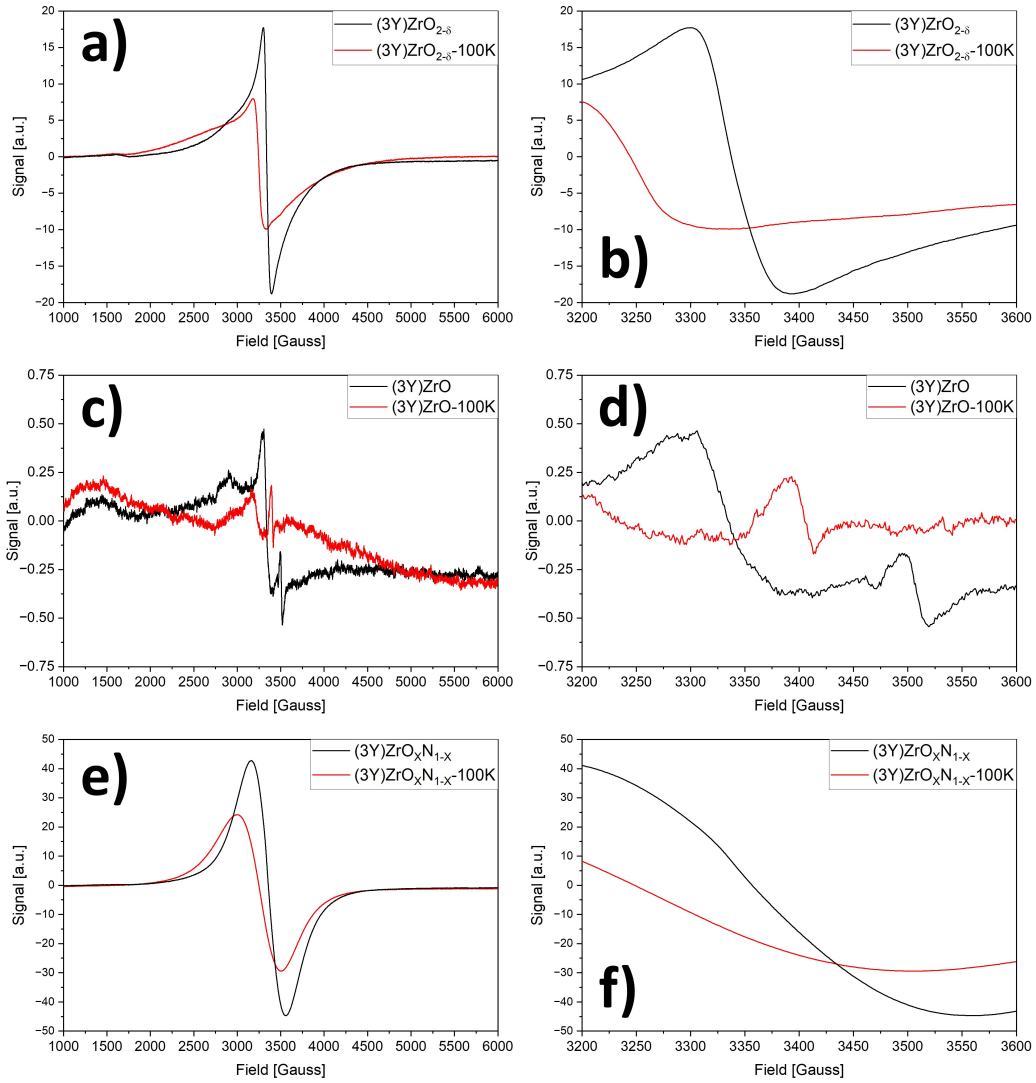


Figure 5.30: EPR spectrum of electrically loaded 3YSZ in a) air; b) Ar; c) N_2; at room temperature (black) and 100 K (red).

indicating a fundamental difference in the magnetic characteristic and origin of the defects present. The differentiated signal (Figure 5.31 c) reveals several peaks which can be deconvoluted into two peaks, g-factor of 2.082 and 1.975, being significantly stronger compared to the other peaks in these spectra (Figure 5.31

d). If temperature is decreased the signal obtained at a g-factor of 2.062 almost disappears, whereas the signal at a g-factor of 1.975 only shifts by 0.002 towards 1.973 and the intensity of the signal is almost unchanged.

For (3Y)ZrO_xN_{1-x} electrically loaded in N_2, two peaks with g-factors of 2.06 and 2.07 are detected at room temperature (Figure 5.31 e) with an overall g-factor of 2.074. At 100 K an overall g-factor of 2.159 was measured (Figure 5.31 f).

A comparably long relaxation time (EPR peak width) and a strong temperature-dependence (temperature-dependent decrease in intensity) are observed for the defects responsible for EPR-signals at g-factors of around 2.08, shown in Figure 5.31. These properties lead to the assumption that the presence of $V_O^{\bullet}$ connected to a Zr^{3+}-ion, showing a strong paramagnetic character [109, 199, 207, 208, 209, 210], are the most likely explanation for it, out of the potential charge balancing possibilities described in the Literature Review in section 2.1.4 in Figure 2.3.

However, the defect represented by a g-factor of 1.98 in (3Y)ZrO is different to the other defects in a way that it shows a really short relaxation time, visible in the narrowness of the peak, a temperature independence in g-factor and intensity, a negligible change in peak location and intensity at various temperatures, and, a symmetrical peak shape. Based on these properties this kind of defect can most likely be associated with the presence of a V_O^X, which is filled with two electrons. A defect which is based on rather ionically bonded electrons would show

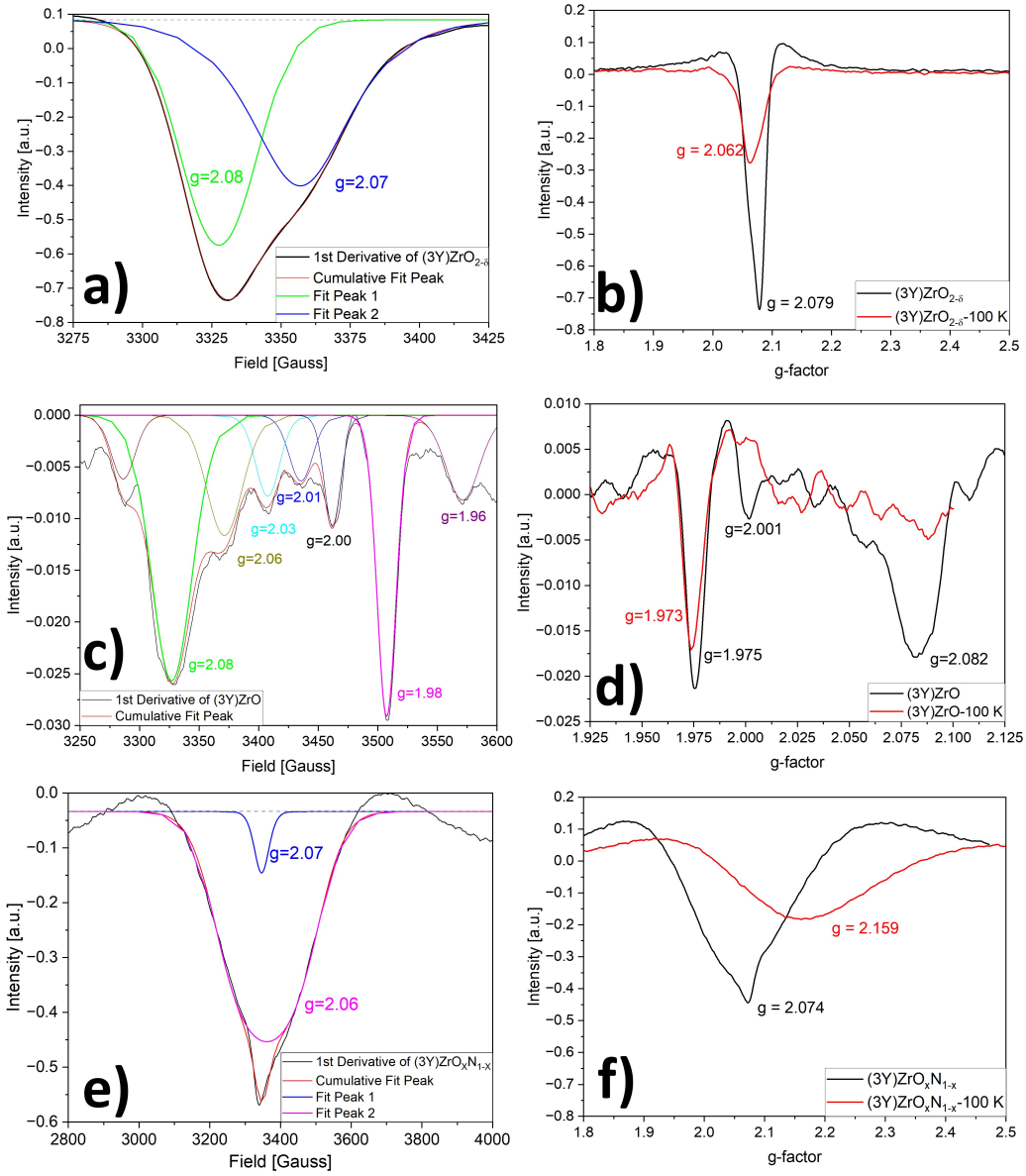


Figure 5.31: 1st derivative of EPR spectra taken from electrically loaded 3YSZ in air (a and b), Ar (c and d) and N_2 (e and f) including the deconvoluted derivatives at room temperature over applied field (a, c, e) as well as the comparison between room temperature (black) and at 100 K (red) over the calculated g-factor.

a longer and temperature dependent relaxation, which would result in a generally wider peak and a stronger temperature dependence, as shown for other defects as-

sociated with a Zr^{3+}-ion formation. Furthermore, similar peak-shape parameters were reported by Thorp et al. [109], who conducted a comparable experiment and reported the occurrence of *Type-C* lines, but no further investigation or discussion of the potential kind of defect was reported. Compared to the signals obtained from other (paramagnetic) defects, the intensity of signal from these $V_O{}^X$ is rather low, which could be due to a weak response to the measurement or a rather low concentration of such defects or a combination of both.

In the past defects detected by EPR were sometimes associated with the presence of impurities, which can be ruled out here, since all of the 3YSZ samples investigated are manufactured from the same original powder and similar processing. The only difference is in the atmosphere during electrical loading.

5.3.6 Room temperature electrical conductivity

Electrical conductivity measurements at room temperature, after FS or electrical loading in Ar or N_2, showed a resistance between 3 and 7 Ω, giving a nominal resistivity between 0.15 and 0.35 Ω cm (or a conductivity of 2.9-6.7 S/cm). No conductivity was measurable after electrical loading in O_2 or air.

5.4 Discussion

Based on the previously shown results, such as greying and blackening, a separation of the stages of electrochemical reduction in YSZ can be done. In this section the two different stages of electrochemical reduction of YSZ, and in some parts yttria stabilised hafnia, will be elaborated in terms of the fundamental material structure, related properties, their implications and consequences for FS.

Since, it was shown that the electrochemical reduction and the related phase transformations happen independent of the amount or kind of stabilising agent, stabilisers will (mostly) not be included in the description of the reduction stages of zirconia itself.

5.4.1 Electrochemical reduction of (stabilised) zirconia stage I: $ZrO_{2-\delta}$

5.4.1.1 Fundamental (defect) structure

The first of the two stages of electrochemical reduction signified by a grey colour was realised by electrical loading in air which led to a slight reduction from ZrO_2 to $ZrO_{2-\delta}$, which contains defects in the form of Zr^{3+}-ions connected to an extrinsic oxygen vacancy filled with one electron ($V_O^{\cdot}$) .

Indicators, which support the assumption of the formation of single charged oxygen vacancies in combination with paramagnetic Zr^{3+} ions by FS-induced electrochemical reduction in stage I can be found in the XPS (Figure 5.26 d) and EPR (Figure 5.28 and 5.29) results presented in this work.

Furthermore, the report of blue photoluminescence in 3YSZ prepared by DC- and AC-FS (100 Hz) at room temperature post-FS, if excited by UV-light, is another indicator for the proposed defect structure. The researchers assumed that the blue photoluminescence occurs due to the formation of singly ionised associated oxygen vacancy defects, with some of them being highly stable even after annealing at 1400 °C in air for 1 h [119, 120].

Beside the experimental observation researchers such as Dong et al. showed that under dynamic and extreme thermal/field/irradiation conditions the defect structure in zirconia can change. Dong et al. suggested [211] that a transitory complex of a polaronic electron or hole and a migrating counterion, described as polaronium, form. This complex becomes highly mobile when the counterion comes from a d^0 or f^0 cation (e.g., Zr^{4+}, Ti^{4+} and Ce^{4+}) or a p^6 anion (e.g., O^{2-}) in the host compound. The changed defect structure influences the materials´ behaviour, which according to the researchers [211] can lead to an enhanced kinetics and an improved densification during FS for example.

Based on the observed results from this work, the blue post-FS photolumines-

cence [119, 120] and the theoretical investigations [211], it can be concluded that AC-, as well as DC-, FS under various experimental conditions introduces abundant defects in YSZ and leads to the formation of (Y)$ZrO_{2-\delta}$, as was detected and defined in the electrochemical reduction stage I in this work.

Another effect, often detected in various defective transition metal oxides [212, 213, 214] such as TiO_2 [215], ZrO_2 [216, 217, 218, 219, 220] and HfO_2 [221, 222] is room temperature ferromagnetism (FM). Based on the EPR-results from this work, showing a strong paramagnetic response for YSZ reduced to (Y)$ZrO_{2-\delta}$ in stage I of the electrochemical reduction, it can be assumed that such electrochemically induced defects, based on paramagnetic Zr^{3+} ions and $V_O^{\cdot}$, can be responsible for such room temperature ferromagnetism (FM), which is also supported by other theoretical investigations [220, 223].

The observations of blue photoluminescence in 3YSZ prepared by DC- and AC-FS at room temperature post-FS and the changed magnetic properties show that electrochemical reduction during FS is a way to tailor optical and magnetic properties. Tailoring optical and magnetic properties by electrochemical reduction provides one way to generate new materials, which is worth investigating in the future.

Since the reduction changes the fundamental structure and properties, the material in this stage I of reduction should not be described as conventional tetragonal (t)

zirconia, which is fully oxidised. Furthermore, a clear separation to other previously reported phase configurations has to be made because of the induced extrinsic defects which make the electrochemically reduced materials fundamentally different from phases formed due to varying dopant-contents or thermal history, such as $t´$ and $t´´$ [58, 60], both of them being metastable phases at room temperature. Thus, the introduction of a new nomenclature for (originally tetragonal yttria-stabilised) zirconia, which is in the first stage of electrochemical reduction, is proposed as t*.

5.4.1.2 Effect of electrochemical reduction on the tetragonal YSZ phase

Another effect of the stage I electrochemical reduction and the described formation of Zr^{3+} ions and $V_{O}^{\cdot}$ is a change of the lattice parameters of the tetragonal phase and the expansion of the crystal structure in a and its contraction in c, leading to a decrease in tetragonality and a net increase in unit cell volume with ongoing reduction. The same effects are seen on increasing the Y content of YSZ, and consequently the concentration of O-vacancies [58, 60, 224, 225, 226, 227, 228].

It has been suggested previously [229] that the effects on phase content of the introduction of oxygen vacancies by reducing pure zirconia to form $ZrO_{2-\delta}$ are similar to those of adding Y^{3+}, particularly if charge compensation is maintained by reducing Zr^{4+} to Zr^{3+}, which would then play a similar role to Y^{3+} in YSZ. The

trends in the tetragonal zirconia unit cell with electrochemical reduction observed here are consistent with this explanation.

During in situ synchrotron experiments in air, Lebrun et al. [78] saw the gradual emergence of a new phase consistent with the cubic fluorite (FCC) structure of ZrO_2 during flash sintering of originally tetragonal 3YSZ when the sample temperature was greater than 1200 °C. The Y_2O_3-ZrO_2 phase diagram [60, 70] shows that this is also consistent with the idea that electrochemical reduction acts like an increase in the Y_2O_3 concentration; this would also lead to the formation of cubic phase above 1200 °C. On turning off the electric current, the FCC fluorite phase in Lebrun´s experiments disappeared again, presumably because the air re-oxidised the sample, removing the excess oxygen vacancies and moving the effective composition back towards the tetragonal phase field.

The occurrence of a FCC fluorite cubic structure due to a combination of electrochemical reduction and temperature leads to the assumption of another electrochemical reduction-induced stage which leads to the formation of a more cubic like crystal structure forming from the previously described tetragonal *t** structure, which shows a consistent lattice parameter in all three dimensions, which is not the case for *t**. Because this cubic structure, like *t**, is fundamentally different to the already known fully oxidised YSZ structures the proposed nomenclature for this stage of electrochemical reduction is *c**.

Unlike the metastable phases *t´*, which forms at lower Y concentrations, and *t´´*, which forms at higher Y contents, both described in the Literature Review, *t** and *c** form independent of the dopant concentration, but depend on the grade of reduction and the associated formation of oxygen vacancies and Zr^{3+}-ions.

Cubic fluorite *c** phase may also have formed in our experiments during FS but because our samples were quenched and the structure measured at room temperature, any cubic fluorite would have transformed back to a tetragonal phase [59, 224], which is consistent with the lower tetragonality observed in our results, originating from its thermal history as described for t´ [59, 224] or due to electrochemical reduction towards *t**. It could also be possible that the cubic phase formed got reduced further which led to Stage II of the reduction, described later.

Following the previous assumption of similar effects of electrochemical reduction and Y-content, some calculations were conducted which are shown in the Appendix in Figure A.13. According to the calculations a time of 47 or 125 s would be necessary to achieve 1.5 or 4 mol.% oxygen vacancies in undoped ZrO_2 if a sample weight of 1 g and a current of 1 A is considered and the current is solely based on the removal of oxygen ions without reincorporation of atmospheric oxygen into the material. The calculated times and the set parameters (sample weight and current) are in the range of FS parameters and thus the scenario described is not unrealistic. It also shows how quickly the introduction of abundant oxygen

vacancies could happen under such circumstances.

Setting the calculated values into perspective and comparing them to experimentally obtained results can be done, again, on the basis of the in situ experiments conducted by Lebrun at al. [77, 78, 230]. Based on the information given in [230] a sample weight of $\approx$ 1 g and a current of 0.1 A can be estimated in their research. Since, only a part of the sample in this setup is located between the electrodes and, furthermore, the current localises in some regions of the sample, it can be summarised that the parameters used for the theoretical calculations in this work (I = 1 A, m = 1 g, Appendix Figure A.13) are not far from the reported experimental conditions.

If the in situ investigations reported by Lebrun and Charalambous et al. [77, 78, 79, 230] are seen as one continuous process, a continuity in their results can be seen.

I) Broadening of tetragonal zirconia peaks above a certain power/current level within the first few seconds [77].

II) Lattice expansion in mostly *a* in the tetragonal phase during a measurement time of 60 s [230].

III) Emergence of the cubic fluorite phase from the initially tetragonal phase after approximately 5 min [78].

IV) Emergence of FCC rocksalt zirconium oxynitride from cubic fluorite phase after one minute of DC-FS [79].

Since the theoretical calculations in this work, which show that within a relevant time for FS-standards a substantial amount of oxygen extraction could happen under FS-conditions, match the observed crystallographic effects post electrical loading conducted in this work and the observations during in situ experiments by other researchers [77, 78, 79, 230], the conclusion of the formation of extrinsic oxygen vacancies having a comparable effect as Y-introduced intrinsic vacancies, is supported.

Even if the formation of a c^* phase out of the t^* phase is the logical continuation and was observed during in situ experiments, this stage of electrochemical reduction needs more investigation in the future.

5.4.1.3 Change of electrical properties

In the experiments conducted, where the conditions applied are in the range of moderate FS-conditions, a current density of $\approx$ 2.5 A/cm^2 in fully dense pre-sintered 3YSZ was measured in the voltage-controlled stage (25 V/cm) in O_2 or air (Figure 5.4) at a furnace temperature of 800 °C.

According to a previous investigation by Grimley et al. [27] the maximum current in 8YSZ in air at 1200 °C, which, according to previous theories [104, 105],

can be maintained based on O^{2-}-ions as charge carrier, is 0.18 A/cm^2 under such circumstances. Even if experimental circumstances in the research in this thesis are different, the suggested value (0.18 A/cm^2) [27] is in the range of 7 % of the current in this stage (2.5 A/cm^2) of the present research.

From this and several other previous investigations it is known that electrochemically induced intrinsic defects, such as oxygen vacancies and Zr^{3+}-ions, cause a decreasing bandgap and an increase in electronic conduction in (stabilised) zirconia at elevated temperatures [29, 98, 211, 231, 232, 233].

This leads to the conclusion of the electronic conduction, alongside the initial ionic conduction, being responsible for the current flow in slightly reduced (3Y)$ZrO_{2-\delta}$ at elevated temperatures, as occurs even under moderate FS-conditions from an early stage onwards, which also agrees with results from other investigations [98] and observations made for gadolinium doped ceria [234], which is another transition metal oxide. This rules out the assumption of YSZ being a pure ionic conductor under FS-conditions.

5.4.2 Electrochemical reduction of (stabilised) zirconia Stage IIa: ZrO

If the electrochemical reduction of (yttria stabilised) zirconia continues and reaches stage II, the fundamental structure and phase composition transforms towards a defective FCC rocksalt ZrO structure within seconds during FS or electrical loading under comparable conditions, which is accompanied by a colour change from grey to black, as will be discussed in this section.

The research presented here enabled the synthesis of a substantial amount of ZrO which was retained at room temperature for the first time. Its fundamental properties were studied in terms of the fundamental crystallographic and defect structure as well as electrical conductivity. It also extends previous work in the perspective of FS [79, 83], but also other work about the electrochemical reduction and blackening in zirconia conducted by researchers such as Thorp [109, 110], Casselton [94, 95, 112], Caillet [114] and Janek and Corte [29].

5.4.2.1 Fundamental structure of the FCC rocksalt transition metal monoxide phases

The following section of the discussion includes results about electrical loading of yttria-stabilised hafnia shown in the Appendix, which, due to their relevance to

this section, are partially discussed in the following paragraphs.

Group IV transition metals (Me), including Ti as 3d, Zr as 4d and Hf as 5d transition metal, are similar in many perspectives due to strong d-orbital electron bonding [235, 236, 237]. Particularly, Zr and Hf are alike in many aspects relevant to this research. The most relevant similarities are discussed in the following paragraphs.

I) At low temperature the metals form a hexagonal (hcp) α-phase which transforms to a cubic (FCC) structure β-phase at higher temperatures (Table 5.2).

II) The (di-)oxides of Zr and Hf form three different phases with temperature-dependent phase transitions from monoclinic to tetragonal to cubic [228, 238]. In this perspective titanium behaves differently. An overview is shown in Table 5.2.

III) All three form well-known intermetallic carbide and nitride compounds with an FCC rocksalt structure as shown in Table 5.3, which are described as δ-MeC and δ-MeN respectively.

IV) Based on the results from this work and other investigations [80, 239, 240, 241] it is now confirmed that Ti, Zr and Hf can form FCC rocksalt monoxide structures (δ-MeO).

About their FCC rocksalt monoxide structures it can be said that the refined δ-HfO lattice parameter is 0.4527 nm (shown in Appendix section A.15), which is

Table 5.2: Group IV transition metals and their dioxides including their crystal structure at low, intermediate or high temperature.

	Temperature	**Ti**	**Zr**	**Hf**
Metal	Low	hcp-α	hcp-α	hcp-α
	High	FCC-β	FCC-β	FCC-β
Dioxide	Low	Anatase | Brookite | Rutile	Monoclinic	Monoclinic
	Intermediate	Rutile	Tetragonal	Tetragonal
	High	Rutile	Cubic	Cubic

0.0053 nm smaller than the lattice parameter of ZrO reported in this thesis, and 0.0345 nm bigger than the TiO lattice parameter reported in [239]. Furthermore, the ZrO lattice parameter agrees well with the values which were suggested by in situ experiments conducted by Charalambous et al. (0.46 nm) [79] when thermal expansion is allowed for, and with the previous report of ZrO in [80], which was used as a reference in the work by Charalambous and co-workers.

The difference between the lattice parameters of δ-MeO structures is in the same range and follows the same trend as the differences between the δ-MeN and δ-MeC structures. Furthermore, the comparison of δ-MeX lattice parameters shows a significant difference between δ-MeC and δ-MeN structures (Figure 5.32). However, the difference between δ-MeN and δ-MeO in case of Zr and Hf is rather small or even reversed, compared to the difference detected for Ti-based structures.

An explanation for this deviating trend can be found in the atomic radius of the transition metals, which is 0.147 nm for Ti [228], 0.160 for Zr [228] and 0.159 for Hf [242]. On the basis of their metallic radii the theoretical lattice parameters

for metallic FCC Ti, Zr and Hf can be calculated by $4xr/\sqrt{2}$. The results for the calculated metallic FCC lattice parameters are shown in Figure 5.32 and Table 5.3 alongside all other known δ-MeX (Me = Ti, Zr, Hf; X = C, N, O) lattice parameters. The summary of the δ-MeX lattice parameters highlights, that δ-ZrN and δ-HfN show a lattice parameter in the same range as their related δ-MeO structure as well as the theoretically calculated FCC-Metal structure. Thus, it can be concluded that the atomic radii of the Zr and Hf species define the lattice parameters in their nitride and monoxide phases. This conclusion also agrees with the previously reported finding that a rather small change in lattice parameters occurs even over an extensive range of N-content in δ-HfN_{1-x} [243].

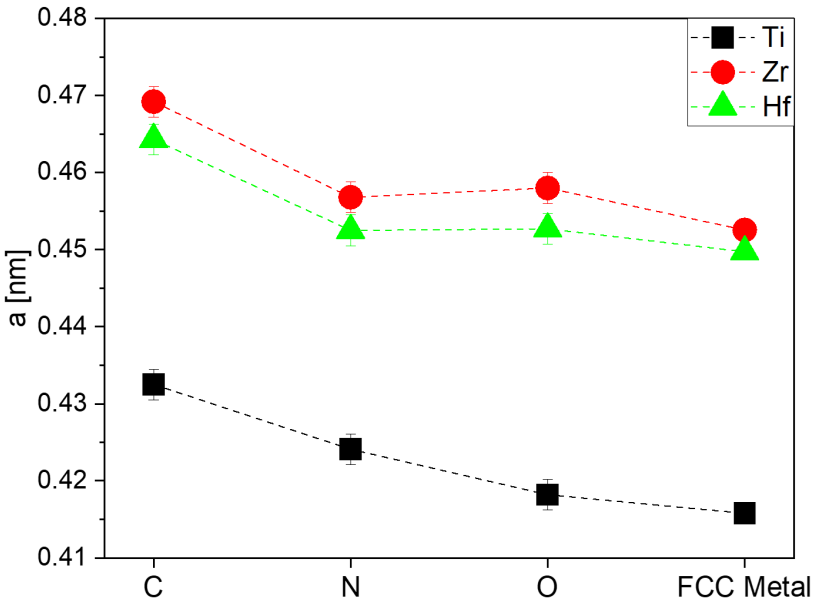


Figure 5.32: Lattice parameters of all known δ-MX structures as well as the calculated FCC Metal lattice parameters for pure metals based on their atomic radii.

Table 5.3: FCC rocksalt group IV transition metal based intermetallic δ-MeX compounds (Me = Ti, Zr, Hf; X = C, N, O) including their lattice parameters in nm and references.

	Ti	**Zr**	**Hf**
C	0.4325 [244]	0.4692 [245]	0.4643 [246]
N	0.4241 [247]	0.4568 [84]	0.4525 [248]
O	0.4182 [239]	0.4580 [This work]	0.4527 [This work]
FCC Metal	0.4158 [228]	0.4526 [228]	0.4497 [242]

In this perspective the comparison of the lattice parameters, shown in Figure 5.32 and Table 5.3, helps to partially understand the materials properties and fundamental structure. From previous investigations it is known that δ-ZrN as well as δ-HfN, compared to δ-ZrC and δ-HfC form rather metallic bonds because of the strong interaction between the non-metallic 2p orbital and the 3d, 4d, or 5d orbitals, as present in Ti, Zr, or Hf, respectively [249]. Metallic bonds in δ-MeX structures arise when metal atoms are positively ionised and delocalised electrons are able to move through the lattice, leading to a high electrical conductivity [235, 236, 249, 250]. If this known trend is continued based on an increasing electronegativity from carbon to nitrogen to oxygen, the expectable interaction between the non-metallic 2p and the metallic d-orbital, as well as the metallic character, should increase in intermetallic FCC rocksalt transition metals in the order of carbides (δ-MeC), nitrides (δ-MeN), and monoxides (δ-MeO).

The described trend explains the experimentally detected metallic character of the FCC rocksalt ZrO and HfO phases, with their good electrical conductivity

at room temperature and the PTC behaviour if temperature increases, based on positively ionised cations and delocalised electrons. Beside the described fundamental crystallographic structure, a potential defect structure in FCC rocksalt ZrO and HfO needs to be considered because the results from Raman spectroscopy, EPR, and XPS, shown in this work, are only partially explainable by the previously discussed effects and thus suggest the formation of rather defective δ-ZrO and δ-HfO structures. Particularly the Raman spectra taken from samples containing FCC rocksalt ZrO or HfO samples show some degree of disordering and symmetric breakdown in their crystal structure because otherwise no Raman signal would be obtained from an ideal non-defective rocksalt FCC structure [183, 184, 185, 186, 251].

According to the experimental results various indicators for the formation of mainly anionic defects, in the form of double filled oxygen vacancies (V_O^X), as the most likely kind of defects, are found and discussed in the following paragraphs.

I) The Raman peak around 600 cm^{-1} (Figure 5.22, 5.23 and 5.24), which only appears in ZrO-containing samples in this work, and the comparison of these peaks to other investigations on $BaZrO_3$ and $SrTiO_3$ where comparable Raman peaks were observed at slightly higher Raman shifts and comparable width [251, 252, 253], suggest that these peaks can most likely be associated with the formation of V_O^X.

II) The EPR results, elaborated in section 5.3.5, provide another potential indicator for the formation of double filled oxygen vacancies (V_O^X) if these results are compared to other previous investigations [109]. The proposed anionic defect structure in FCC rocksalt ZrO is consistent with the postulated idea by Caillet et al. [114] who suggest the formation of free vacancies by electron injection from the cathode into the material as one important mechanism for the defect formation.

III) The XPS spectrum taken from the ZrO-containing material shows another peak pair at lower binding energy (BE) (Figure 5.25 and 5.26), which is not solely explainable by a positive ionisation due to the strong non-metallic 2p orbital and metallic d-orbital interaction as discussed before. However, it can be caused by the formation of a lower Zr oxidation state or a changed environment. Since a decrease in oxidation state would also increase the EPR response, which is not the case, it seems most likely that a changed environment is at least partially responsible for this BE shift.

The formation of V_O^X and the associated trapping of two electrons could be one such mechanism, which will have the consequence of a decrease in BE of the surrounding Zr-ions compared to fully oxidised Zr^{4+}-ions. Furthermore, a more metallic character of these Zr-species close to such a vacancy partly explains the 40 % narrower FWHM of this peak-pair located at lower BE, which is also supported by the strong interaction between the non-metallic 2p orbital (O) and the

transition metal 4d orbital (Zr) leading to positively ionised metal atoms and delocalised electrons on the non-metal site and a generally more metallic behaviour [235, 236, 249, 250].

Based on the discussed observations, it seems most likely that the fundamental FCC rocksalt ZrO structure consists of a mix of ionic and metallic bonded structures, whereby the metallic character originates from a strong non-metallic 2p orbital and metallic d-orbital interaction. Furthermore, the experimental results suggest the formation of double filled oxygen vacancies (V_O^X) as another mechanism explaining the observations. Even if the experimental results obtained from this work, which are the first of their kind, shed light on the structure of FCC rocksalt ZrO and HfO, a better understanding of the complex bonding structure in these structures could be achieved by DFT modeling or other theoretical calculations and is one suggestion for further work in this area.

5.4.2.2 Formation and properties of ZrO_xN_{1-x} during electrical loading of (yttria-stabilised) zirconia

ZrN and ZrO_xN_{1-x} are well-known interstitial compounds. Thus, the discussion of the ZrO_xN_{1-x} properties will be rather short compared to the previous discussion of ZrO properties.

The experiments from this work which were conducted in N_2 reproduced the rock-

salt structured ZrO_xN_{1-x} found by Charalambous et al. and Morisaki et al. [79, 83] during FS in air. In N_2 the measured lattice parameter of 0.4577 nm is within 0.7 % of Morisaki´s [83] (0.46 nm) reported value. This is also in the range of the lattice parameter known for pure ZrN [84, 85] and ZrO. Charalambous et al. did not specify the ZrO lattice parameter, they used a value of 0.46 nm for their investigation, which is based on a result published by Schoenberg in 1954 in the footnotes of [80], which says: "*The cube edge of the ZrN phase was found to be a = 0.4537 - 0.4562 nm and that of the ZrO phase a = 0.4854 - 0.4620*", but no further evidence for the ZrO phase or its characterisation is mentioned in [80].

Compared to ZrO, ZrO_xN_{1-x} forms rather ionically bonded structures, however with some metallic character remaining due to the strong interaction of the non-metallic 2p and the metallic d-orbital [235, 236, 249, 250]. This can be explained by the inclusion of N into the material, confirmed by EDS and XPS, and the formation of paramagnetic Zr^{3+} ions, confirmed by XPS and EPR, as is known from ZrN [196, 197].

The Raman spectra taken from the ZrO_xN_{1-x} samples also show the expected signals for such a defective FCC rocksalt structure as presented previously for ZrO_xN_{1-x} and other sources [183, 184], without significant abnormalities.

The electrical conductivity measured for the ZrO_xN_{1-x} containing sample is also comparable to the ZrO-containing sample.

5.4.2.3 Change of electrical properties in YSZ reduction stage II

The electrical conductivity of the reduced tetragonal $ZrO_{2-\delta}$ matrix is negligible at room temperature, as the slightly greyed sample after electrical loading in oxygen showed in this research, so the high nominal electrical conductivities (3-7 S/cm) and metallic appearance of the ZrO samples strongly suggest that ZrO is an electronic conductor following a PTC behaviour as shown in Appendix Figure A.2.

Furthermore, since the continuous path of the ZrO phase in the synthesised samples seems to be mainly in a surface layer 1-10 μm thick, its actual conductivity must be 2 or 3 orders of magnitude higher than the nominal value based on the dimensions of the whole sample, i.e. 10^2 - 10^3 S/cm. This approaches genuinely metallic levels of conductivity.

Given the essential similarity between our methodology, and methods presented elsewhere [53, 86, 254], in passing high currents through zirconia-based samples whilst excluding O_2 and maintaining that exclusion during cooling to room temperature, there can be little doubt that the explanation for the observations of high room temperature electrical conductivities in [53] and [86] are a result of the electrochemical reduction of YSZ to form rocksalt Zr(O,N).

Beside the detected electronic conduction in ZrO at room temperature its influence

during the ongoing electrochemical reduction and phase transformation process is important to understand the electrical results during FS shown in Figures 5.4 and 5.6. To investigate this correlation the results in these figures are used as a basis for the discussion of the electrical properties and the ongoing changes during electrochemical reduction of pre-sintered fully dense polycrystalline stabilised zirconia under the present circumstances.

According to the inverse Arrhenius plot (Figure 5.6) the electrical resistance throughout the electrical loading process seems to be continuous up to the point where the power spike happened. At the beginning of the electrical loading process a potential improvement of the contact between the applied Pt-paste and the sample could decrease the electrical contact resistance at this part of the sample, which would also influence the apparent activation energy (slope) of the electrical conductance over temperature. However, if the ongoing electrochemically induced phase transformation (blackening) connects cathode and anode the power spike happens and the current localises strongly. Based on that, the reason for the continuing trend of electrical conductance over estimated sample temperature can be found in the competing mechanism of ionic conduction in (slightly reduced) YSZ, which shows NTC behaviour, and the PTC-behaving electronic conduction in ZrO, which are present as parallel phases, giving two possible routes for conducting electrical charges through the sample.

This explains why at the beginning of the reduction process the ionic conduction is more important, as is supported by the changed defect structure after FS or/and electrical loading in air or O_2. This is also represented by the higher activation energy at the early stage of reduction which is in the range of the reported activation energy for oxygen ion conduction in YSZ. However, with an ongoing reduction process the contribution of electronic conduction compared to ionic conduction overtakes as described in stage I and leads to a continuing decrease in activation energy.

According to the procedure applied and the SEM and EDS investigation of the early stages of electrochemically induced phase transformation shown in Figure 5.9, it can be concluded that the transformation of only ≈ 0.01 % of the cross section towards ZrO changes the overall electrical behaviour of the material under electrical load at elevated temperature. Such a significant influence of such a small amount of phase transformation is possible because the orientation of the ZrO-propagation follows the electrical field.

In the perspective of this work and the discussed influence of phase transformation towards ZrO and its electrical conductivity it should also be mentioned that presintered and fully dense samples which remain in the electrochemical reduction stage I show no current localisation or inhomogeneous sample heating. However, during most experiments investigating (DC-)FS green bodies, a current concentra-

tion happens, which is often explained by the loss of thermal heat on the sample surface due to radiation [25, 182, 255, 256].

Heat loss by radiation is surely one reason for inhomogeneous sample heating, however, localised sintering where the generated heat is concentrated, a generally larger sample size and the significantly lower thermal conductivity of a green body or a less dense section of the sample, at the beginning are contributing to an inhomogeneous heating path. Nevertheless, the question arises, why the heat distribution during FS of YSZ, starting as a green body, is so different to the heat distribution in a pre-sintered dense sample even if the same electrical power is dissipated and the sample (supposedly) densifies during the first few seconds of the FS-process up to full density.

The results presented here show that electrochemical reduction and a related phase transformation can happen in the centre of the sample during FS with the consequence of current concentration and inhomogeneous sample heating, which was not seen to such an extent without the electrochemically induced phase transformation. Thus, the electrochemical reduction in the sample centre can be seen as the more important mechanism compared to thermal (surface) radiation for explaining heat and current concentration during FS.

Comparing the relative homogeneity of the samples run in O_2 with the inhomogeneity of the current and heating in oxygen-free atmospheres (Figure 5.7) and,

in particular, the tendency for the current to be concentrated into a narrower channel at the cathode in these specimens also confirms the role of electrochemical reduction in increasing the conductivity and thereby stimulating runaway and localisation from an early stage on as was also suggested previously [28, 30, 234].

Furthermore, most models about heat distribution during FS of YSZ and FS [5, 20, 24, 182] in general do not include the issue of insufficient availability of oxygen as a charge carrier, as was shown by calculating the volume of air necessary to be processed and oxygen being removed from it, which is 200 cm^3 at a current of 1 A at 800 °C T_f, shown in Figure A.13 in the Literature Review, and do not include the explicit possibility of electrochemical reduction. A potential involvement of electrochemical reduction is partly covered by the activation energy used in such models, however, further improvement of such models is required to enable a more accurate prediction of the material behaviour and when electrochemical reduction will happen under FS-conditions.

5.4.2.4 Stability of ZrO

Even if a substantial amount of ZrO was synthesised at room temperature in this work it became clear that if the ZrO-containing samples were exposed to air, the material reoxidised and incorporated N over time, as happened between FS or electrical loading and SEM/EDS characterisation (Figure 5.9 and 5.10), suggest-

ing a high instability of the ZrO phase. Furthermore, the instability of ZrO is also shown in the reoxidation experiment, which shows that at 800 °C ZrO reoxidises within seconds.

This instability of ZrO is consistent with the fact that ZrN is a common material that is produced commercially but rocksalt ZrO is known through only very few research reports. ZrO does not appear in the Zr-O equilibrium phase diagram [257] and prior to this study reports of ZrO formation have been only in response to the oxidation of metallic Zr [80, 81]. In addition, the most probable structure of ZrO in [81] was identified as hexagonal, based on EELS and DFT modelling results. However, in contrast to this and all other experimental work, the DFT modelling in [81] was for pure zirconia at low temperature (0 K), which is one reason why the modelling results can be different to the experimentally obtained ones.

Nevertheless, it should be pointed out that the formation and stability of defective rocksalt FCC ZrO, which has been identified in this study, may also partially be attributed to the following considerations:

I) None of the previous experimental reports concerns "pure" ZrO - our material contains Y in addition to Zr and there may be extra stabilisation of ZrO from N impurities, whilst the experimental part of [81] concerned the oxidation of alloys containing Sn and other elements. However, in this work the formation of a sub-

stantial amount of ZrO was shown for Y-contents between 1.5 and 10 mol.% as well as Mg-stabilised zirconia, which points towards the kind of stabiliser being less important. No N was present according to the EDS results, so this does not seem to be important in stabilising the ZrO rocksalt structure. This phenomenon is also consistent with the idea of dopants working as the initial mechanism leading to the formation of oxygen vacancies which are then used for ionic conduction and the following reduction in the material but are not mandatory for the following phase transformation.

A certain amount of impurities was always present in the investigated materials. Some of the impurities show a fundamentally changed behaviour as soon as the phase transformation happens and could even be used as indicators for detecting an ongoing phase transition. For instance, Fe shows a strong EPR signal at a g-factor of 4.27 due the formation of Fe^{3+} in Fe_2O_3, which disappears completely during the reduction process if a phase transformation happens. Furthermore, the R_1 and R_2 peaks of Cr^{3+} in alumina are strongly present in the Raman spectra taken from the alumina-doped samples before the phase transformation happens but also disappear after the phase transformation along with the rest of the alumina spectrum, suggesting that the alumina, or at least the Cr^{3+}, goes into solid solution in the ZrO.

However, the phase transformation was also observed in materials which only

contained a very small amount of Fe_2O_3 and no Al_2O_3 pointing towards a possible but not necessary mechanism of impurity induced stabilisation.

II) The small size of the ZrO-particles formed here may also be of relevance, as the formation or decomposition of ZrO with a lattice parameter of 0.4580 nm involves a large volume contraction of ≈ 29 %, compared to fully oxidised ZrO_2 with a lattice parameter of 0.5137 nm [58].

5.4.2.5 Appearance and location of ZrO

The micrographs presented in this work reveal that ZrO initially forms as fine grains ≈ 30 nm in size. Furthermore, the decreasing FWHM of the $\{111\}$ peak of this phase with increasing power dissipation points towards a growth of the phase with ongoing reduction and higher temperature. This could be one reason why in the very early stage of blackening, the ZrO-formation, in the form of particles, is hardly detectable by SEM for example.

The closest report to our observation of the ZrO-formation in the form of fine grains is the TEM-study conducted in 1983 Moghadam et al. [113]. They reported the appearance of metal-like cubic zirconia-containing particles in scandia doped zirconia after electrochemical reduction, but no further characterisation was reported and otherwise the material remained uncharacterised.

Based on the micrographs taken from ZrO-containing tetragonal 3YSZ and cu-

bic 8YSZ, a fundamental difference can be seen dependent on the structure or composition of the parent-phase. If the parent phase is tetragonal whole grains of tetragonal 3YSZ were transformed towards smaller crystals ($<$ 100 nm), whereas in cubic 8YSZ the ZrO formation happens mainly along the grain boundaries and triple points and sometimes in the form of a precipitated phase in the grains themselves. This points towards a different stability of the parent phase against electrochemical reduction and the potential transformation of ZrO. Another potentially important parameter is the grain size of the parent phase, which is significantly bigger for 8YSZ compared to 3YSZ and might change the stability of the parent phase/crystals in general. However, this needs further investigation.

The localisation of the current during DC-FS of a green body is significantly different to electrical loading of pre-sintered samples described before due to the part of the sample where electrochemically induced phase transformation happens, as was shown by Raman and EDS in this work.

The reoxidation process, which happened during the TGA measurement of a 3YSZ-FS-CD-He (Appendix Figure A.10), showed a weight increase by 1.25 %. This suggests that $\approx$ 10 % of the sample transformed towards ZrO during the FS process in He, if the sample is considered to be either ZrO_2 (123.2 u) or ZrO (97.2 u), with no other suboxidic structure and yttrium doping being considered. This shows that even if the sample is loaded for a comparably long time ($\approx$ 3 h), only

a part of the green body transitions towards ZrO, which indicates that if FS is conducted for a shorter time of a few seconds or minutes, a significantly lower amount of ZrO is formed.

In the present electrical loading experiments the shortest distance between the electrodes, and therefore highest electric field in these samples is along the surface, between the layers of Pt paste painted on the sample surface, the wires connected to the power supply being set further apart. Current therefore first started to flow near the surface, and its proximity to the oxygen free atmosphere, then encouraged the rapid formation the ZrO. Since this is evidently highly conductive, the current remained concentrated at the surface thereafter. A comparable result was reported by others who reported a 30 nm thick surface layer of electrochemically reduced 8YSZ after electrical loading of a single crystal in inert atmosphere [254].

Another effect which is notable in this perspective is abnormal grain growth (AGG) detected in 3YSZ post DC-FS. AGG in such samples was detected in the exact same regions of the sample where electrochemical reduction and the induced phase transformation towards Zr(O)N in stage II of the electrochemical reduction would be expected to happen. Since even higher electrical fields and currents were applied in [124], it can be assumed that an electrochemical reduction and the induced phase transformation happened but the field was turned off at elevated fur-

nace temperatures [123, 124], which is why reoxidation made the identification of reduced regions rather difficult or impossible.

One important question that remains unanswered is how the reoxidation of the electrochemically reduced and transformed regions affects and defines the final crystal structure and orientation within the mainly tetragonal structure/abnormal grain. A potential mechanism could be a rather local reduction and phase transformation along the particle surfaces, which become grain boundaries during densification, in the region where AGG is detected. The local oxygen deficit would lead to diffusion of surrounding oxygen in to these regions after the field is turned off, which affects the surrounding lattice as well as the grain boundary structure. It is known that the tetragonal structure in YSZ can be stabilised over a wider range of oxygen (vacancy) content and, furthermore, diffusion is enhanced in reduced regions [211, 258, 259, 260], both phenomena support the suggested mechanism. The suggested mechanism is somehow comparable to low temperature degradation (LTD), where the diffusion of oxygen from the environment leads to a change in crystal structure. Examination of the suggested mechanism could be done by high resolution TEM, EDS or potentially EBSD within the abnormally grown region, which could also be cooled down more quickly or in inert atmosphere, to try to *freeze* the structure prior to reoxidation.

5.4.2.6 Plastic deformation in YSZ during flash sintering and under electrical load

Unusually, high plastic deformability during FS of 3YSZ and 8YSZ [126, 127, 128, 129, 130, 261, 262] as well as spark plasma sintering of YSZ/Al_2O_3/$MgAl_2O_4$-composites, containing around 40 % YSZ [263], was previously reported and cannot be explained solely by (Joule-)heating.

In all reported investigations about extensive plastic deformation under electrical load, either a strong electric field, which depends on the furnace temperature [126, 127], or a low oxygen partial pressure [128] were applied. Since the reported onset of superplasticity with electrical heating happens under the same conditions and the same region of the material as the reported phase transformation towards FCC rocksalt ZrO, it can be concluded that the reported phenomenon of extensive plastic deformation is caused by the ongoing electrochemical reduction, and the related phase transformation towards FCC rocksalt ZrO happening in stage II of the electrochemical reduction. The assumption of the electrochemically induced phase transformation being one important factor for the enhanced plastic deformability, and the results about the phase transformation in blackened zirconia starting on the cathode shown in this work, also explains the higher degree of plasticity observed on the blackened cathode side in 3YSZ reported in [128].

It should be mentioned that superplasticity is a well-known behaviour of materials, such as YSZ, at high temperatures also without the presence of an electrical field. However, in the FS investigations in [127] reference samples showed that the electrical field under the present circumstances is mandatory for the reported superplasticity and temperature is not solely the reason for this effect.

Particularly for 8YSZ, where grain boundary sliding was suggested [129, 130] as the main reason for enhanced plasticity, the electrochemical reduction and the observed phase transition mostly located on the grain boundaries can be seen as the reason for this athermal effect. The assumption of a changed grain boundary structure in 8YSZ under electrical load is supported by this work showing the formation of ZrO mainly along grain boundaries in 8YSZ (Figure 5.16 and 5.15).

The observed extensive plastic deformation is possible because the electrochemically induced FCC rocksalt ZrO phase shows a more metallic behaviour, and a changed bonding structure, as suggested by the XPS and EPR results, and provides a higher symmetry which generates more possibilities of slip bands and planes. The reduction mechanism and extraction generates abundant vacancies, which can be seen as dislocations, also influencing plastic deformability. A comparable mechanism was even reported in an additively manufactured metallic hexagonal titanium alloy (Ti-6Al-4V) which showed an increased plastic deformation after introducing oxygen-stabilised FCC rocksalt Ti(O) structures [240].

Furthermore, it can be assumed that the superplasticity observed during SPS [263] is also caused by (electrochemical) reduction of the material because of the elevated temperatures, current flow, and reducing environment caused by the surrounding carbon, which are present during SPS. Whether a phase transformation towards FCC rocksalt ZrO(N,C) happened remains unclear and needs to be confirmed in the future. This phenomenon could be a potential research question in the future to enable the production of enhanced plasticity in reduced oxide ceramics or produce more complex shapes which could be reoxidised subsequent to SPS.

It can be concluded that due to a potential electrochemically induced phase transformation towards a rather metallic material, which also shows a changed bonding and grain boundary structure compared to the fully oxidised material, an unusually high plastic deformability in transition metal oxides, such as (yttria stabilised) zirconia, can be observed during field assisted sintering methods such as FS or SPS.

5.4.2.7 Influence of reoxidation on the densification of YSZ during flash sintering

In most FS-experiments the field is turned off at furnace temperatures of a few hundred °C, and sample temperatures of $>$ 1000 °C, leading to reoxidation of the

electrochemically reduced material, which causes several effects such as increase in volume.

If undoped zirconia is used as an example, the unit cell volume of FCC ZrO_2 (a = 0.515 nm) is $\approx$ 40 % bigger in its volume compared to the unit cell volume of FCC ZrO (a = 0.4580 nm). Thus, reoxidation of ZrO to ZrO_2 leads to a significant expansion and potentially cracking of the material, as the TGA results (Appendix A.10) showed, but also, potential closure of pores. Pore closure could happen if reoxidation would lead to an expansion of the electrochemically reduced and transformed region into the open pores of the material by transformation from the FCC ZrO rocksalt phase back to the cubic ZrO_2 phase.

Since a cracking of FSed samples in successful experiments is usually not the case, and the ZrO phase is not detected after reoxidation, it seems unlikely that this happens on a regular basis. This could either be related to a low amount of ZrO being formed during FS, which makes the volumetric expansion less critical, or, if ZrO is being formed in the form of tiny channels in the submicron range, they might not be detected post-FS. The latter case is rather unlikely since the reoxidation of ZrO at elevated temperatures would happen. However, considering the (usually) short processing time of FS, and the results of 0.01 % of the cross section being sufficient for an overall change in the materials´ behaviour shown in this work, it seems more likely that only a low amount of ZrO is formed and

reoxidised during usual FS, not causing cracking of the overall sample.

The process of pore closure due to oxidation is known in other fields such as thermal spray coating [264]. However, if this mechanism occurs and is important to the densification during/post FS strongly depends on the FS-conditions but seems rather unlikely and needs further investigation.

5.4.3 General implications for flash sintering

5.4.3.1 Predicting the onset of flash sintering

In the Literature Review the most commonly used models were explained, whereby the models by Todd et al. [5, 25] and Zhang and co-workers [24] are the ones that are most accepted by the scientific community.

Since both models are based on results obtained by experiments conducted with materials, YSZ [5] and ZnO [24], which show an onset of FS at lower temperatures at low oxygen partial pressures [23, 181] compared to higher oxygen partial pressures it is obvious that electrochemical reduction can happen before the onset of FS is detected.

The experiments in this work confirmed this assumption in various ways such as an atmospheric influence on the onset of FS, current and conductivity dependency on atmospheric oxygen partial pressure, change in activation energy, as well as insufficient oxygen availability under (DC-)FS conditions.

Another interesting parameter for predicting the onset of FS could possibly be found in the energy necessary to extract oxygen from the material, such as transition metal oxides, leading to the formation of oxygen vacancies and an increase in electrical conductivity, which could lead to an electrochemically induced runaway in combination with the proposed thermal runaway [5, 24].

For semiconducting materials, such as carbides, electrochemical reduction is less important since electronic conduction is fundamental from the beginning and an ongoing densification is more important to the onset of FS as shown before [26].

5.4.3.2 Rapid densification by flash sintering

The main contributor to the densification during FS, but also other rapid sinter techniques without electrical fields, is Joule-heating and the rapid heating as was shown in the past [38] and mentioned in the Literature Review. However, the research conducted here shows that electrochemical reduction happens under FS-circumstances in some materials such as YSZ, which is why an electrochemically induced effects on the densification must also be considered as a potential parameter. The influence of (electrochemical) reduction on parameters such as grain boundary or cation mobility was investigated by other researchers such as Dong and Chen [259, 260], which showed a strongly increased diffusivity and mobility in a reduced state which can also lead to an improved densification.

5.4.4 Electrochemical reduction of YSZ in the perspective of SOFC and SOEC

Solid oxide fuel cells (SOFCs) and solid oxide electrolyser cells (SOECs) are usually used for energy storage and production and ideally operate under demanding conditions for several years.

The degradation mechanisms occurring and reasons for failure are often unclear and the electrolyte is almost never considered as a potential weak link. Especially, the complication of YSZ being used as a thin electrolyte layer of a few μm makes it difficult to characterise the material properly after the device has failed or degraded.

In one of the few long-term investigations, the electrochemical performance and degradation of an SOFC, made from two stacked cells, was tested and documented over 100,000 h [265]. During the process a continuous voltage drop under constant current was detected over time, indicating a decreasing resistivity during operation and an increase in leakage current over time, which is one of the common reasons for failure of SOFCs.

If the SOFC stopped operating and the current flow stopped for some time due to external reasons such as power shortages etc., the system was able to recover and the resistivity increased again after re-starting the device but started decreasing

again after some time. [265]

Based on the results from this research, the most obvious reason for the described degradation in electrochemical performance in SOFCs, like reported in [265], is an ongoing electrochemical reduction of the YSZ-electrolyte layer. Since the circumstances under which SOFCs and SOECs are operated, are a combination of elevated temperature ($>$ 700 °C), high current flow and field strength, which are at least as extreme as in this research. This assumption is also supported by other investigations showing that 0.4 V, which is below the proposed degradation voltage of 2 V, are sufficient to reduce YSZ [266]. Further indication for an ongoing electrochemical reduction of the YSZ-electrolyte layer is the recovery of the resistivity after interruptions [265], which is similar to the behaviour observed in our reoxidation experiment while electrical loading.

Another aspect which is rarely considered and is supporting the previous assumption is the presence of a reducing atmosphere, which is in direct contact with the YSZ-electrolyte and reduces ZrO_2 at a temperature of 450 °C [267].

To highlight how likely an electrochemical reduction of the (8)YSZ electrolyte layer in SOFCs under conditions as reported in [265] is, theoretical calculations, shown in the Appendix Figure A.14, were conducted. The calculations showed that if only 1 % less O is taken in, compared to the fully O-ion-based current flow, it would take 56 s to achieve an O-vacancy concentration equal to a 3 mol.%

yttria doping in pure zirconia. If only 1 ppm less O is taken in it would take 157 h to achieve the same amount of vacancies. These results show that even if the O-intake is slightly too low, the fundamental structure of the material and its properties can change within a short time in the range of seconds, like shown in this work.

Regarding the stage of electrochemical degradation, the YSZ electrolyte is probably in the first stage of electrochemical reduction and forms a $(Y)ZrO_{2-\delta}$ phase. Nevertheless, an ongoing reduction could lead to the reported electrochemically induced phase transition, which will lead to shortcutting and an even more severe and sudden decrease in resistivity.

Since the electrochemical reduction of a thin layer is difficult to detect, the research and the applied techniques used in this thesis showed that in the first stage of electrochemical reduction EPR is the best technique to characterise a potential change in the material because of an increased number of paramagnetic Zr^{3+} species, which will form if oxygen is retracted from the material.

5.4.5 Summary of electrochemical reduction stages in (stabilised) zirconia

The chart shown in Figure 5.33 summarises the different stages of electrochemical reduction which can be reached during FS, the most important defects, and the generated properties identified in this work, starting with the unreduced tetragonal zirconia structure.

	$(Y_a)Zr_{1-a}O_{2-0.5a}$	$(Y_a)Zr_{1-a}O_{2-0.5a-\delta}$	Zr_1O_1
Electrochemical Reduction	Increasing →		
Colour of the material	→		
Anion / Cation ratio	2-0.5a	2-0.5a-**δ**	1
Formed Defect Structure	-	Zr^{3+} + $V_O^{\cdot}$	V_O^{x}
Crstallographic Symmetry	t	t* Increasing fluorite cubic/c*	Rocksalt FCC
Plasticity	low	Increasing low	plastic
Electronic Conductivity	low	Increasing at high T	good at room temperature
Paramagnetic defect concentration	none / very low	high	low

Figure 5.33: Based on the presented results and discussion a summary of the electrochemical reduction stages in (yttria stabilised) zirconia is shown which includes various parameters characteristical for each stage of reduction from unreduced (left) to reduced (right).

In stage I of reduction the formation of single-charged oxygen vacancies and paramagnetic Zr^{3+}-Ions was detected, which is described as *t** structure. Based on the results of this work it can be assumed that this stage of electrochemical reduction

is reached in most FS experiments.

In stage II of reduction FCC rocksalt ZrO is formed, which contains double charged oxygen vacancies and shows electronic conductivity following a PTC-behaviour. This stage of reduction, where phase transformation happens, can be reached during FS experiments which are conducted under a high electrical load.

The results shown and discussed in this chapter of the thesis highlight the importance of the effect of electrochemical reduction and its significant influence on the characteristics of (stabilised) zirconia (and hafnia) during processes, which combine electrical load and elevated temperatures, such as flash sintering.

6 | Plasma formation and characteristics during flash sintering of boron carbide

6.1 Plasma pre-treatment flash sintering boron carbide at constant power in argon

Figure 6.1 a) and c) show the electrical parameters measured during FS of B_4C in He under an applied voltage of 50 V ($\approx$ 25 V/cm). The voltage-controlled stage lasted for 3 s before the rapid increase in current led to the transition to power control (700 W, $\approx$ 2.3 W/mm^3).

Video stills of the sample at the different stages of FS can be seen in Figure 6.1 a) (i)a - iii)a) with the corresponding times shown along the top of the images. During the transition from voltage- to power-control the current initially concentrated in the sample centre (Figure 6.1 iia) but heating became more homogeneous during sintering as densification continued (Figure 6.1 iiia). This behaviour resembles that of SiC under similar conditions [26].

The results of using the same electrical parameters and furnace temperature but with an Ar atmosphere are shown in Figure 6.1 b) and d). Unlike the previous experiment in He, the switch from voltage to power control occurred after fractions

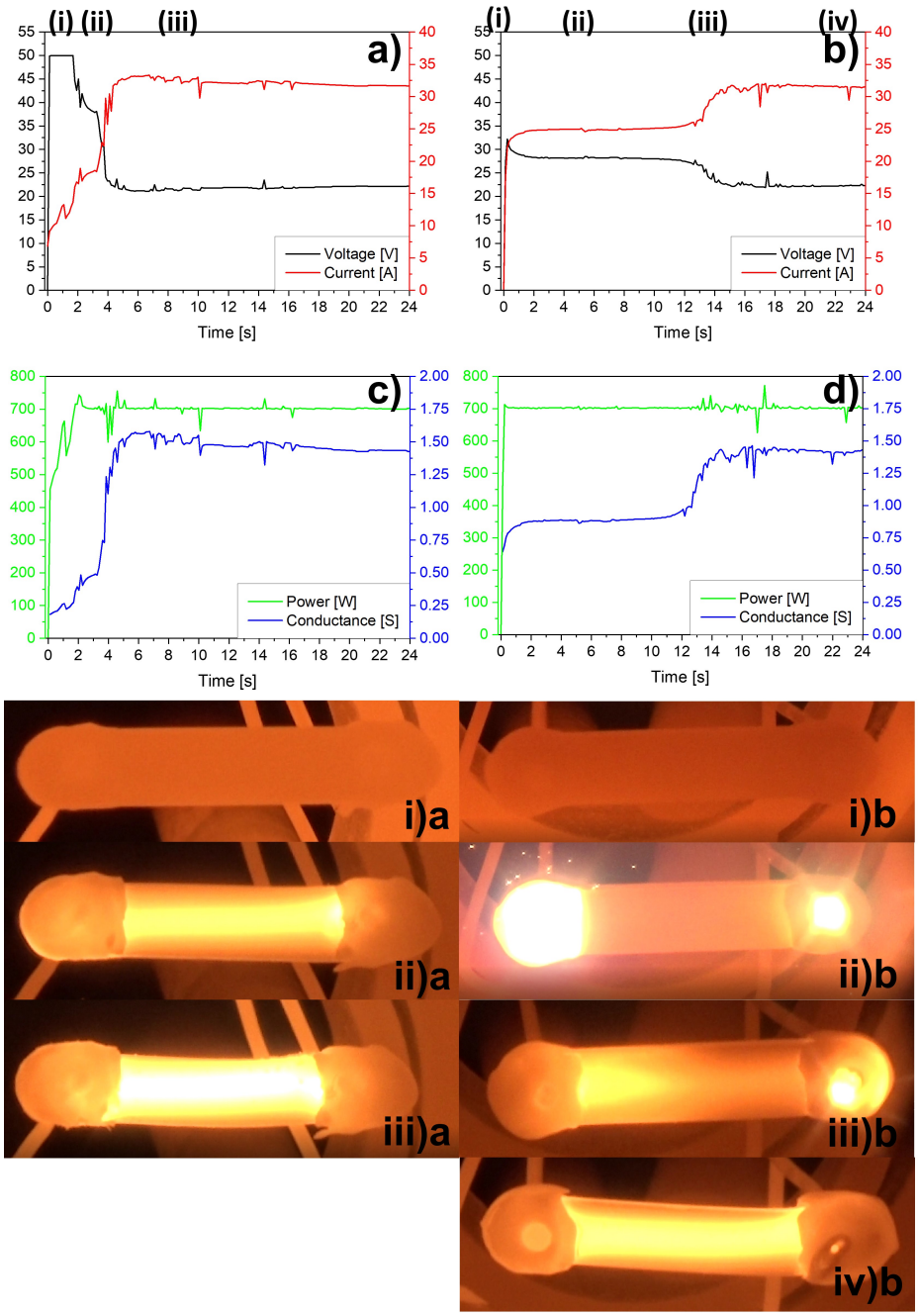


Figure 6.1: Electrical parameters (a-d) and investigated sample during FS of B_4C in helium (a and c) and in argon (b and d) which includes the pre-plasma stage. The cathode (-) is on the right and the anode (+) on the left side of the sample.

of a second because atmospheric breakdown led almost immediately to plasma formation, which dissipated power at the pre-set limit of 700 W (Figure 6.1 iib). The plasma remained stable for $\approx$ 15 s. After this time the plasma collapsed and current flow transitioned into the sample itself (Figure 6.1 iiib). This transition is accompanied by another increase in conductance (Figure 6.1 d). Because of the appearance of the plasma before the transition to FS, this process is described as Plasma Pre-Treatment Flash Sintering (PPT-FS).

The early stages of plasma formation were recorded with a high-speed video camera (Figure 6.2). Some initial heating of the electrodes is visible before formation of the plasma (Figure 6.2 b). It is evident that the initial formation of the arc is on the far side of the sample, where some of the details cannot be seen. However, the discharge around the cathode and bright plasma formation on the far side of the anode as the arc forms in Figure 6.2 c) and d) show that the preferential path of the plasma was outside the sample and not within the sample itself. Figure 6.2 covers 30 ms of the initial plasma formation. The heating of the cathode is concentrated at the tungsten wire, where electrons are emitted. Once the plasma has stabilised, as seen in Figure 6.1 iib, the anode is hotter than the cathode.

The video images taken throughout the process (Figure 6.1 i-iii)b) show that sample heating was slight and shrinkage was negligible during the plasma stage. However, as soon as the plasma collapsed and the transition happened, heating and

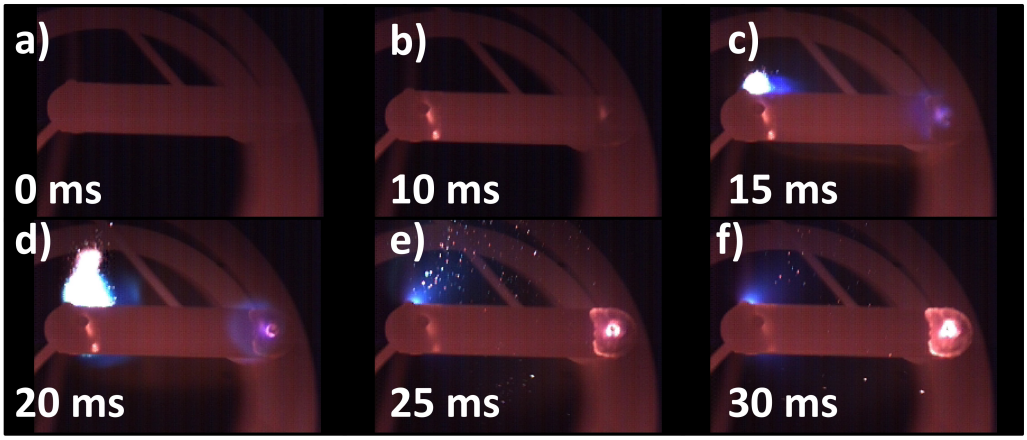


Figure 6.2: Images show the high-speed video camera images taken at the very beginning (30 ms) of the plasma formation around a B_4C sample (green body) in Ar at 1500 °C furnace temperature. Cathode (-) located on the right, anode (+) on the left side of the sample.

shrinkage of the sample occurred.

After the plasma collapsed sample heating in Ar was very similar to the experiment conducted in He. Furthermore, the conductance of the samples in both atmospheres remained comparable after $\approx$ 20 s.

6.2 Electrical characteristics of PPT-FS for boron carbide and silicon carbide

The development of the different stages of pre plasma treatment flash sintering (PPT-FS) were investigated as a function of the pre-set power level for B_4C and SiC. Electrical data recorded during PPT-FS for SiC are shown in the Appendix,

Figure A.23. Figure 6.3 shows the conductance (I/V) for each stage of the PPT-FS process in Ar for samples each with a different power limit. The duration of the stage where a plasma was present was typically 15 s for B_4C and 240 s for SiC. For reference the conductance of the plasma itself (*plasma alone*) in Figure 6.3) was measured in the same setup but without mounting a sample between the W wires (setup shown in Figure A.24 in the Appendix).

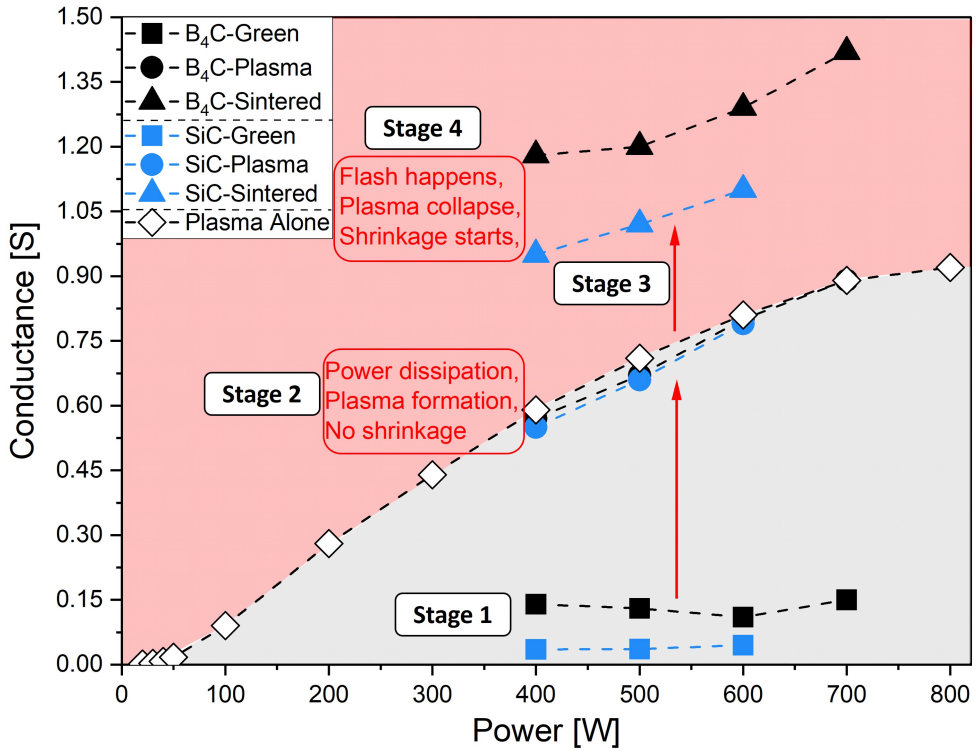


Figure 6.3: Conductance (I/V) of B_4C (black) and SiC (blue) as a green body, during the plasma formation and after the plasma collapse and densification of the material towards a sintered material, dependent on the dissipated power. As a reference, the white symbols (*plasma alone*) represent the measured conductivity of a plasma for various power dissipations measured in the same setup without a mounted sample.

Stage 1 shows the conductance for green samples measured as a reference value for each sample with a power dissipation of 10 W ($\approx$ 0.03 W/mm^3) to prevent densification and measure the conductance of the green body. Thus, the power values on the X-axis are not relevant for these data points.

Stage 2 represents the pre-sintering plasma stage where the defined power was dissipated in the plasma, which is why no significant difference in conductance between plasma alone, B_4C and SiC was measurable. Based on this, it can be assumed that the materials´ conductance in this stage was below the conductance of the plasma and the current was mainly flowing through the plasma.

Stage 3 is the transitional stage where the conductance rapidly increased, the plasma collapsed, and the sample began to heat significantly, leading to Stage 4.

Stage 4. In this stage a material and power dissipation-dependent conductance can be observed which exceeds the conductance of the plasma alone. This indicates that the solid material became the dominant, high conductance current path, leading to heating of the sample above the furnace temperature.

6.3 Plasma formation under flash sintering conditions

To establish under which circumstances the plasma can form, the breakdown voltage (VB) was measured under various conditions. Figure 6.4 a) shows VB for the two W wires in the absence of a ceramic sample in various atmospheres (Ar, He, or N_2) and electrode distances of 1 or 2 cm at various temperatures between 1400 and 1500 °C. The closer the electrode distance and the higher the temperature, the lower is VB. Furthermore, Ar shows the lowest VB of the three gases, which agrees with the PPT-FS experiments, in which a plasma formed in Ar under the FS conditions used, whereas in He no plasma appeared.

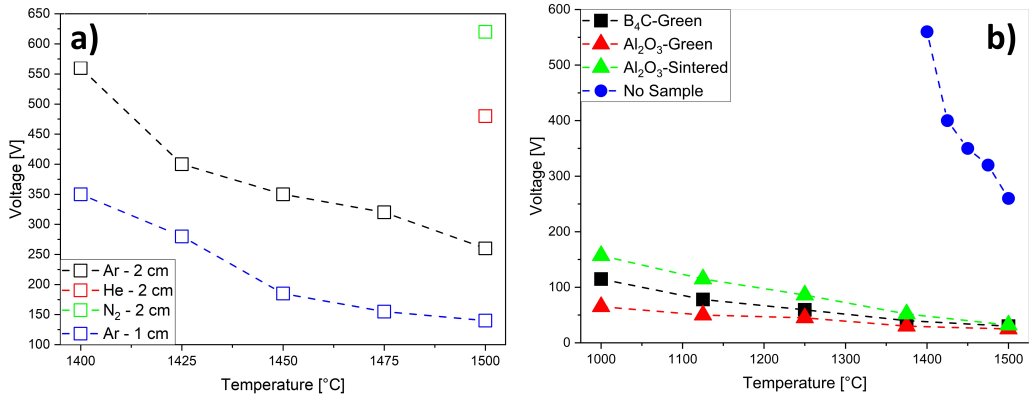


Figure 6.4: a) breakdown voltage VB in different atmospheres and distances without a mounted sample; b) breakdown voltage if samples made from different materials are mounted between the electrodes with a distance of 2 cm.

The influence of mounting an electrically insulating or conductive sample on VB

is summarised in Figure 6.4 b). Compared to the same experimental setup without a mounted sample, the experiments including a sample showed a substantial decrease in VB. In the case of an alumina (Al_2O_3) sample, VB for a green body was lower compared to a fully dense sample. However, no plasma collapse happened with an Al_2O_3 sample even if the plasma was maintained for several minutes because at no point during the experiment did the conductance of the Al_2O_3 exceeded the conductance of the plasma.

The Al_2O_3 green body also gave a lower VB than a B_4C green body over the whole temperature range (1000 °C - 1500 °C). At higher temperatures VB decreased and became similar for all samples.

6.4 Plasma properties under flash sintering conditions

6.4.1 Optical spectroscopy

The plasma properties were characterised to identify its behaviour and potential influence on the material. One way to characterise plasmas and their properties is optical spectroscopy.

Figure 6.5 a) shows the spectrum of the emitted light from the Ar-filled alumina

tube furnace at 1500 °C without a plasma (0 W) with an Al_2O_3 sample in place. The decay in intensity above 900 nm is an artefact of the spectrometer, the efficiency of which falls to zero at about 1100 nm, shown in chapter 4 in this work. It should be noted that these are raw results and have not been corrected for the detector efficiency and other characteristics of the optical setup. The lower wavelength results show the expected black body radiation as well as three sharp peaks at 590, 767 and 770 nm, which cannot be explained by thermal radiation. Since the peaks were not present if the inside of the furnace tube was covered with C-foil under otherwise identical circumstances (shown in chapter 4), these peaks can be associated with light emitted from the alumina tube at this temperature, which is shown in more detail in the Appendix Figure A.26.

When a plasma is formed ($>$ 0 W) the overall intensity of the spectra increases with power and additional sharp peaks appear which also increase in intensity with power. The spectrum emitted during the plasma stage with an Al_2O_3 sample in position and a power of 400 W is reproduced in Figure A.27 in the Appendix along with the species responsible for the peaks. With the exception of the peak at 820 nm, all the additional peaks appearing in the presence of the plasma could confidently be assigned to either Al or AlO; none of these peaks was present with a B_4C sample. The peak at 820 nm was present with both B_4C and Al_2O_3 samples and was tentatively attributed to C.

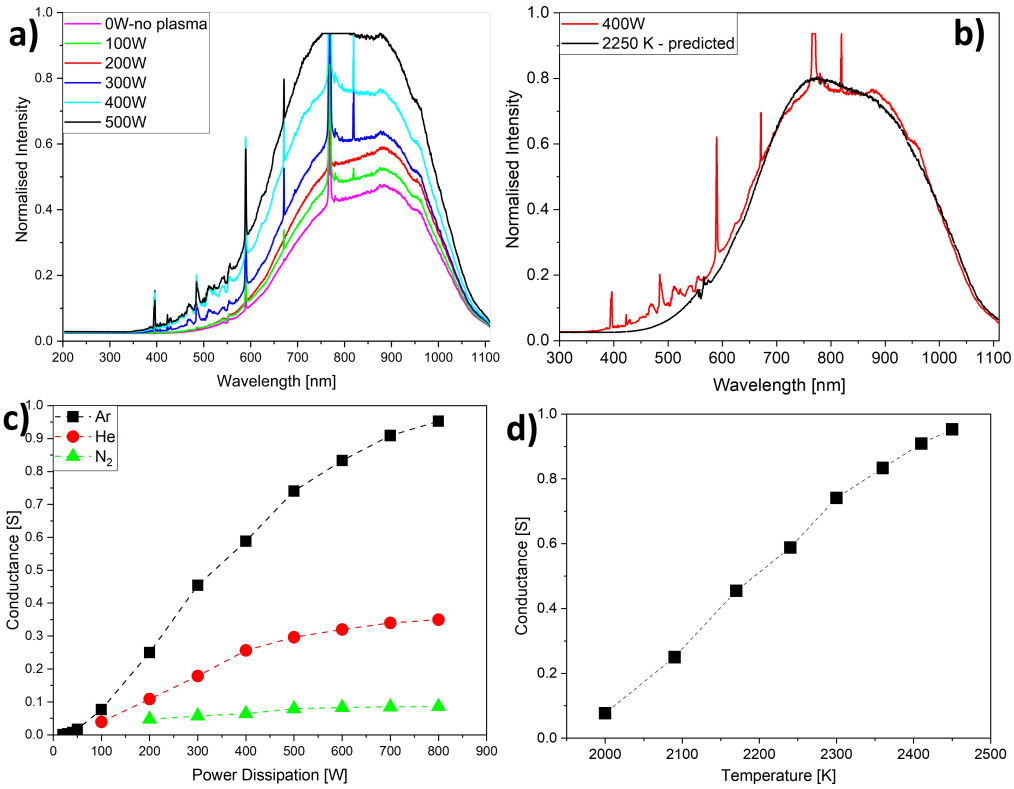


Figure 6.5: a) emitted spectra at a furnace temperature of 1500 °C (0 W) in Ar and if a plasma is formed at different power dissipations between 100 and 500 W with an Al_2O_3 sample mounted between the electrodes; b) shows the spectrum emitted during the formation of a 400 W plasma in comparison to the predicted spectrum of an ideal black body radiator at 2250 K; c) conductance of plasmas formed in different atmospheres at different power dissipations; d) conductance vs estimated electrode temperature for Ar plasma.

Figure 6.5 b) shows the spectrum emitted during the formation of a 400 W Ar plasma around an Al_2O_3 sample compared to the predicted spectrum for a 2250 K black body radiator, calculated using the spectrometer characteristics as described in previous publications regarding optical spectroscopy during FS, shown in chapter 4. The general agreement is reasonably good, except for the sharp non-thermal peaks. It is evident from Figure 6.1 that most of the visible light emitted whilst

the plasma is sustained is from the specimen electrodes so temperatures deduced by this procedure are taken to be an approximation to the electrode temperature.

6.4.2 Plasma conductance

Figure 6.5 c) summarises the experimental conductance values for plasmas formed in argon (Ar), helium (He) and nitrogen (N_2) for various power dissipations. A general increase in conductance with power can be seen independent of the atmosphere. However, the conductance in Ar which is ≈ 0.75 S at 500 W is one order of magnitude higher than the conductance in N_2 and about 3 times higher than He if the same power is dissipated. Furthermore, under the present circumstances the conductance for all atmospheres starts to plateau at a certain power dissipation.

If the results from the temperature estimation as in section 6.4.1 and conductance measurements are combined, an almost linear trend for Ar plasma conductance over estimated electrode temperature can be seen (Figure 6.5 d). The electrode temperature at the maximum power of 800 W reached ≈ 2450 K.

6.4.3 Plasma infiltration into powder compacts

Figure 6.6 shows a zirconia doped B_4C-sample that was stopped after the pre-sintering plasma stage during PPT-FS, shortly after the plasma collapsed. The SEM image of the polished cross section of the sample in Figure 6.6 a) shows

an elliptical zirconia-depleted region in the centre of the sample. This is visible because of the strong atomic number contrast between the zirconia (light) and the B_4C (dark). The shortest distance from the centre of the cross section to the surface of the sample is approximately 1.5 mm.

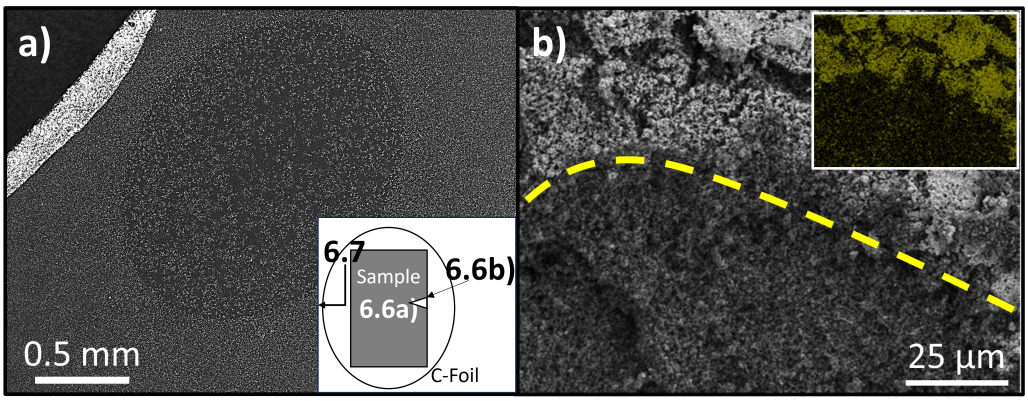


Figure 6.6: a) cross section of a zirconia doped B_4C-sample shortly after the transition from the plasma stage to the Joule heating stage; the insert shows a schematic diagram of the investigated positions of the sample shown in this Figure 6.6 and Figure 6.7, surrounded by a C-Foil loosely wrapped around it; b) surface of the same sample with a scratched region (bottom) and an inserted EDS-map showing the Zr-distribution across the surface.

A layer of redeposited material was found on the surface of this sample. Figure 6.6 b) shows a region of the surface that was scratched through to the underlying material. The lower part of the micrograph is the scratch, and the dashed yellow line shows the transition to the surface layer, outside the scratch, in the upper part of the micrograph. The insert shows a Zr EDS map of this image. There is a strong Zr-concentration in the surface layer and a significantly lower Zr-concentration in the material beneath it.

The results of Figure 6.6 demonstrate that even before the sintering stage, where Joule heating and densification of the sample are negligible, transport of material from the interior to the sample to the surface happened during the plasma treatment stage. The zirconia here acted as a marker but it should be noted that carbide was also transported in this way. This is demonstrated by a layer of material that was found to be deposited not only on the sample surface, but also beyond it, on a layer of C-foil that was loosely wrapped around one particular SiC-sample (no ZrO_2 included) for thermal insulation. The redeposited material on both the sample surface and the inside of the foil showed interesting morphologies, some of which are shown in Figure 6.7. EDS showed that the redeposited material was mainly Si in this case, indicating that the SiC had decomposed. Furthermore, unusually big, and well-structured crystals were formed found along the cracks on the sample surface after the plasma stage as is shown in Figure A.28 in the Appendix. All these features were absent when a He-atmosphere was used, so that no plasma was formed.

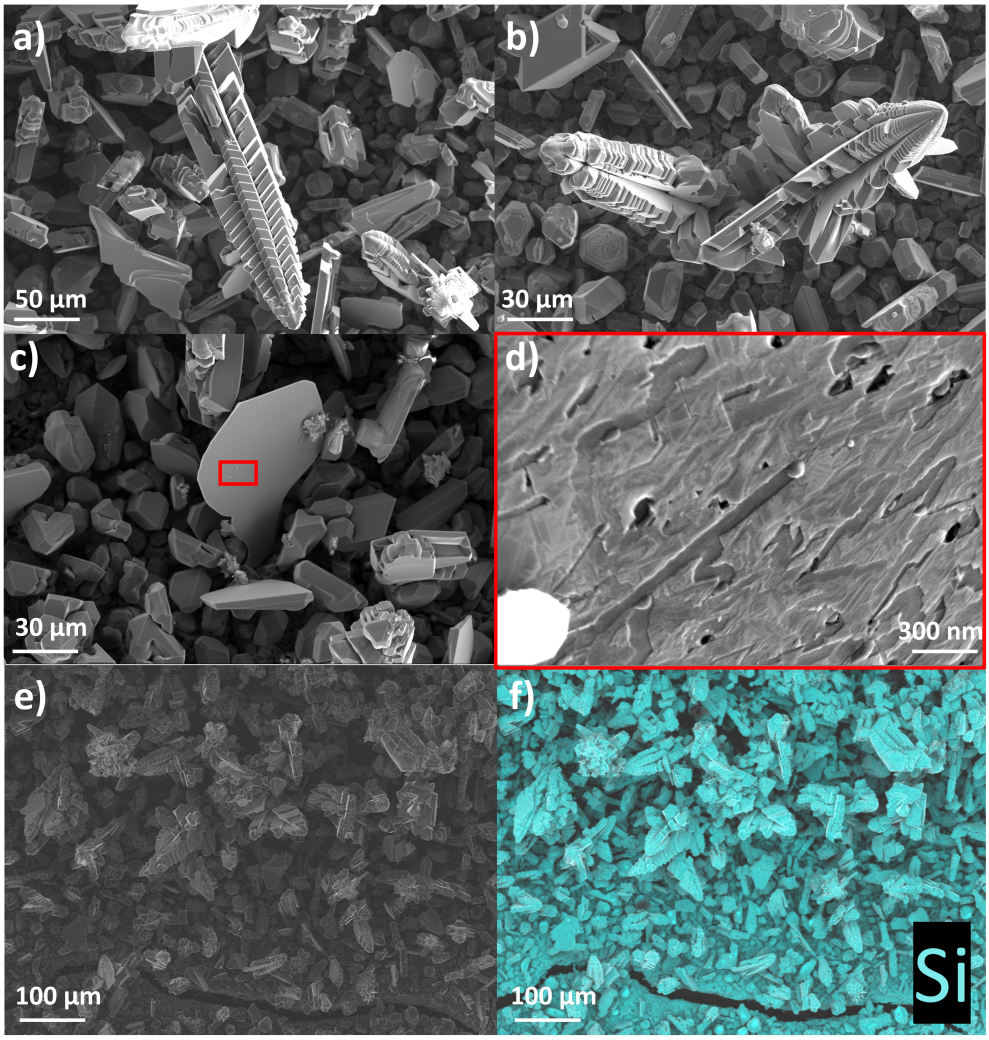


Figure 6.7: Structures formed on sample surfaces or C-foil wrapped around the samples during pre-plasma flash sintering shown in Fig 1b). d) Is a higher magnification image of the red rectangle in c). e) shows the SEM image of the Si-EDS-map shown in f).

6.5 Discussion

6.5.1 Initial formation of the plasma

As a starting point for understanding the conditions for plasma formation, we first compare the results of the experiments with no sample located between the electrodes with the predictions of Paschen´s Law [167, 268, 269], in combination with the temperature correction suggested by Peek [268] (see Appendix). Although the trends with electrode separation, temperature and inert gas used are consistent with the predictions of the Paschen equation, the observed breakdown voltages (VB) are significantly lower than the equation predicts. For example, for an Ar atmosphere under atmospheric pressure (760 Torr) and an electrode distance of 1 cm (without a mounted sample) a VB of 2.9 kV was calculated for a temperature of 1500 °C, whereas the experimentally obtained value was 150 V for these conditions, Figure 6.4 a). This is considered to be the result of mechanisms not included in the Paschen approach, which was developed for parallel plate electrodes at low temperature, such as the thermionic emission of electrons from the tungsten wire in the cathode and the field concentrating effect of the wires.

The investigated gases showed different VB which were lowest for Ar followed by He and N_2, (Fig. 6.4 a). For the gases investigated a similar VB-trend, which depends on the ionisation energies, cross sections and other parameters, was sug-

gested in previous investigations [269, 270, 271].

When a sample was mounted between the electrodes, the experimental VB decreased by 80 % at 1500 °C in Ar (Figure 6.4 b). This can be explained by a flashover mechanism happening along the solid-gas-interface where a changed electronic structure, due to gas adsorption, solid-gas-reactions, trapping free electrons, or other processes, decreases breakdown resistance [271, 272, 273, 274, 275]. This is an additional mechanism not accounted for in Paschen´s law.

The conclusion that flashover is responsible for the initial atmospheric breakdown is supported by previous investigations of gas-discharge induced FS [163, 164], conducted at higher voltages (13 kV) and various pressures at room temperature, indicating that as soon as any material is present, flashover is the main mechanism responsible for atmospheric breakdown under a wide range of conditions.

Simulations by Holland et al. [276] have shown that the field strength can be concentrated at small dielectric particles such as those in the green body and indeed the insulating Al_2O_3 as well as the more conductive B_4C green bodies in this work exhibited a lower VB than sintered Al_2O_3 (Figure 6.4 b). However, the ability of the dense sintered Al_2O_3 also to induce flashover at a voltage of the same order, and the similarity between the Al_2O_3 and B_4C green bodies, which have very different dielectric constants, suggest that the effects considered by Holland [276] do not have a great influence on plasma formation in this case. It seems likely that

the extra surface area for gas absorption etc. in the green body is the main reason that its VB is lower than for the sintered sample.

Other investigations of gas discharge induced heating of YSZ from room temperature followed by FS were conducted at various pressures and significantly higher voltages or fields (13 kV [164] or 5.5 kV/cm [163]) which again makes the circumstances of the plasma formation different from this work, but the fundamental mechanisms and properties are similar.

6.5.2 Classification of the plasma

The combination of experimental conditions and electrical characteristics indicate that the plasmas generated can be specified as high pressure arc discharge [277]. Compared to other investigations which reported contactless flash sintering based on cold plasmas [13] or plasma electrodes [12], realised by a transformer welder, the conditions of plasma formation and properties are different in this work and the plasma properties can be controlled and adjusted if necessary.

6.5.3 Steady state plasma properties

As is indicated by the higher temperature of the positive electrode in Figure 6.1, the electrons in the plasma impart more energy to a surface than the ions, because of the greater mean free path and higher collision frequency of the electrons. The

electrons in the plasma are also important to maintaining it, by ionising further Ar atoms. Assuming the size of electrons and the velocity of the ions can be neglected, the mean free path of the electrons, λ, is given by equation 6.1.

$$\lambda = \frac{1}{N\sigma} = \frac{4k_B T}{\pi d^2 P} \tag{6.1}$$

Where:

N = number density of atoms,

σ = cross section for electron-atom collisions,

k_B = Boltzmann constant,

T = temperature,

d = atom/molecule kinetic diameter (He: 260 pm, N2: 364 pm, O2: 346 pm, Ar: 340 pm taken from [278, 279]),

P = pressure.

For a plasma temperature of $\approx$ 2000 K, λ is 3 μm in Ar. If the electric field were uniform, this would be much smaller than the distance required for an electron to accelerate to the ionisation energy of an Ar atom (15.7-15.8 eV [279, 280, 281]) in between collisions. With the steady state plasma voltage of 27 V in Figure 6.1

b), the required distance would be > 1 cm. Although electrons can continue to accelerate after a collision that does not remove all of its energy and there is a distribution of path lengths such that many electrons have a greater distance over which to accelerate between collisions, the scale of this disparity suggests that only a small fraction of electrons in the main body of the plasma cause ionisation and that most of the charged particles in the plasma originate from the electrodes and the region of concentrated field in their vicinity. This suggests a rather weakly ionised plasma, as is consistent with the high light emissions from the electrodes compared with the plasma and the lack of Ar emissions in the optical spectrum.

The representative electrode temperature of 2250 K, as estimated from the black body emission fit in Figure 6.5 b), is similar to the simulated electrode temperatures resulting from the arcs in 3YSZ in air at room temperature in [164]. The plasma itself emitted less light than the electrodes, because of its rarified nature and the limited extent of ionisation, and its temperature remains unknown.

Most importantly for sintering, however, Figure 6.1 shows that the specimen temperature is significantly lower than 2250 K during the plasma stage, as is confirmed by the absence of sintering during this stage. This is because most of the electrical power is dissipated at the electrodes and in the plasma outside the sample rather than in the gauge length of the sample.

None of the characteristic peaks associated with Ar plasmas [282, 283] was de-

tected in the spectrum in the presence of a plasma, which is consistent with the low emission level from the plasma itself discussed above. The association of most of the plasma-induced peaks in the presence of an Al_2O_3 sample with Al or AlO demonstrates that these are a consequence of interaction of the plasma with the sample, sputtering material from the surface. The carbon peak at 820 nm was seen with both types of samples and can be attributed to interaction with the carbon paste at the electrodes, where the plasma was most concentrated. No additional peaks were observed with a B_4C sample, possibly because of its refractory nature.

Saunders et al. conducted atomic emission spectroscopy during simulated (F)SPS of W powder in Ar at atmospheric pressure and observed the emission of BBR in combination with many sharp ionisation peaks [160], including some assigned to Ar and W which were absent in the present work despite the use of W electrodes and the same atmosphere. The conditions were more energetic in [160], however, involving higher currents and powers, which may explain the higher intensity of these characteristic peaks.

Furthermore, a plasma conductance of up to 1 S was achieved at a power dissipation of 800 W at 1500 °C in Ar. Compared to [164], where a power dissipation of $\approx$ 500 W in the generated arc discharge led to a conductance of $\approx$ 1 mS, the conductance achieved in the N_2 plasma in this work is two orders of magnitude

higher, or three orders of magnitude, if it is compared to the plasma generated in Ar at a similar power dissipation. This deviation can mostly be explained by the ambient temperature difference of $\approx$ 1500 °C.

6.5.4 Plasma infiltration of the green body

The results of Figure 6.6 and 6.7 demonstrate unequivocally that the presence of plasma within a green body is possible and that it can interact with the ceramic particles within it. This interaction was not observed without the plasma. The material transported to the surface must therefore have been sputtered from the powders by plasma within the pores of the green body. Although it is evident that the plasma does not lead directly to sintering, it will be shown in Chapter 7 of this thesis that changes to the surface chemistry of the powders have a beneficial effect on sintering during the subsequent stage of flash sintering, in which Joule heating increases the sample temperature (in the absence of a plasma) so that densification occurs. It is therefore important to understand the conditions required for this phenomenon.

The mean free path of $\approx$ 3 μm is larger than the pores in the green body (powder d_{50} = 0.3-0.6 μm), which suggests that sustaining the plasma independently within the green body would be difficult because only the short electron paths in the distribution would be available for ionisation. Such collisions would be fewer in

number and less energetic than those from the longer paths available outside the specimen. We suggest, therefore that the presence of the external plasma may be necessary to supply electrons and ions for the plasma to infiltrate the green body. This is supported by evidence shown in Chapter 7 of this thesis that the effects of the plasma in modifying the surface morphology and chemistry of the carbide powders were significantly more pronounced near the surface of the green body than in the centre of the cross section.

This being the case, it is not entirely clear why the depletion of the zirconia marker material was greatest in the centre of the sample (Figure 6.6 a). We tentatively attribute this to the temperature gradient within the green body: the hottest part of the system during the plasma stage was evidently the electrodes (Figure 6.1 b) and heat would have been conducted along the gauge length and lost at the surface, leading to a lower temperature there. The Joule heating of the sample would also contribute to higher temperatures at the centre of the cross section, even though it is relatively small during the plasma stage. Highly refractory ceramic constituents within the plasma would therefore be more liable to condense towards the cooler surface of the sample. The interesting morphologies of the deposits in Figure 6.7 are indeed consistent with vapour phase deposition.

The fact that the mean free path is longer than the gaps between adjacent particles in the green body explains why any field-focusing effect of the particles

would be ineffective in initiating a plasma in the gas between them (Section 6.5.1). Thermionic emission from the particles themselves and dielectric breakdown may be possible under some circumstances by field focusing near particle contacts, as has been thoroughly discussed by Holland et al. [276], but no experimental evidence of that was found in this work.

6.5.5 Collapse of the plasma

The power dissipated within the plasma and electrodes is an important indicator of whether a plasma can be maintained or not. If the power dissipated is high enough, sufficient electrons are being provided by the electrodes and ionisation processes to maintain the plasma as described in the Townsend criterion [168]. This correlation of plasma stability and power dissipated is also demonstrated by the increasing conductance with power shown in Figure 6.3 and 6.5. Conversely, decreasing the power density can lead to the collapse of the plasma. For the *plasma alone* experiments in Figure 6.3, for example, the plasma was found to collapse if the power dissipation in the plasma was reduced below 20 W.

In the presence of a ceramic sample, the electrical loading of the plasma and the sample is in parallel and most of the power is dissipated in the component with the higher conductance. Initially, comparison of Figure 6.1 a), 6.1 iia) (He atmosphere, no plasma) and Figure 6.1 b), 6.1 iib) (Ar atmosphere, with plasma),

shows that a plasma has a higher conductance than a B_4C green body so that plasma carries the bulk of the current. As time passes, however, the conductance of the sample increases and, for the sample in Ar, surpasses that of the plasma so that the majority of the power becomes dissipated in the sample and the plasma collapses. This occurs at stage (iii) in Figure 6.1 b), at a time of $\approx$ 13 s. The increase in conductance of the sample occurs because of (I) the gradual heating from the plasma (both direct and by thermal conduction from the electrodes, Figure 6.1iib), (II) the initial stages of sintering, which improves particle-particle contacts [25, 26], and possibly (III) because of the cleaning of oxide from the particle surfaces, as suggested by the sputtering effect demonstrated in Figure 6.6 and Figure 6.7, and direct observation in Chapter 7 of this thesis. A similar transition has been shown in other previous work [163, 164].

The same competition between plasma and sample explains why no plasma was seen in a He atmosphere under our conditions (Figure 6.1 a). The He atmosphere was able to withstand the initial voltage applied (50 V) without breaking down so all the current and therefore the electrical power was dissipated in the relatively low conductance green body.

6.5.6 Relevance to plasma formation in other field assisted sintering techniques

In the general perspective of FS, the results presented confirm that during FS of YSZ or other materials at lower temperature and atmospheres with higher VB, such as air or N_2, no plasma formation is involved under the conditions normally used and can be ruled out as a potential sintering mechanism. Also, plasma formation during SPS seems unlikely because usually a carbon die contains the powder and even if the powder is highly insulating, the die itself is sufficiently conductive to conduct the current and prevent the atmosphere from breaking down, which agrees with previously reported results [160].

Nevertheless, a change in atmospheric gas and pressure or the exclusion of a die, as in FSPS, might change the critical conditions for atmospheric breakdown and plasma formation. Furthermore, it should be considered that if a plasma formation happens it is most likely to happen within fractions of a second at the very beginning when an external field is applied. The rapid increase in conductivity on the initial application of the electric field observed in Figure 6.1 d) ($\approx$ 0.3 s) compared with Figure 6.1 c) ($\approx$ 3 s) is a good indication that a plasma is being formed since it is not controlled by the gradual heating and sintering of the green compact, as is the case in the absence of a plasma.

Another observation that could be an indicator of a plasma is the growth of large and well-structured crystals such as those in Figure 6.7 and Figure A.28 shown in the Appendix. The growth of crystals aligned with the electric field at surface cracks during FS of ZnO under a high current density was also reported by Zhang et al. [24] and was attributed to a potential liquid phase formation. However, since the hottest part of the sample during FS is the centre, and a crack would interrupt the local current flow, it seems unlikely that the surface region is melted, and the interior does not show such features. Plasma formation across the crack, which concentrates the field, provides an alternative explanation for the observed crystal growth.

7 | Effect of plasma formation on flash sintering and optimisation of process variables

7.1 Constant voltage-constant power tests

Figure 7.1 shows the electrical power dissipation against furnace temperature (T_f) with different applied electric fields whilst heating B_4C green bodies at a rate of 600 °C/h in an Ar atmosphere. As with many FS systems, a rapid increase in power dissipation occurred beyond a specific furnace temperature, which decreased with increasing applied field (*runaway* [5, 24, 182]).

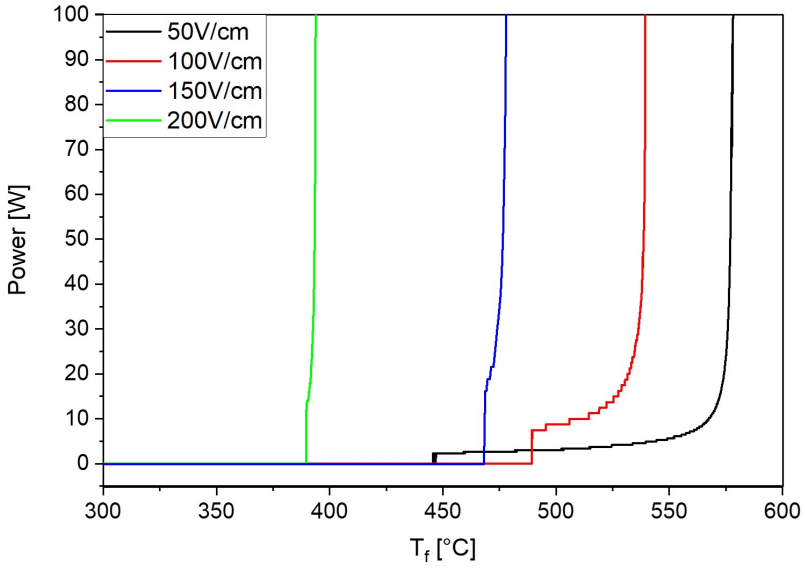


Figure 7.1: Power dissipation and runaway behaviour in boron carbide (B_4C) at various field strengths between 50 and 200 V/cm dependent on the furnace temperature (T_f).

The initial rate of power increase at the critical temperature also increased with increasing field. Note that the initial sudden step up in power dissipation originates from the lowest current (0.06 A) detectable by the power supply multiplied by the applied voltage.

Although these results show that FS is possible in principle at furnace temperatures that are very low compared with the usual sintering temperature, current concentration and hot-spot formation resulted in inhomogeneous heating and local melting of the material as previously reported for FS of carbides by other researchers [26, 134], even if the power dissipation limit was reduced to 100 W.

No plasma formation or other unusual phenomena occurred in these runaway experiments.

7.2 Isothermal flash sintering

Since the runaway experiments under constant electric field described above showed strong hot-spot formation, the effects of various processing parameters were investigated with isothermal flash sintering to improve densification of B_4C. This allowed FS to be conducted at a furnace temperature of 1500 °C, which was much higher than the runaway temperature in constant voltage experiments. This helped to avoid the localisation of heating.

7.2.1 Power dissipation limit

Power limits between 500 W and 800 W were applied during isothermal Plasma Pre-Treatment Flash Sintering (PPT-FS), described in Methodology section 3.2.3.2. Up to 700 W, density increased with power as shown in Figure 7.2 a). According to the BBR model a power dissipation of 700 W resulted in an estimated sample temperature of $\approx$ 2300 °C.

If a power dissipation of 800 W was applied the contact regions between sample and electrode deteriorated significantly and the isothermal FS-experiment failed. This is consistent with the predicted temperatures, which approached the melting temperature of B_4C [171] under such conditions ($\approx$ 2320 °C [284]).

7.2.2 C-foil wrapping

Figure 7.3 shows 4 wt.% C-containing B_4C-samples during the Joule heating stage of isothermal PPT-FS at 1500 °C and a power of 700 W without and with C-foil as thermal insulation.

In the latter case the straighter sample shape indicates a more homogeneous and improved densification of the sample, as is also confirmed by the density measurements which indicated a RD increase by more than 7%, (Figure 7.2 a). For this reason, the C-foil was used in the standard conditions, described in section

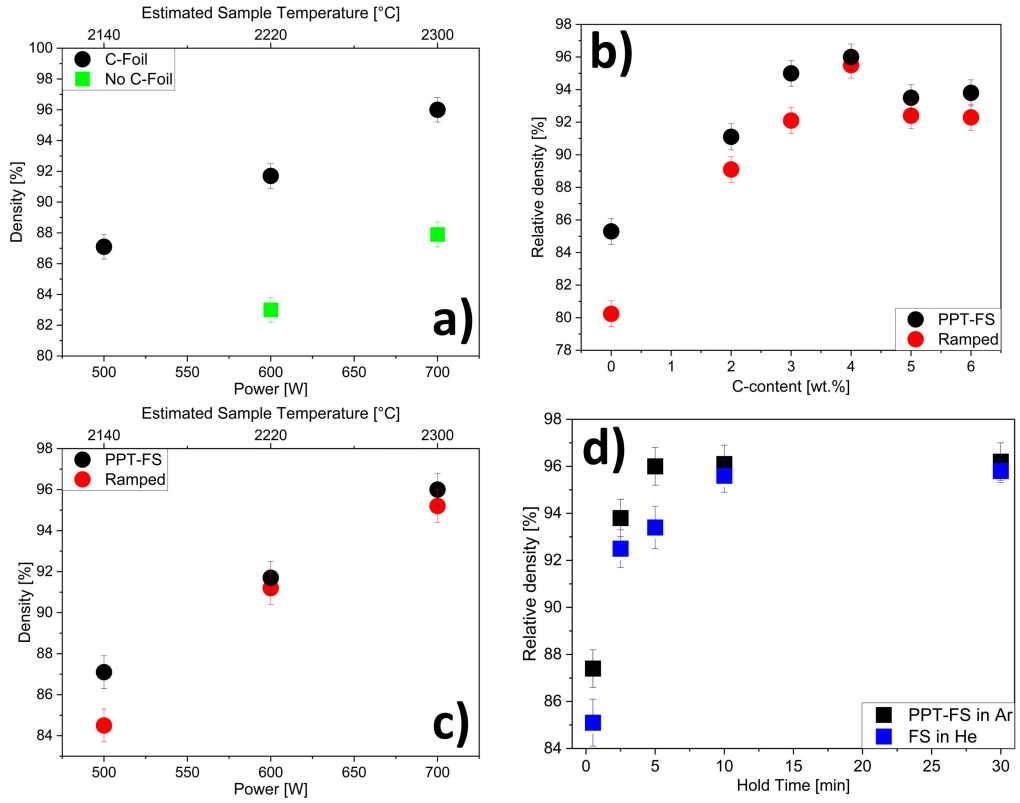


Figure 7.2: Measured relative density of (PPT-)FS B_4C dependent on a) presence of thermal insulation and power dissipation during PPT-FS with the estimated sample temperature shown on the top X-axis (estimated according to [20] without consideration of the thermal insulation); b) different heating approaches in Ar (PPT-FS or ramped) and C-content; c) heating approach in Ar and power dissipation; d) PPT-FS in Ar or FS-He and hold times between 30 s and 30 min after the application of maximum power (700 W). The standard conditions in the Methods section were used for unspecified experimental variables.

3.2.3.2.

Furthermore, the thermally insulating C-foil was significantly colder on the outside indicating that almost no current was flowing through the foil itself, which is confirmed by an equal conductivity with and without C-foil. Most of the heat generated within the sample was reflected back to it.

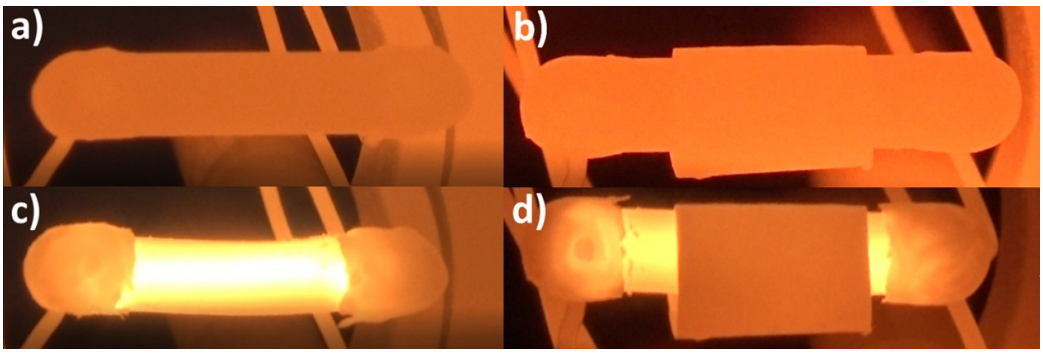


Figure 7.3: B_4C sample before and during the FS stage of PPT-FS, without (a and c) and with (b and d) a C-foil wrapped around the sample for reduction of heat loss by thermal radiation from the sample surface.

7.2.3 C-content

Figure 7.2 b) shows that even for the PPT-FS specimens, which gave the highest densities, the addition of C is essential for successful sintering. For the range of additional C investigated, the maximum density was achieved for a C-content of 4 wt.% after PPT-FS of B_4C and with thermal insulation (Figure 7.2 b). Note that residual C from thermal degradation of the 1 wt.% PVB binder during debinding was not included in these values since it is difficult to specify how much C remained. If PVB is seen as $[C_8H_{14}O_2]_n$, the maximum residual C content possible, is 0.67 wt.%.

According to the Raman spectroscopy results shown in Figure 7.4, unreacted C residues were present if the additional C-content exceeded 2 wt.%, particularly at the outside (O) of the cross-section. This is shown by the presence of the D- and G-Bands located at Raman shifts of $\approx$ 1350 and 1580 cm^{-1}, respectively. If

the content exceeded 4 wt.%, residual C could also be found in the cross-section halfway (M) between the sample centre (C) and the outside (O).

Beside the D- and G-Bands of unreacted C, all the major peaks in the Raman spectra can be associated with B_4C [285]. In particular, the well-defined and narrow Raman peaks at 481 and 534 cm^{-1} are representative of B_4C with a well-ordered C-B-C chain in the stoichiometric B_4C-crystal containing 20 at% C [286].

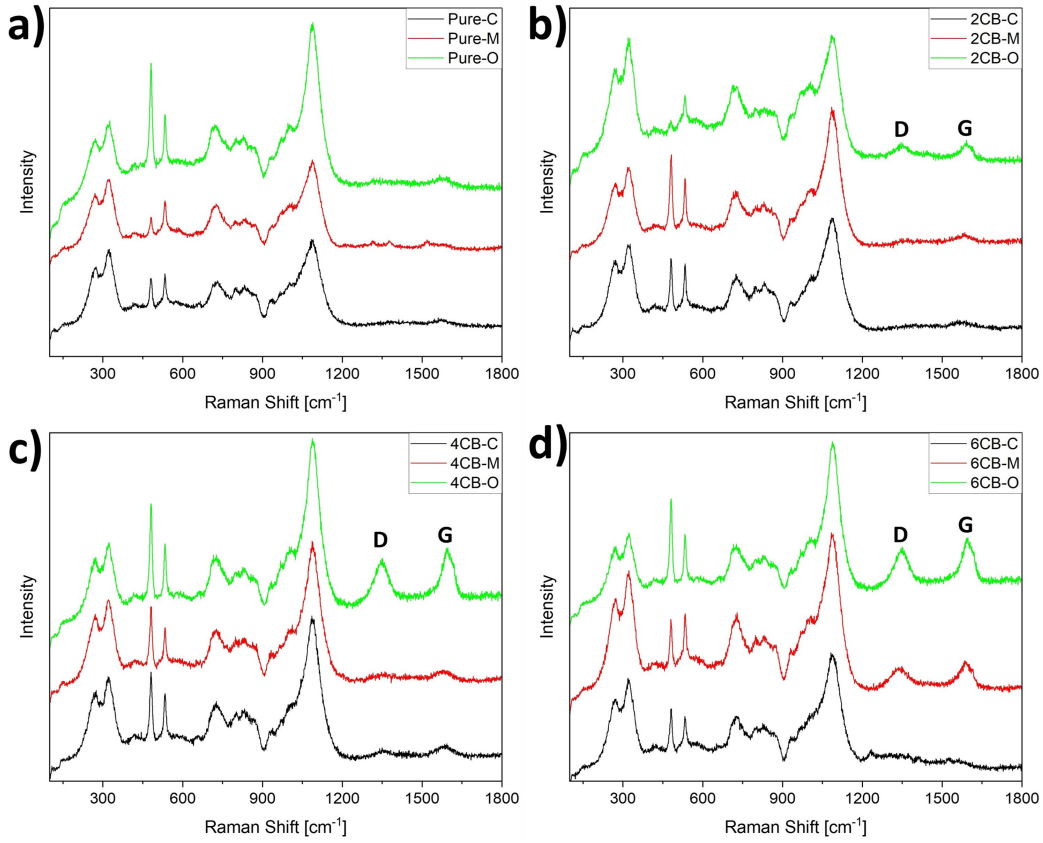


Figure 7.4: Raman spectra taken from the centre (C), between the centre and the outside (M), and outside (O) of PPT-FS B_4C cross sections with a) no additional carbon black (CB); b) 2 wt.% CB, c) 4 wt.% CB and d) 6 wt.% CB. Residual CB can be observed in the D and G bands at Raman Shifts of ≈ 1350 and 1580 cm^{-1}.

7.2.4 Heating rate and initial presence of plasma

The heating rate with the PPT could not be varied in isolation because the switch from electrical conduction through the plasma, with minimal sample heating, to conduction through the sample, resulting in rapid Joule heating to the sintering temperature, depended on the properties of the plasma and the sample rather than directly controllable experimental variables.

However, the results for the power ramped samples and FS-He samples in Figure 7.2 b) and d) allow a comparison between different heating rates in the absence of the PPT, because the gradual increase in power in the ramped tests avoided the initial formation of plasma and the high breakdown strength of He prevented plasma formation in the FS-He samples. However, the ramped samples took up to 7 minutes to reach the maximum temperature under electrical heating, whereas the FS-He samples took only a few seconds, shown in the previous chapter. The 4% C ramped result in Figure 7.2 b) and the 5 min FS-He result in Figure 7.2 d) were obtained under the same conditions apart from the heating rate (and inert gas in the atmosphere) and the ramped sample had a slightly higher RD (95.4%) than the much more rapidly heated FS-He sample (93.3%).

The plasma-free FS-He samples, which experienced comparable heating rates to those for PPT-FS in Ar as shown in the previous chapter, displayed a significantly

lower RD for all applied hold times (Figure 7.2 d), showing that the PPT was beneficial to sintering. All PPT-FS samples also gave higher densities than the slowly heated ramped samples for all C contents and power levels (Figure 7.2 b-c). The difference was stronger at shorter hold times, particularly up to a hold time of 5 min.

7.2.5 Hold time

A significant increase in RD for PPT-FS in Ar was seen as hold time increased up to 5 min (Figure 7.2 d). Since longer hold times could lead to sample or setup failure and material degradation but did not yield an improvement in density, 5 min hold time was determined as ideal. The FS-He samples without plasma formation took twice as long as this to reach their maximum density.

Based on the above results, the ideal FS conditions for B_4C are 1500 °C T_f, instantaneous application of maximum electric field in Ar to form a plasma (PPT-FS), power dissipation of 700 W, 4 wt.% carbon additives, 5 min hold time, and C-foil wrapped around the sample for thermal insulation.

7.3 Hardness

If the optimum conditions (PPT-FS in Ar at 1500 °C, 700 W power dissipation, 5 min hold time, 4 wt.% additional C, and thermal insulation) were applied so that

a sample density of 96 % was achieved, a hardness (HV1) of 31 $\pm$ 0.2 GPa was measured.

7.4 Microstructure

7.4.1 PPT-FS samples

SEM images of a fractured cross section of a 96 % dense B_4C sample processed under the optimum conditions can be seen in Figure 7.5 at various magnifications. The majority of the pores are located along the grain boundaries with a minor number of intra-granular pores (Figure 7.5 b). Some of the pores are filled with unreacted carbon, confirmed by EDS and highlighted with a white arrow in Figure 7.5 c).

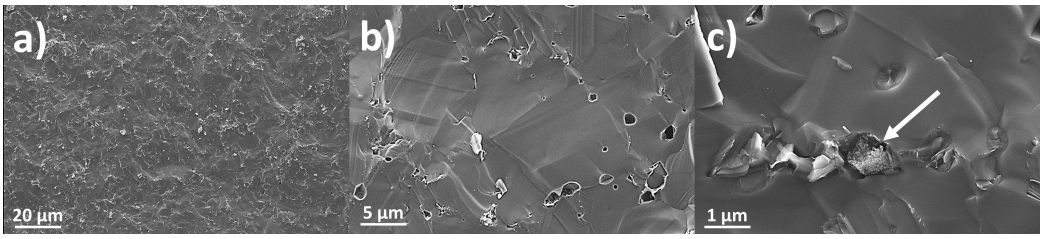


Figure 7.5: SEM images at various magnifications of a fractured cross section of a 96 % dense B_4C sample containing 4 wt.% additional carbon, densified by PPT-FS for 5 min at 1500 °C T_f under a power dissipation of 700 W including thermal insulation; a) shows the overall fractured microstructure; b) a more detailed section showing the major porosity along the grain boundaries with some minor intragranular porosity; c) shows unreacted carbon within the B_4C matrix.

Microstructures of the centre of polished PPT-FS B_4C densified to 87 % and 96 %

RD are shown in Figure 7.6 a) and b), respectively. The SEM images show that small pores disappear during densification, whereas the bigger pores in the range of several μm coarsen and remain. This can also be seen in the SEM images showing the 96 % dense microstructure at various other magnifications (Figure 7.6 c-e). As already mentioned for the fractured cross section shown in Figure 7.5, some of the bigger pores contain(ed) unreacted carbon. This can be seen by the fine carbon structures, also confirmed by EDS, contained in the big $\approx$ 25 μm pore shown in Figure 7.6 f). SEM images of other regions of the 96 % RD PPT-FS sample, shown in Figure 7.7 show that the density first decreases slightly in moving outwards from the centre, which is usual for flash sintering because of the through-thickness temperature gradient. However, there is also a dense layer of up to 0.5 mm thickness at the surface, which is unusual in conventional FS.

To reveal the grains, an EBSD-pattern quality map and a forescattered electron image of 96 % dense PPT-FS B_4C can be seen in Figure 7.6 g) and h). The grain size in the centre of the sample was 8.0 $\pm$ 0.6 μm and almost all grains show several well-defined twins.

7.4.2 Plasma-free samples

The FS-He 93 % dense microstructure produced under otherwise standard conditions (Figure 7.8) shows a bimodal pore distribution, including the several mi-

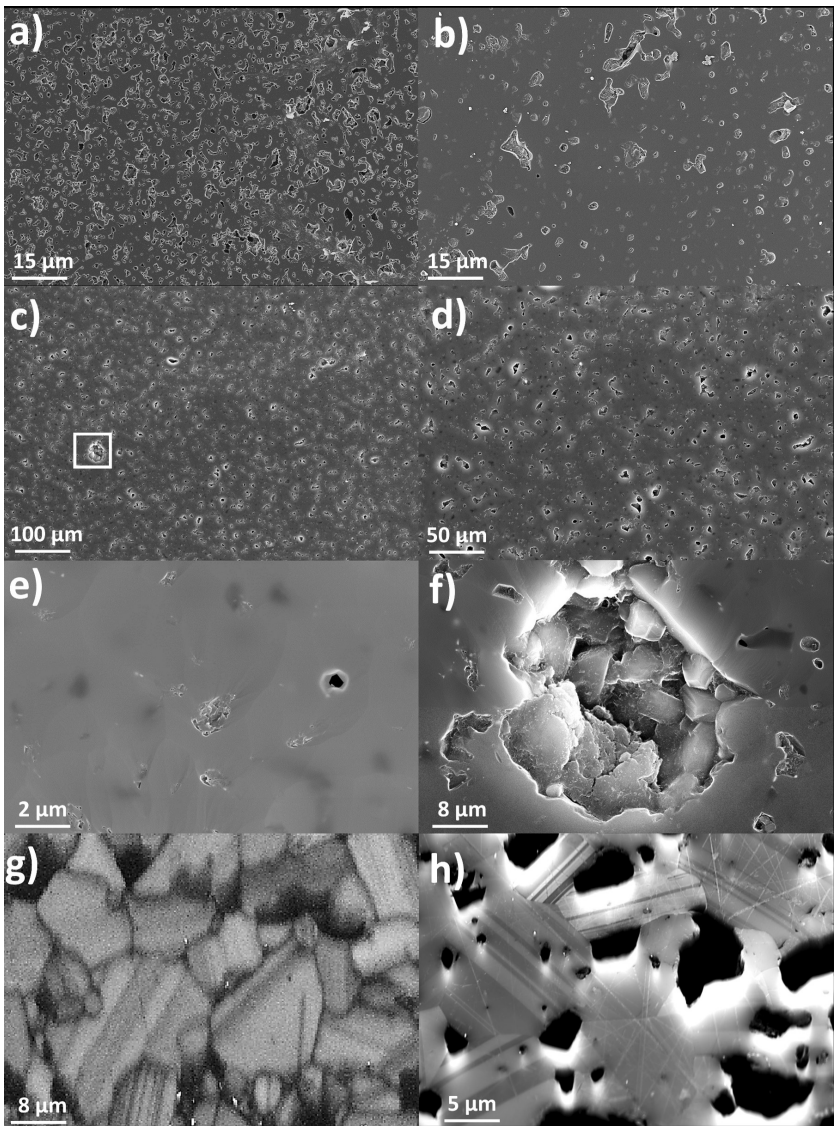


Figure 7.6: Polished microstructure of the cross section of: a) 87 % dense and b) 96 % dense thermally insulated PPT-FS B_4C-samples containing 4 wt.% C, densified at 1500 °C T_f for 5 min by power dissipation of 500 W and 700 W, respectively; c)-e) show the 96 % dense polished microstructure at various magnifications; f) shows a more macroscopic pore which is highlighted in c); g) EBSD-pattern quality map visualising grain structure and twinning; h) shows a forescattered electron image of the microstructure, including some non-diffracting regions (black).

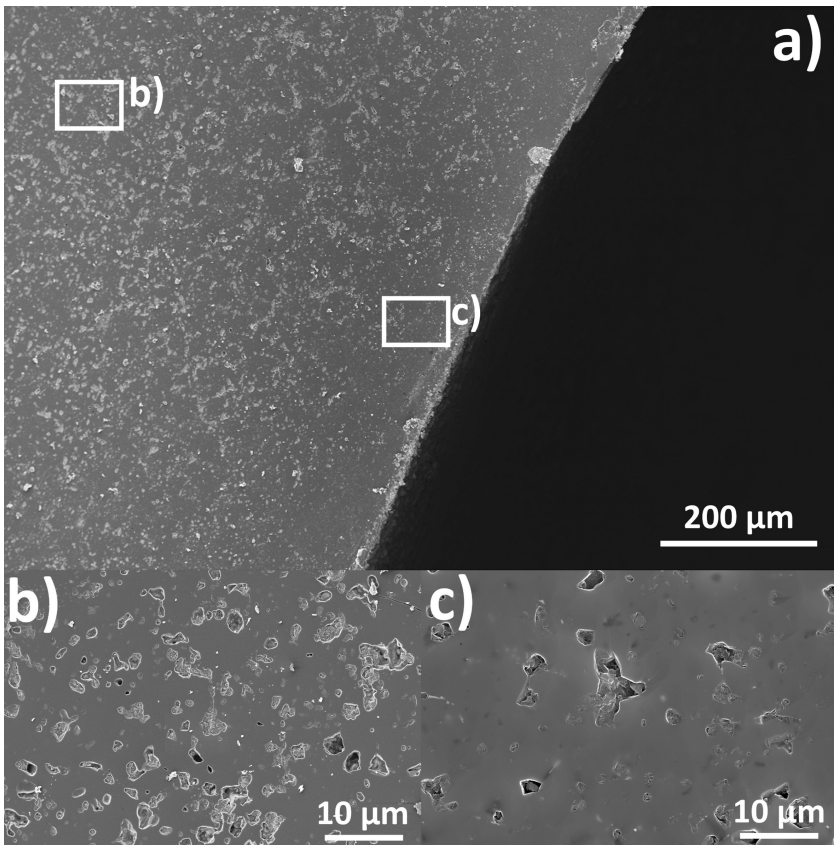


Figure 7.7: Polished microstructure of B_4C PPT-FS in Ar in the outer region of the sample at various positions and magnifications. Hold time 5 min, 700 W power dissipation applied from the beginning, 4 wt.% C-content and C-foil wrapped around the sample.

crometre intergranular pores present in the PPT-FS samples but also a greater population of submicron intragranular pores.

The plasma-free samples also had larger grain sizes than the corresponding PPT-FS samples, particularly for the power-ramped samples, as is summarised in Table 7.1.

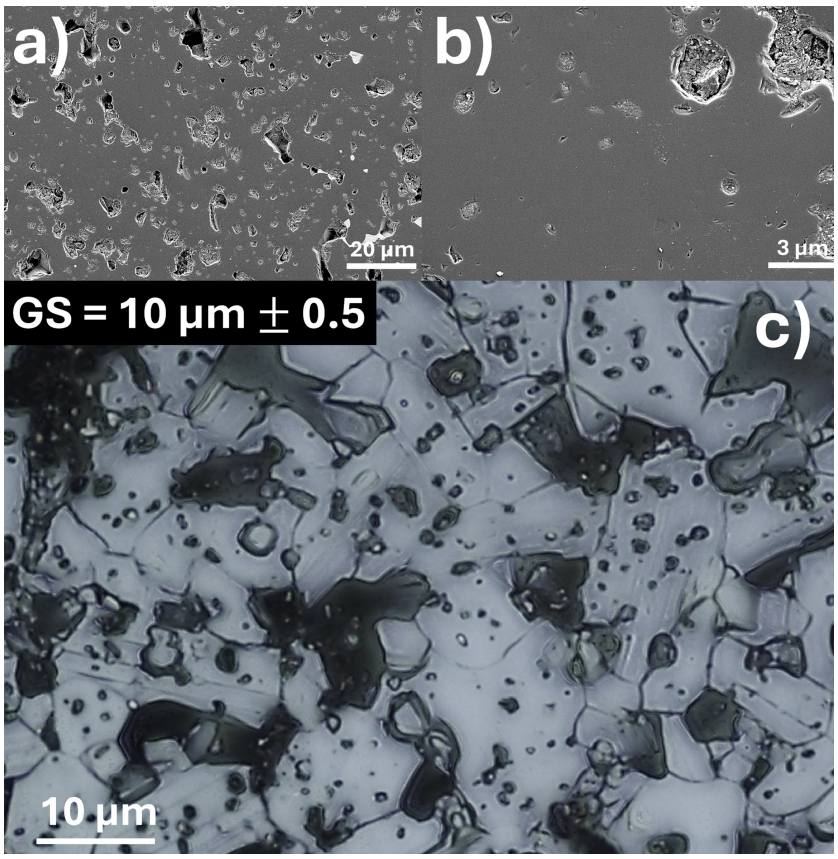


Figure 7.8: Polished (a and b) and etched (c) microstructure of 93 % dense B_4C flash sintered in He without initial plasma formation. Hold time 5 min, 700 W power dissipation applied from the beginning, 4 wt. % C-content and C-foil wrapped around the sample.

7.5 Influence of plasma on boron carbide particles

According to the results in Section 7.2.5, a plasma pre-treatment stage prior to Joule heating is beneficial for the densification of B_4C. The effects and the influence of plasma on the microstructure and chemistry of the B_4C are investigated in the following section.

Table 7.1: Grain sizes produced and relative density resulting from different flash sintering conditions.

FS conditions	relative density [%]	grain size [μm]
PPT-FS	96	8.2 $\pm$0.6
FS-He	93	10.2 $\pm$0.5
Ramped Power	95	14.8 $\pm$0.7

7.5.1 Plasma induced change in surface morphology

The morphology and structure of B_4C particles before and after the pre-treatment plasma stage in Ar, which was stopped after a plasma formation of 12 s, just before the plasma would most likely collapse according to the results from the previous chapter, is shown in Figure 7.9.

The particles before the plasma treatment (Figure 7.9 a) and b) show a rather smooth surface. After the plasma treatment the particles in the centre of the sample cross section (Figure 7.9 c) and d) show a slightly roughened surface, and this surface roughening is much more pronounced for particles near the surface of the B_4C-sample (Figure 7.9 e) and f).

Beside the roughened surface of the particle, no sign of densification is observed in this stage of PPT-FS.

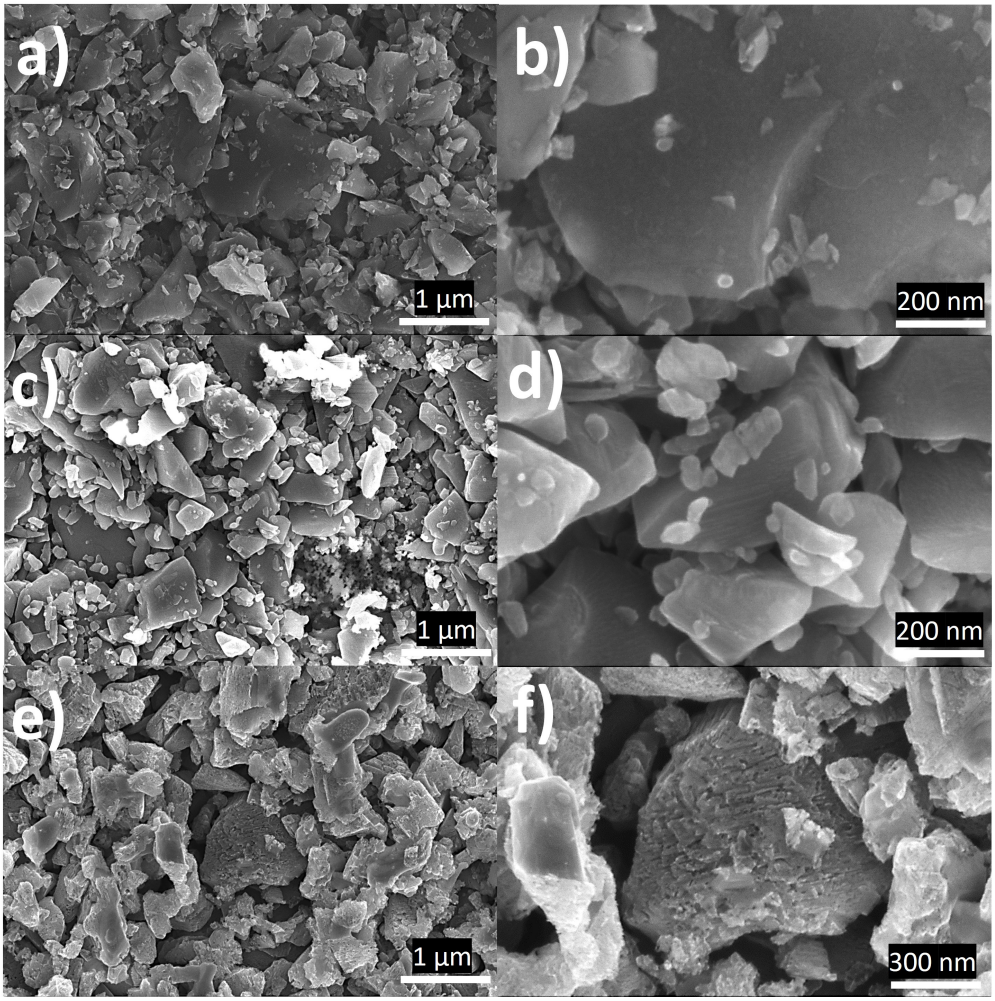


Figure 7.9: Boron carbide particles before (a and b) and after plasma pre-treatment stage during PPT-FS; c) and d) show particles in the cross section of the sample; e) and f) on the surface.

7.5.2 Plasma induced change in surface chemistry

The plasma induced change in surface chemistry was investigated by XPS on various samples, which were treated under various conditions, summarised in Table 7.2.

Table 7.2: Sample description and processing parameters for the samples investigated by XPS. *Temp.* represents atmospheric temperature, *C-add.* carbon additives, *Pl.Ch.* plasma chamber, *PPT* pre-treatment plasma, *PPT-FS* pre-treatment plasma flash sintering, *SU* surface, and *CS* cross section. P represents powder (compacts), prior to densification. Densified samples are labelled with D.

sample	Temp. [°C]	C-add.	Pl. Ch.	PPT	PPT-FS	SU	CS
P	20						
P-1500 °C	1500						
P-C-1500 °C	1500	X					
P-C-PlCh	20	X	X				
P-C-PPT-Su	1500	X		X		X	
P-C-PPT-CS	1500	X		X			X
D-C-PPT-FS-Su	1500	X			X	X	
D-C-PPT-FS-CS	1500	X			X		X

Figure 7.10 a) shows the XPS survey scan for each of the samples in a BE range between 0 and 1050 eV. Some significant differences can be observed. The most important are shown in separate graphs as follows.

Figure 7.10 b) shows the core-level spectra for B 1s in more detail for all samples, showing two different peaks around 187.5 eV and one around 193 eV. The peak around 187.5 eV can be deconvoluted into two single peaks representing two different kinds of bonding interactions as will be elaborated later.

Figure 7.10 c) shows the core-level spectra for C 1s suggesting the presence of

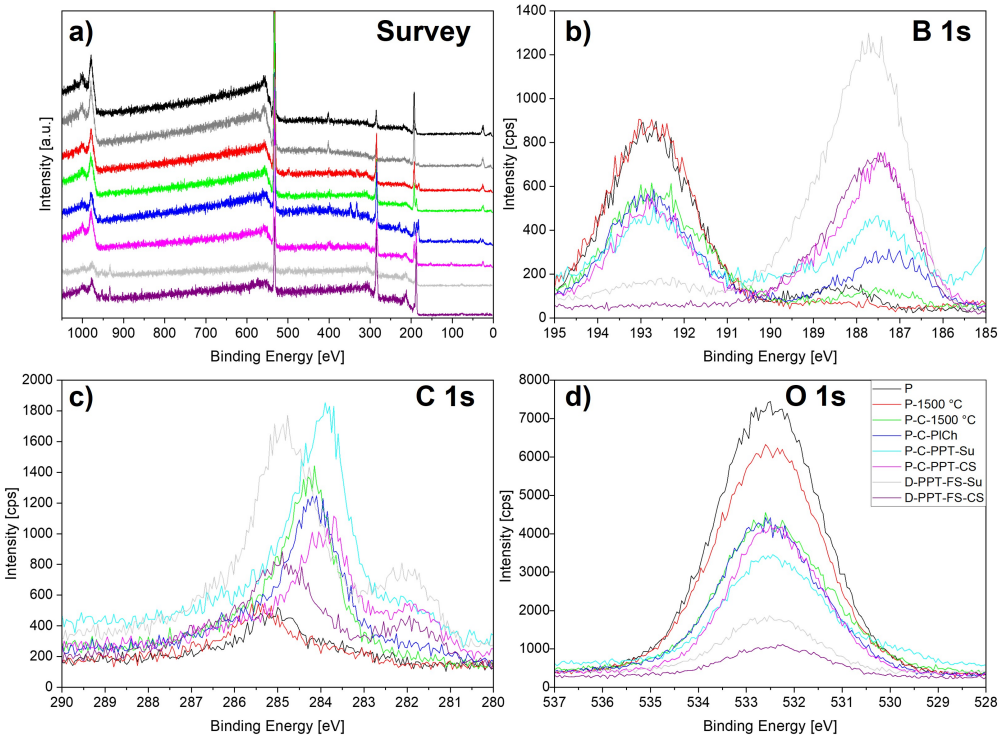


Figure 7.10: a) XPS Survey; b) B 1s; c) C 1s and d) O 1s region of the XPS signal of various B_4C samples with and without plasma and heat treatments. The legend applies to all panels.

multiple peaks. Samples P-C-PPT-Su and D-PPT-FS-Su (sample nomenclature is summarised in Table 7.2) show the most intense signal in this range.

The O 1s spectrum as depicted in Figure 7.10 d) is most intense for the pristine powder (P), followed by that for the heat-treated powder compact without additional C (P-1500 °C). The least intense O 1s spectra was obtained in the middle of the dense flash sintered sample (D-PPT-FS-CS). Since some samples are less dense than others and the flatness of the characterised surface varies, direct comparison of the spectra from one sample to another should be treated with caution.

However, the spectra provide a basis for binding environment for different elemental species and their quantification within the same sample.

From the B 1s spectra the potential presence of B_2O_3 can be inferred from the peaks obtained at BE characteristic of B-O bonds, and of boron carbide (B_4C) from peaks characteristic of B-C and B-B bonds. The deconvoluted B 1s XPS spectra in Figure 7.11 show that the pristine powder (Figure 7.11 a) contained predominately B-O bonds, whereas, for dense samples after PPT-FS the peak characteristic of B-O is less intense and barely present at all in the cross-section (D-PPT-FS-CS).

To highlight the changing ratio of B_2O_3 to B_4C, the peak area ratio of the B-O peak (blue area in Figure 7.11) to the combined B-B/B-C peak (green and red area in Figure 7.11) was calculated and is shown in Figure 7.12. Based on the XPS-results, a ratio of 10 is calculated for the pristine powder (P). If no C was added and the green body powder compact was heated to 1500 °C in Ar (99.998 % pure), this ratio increased by almost 10 times (P-1500 °C), whilst in the presence of additional C it remained almost the same (P-C-1500 °C). After a plasma cleaning treatment at room temperature for 30 min, the ratio decreased by 80 % (P-C-PlCh) and decreased even more if treated by the plasma during the pre-plasma stage of FS (P-C-PPT-Su and -CS). The lowest ratios were in the PPT-FS samples, especially the cross section (D-PPT-FS-CS), which had a ratio of 0.05.

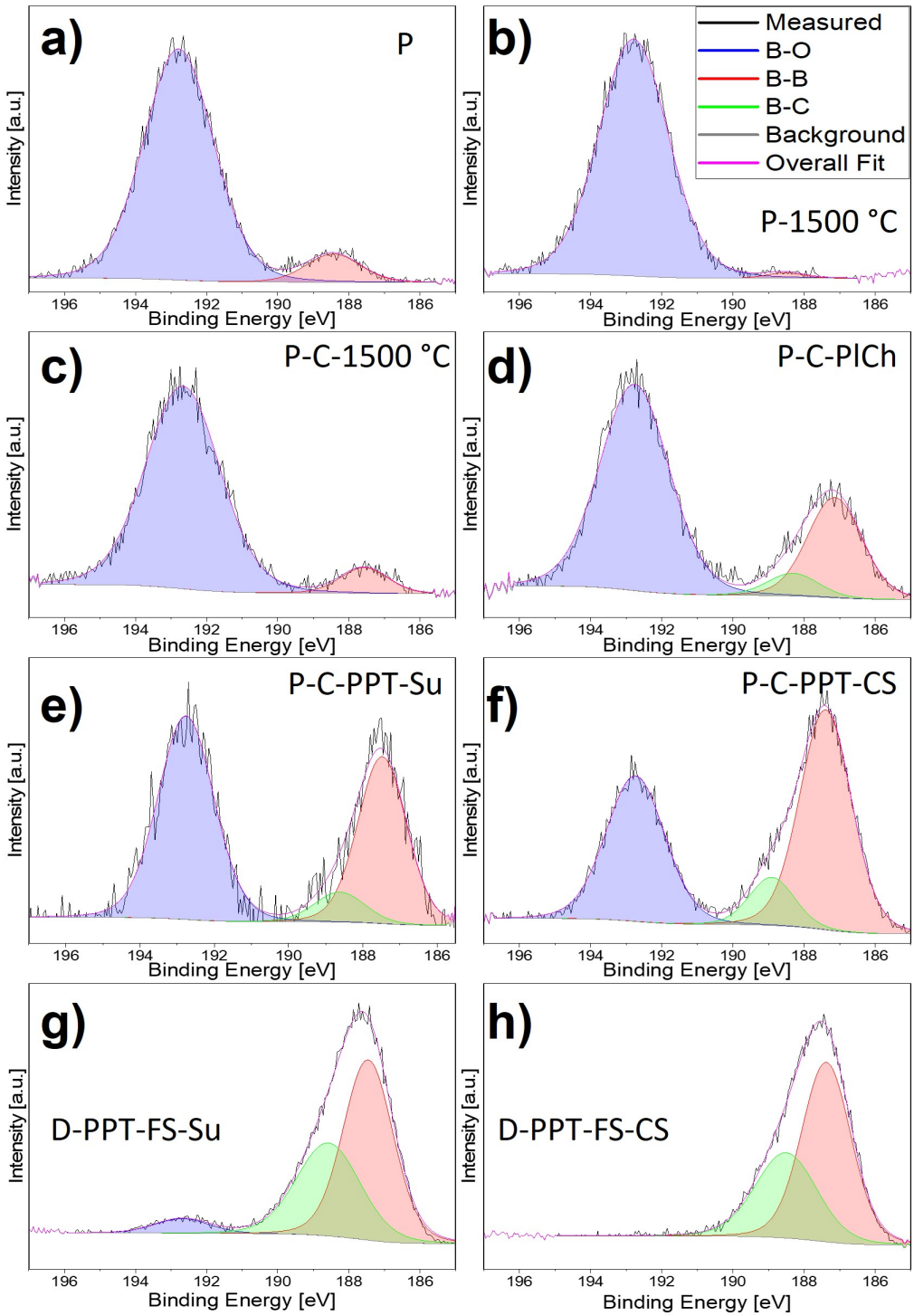


Figure 7.11: B 1s region of the XPS spectra taken from samples treated in various ways prior to the characterisation. The B 1s is deconvoluted into B-O (blue), B-B (red) and B-C bonds (green). The legend applies to all panels.

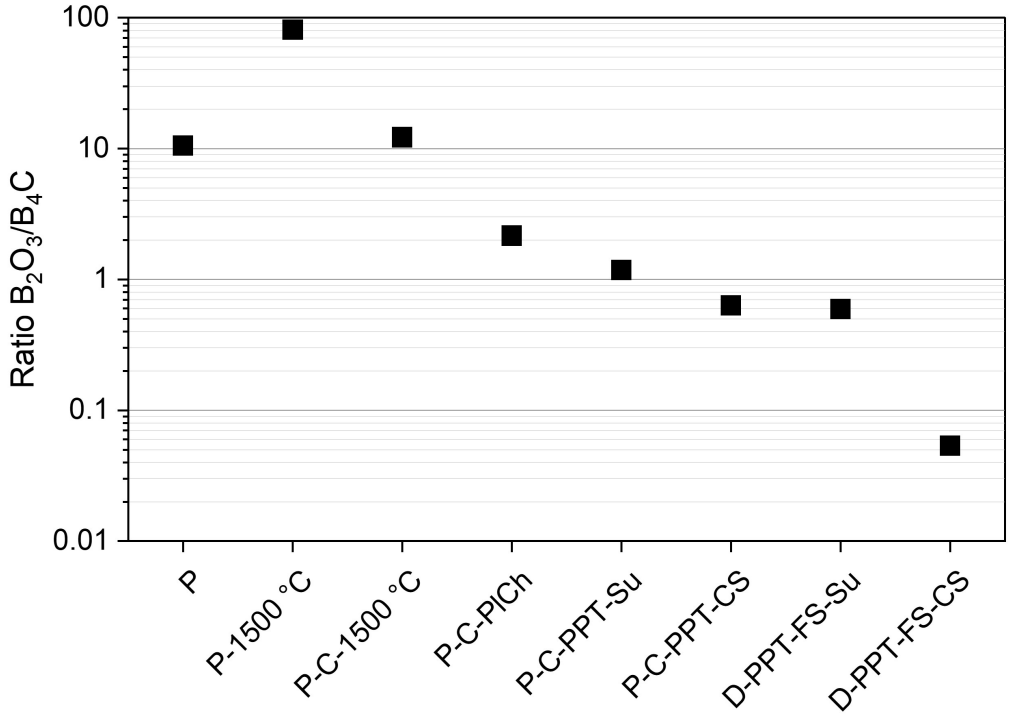


Figure 7.12: B_2O_3 to B_4C ratio of various samples calculated based on the deconvoluted B 1s XPS signal.

7.6 Discussion

7.6.1 Boron carbide runaway behaviour at low furnace temperatures

B_4C is a semiconducting material with a bandgap of 2.09 eV [285, 286, 287, 288, 289]. Thus, it is not surprising that the B_4C green bodies subjected to moderate temperature and electric field were able to exhibit a rapidly increasing current. This thermal runaway is associated with the NTC resistivity expected of a semiconductor [5, 24]. However, when combined with the temperature gradients associated with the thermal emissions from the electrically heated sample as shown in chapter 4 of this thesis and [9] to the cooler furnace atmosphere, such conditions are also known to lead to the current concentration in the sample centre observed here and by Rosenberger et al. [134], such that uniform densification cannot be achieved. The more severe localisation seen by Rosenberger et al. [134] may be a consequence of their thicker samples and lower furnace temperatures on this basis.

Other factors such as improving particle-particle-contacts during densification, and the removal or breakdown of oxide layers between the particles, can also be the origin of current localisation in carbides. In contrast, electrochemical reduc-

tion, which is known to influence current localisation during FS of oxide ceramics such as YSZ as shown in chapter 5 of this thesis and [146], is not known to such an extent in carbides, and is therefore a less important factor in FS of SiC and B_4C.

The results are also consistent with previous work on SiC which has a higher bandgap between 2.3 and 3.3 eV [290, 291] depending on its phase. SiC shows a rapid increase in current around 800 °C if a field of 40 V/cm is applied [26], which is $\approx$ 200 °C higher than observed here for B_4C. As in our results on B_4C, attempts to FS SiC [26] with a low furnace temperature (1032 °C) also resulted in insufficient overall densification of the material (78 %).

We conclude that there is an inherent limitation in using FS for semiconducting carbides at low environmental temperatures (< 1000 °C) because the great difference with the temperature required for sintering such ceramics (> 2000 °C) leads to high temperature gradients between the centre of the cross-section and the edges, which are exacerbated by localisation of the current.

7.6.2 Factors affecting sintered density

7.6.2.1 Specimen heating: influence of furnace temperature and C-foil insulation

The use of a higher furnace temperature (1500 °C) in isothermal FS was successful in suppressing localisation of the heating sufficiently for high densities to be achieved. This is also consistent with previous work on FS of SiC [26]. This furnace temperature is 700-800 °C below the temperature for conventional sintering of these carbides and allows the use of less expensive equipment, saves a substantial amount of energy, and leads to significantly shorter heating and cooling times.

The presence of the C-foil is also beneficial to RD (Figure 7.2 a). At such high temperatures, radiation is the primary mechanism of heat loss and the relatively low temperature of the foil apparent in Figure 7.3 d) indicates both that the foil is not acting as a short circuit for the current and also that it was effective in reflecting much of the thermal radiation from the sample back towards it. Not only did this reduction in surface heat loss lead to more uniform heating, as noted in Section 7.2.2, but also it would increase the specimen temperature for a given power, enabling better sintering without degradation of the electrodes (Section 7.2.1). This improvement of densification with thermal insulation agrees with

previous work on FS of 8YSZ [292].

In the situation where the small amount of oxygen in the flowing Ar atmosphere, or oxygen diffusion through the alumina tube, is able to oxidise the B_4C, as is discussed in more detail in section 7.6.2.3, an additional benefit of the wrapping may be a further suppression of the oxidation, by shielding the sample from direct impingement of the flowing Ar and reduction of atmospheric oxygen, where the presence of solid carbon in the vicinity of flash sintering SiC samples was found to be critical in optimising the density. Given the presence of several other controls on oxidation, however, we suggest that the main benefit of the wrapping on sintered density seen in Figure 7.2 a) is through its intended purpose of thermal management.

7.6.2.2 B_2O_3 I: Effect of heating rate and C additions

The use of C additives in sintering B_4C is well known but one factor that distinguishes FS from conventional sintering is the high sample heating rate. The variation of the electrical results in chapter 6 shows that the final stage of heating from close to the furnace temperature of 1500 °C to the sample sintering temperature of $\approx$ 2300 °C occurs over a similar time scale of $\approx$ 3 s for both FS in He and PPT-FS in Ar, with the only difference being the pre-plasma stage in PPT-FS, during which sample heating was limited. This gives an estimated heating rate of

up to 270 °C/s, or 16000 °C/min. The ramped sample heating rates were much slower at ≈ 150 °C/min.

The findings of Dole et al. [35, 36, 37] provide a useful starting point for the discussion of the effect of heating rate and C-addition. These authors found that the main problem with conventional sintering of undoped B_4C is that the presence of B_2O_3 on the surface of the powder particles leads to rapid coarsening in a temperature range around 1800 °C, which subsequently prevents the attainment of high density when the sintering temperature (2250 - 2300 °C) is reached. Two solutions were investigated.

The first was to increase the heating rate used from 30 °C/min to ≈ 300 °C/min [37]. This minimised the time spent in the coarsening temperature range and enabled densities of up to 90 % to be achieved, though coarsening still prevented the attainment of higher densities. All the FS results in this work, with their even higher heating rates should also have benefitted from this "fast firing", which is also well known in other ceramics, in which different low temperature coarsening mechanisms can operate [31, 32, 33, 34, 38, 44]. Figure 7.2 b) shows that even with their very high heating rate, the PPT-FS results for samples with no added C only reached 85% RD, so as for the results of Dole et al., any effect of high heating rate on its own was limited.

Taken at face value, the comparison of the power ramped and FS-He samples

with otherwise identical sintering parameters (section 7.2.4) suggests that in fact slower heating is advantageous, at least in the absence of a plasma. However, the ramped samples spent much longer at high temperature than the FS-He samples owing to their slow heating rate and is the probable reason for their slightly higher sintered density. Although "slow" in the context of the present work, the ramped heating rate of 150 °C/min is towards the higher end of those investigated by Dole et al. and while the grain size was higher than for the FS-He samples (Table 7.1), the ramped heating rate was evidently sufficient to avoid the worst effects of coarsening during heating.

The other, more effective solution to the coarsening problem advocated by Dole et al. was to remove the B_2O_3 by adding C to carbothermally reduce it. This was also effective in our work and a reduction of B_2O_3 content by almost an order of magnitude of powders heated to 1500 °C on adding C was confirmed by XPS (Figure 7.12). The optimum amount of 4 wt.% C is similar to previous reports of conventional pressureless sintering of B_4C [293, 294, 295, 296, 297, 298], as is the observation of unreacted, C-filled porosity, even with the optimum C content (Figure 7.6) [36, 37]. This is a consequence of the difficulty in dispersing the CB homogeneously. However, the higher C content nearer the surface (Figure 7.4) is peculiar to FS and is attributed to the lower temperature there due to heat loss from the surface and possibly to the increased plasma activity there, as is discussed in

section 7.6.2.3. The observed increase in C throughout the specimen beyond the optimum amount required to remove the B_2O_3 is presumably responsible for the accompanying decrease in sintered density.

7.6.2.3 B_2O_3 II: Effect of plasma

The PPT-FS method developed in the present work adds a further solution to the B_2O_3 problem: removal by plasma treatment. Plasma pre-treatment at 1500 °C reduced the B_2O_3 content by a further order of magnitude compared with a carbon-containing green body (Figure 7.12) and led to clear improvements in subsequent sintering under all conditions (Figure 7.2 b-d). It is notable that the lowest B_2O_3 content of all investigated samples is detected in the interior of the fully PPT-FS B_4C which supports the assumption of the plasma induced elimination of the B_2O_3.

This treatment was more effective in removing the B_2O_3 than the commercial plasma cleaner applied at room temperature (P-C-PlCh, Figure 7.12) and importantly, removed it immediately before heating to the sintering temperature on the collapse of the plasma. The significance of this is that simply heating the powder to 1500 °C in Ar led to nearly an order of magnitude increase in oxide (Figure 7.12), so the efficacy of room temperature pre-treatments in improving sintered density is expected to be limited. The continual oxidation of the B_4C particles

during sintering may be the reason that C additions are still required for high densities to be achieved (Figure 7.2 b).

The additional benefits of the plasma pre-treatment enabled a RD of 96 % to be achieved with a hold time of only 5 min at a nominal sample temperature of 2300 °C. For comparison, the FS-He samples in Figure 7.2 d) required 10 minutes to attain their slightly inferior maximum density, and the similar maximum RD of 97 % achieved using conventional heating at the same temperature in [37] used a much longer hold time of 30 minutes.

A comparison of the grain sizes for the PPT-FS and FS-He samples in Table 7.1 confirms that part of the advantage of removing the B_2O_3 immediately prior to densification was that the grain size was almost 25 % larger without the PPT, as expected from the work of Dole et al. [37]. In addition, the FS-He microstructure in Figure 7.8 includes many submicron intragranular pores, which were not seen to such an extent in PPT-FS B_4C. Dole et al. also suggested that the presence of intragranular pores can be explained by evaporation and trapping of B_2O_3 from the surfaces of the powder particles during rapid densification, adding a further benefit from its removal before sintering.

The removal of oxide layers by similar plasmas is well known [167, 169]. One established example is the cleaning and etching process of silicon (Si) wafers to reduce the oxidised layer of the material and improve its properties for further pro-

cessing steps. In the context of sintering, a potential cleaning effect by a plasma was also suggested during (F)SPS of ZrB_2 and W [160].

Chapter 6 of this thesis demonstrated the ability of the plasma pre-treatment to sputter marker material (zirconia) from within the powder compact, which was not seen during FS in He, i.e. without the initial plasma formation under otherwise comparable circumstances, and the same process is presumed to be responsible for the removal of the B_2O_3. Indeed, the etching of the particle surfaces by the plasma is evident in Figure 7.9. The fact that the etching is much more pronounced near the surface than in the centre of the green body supports the conclusion made in chapter 6 that the plasma cannot be sustained independently within the green body because the pores are too small to allow sufficient acceleration of the electrons. Instead, charged particles must enter the green body from the external plasma around it, explaining the maximum etching near the surface. The effect of a higher plasma activity and removal of B_2O_3 near the surface of the sample is also the most likely reason for the dense layer on the outside of the sample after PPT-FS, as shown in Figure 7.7. It may also contribute to the high C levels near the surface of the sintered sample, as the removal of B_2O_3 by the plasma would prevent it from reacting with the C additive.

7.6.3 Hardness of PPT-FS boron carbide

The grain size of 8 μm for the optimum conditions is at the upper end of the range reported in the literature for B_4C pressurelessly sintered to similar densities with C as a sintering aid [299]. This indicates that the rapid sintering in PPT-FS of C-doped B_4C is accompanied by equally rapid grain growth so that finer grain sizes than are possible with conventional sintering are not produced.

Nonetheless, our hardness (HV1) of 31 GPa for the 96 % dense samples is exceptionally high for B_4C pressurelessly sintered with carbon as the sintering additive. Zorzi et al [300], for example, report a value of only 19.3 GPa for 1 kg Knoop hardness of B_4C-4%C pressurelessly sintered to 97.7 % dense. It is difficult to establish the reasons in this case because no microstructural information is available in [300]. Roy et al. [301] used similar additives to this investigation and achieved a hardness (HK100) of 24-25 GPa for a 90 % dense pressurelessly sintered sample, which is also hard to compare due to the significantly lower density, missing grain size and difference in hardness testing procedure.

Gubarevich et al. [302] achieved a hardness (HV3-10) of 30 GPa for $\approx$ 95 % dense B_4C without additives and a grain size ranging from 3.7 - 10.3 μm, which is comparable to the values achieved here. The material in [302] was densified via rapid pressureless densification with electromagnetic induction assistance, an-

other method of rapid heating.

It should be noted that similar hardness values to ours have been reported in pressurelessly sintered B_4C with other additives [299, 303, 304, 305, 306], but some of these hardness tests were performed by micro- or nano-testing in which the significantly lower loads would give a higher hardness because of the indentation size effect.

A reliable comparison with SPSed material is available, however. Moshtaghioun et al. [307] found a similar hardness to ours of HV1 = 33 GPa for 99.2 % RD B_4C with a grain size of 17 μm. Moshtaghioun et al. [307] argue that the twin spacing may give a better indication of Hall-Petch-type hardening than the grain size. The ability of the PPT-FS process to produce such hard material may therefore be related to the twinning observed in Figure 7.6.

Twinning is known to develop mainly at low temperature and to anneal out at high temperature [308] and is common in B_4C because of its low stacking fault energy [309, 310, 311, 312]. The short sintering times with PPT-FS and SPS may enable the twinning, and the increased hardness that accompanies it, to be retained to a greater extent than in slow, conventional sintering where it may have time to anneal out. However, this matter needs further investigation.

8 | Conclusions

8.1 Flash sintering and electrical loading of (stabilised) zirconia

Optical spectroscopy of the light emitted during flash sintering of YSZ showed that the observed spectra can fully be explained by the thermal radiation of the sample under electrical load if the response and influence of the optical setup is considered. This includes absorption by all components included, such as optical lenses, fibres, and filters. This result rules out the often proposed mechanism of Frenkel defect formation during flash sintering as the explanation for the light emitted in the visible range.

The experiments conducted on various (stabilised) zirconia materials under atmosphere-dependent DC flash sintering and electrical loading revealed significant findings regarding electrochemical reduction processes. Even under moderate FS conditions, such as 25 V/cm at 800 °C furnace temperature, these materials exhibited electrochemical reduction, leading to structural changes that were extensively studied, particularly in YSZ.

The electrochemical reduction process in YSZ was observed to occur in two dis-

tinct stages:

I) Formation of single-charged oxygen vacancies and paramagnetic Zr^{3+}-Ions: Initially, single-charged oxygen vacancies formed, which were compensated by the generation of paramagnetic Zr^{3+} ions. This phenomenon resulted in a decrease in the bandgap of the material, enabling electrical conduction at high temperatures and producing a strong paramagnetic response, often characterised by a greying of the material. During this stage the material can be described or characterised as $(Y)ZrO_{2-\delta}$.

II) Phase transition to ZrO or ZrON: Subsequently, a phase transition occurred towards ZrO or ZrON depending on atmosphere, adopting a defective FCC rock-salt structure. In this phase, double-charged oxygen vacancies were observed, altering the environment around Zr and leading to behaviour resembling metallic conductivity at room temperature. This phase transition was confirmed through techniques like Raman spectroscopy and EDS. The phase transition is notably associated with the blackening of (yttria-stabilized) zirconia.

Depending on the specific conditions of the flash sintering process, the electrochemical reduction in YSZ may remain in stage I, particularly under low currents in DC fields or even under AC fields, which is also the case in air or O_2. However, under more extreme conditions typically used in DC flash sintering experiments, or in inert atmosphere, transition to stage II occurs. Rapid reoxidation during flash

sintering experiments where fields are turned off at elevated furnace temperatures often masks the observation of this phase transition.

In general the conducted research indicates that the application of electrical fields at elevated temperatures on transition metal oxides leads to the extraction of oxygen from the material itself from an early stage of the flash sintering process, which is one parameter to consider in the context of flash sintering of (transition) metal oxides.

8.2 Plasma formation during flash sintering of boron carbide

8.2.1 Plasma characteristics

Plasma formation in Ar at a furnace temperature of 1500 °C under FS-conditions was investigated. The results suggest that flashover is the fundamental mechanism for atmospheric breakdown, which led to a plasma sustained between the electrodes and around the samples. This was observed with green bodies and pre-sintered specimens, of both Al_2O_3 and B_4C.

The plasma formed was classified as high-pressure arc discharge. This did not densify the green bodies, but it did lead to transport of matter from within the

green body to the surface and beyond by a sputtering effect. It was shown definitively that such a plasma can infiltrate a green body of $\approx$ 50 % density and particle size of 1 μm to a depth of more than 1 mm.

At a certain point the material became more conductive than the plasma, which led to a collapse of the plasma and transition of the current flow into the material itself which, due to Joule heating, then started to densify.

Based on the results, it seems unlikely that such atmospheric plasma formation is involved in normal FS of oxide ceramics or in SPS.

8.2.2 Effect of plasma on sintering and parameter improvement

DC-flash sintering of boron carbide (B_4C) was investigated under various conditions, revealing that high environmental temperatures of 1500 °C are necessary for uniform densification due to strong current concentration at lower furnace temperatures.

The application of high electric fields in an Ar atmosphere led to the formation of a plasma around the specimen. SEM and XPS are consistent with the finding of Chapter 6 of this thesis, that the Ar-plasma can enter the green body and show that it interacts with the solid particles, the strongest interaction being near the sample

surface.

The plasma did not cause significant densification itself, but was shown to significantly reduce the oxide layer on the particle surface and thereby enhanced the subsequent densification of the material when the plasma collapsed, and Joule heating raised the sample temperature to $\approx$ 2300 °C.

The use of this Plasma Pre-Treatment-Flash Sintering process with carbon sintering aids and optimised process parameters enabled B_4C with density, grain size and hardness of 96 %, 10 μm and 31 GPa (HV1) to be produced without the application of pressure, using a furnace temperature of 1500 °C and a hold time of only 5 minutes. The high hardness was tentatively attributed to the retention of a high concentration of twinning owing to the short sintering time.

9 | Suggestions for further work

9.1 Flash sintering and electrical loading of zirconia and hafnia based ceramics

Since the temperature estimation and measurement during FS is difficult and most of the methods used are insufficient to determine the temperature in an accurate and reliable way, other techniques are necessary to enable a more detailed investigation of the process.

In this thesis optical spectroscopy was used and the spectra were carefully evaluated which led to an appropriate way of measuring the sample temperature during FS. Thus, further investigations using optical spectroscopy could provide a way to improve the contact-less temperature measurement. Dependent on the integration time this technique also enables the highly time-resolved possibility to do so.

As shown in this and other previous work [77, 78, 79, 230] the electrochemical reduction of YSZ during flash sintering or electrical loading can lead to phase transformation(s). In order to observe the ongoing changes in the material it would be useful to conduct in-situ XRD experiments to characterise the various steps of reduction as they were proposed before. This would connect all potential phases

formed during the electrochemical reduction process and enables the detection of the points when phase transformation(s) happens.

Furthermore, in-situ XPS and EPR characterisation of the electrochemical reduction process would be helpful to characterise the ongoing change in the oxidation states of the transition metal oxides without a post-treatment reoxidation.

The suggested in-situ characterisations should be done in various atmospheres to enable the separation of reoxidation and field induced reduction.

Subsequent to the electrochemical reduction, mechanical testing of reduced YSZ would reveal the effect of electrochemically induced defects on the macroscopic behaviour of the material.

Generally, further characterisation of group IV transition metal monoxides such as ZrO and HfO is necessary to get a better understanding of their structure, properties and potential applications. For instance, it is known that ZrO_xN_{1-x} and ZrN show superconductivity below a critical temperature. Since, ZrO shows some similarities to ZrO_xN_{1-x} and ZrN a potential superconductivity in ZrO could be investigated. In this perspective theoretical modeling such as DFT will help to improve the understanding of the fundamental structure including its potential defects.

Like for stabilised zirconia, in-situ XRD and/or Raman spectroscopy during flash

sintering of undoped pure zirconia, will help to understand the influence of electrochemically induced oxygen vacancies on the zirconia structure. Such an investigation might show that a transition from monoclinic towards tetragonal or cubic zirconia can be achieved by the reduction and, dependent on the atmosphere and the thermal process, could potentially be stabilised at room temperature. The stabilisation of tetragonal and cubic zirconia at room temperature by the electrochemical removal of oxygen would support the results, which are based on a theoretical model, by Fabris et al. [66].

9.2 (Pre-plasma) flash sintering of boron and silicon carbide

A high degree of twinning was observed in the grains of B_4C subsequent to flash sintering which could change the mechanical properties compared to conventionally sintered and hot-pressed materials as suggested by others on conventionally sintered B_4C [307]. The investigation of the mechanical properties would be the next step to identify the macroscopic effects introduced by the microstructural changes, which includes measurements of strength and toughness of flash sintered B_4C as another possibility for further research.

The work conducted, particularly the plasma-related investigations, showed that

plasma(s) can improve and change processing of ceramics as is already known and has been used for many years on an industrial scale for metals and polymers.

Plasmas could be used for processes such as surface activation/cleaning/etching of carbide powders which improves their densification behaviour due to the reduction of the passivating oxide layer formed on their surface. This could be done on various carbide powders prior to conventional sintering to improve their densification and potentially lower temperature and time to enable energy and time savings and make the production of such high temperature materials more sustainable.

Furthermore, plasma treatments could be used for other purposes such as in-situ graphene formation in ceramic powders which contain some kind of precursor, such as organic additives/polymers which get cracked during heating in inert atmosphere and later on restructured in a plasma environment within the green body itself.

A | Appendix

A.1 Light emission during flash sintering of stabilised zirconia

Figure A.1 shows the attenuation of the fibers used for the optical spectroscopy measurements.

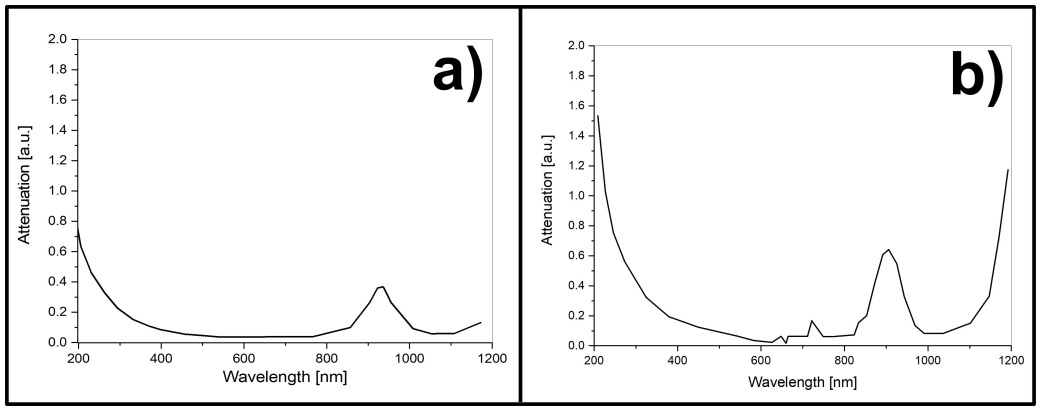


Figure A.1: Fiber attenuation of a) QP400-2-VIS-BX and b) QP400-2-SR-BX fibres. Diagrams are recreated based on the manufacturers data by using Web-PlotDigitizer.

A.2 Flash sintering and electrical loading of stabilised zirconia

Some of the following investigations and results were conducted on other types of stabilised zirconia than tetragonal stabilised 3YSZ (TY-3YB) and cubic stabilised 8YSZ (TZ-8YB). A summary of all investigated stabilised zirconia powders can be found in table A.1. The powders were treated similar to the other YSZ powders mentioned in the main thesis.

Table A.1: Investigated (stabilised) zirconia powders with specifications from product data sheets.

Name	Manufacturer	Stabiliser	Stab. Ratio [mol%]	D_{50} [μm]
TZ	Tosoh Corp.	-	0	0.04
TZ-1.5YB	Tosoh Corp.	Y	1.5	0.04
TZ-3YB	Tosoh Corp.	Y	3	0.04
TZ-3YB-E	Tosoh Corp.	Y	3	0.04
TZ-5YB	Tosoh Corp.	Y	5	0.04
TZ-8YB	Tosoh Corp.	Y	8	0.04
TZ-10YB	Tosoh Corp.	Y	10	0.04
M8SZ	Daiichi Corp.	Mg	8	0.04

A.2.1 Resistance test 3YSZ loaded in argon

A power dissipation of 5 W was dissipated in a 3YSZ-EL-CD-Ar sample while heating up the furnace from room temperature up to 800 °C. An increase in resistance by approximately two times was detected during the heating process,

indicating a PTC behaviour of the sample after electrical loading in Ar.

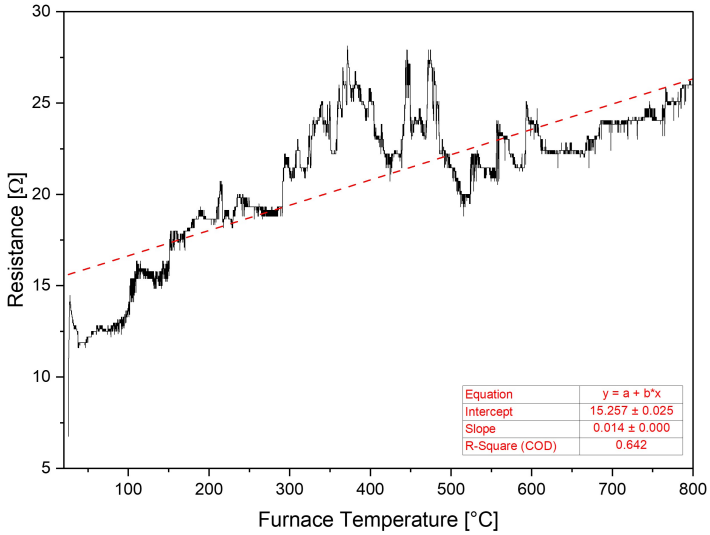


Figure A.2: Resistance (U/I) during a constant power dissipation of 5 W in a 3YSZ-EL-CD-Ar sample from room temperature up to a furnace temperature of 800 °C.

A.2.2 Electrical loading of 8YSZ

Figure A.3 shows the electrical parameters recorded during electrical loading of pre-sintered 8YSZ as it is shown for 3YSZ in the main text with cathode left and anode right side of the sample.

At the very beginning local heating on the electrode material interface suggests a high resistivity due to its O-ion blocking behaviour. However, the local heating on the interfaces disappears which indicates the transition towards electronic conduction.

After plateauing of current voltage was increased from 30 to 40 V, still in O_2, which raised the current level and Joule heating within a few seconds.

Changing atmosphere from O_2 to air did not cause any significant change in the electrical response, indicating an electronic conduction which independent of the oxygen partial pressure at this point as it is also indicated by the appearance of the sample which shows inhomogeneous heating concentrated on the anode side (right).

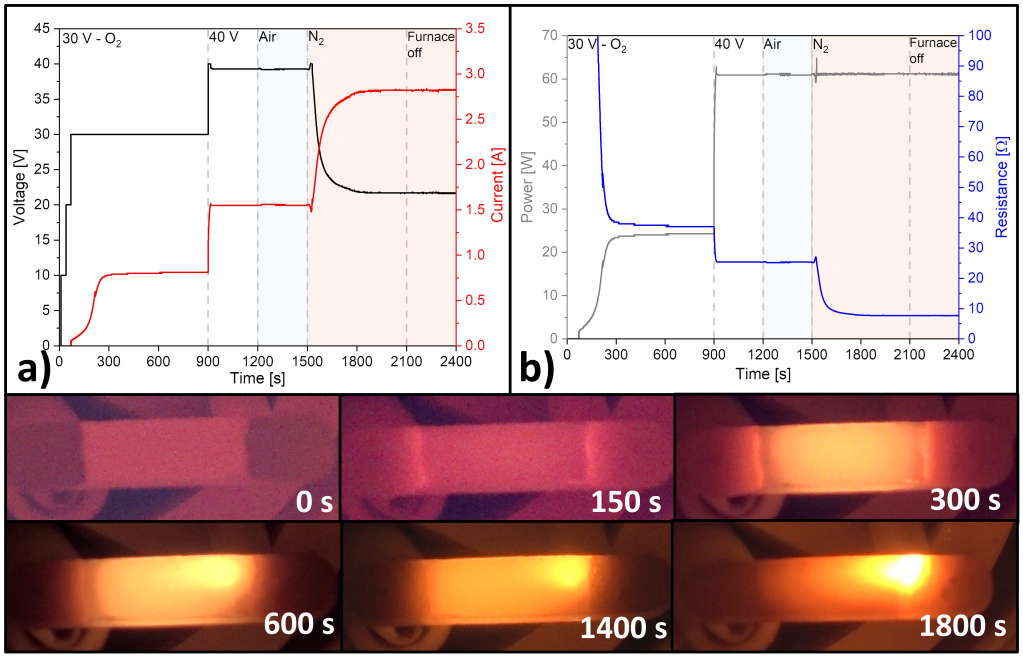


Figure A.3: Electrical Loading of pre-sintered 8YSZ in changing atmospheres under 30 V which is increased to 40 V during the process. The images show the sample at various stages throughout the process.

A.2.3 SEM and EDS

3YSZ

After electrochemical reduction reached stage II, Raman signal changed not only for originally tetragonal 3YSZ towards FCC rocksalt ZrO(N), but also the signal caused by alumina (Al_2O_3) started to disappear after phase transformation happened.

Figure A.4 shows SEM images and EDS maps of the center of the cross section of a sample which was only slightly reduced (a-c) and the surface close region which underwent phase transformation (d-h). The EDS maps show that the originally well-defined grain structure changed after the electrochemical reduction as well as the oxygen and aluminium distribution. It can be seen that Al started to segregate along the grain boundaries, which did not happen before reduction, showing that also alumina is affected by the reduction process leading to the disappearance of the Raman signal.

8YSZ

Figure A.5 shows SEM images of in Ar electrochemically reduced 8YSZ, which led to the phase transformation towards ZrO as it shown for 3YSZ. The SEM images reveal the formation of small grains (< 100 nm) on the surface of the

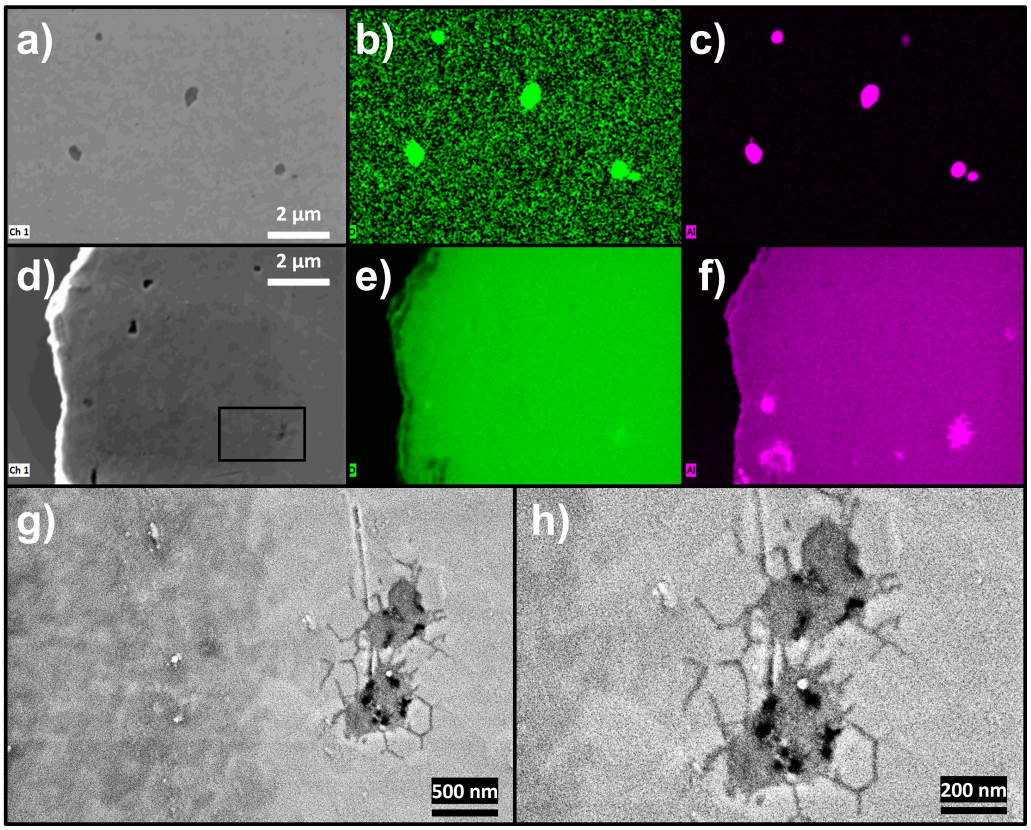


Figure A.4: Pre-sintered 3YSZ sample after electrical loading for a few seconds in Ar; SEM image and EDS map of a-c) slightly reduced center of the cross section and d-h) electrochemically reduced region close to the surface of the sample with g) and h) showing higher magnified region highlighted in d). EDS maps show O in green and Al in magenta.

sample and cracking which are most likely caused by the phase transformation-induced volumetric change.

Figure A.6 shows a polished and not etched cross section of a fully dense pre-sintered 8YSZ sample before and after electrochemical reduction in Ar which led to phase transformation towards ZrO in the reduced sample which shows pores located along the grain boundaries where phase transformation in 8YSZ mostly

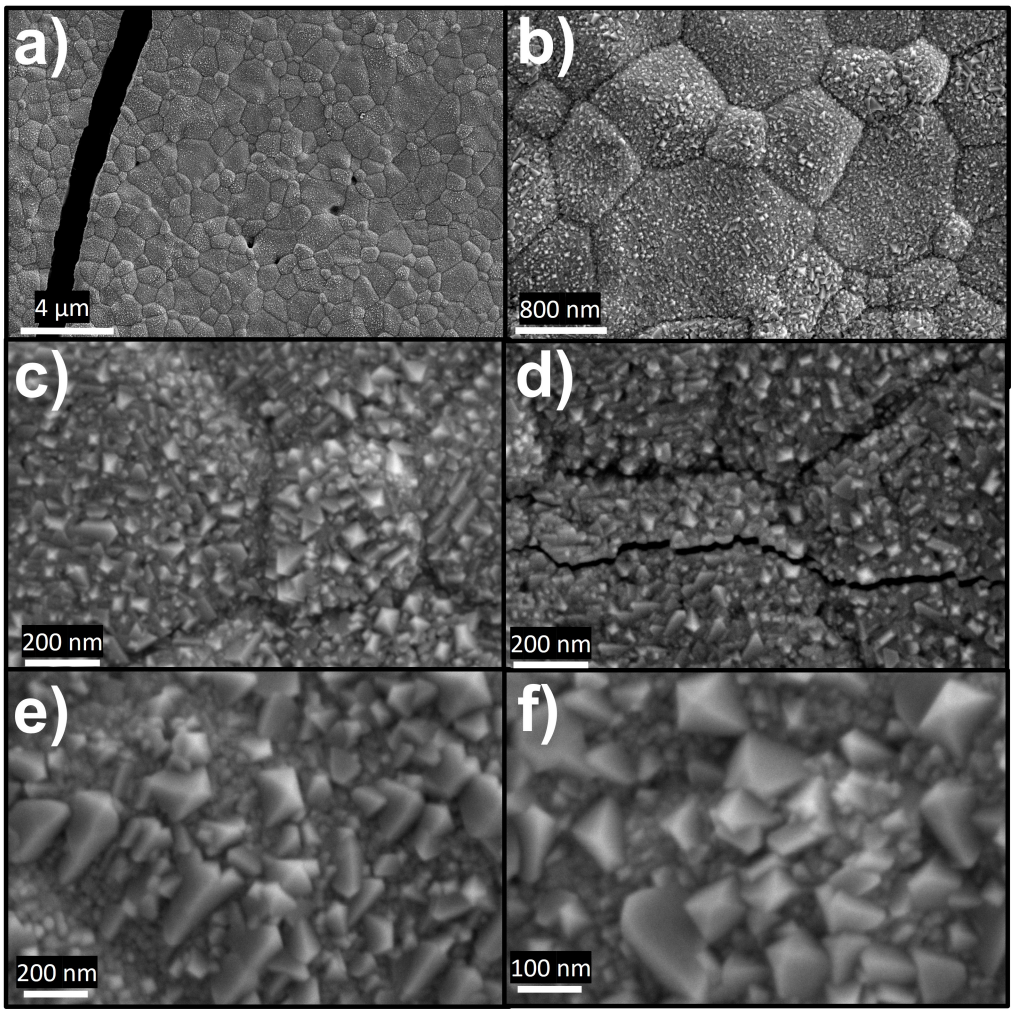


Figure A.5: SEM of surface of a pre-sintered 8YSZ sample electrically loaded in Ar at various magnifications.

happened.

The phase transformation towards FCC rocksalt ZrO and the related volume contraction also explains the observation by Dong and Chen [260] who assumed that the cavities formed due to oxygen-vacancy condensation on grain boundaries.

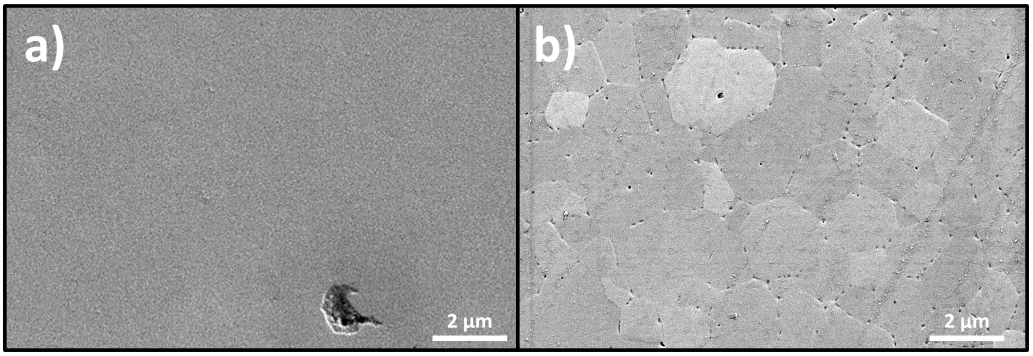


Figure A.6: SEM images of a polished (not etched) cross section of a fully dense pre-sintered 8YSZ sample a) before and b) after electrochemical reduction which led to phase transformation.

A.2.4 XRD

Figure A.7 shows the XRD pattern taken from 8YSZ samples after electrochemical reduction which shows the formation of ZrO as it is discussed in greater detail for 3YSZ in the main text.

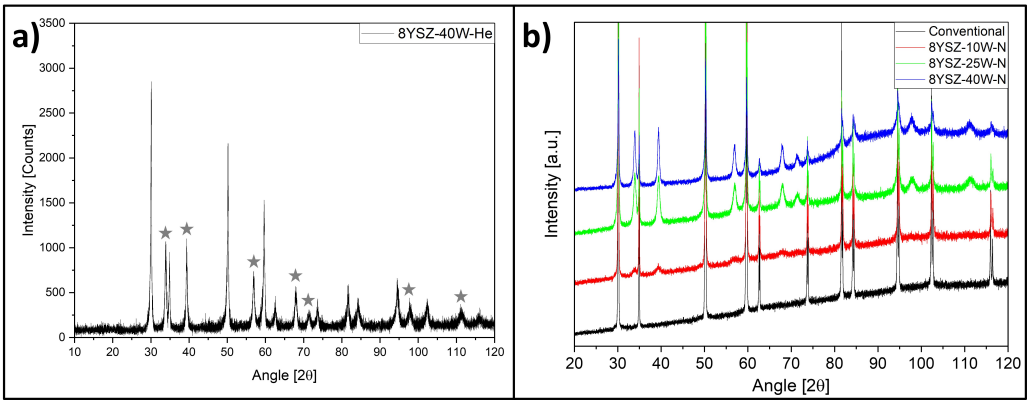


Figure A.7: XRD pattern taken from a pre-sintered 8YSZ sample a) after electrical loading (40 W) in He with the FCC rocksalt ZrO peaks highlighted with grey stars and b) a series of samples including conventionally sintered and electrically loaded 8YSZ in N_2 with 10, 25 or 40 W which shows the formation and evolution of the FCC rocksalt ZrON phase.

A.2.5 Raman Spectroscopy

Figure A.8 shows the Raman spectra taken from YSZ samples with various yttria contents between 1.5 and 10 mol.% after electrochemical reduction. All samples show the spectra which can be associated with the formation of FCC rocksalt ZrO(N).

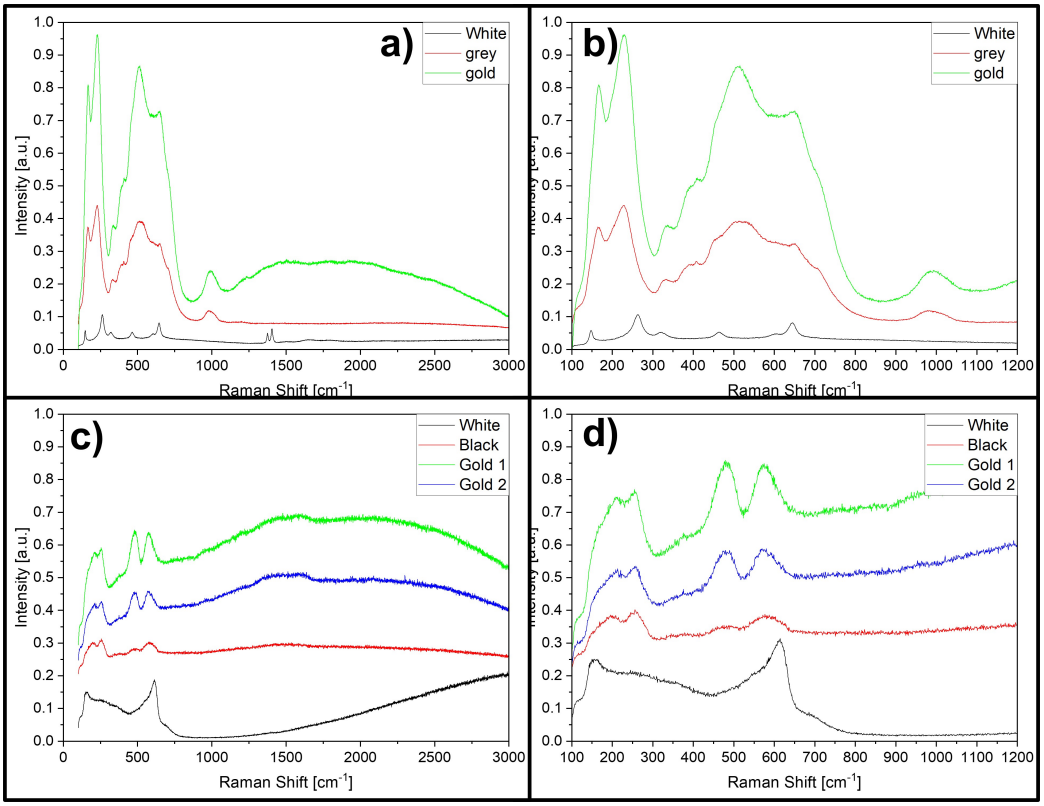


Figure A.8: Raman spectra at two different scales of (a and b) tetragonal 1.5YSZ and (c and d) fluorite cubic (FCC) 10YSZ before and after electrical loading, which led to a change in the material which evolved from white to grey to black to gold.

A.2.6 XPS

Figure A.9 shows the detected XPS spectra in the C1s and Y3p3/2 region which includes the C-signal normalised to 248.8 eV for all samples to correct for charging effects if necessary.

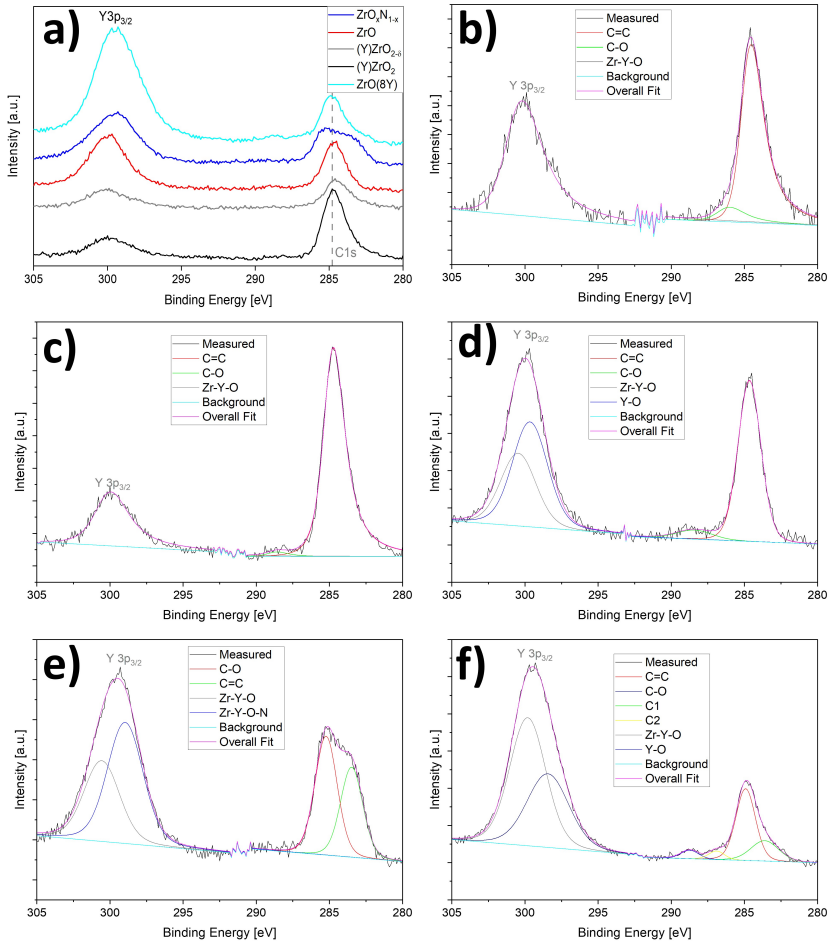


Figure A.9: XPS spectra in the C1s and Y3p3/2 region. a) Overview, b) Reference, c) partially reduced, d) fully reduced in Ar, e) fully reduced in N_2, f) 8YSZ fully reduced in Ar. The dashed vertical line visualises a binding energy of 248.8 eV, which was used as one indicator for the correction of the spectra due to charging if necessary.

A.2.7 Thermogravimetric Analysis

Thermogravimetric Analysis (TGA) was conducted on a piece of 3YSZ green body FSed in He and a conventionally sintered sample in air to detect at which temperature the reduced material shows an increasing weight due to reoxidation.

The results (Figure A.10) show that from the very beginning (room temperature) the weight starts increasing with an increasing rate at higher temperatures. This result highlights the instability of ZrO which tends to reoxidise even at lower temperatures around room temperature, which is why in most FS-experiments the material fully reoxidises during furnace cool down.

At higher temperatures the weight decreased rapidly which can not be explained based on reoxidation. It should be mentioned that the alumina crucible, containing the samples, broke apart after taking the crucible including the reoxidised sample from the measurement device, which did never happen for any other measurement. Potentially, the alumina crucible itself got slightly reduced, which would agree on the change in alumina Raman signal, which could have led to unexpected weight changes as the one at higher temperature.

The reduced sample, which showed blackening prior to TGA, turned white after the measurement without any blackening left and the sample fell apart as shown in Figure A.10 b) and c).

The weight of the conventionally sintered sample did increase slightly at higher temperatures but the sample did not show any significant changes, shown in Figure A.10 d) and e).

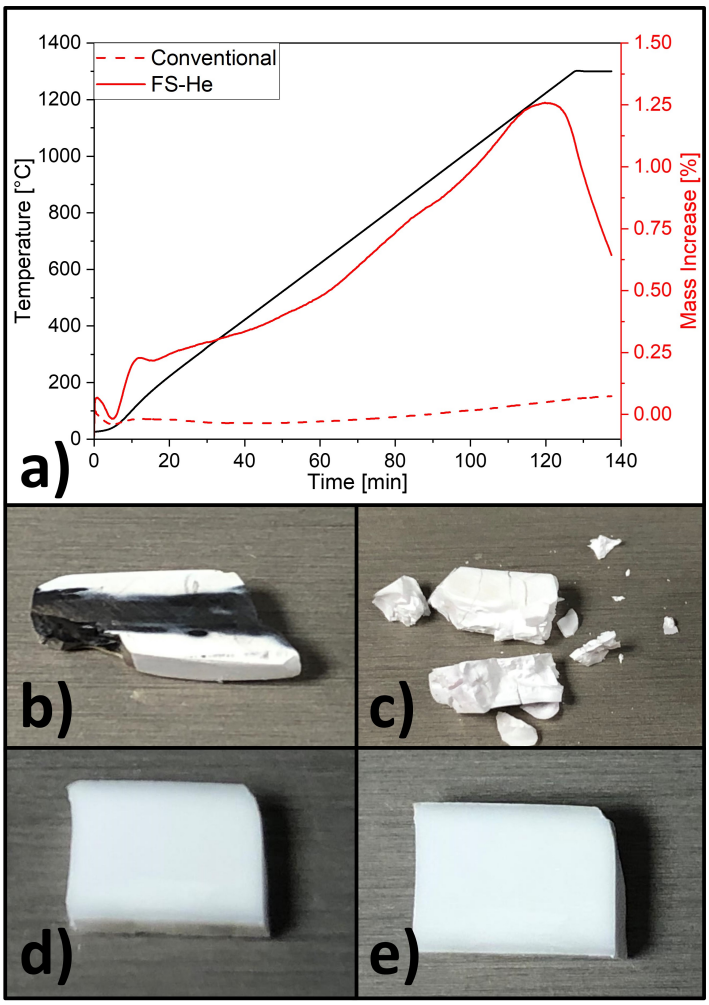


Figure A.10: a) TGA results of reoxidation of a 3YSZ green body FSed in He and conventionally sintered 3YSZ; b) and d) show the samples before and c) and e) post measurement.

A.2.8 Electrical loading of magnesia stabilised zirconia

Figure A.11 shows a magnesia stabilised zirconia (MSZ) sample after electrical loading in Ar, including power dissipation during furnace cool down.

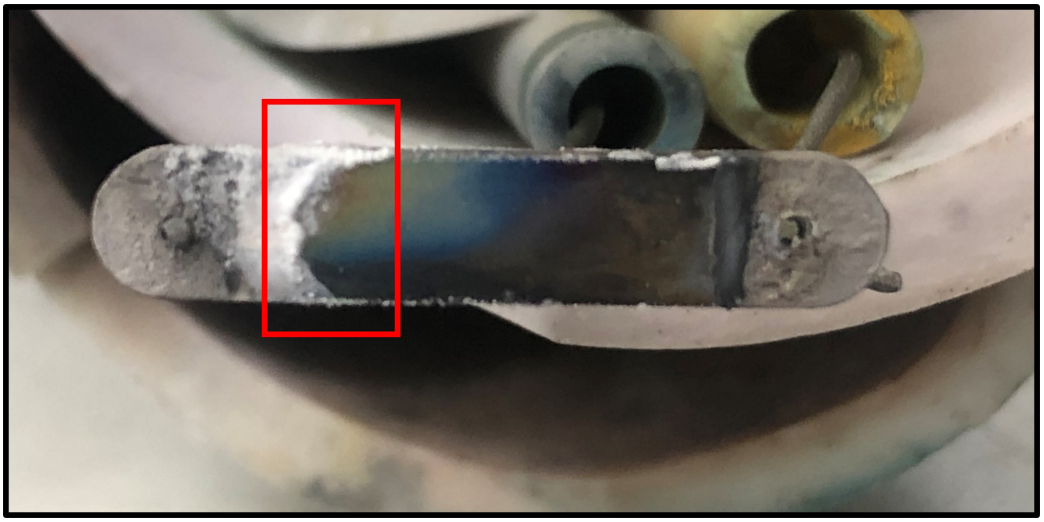


Figure A.11: Magnesia stabilised zirconia after electrochemical reduction in Ar with the anode/sample-interface as highlighted area investigated by EDS.

Figure A.12 shows the EDS maps taken from the anode side of a magnesia stabilised zirconia (MSZ) sample subsequent to electrical loading in Ar. The EDS maps show that Mg strongly concentrated on the anode/sample interface, which can be seen by seen by eye as white material/powder strongly segregated at the anode (Figure A.11).

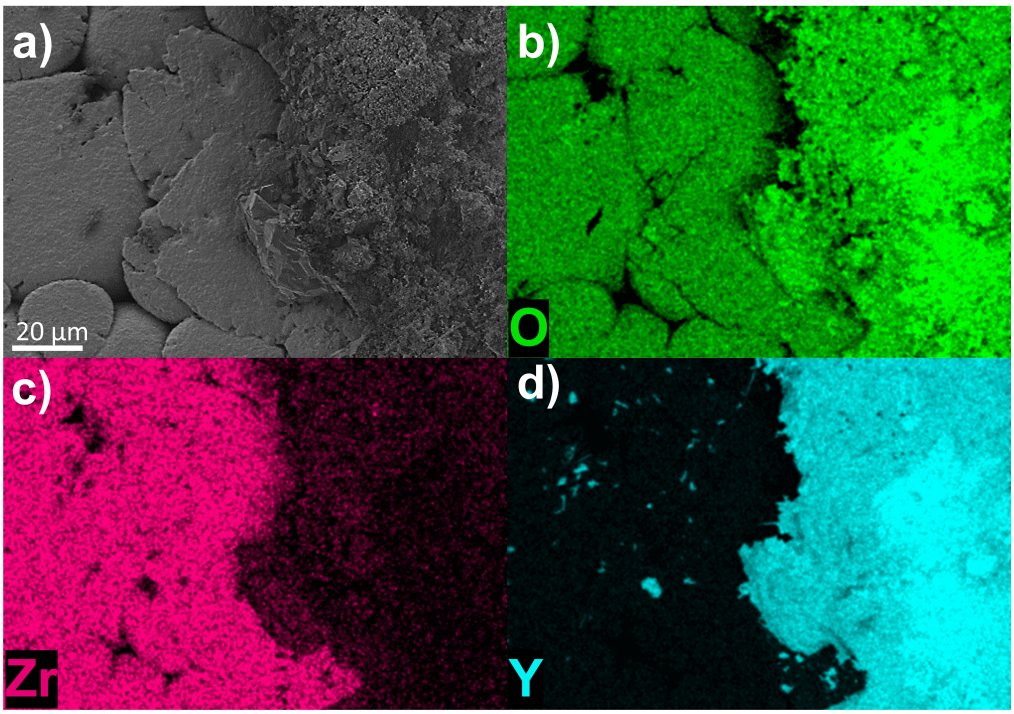


Figure A.12: a) SEM image and EDS maps of MSZ after electrical loading in Ar showing b) O in green, c) Zr in magenta and d) Mg in blue.

A.2.9 Calculations

Figure A.13 shows the calculations for the time necessary to extract a certain amount of oxygen from ZrO_2 by electrochemical reduction.

Oxygen Extraction Calculation

Defined parameters	Sample Weight		Current		Elementary charge	
	1g		1A		1.60E-19	As
					Charge of O2- Ion	
					3.20E-19	As
ZrO2	Zr	O				
Atomic-Number	40	8				
Atom weight	91	16	g/mol			
Weight ratio in ZrO2	0.739837398	0.2601626				
Weight per element	0.739837398	0.2601626	g			
Mol per element	0.008130081	0.0162601 6	mol			
Avogadro Constant	6.02E+23	6.02E+23	1/mol			
number of atoms per element in defined weight	4.89E+21	9.79E+21				
O atoms in the ZrO2 sample	9.79E+21					
Charge of each O2- Ion in [As]	3.20E-19					
for generating 1.5 % O-vacancies in ZrO2 equivalent to 3YSZ		for generating 4 % O-vacancies in ZrO2 equivalent to 8YSZ				
47.0s		125.5s				

Figure A.13: Calculation for estimating the time which is necessary to extract 1.5 or 4 mol.% oxygen ions from 1 g of ZrO_2 if a current of 1 A is solely based on oxygen ions to generate the same amount of oxygen vacancies present in 3YSZ or 8YSZ, respectively.

Figure A.14 shows the calculations for the operation of a SOFC according to [265] showing how long it would take to achieve a certain level of oxygen extraction and vacancy concentration (0.75, 1.5 or 4 mol.%) if 1 % or 1 ppm less oxygen is

taken in than necessary to maintain the current flow purely based on atmospheric oxygen.

O atoms in the ZrO2 sample	5.87E+19									
Charge of each O2- Ion in [As]	3.20E-19	As								
			Percent O which is used as charge carrier per second compared to overall O content.							
O ions necessary to maintain	1.56E+18		2.66	%		V=nRT/p	8.314	J/molK	R	
0.5 A per second							973	K	T	
							101300	N/m2	p	
Oxygen in mol% compared to Y generated vacancies							7.43E+18		n	
0.75	1.5	4				V	9.86E-07	m3		
Oxygen absolute number of atoms necessary to retract				Volume of air that		V	0.99	cm3		
4.40E+17	8.81E+17	2.35E+18		needs to be cycled						
Time in seconds necessary to generate the amount of O-vacanciesif no current is substituted at all				completely to generate						
0.28	0.56	1.51		the necessary oxygen intake per second						
If only 1 % less oxygen is taken in over the whole time it would take ... s						10	µm	8YSZ		
28.23	56.45	150.54				80	cm2 active cell area per layer			
						700	°C			
1 ppm less O is taken in						air	0.21	oxygen content		
282264.5854	564529.171	1505411.12	s				0.40	% used fuel		
4704.409756	9408.81951	25090.1854	min			used O	0.084	is the used volume of the air		
78.40682927	156.813659	418.169756	h					oxygen content used		
3.26695122	6.53390244	17.4237398	d			density 8YSZ	6	g/cm3		
						per cm2	0.006	g		
						per 1 cm2	6	mg		

Figure A.14: Calculation for estimating the time which is necessary to extract 0.75, 1.5 or 4 mol.% oxygen ions from a SOFC during operation under conditions reported in [265] if 1 % or 1 ppm less oxygen is taken in than necessary to maintain the current purely based on oxygen ions.

A.3 Electrical loading of yttria-doped hafnia

The behaviour of (yttria stabilised) hafnia ($Y_{0.15}Hf_{0.85}O_{1.925}$), as another group IV transition metal in addition to the previously investigated YSZ, was investigated under electrical load in various atmospheres. Therefore, the composition mentioned before was made by mixing the original powders in a water-based slurry including 1 wt.% PVA before drying, sieving, uniaxial pressing, debinding and conventional sintering at 1400 °C for 2 h, as mentioned in the Methodology section of the thesis for other powders. The original powders used are summarised in Table A.2.

Table A.2: Raw powders used for producing yttria-stabilised hafnia.

Material	Manufacturer	Purity [%]	D_{50} [μm]
HfO_2	thermo scientific	99.9	40
Y_2O_3	Alfa Aesar	99.995	0.050 - 0.070

A field of 150 V (75 V/cm) was applied across a pre-sintered $Y_{0.15}Hf_{0.85}O_{1.925}$ at 800 °C furnace temperature in air, which led to a rapid current increase (Figure A.15 a) and Joule heating of the sample after 180 s (Figure A.15 c).

Even before the rapid current increase and the related Joule heating, local hot-spots formed on the sample surface (Figure A.15 b) which disappeared later (Figure A.15 g).

After reaching power-control, the power dissipation (20 W) was maintained for another 100 s in air. During this period sample heating was homogeneous without a significant changes in current and voltage (Figure A.15 d). According to the black body radiation model (BBR) [20] the (estimated) sample temperature at this point is $\approx$ 1050 °C.

After changing atmosphere from air to Ar (300 s), resistance dropped from 370 to 92 Ω within 50 s and the sample heating shifted towards more localised heating on the anode side (Figure A.15 e-g).

After maintaining power dissipation during furnace cool-down, which started after 400 s and took $\approx$ 2.5 h, the power dissipation was stopped and the material was quenched down to room temperature. Some parts of the sample showed the original white colour, but in some regions of the sample the colour transitioned to black/grey to gold (Figure A.15 h-i).

The region of the sample where hot-spots formed on the surface prior to the rapid current increase (Figure A.15 b) also show grey colouring, shown at the bottom part of the sample in Figure A.15 h).

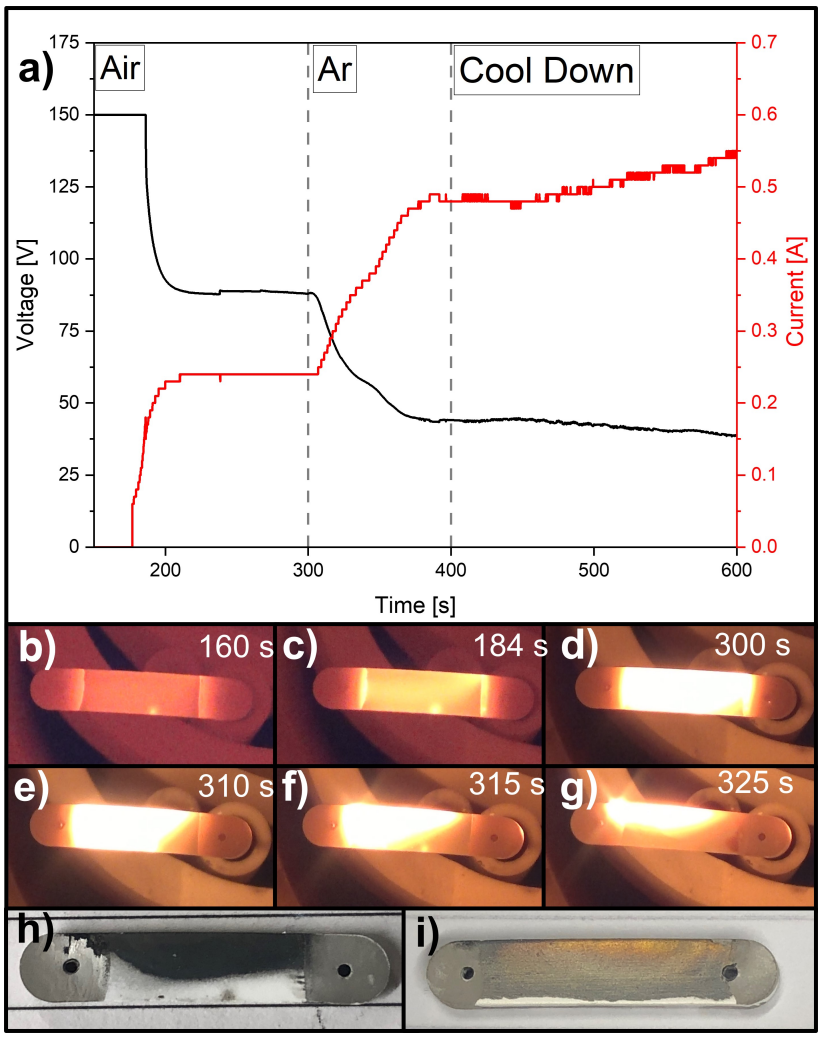


Figure A.15: Electrical loading of pre-sintered yttria-doped hafnia; a) voltage and current detected during electrical loading; b-g) sample under electrical load at certain times; h-i) sample after electrical loading.

A.3.1 Characterisation of electrically loaded yttria-doped hafnia

Since $Y_{0.15}Hf_{0.85}O_{1.925}$ showed a significant change in electrical resistivity and strong discolouring during and after electrical loading, the material was charac-

terised to identify potential changes in the fundamental structure.

A.3.1.1 Raman Spectroscopy

Raman Spectroscopy of electrically loaded $Y_{0.15}Hf_{0.85}O_{1.925}$ was conducted on three different positions of the same sample surface, shown in Figure A.16 a).

The spectrum taken from the white region of the sample, shown in Figure A.16 a), shows several sharp peaks. All of the detected peaks can be associated with the monoclinic hafnia phase, which includes two really strong peaks at 149 and 501 cm^{-1} [313, 314].

Raman spectra taken from the black/grey region are different in the way that the well defined monoclinic peaks are not detected. With the colour changing towards gold, three broad peaks at 158, 500 and 630 cm^{-1} are appearing. The last peak is, like discussed for ZrO, an indicator for the formation of double negative charged oxygen vacancies.

Raman spectroscopy in and around the surface hot-spot formed before the rapid increase in current shows most of the monoclinic peaks as well as a significantly stronger response between 150 and 640 cm^{-1} relative to the detected monoclinic peaks.

Furthermore, the background signal in the unreduced white sample region increases at higher Raman shifts > 800 cm^{-1}, whereas background in reduced parts

of the samples are more constant.

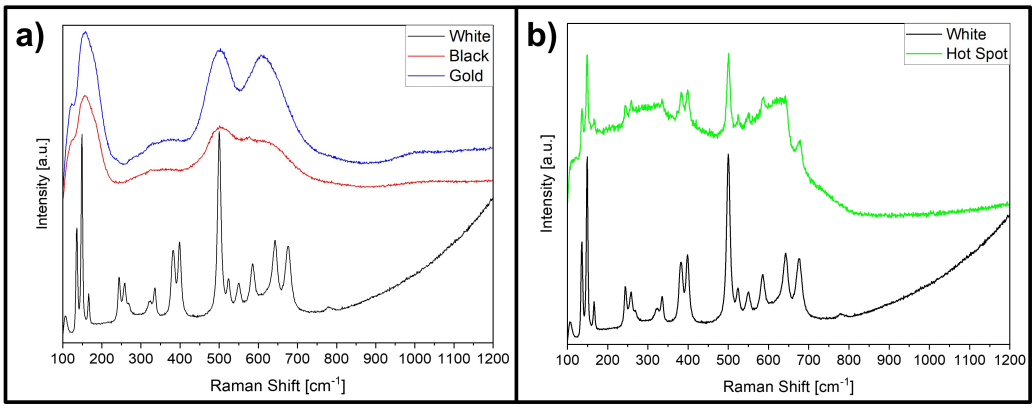


Figure A.16: Detected Raman spectra of a) electrically loaded and electrochemically reduced $Y_{0.15}Hf_{0.85}O_{1.925}$ in the white, black and gold region of the sample; b) hot-spot formed during FS and the surrounding white region of the sample.

A.3.1.2 XRD

XRD spectrum of the unreduced state (Reference) is shown in Figure A.17 and A.18 a). Monoclinic and fluorite cubic (FCC) hafnia is detected. However, after electrical loading additional peaks are detected and highlighted with red stars.

Figure A.17 shows the XRD pattern of the yttria stabilised hafnia samples before and after electrochemical reduction, which reveal the presence of unreacted yttria.

Rietveld refinement was conducted under consideration of three different phases, monoclinic, FCC (Y)HfO_2, and FCC rocksalt HfO. The predicted peak positions of the three phases are shown in Figure A.18 b).

Figure A.18 c) shows the refined spectrum of the electrically loaded sample, which

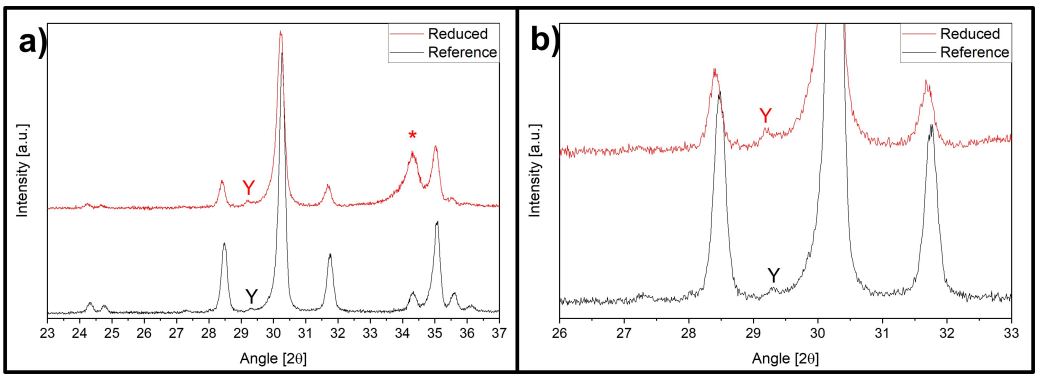


Figure A.17: (XRD spectra of pre-sintered (Reference) and electrochemically reduced (Reduced) yttria-stabilised hafnia showing the new δ-HfO phase (*) as well as the most intense peak for unreacted yttria (Y_2O_3) labelled with Y.

contains FCC as well as monoclinic (Y)HfO_2, but also two peaks located at approximately 34 and 40 °, which agrees well with the predicted FCC rocksalt HfO structure. The detected phases, with their concentrations and lattice parameters are summarised in Table A.3.

Figure A.18 d) shows the refined spectrum of the Reference sample before electrical loading, which contains cubic and monoclinic hafnia-based phases.

The in Vesta [76] generated crystallographic models used for Rietveld refinement are shown in Figure A.18 e-g).

According to the refinement the concentration of the monoclinic and FCC phase decreased during electrical loading by roughly the same amount and transformed to the FCC rocksalt phase.

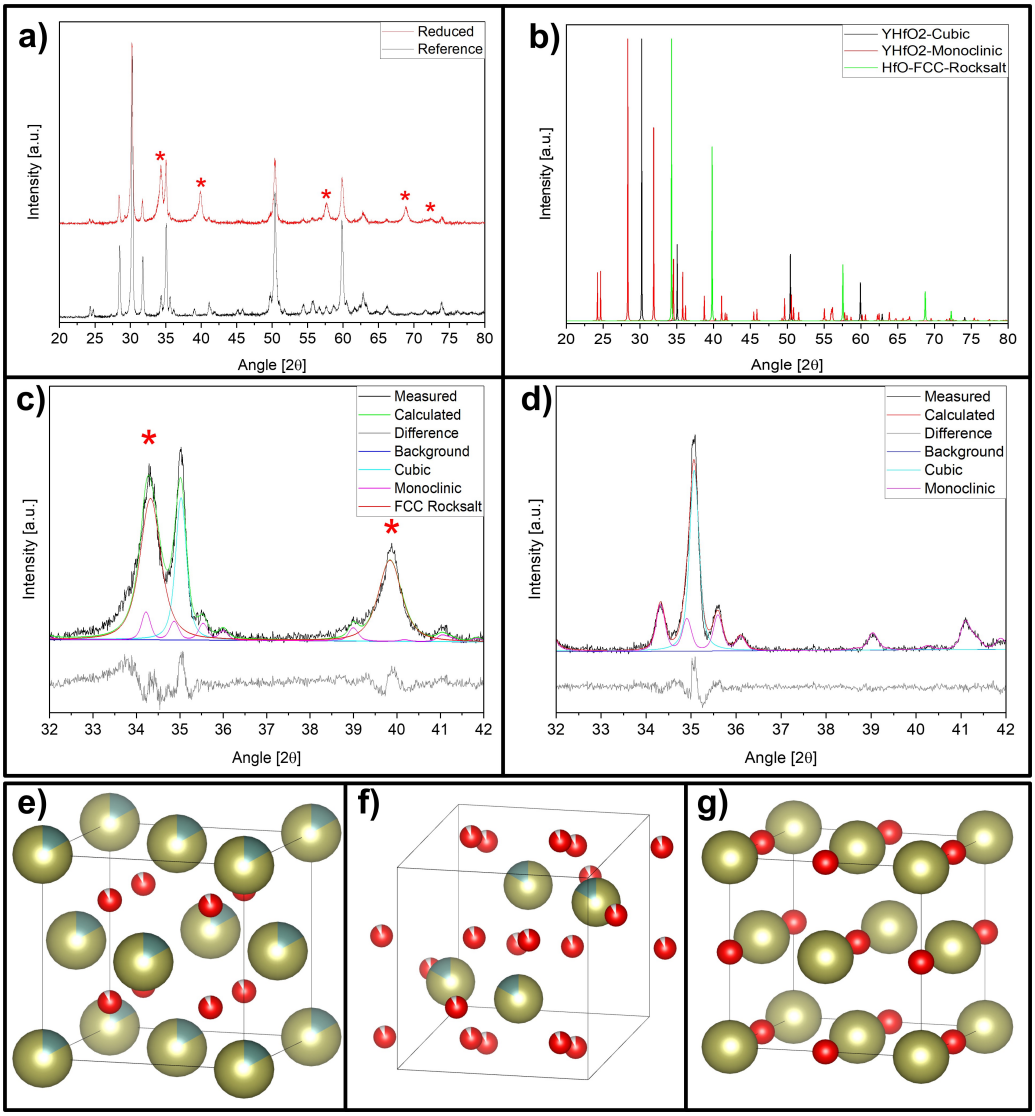


Figure A.18: a) Detected XRD pattern of pre-sintered $Y_{0.15}Hf_{0.85}O_{1.925}$ before and after electrical loading, after electrical loading FCC rocksalt phase peaks appear, which are highlighted with red stars; b) predicted peak locations for fluorite FCC, monoclinic and FCC (Y)HfO_2; Rietveld refined XRD spectrum of c) electrically loaded and reduced $Y_{0.15}Hf_{0.85}O_{1.925}$ and d) unreduced $Y_{0.15}Hf_{0.85}O_{1.925}$; e) fluorite FCC, $Y_{0.15}Hf_{0.85}O_{1.925}$; f) monoclinic $Y_{0.15}Hf_{0.85}O_{1.925}$ and g) FCC HfO unit cells used for Rietveld refinement.

Table A.3: Rietveld refined parameters of electrically loaded and electrochemically reduced $Y_{0.15}Hf_{0.85}O_{1.925}$.

Phase	Lattice Parameter [nm]	Concentration [wt.%]
FCC	a = 0.5125	66
Monoclinic	a = 0.5120 b = 0.5149 c = 0.5309 β = 99.175 °	12
FCC	a = 0.4527	22

A.3.1.3 SEM and EDS

SEM and EDS of $Y_{0.15}Hf_{0.85}O_{1.925}$ was used to visualise the change in the fundamental structure and elemental distribution caused by the electrical loading in inert atmosphere.

SEM images and EDS spectra of fractured cross sections of an unloaded and loaded sample were taken. For the electrically loaded sample images were taken from a region close to the surface of the sample where golden colouring of the material was obvious.

SEM images and EDS maps from the unloaded sample (Figure A.20) are showing a fundamental difference to the loaded sample (Figure A.21) in the grain structure and elemental distribution.

In the conventionally, unloaded sample (Figure A.19 a) and b) some bigger grains are surrounded by significantly smaller grains. The fracture behaviour of the big-

ger grains is rather trans-granular, whereas the smaller grains show a more inter-granular fracture. Furthermore, the unloaded material shows a normal grain structure and mostly homogeneous elemental distribution.

The electrically loaded sample (Figure A.19 c) and d) showed a similar fracture behaviour, however finer grains (< 100 nm) within the fractured original grains can be identified. Such fine grains are also apparent on the sample surface. The elemental distribution shows a separation of Hf and Y, whereby the Y-rich regions are also higher in their O-content.

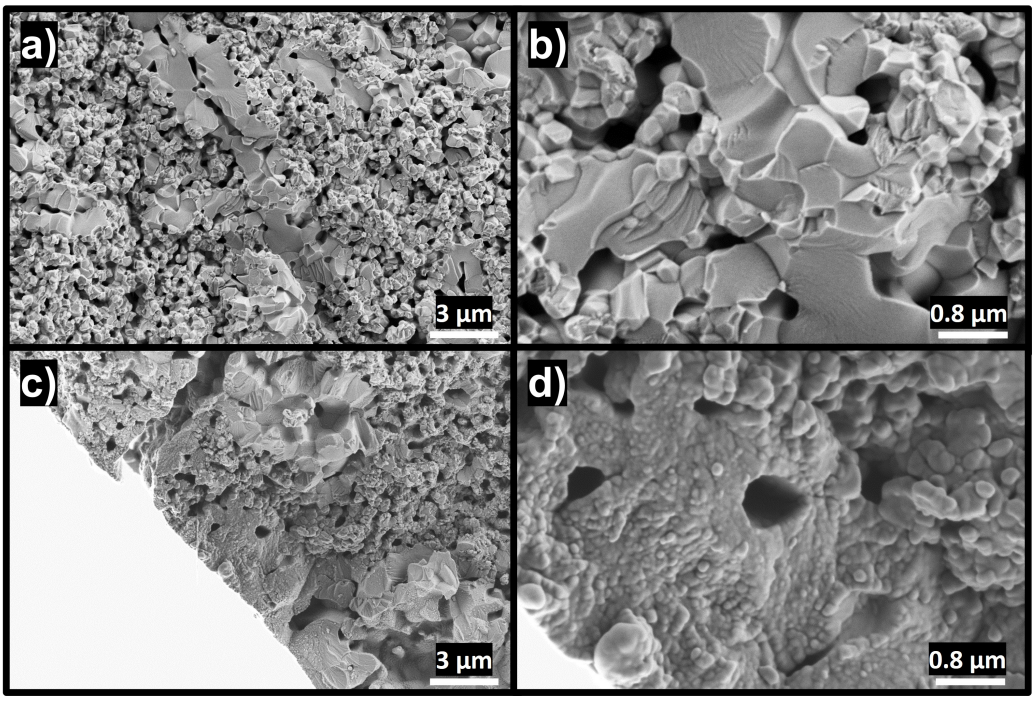


Figure A.19: SEM images of the fractured cross section of pre-sintered $Y_{0.15}Hf_{0.85}O_{1.925}$ before (a-b) and after (c-d) electrical loading.

An EDS map taken at lower magnification shows that a lack of oxygen (Figure

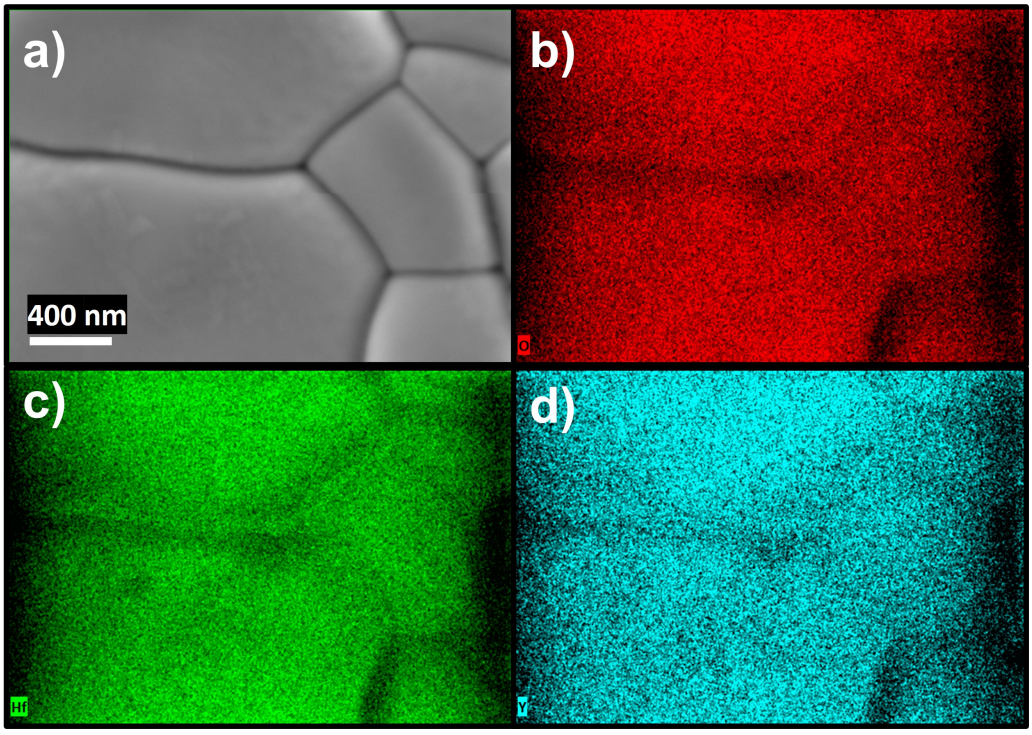


Figure A.20: a) SEM image and b) O, c) Hf and d) Y EDS map of surface of pre-sintered $Y_{0.15}Hf_{0.85}O_{1.925}$ before electrical loading.

A.22 b) occurs up to a depth of 70 μm into the electrically induced coloured area of the sample, where also some Y-rich regions (Figure A.22 d) are visible.

EDS spectra taken from the electrically loaded and oxygen deficient, and the mostly unreduced oxygen rich regions, are shown in Figure A.22 e). The results show that the amount of oxygen after electrical loading and colouring is $\approx$ 50 % of the oxygen content detected in white regions of the sample.

Furthermore, minor changes in the amount of Y and N are detected after electrical loading.

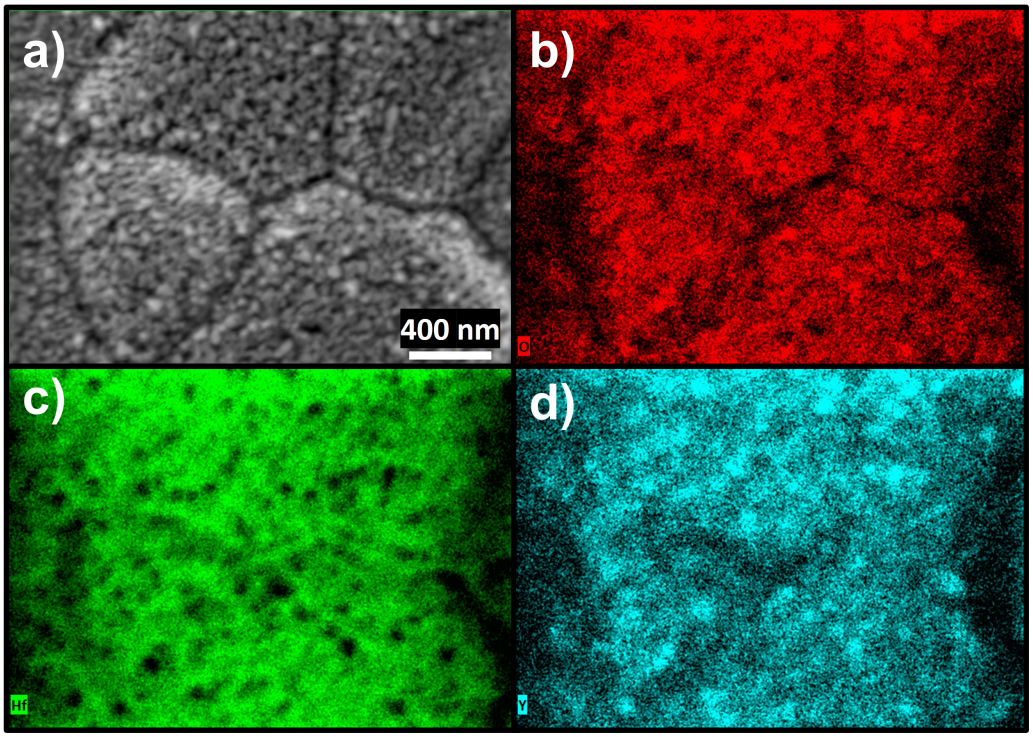


Figure A.21: a) SEM image and b) O, c) Hf and d) Y EDS map of surface of pre-sintered and electrically loaded $Y_{0.15}Hf_{0.85}O_{1.925}$.

The most likely explanation is an ongoing Y segregation from the regions with lower oxygen content, where the material changed its colour. Furthermore, the diffusion of N into the material in-between the electrical loading process and SEM/EDS-characterisation, which was $\approx$ 2 days.

A.3.2 Room temperature electrical resistivity

Electrical resistivity at room temperature was measured after electrical loading using a hand-held voltmeter. An electrical resistance of 9.5 Ω was measured between the two holes on either side of the samples, previously used for connecting

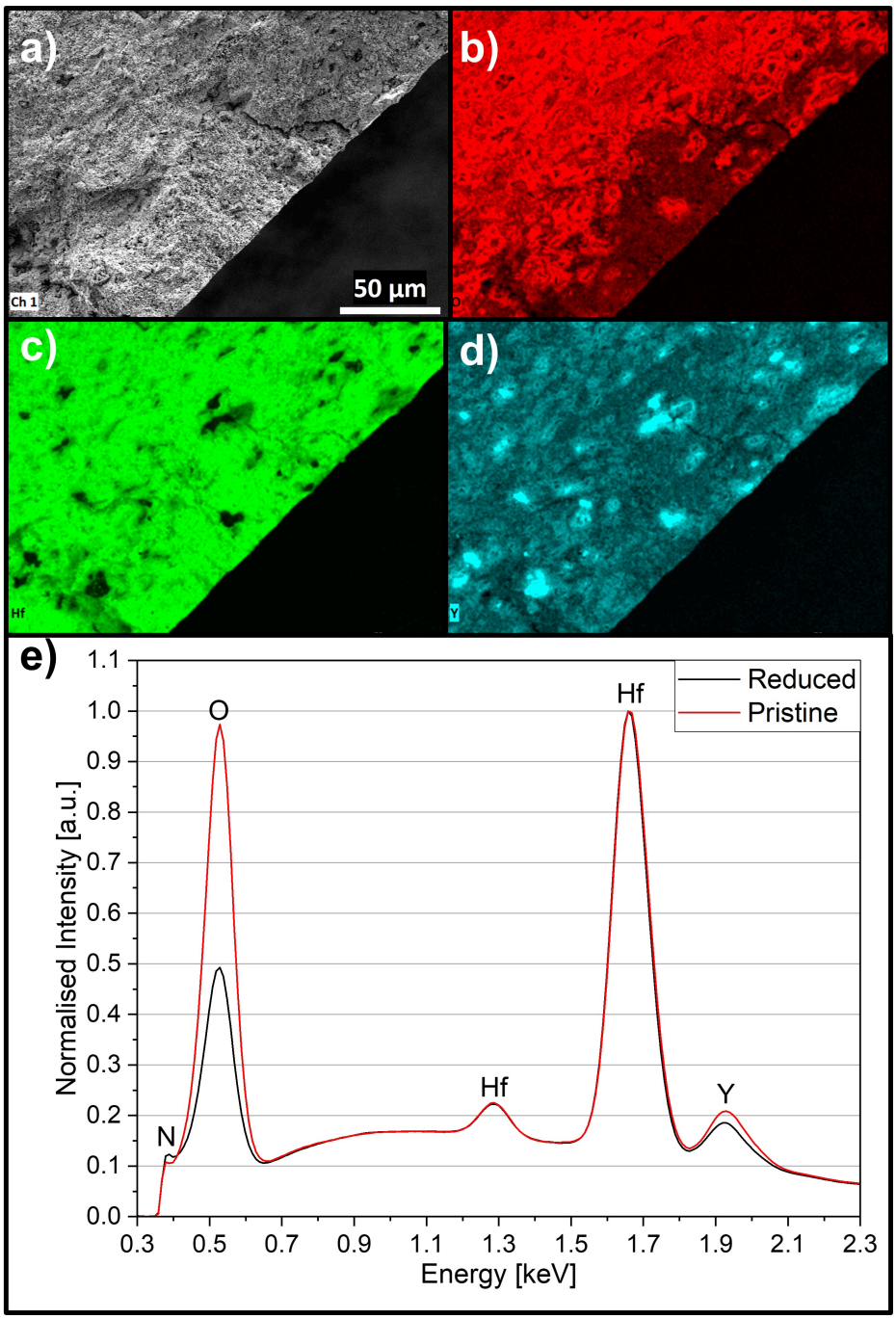


Figure A.22: a) SEM image and b) O, c) Hf and d) Y EDS map of fractured cross section of electrically loaded $Y_{0.15}Hf_{0.85}O_{1.925}$; e) shows the for Hf-normalised detected EDS-spectra from pristine and reduced $Y_{0.15}Hf_{0.85}O_{1.925}$.

electrodes to the sample.

For unreduced $Y_{0.15}Hf_{0.85}O_{1.925}$ the electrical resistance exceeded the measurable range of the voltmeter. Thus, no resistance was measurable at room temperature.

If the whole sample (cross section) of the electrically loaded material is considered to be equally conductive, the electrical resistivity of the material would be 185 Ω/cm. Since, it is known that not all of the material changed its structure to the same extend, the actual electrical resistivity of the transformed regions is much lower and approaches rather metallic levels.

A.3.3 Discussion

Like for YSZ, the electrochemical reduction of yttria-doped hafnia was investigated and the effects of electrochemical reduction on yttria-doped hafnia will be discussed in this section. In general a comparable behaviour was observed as presented and discussed for YSZ.

A.3.3.1 Original phase composition

The pre-sintered samples consists of monoclinic hafnia ($\approx$ 23 wt.%) and cubic fluorite structure yttria stabilised hafnia with a refined lattice parameter of a = 0.5125 nm. The XRD spectra show small peaks for unreacted yttria (Appendix Figure A.17) which points towards yttrium not being completely diffused and

homogeneously distributed, which is confirmed by EDS (Figure A.22).

Since other investigations reported a single cubic fluorite phase composition (a= 0.5115 nm)[315] by using the same composition ($Y_{0.15}Hf_{0.85}O_{1.925}$), this result makes sense. The difference can be found in a more extensive powder processing and sintering at higher temperatures (1750 °C) for longer (16 h) in the other investigation [315].

Thus, the composition of the pre-sintered sample before electrical loading is cubic fluorite yttria-stabilised hafnia with a stoichiometry of $Y_{0.2}Hf_{0.8}O_{1.9}$ rather than $Y_{0.15}Hf_{0.85}O_{1.925}$, a monoclinic hafnia phase which is almost pure HfO_2, and a small amount of unreacted yttria (Y_2O_3).

A.3.3.2 Local hot spot formation on sample surface

At the beginning of the electrical loading process conductivity is mostly ionic as long as the current remains on a low level as it was pointed out by Grimley and Mitterdorfer et al. [27, 104, 105] in the context of FS YSZ.

However, under the present conditions, particularly when the atmosphere is changed from air to Ar, electrochemical reduction of the material happens and the ionic-based conduction shifts towards electronic.

Since the local hot spots on the $Y_{0.15}Hf_{0.85}O_{1.925}$ and YSZ sample surface as well as the locally heated electrode/material-interface only appear at the beginning of

the electrical loading process, where ionic conduction dominates, the most likely explanation for both phenomena is the reduction/oxidation of O-ions at these locations which generates heat. After the electrochemically induced change to electronic conduction the electrode resistance drops significantly and no atmospheric O is reacted on the surface and no heat is generated.

Raman spectroscopy of the hot spot region shows fundamental changes in the materials structure. The spectrum points towards the formation of cubic hafnia (c*) which is formed after the introduction of abundant oxygen vacancies due to the electrochemical reduction in this area. Such a behaviour was reported in investigations about electrical loading and FS of YSZ [229, 241].

The stage of reduction in which the material is in the hot spot region, is most likely a precursor to what is being reduced to δ-HfO after the reduction continued.

A.3.3.3 The FCC rocksalt HfO phase

Various characterisation techniques showed that FCC rocksalt (δ-)HfO forms after electrochemical reduction of monoclinic and cubic fluorite (yttria stabilised) hafnia. From the conducted XRD-characterisation, Rietveld refinement and Raman spectroscopy it can be concluded that δ-HfO crystallises in a defective FCC rocksalt structure with a lattice parameter of 0.4527 nm which, according to the detected Raman spectra, includes double negative charged oxygen vacancies.

SEM images revealed that reduction leads to the formation of very fine grains ($\approx$ 50 nm) which are significantly smaller than the original grains. Similar behaviour was found for the formation of ZrO.

According to the EDS maps two different kinds of fine grains formed:

I) Grains with high Y-content, which are either cubic fluorite yttria stabilised hafnia with an increased Y-concentration or (almost) pure yttria (Y_2O_3). The latter could be present due to an incomplete reaction, already confirmed by the XRD-spectra, or segregation and agglomeration from yttria-stabilised hafnia regions, as suggested by XRD and previously reported for cubic YSZ.

II) Grains with almost no Y-content, are either the newly formed δ-HfO structure or very small monoclinic HfO_2 grains.

Even if the detected Y-concentration in the δ-HfO structures is low, it can not be ruled out that some Y is still present. However, the XRD-results suggest that δ-HfO is also formed from monoclinic hafnia (HfO_2), which points towards Y being useful for starting ionic conduction and the subsequent electrochemical reduction in the bulk material, but is not absolutely necessary for the following δ-HfO formation.

The metallic lustre, electrical conduction at room temperature and the PTC effect indicate a rather metallic character of δ-HfO.

The electrochemically induced change from the unreduced material being an ionic conductor towards the reduced material being an electronically conductor, is very similar to the reversible resistive switching happening in yttria stabilised hafnia under comparable circumstances [316]. This correlation was recently confirmed by other researchers alongside its correlation to ferroelectric behaviour [317]. Based on these results it seems likely that this effect could lead to the transition from a diamagnetic to a para- or even ferromagnetic behaviour as it was previously discussed for ZrO_2.

A.4 Plasma formation and characteristics during flash sintering of boron carbide

Figure A.23 shows the electrical parameters during Plasma Pre-Treatment Flash Sintering (PPT-FS) of SiC in Ar at 1500 °C furnace temperature, which includes the maintenance of a plasma for ≈ 240 s before the plasma collapses and transitions to Joule heating of the sample.

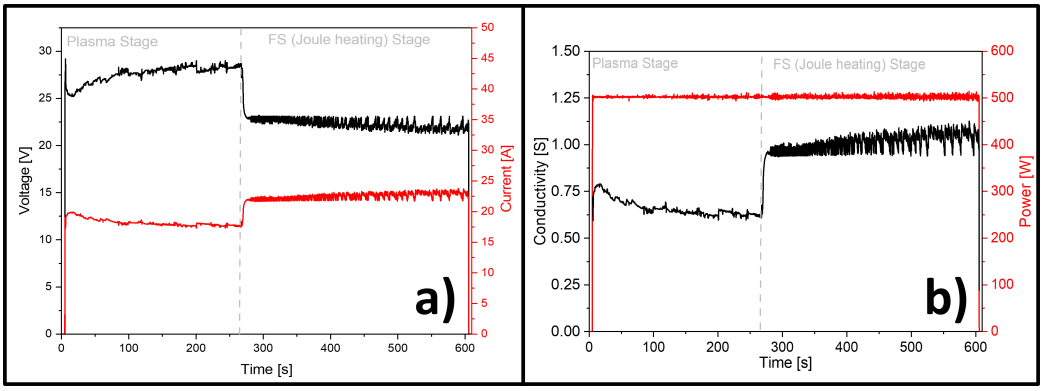


Figure A.23: Electrical parameters a) voltage and current and b) conductivity and power recorded during PPT-FS of SiC.

Figure A.24 shows the setup used for the investigation of the breakdown voltage (VB) in various atmospheres without a mounted sample.

In addition to the experimentally measured VB values, calculations were conducted according to Paschen's law. The following equation was used to calculate Paschen curves, which includes the temperature correction proposed by Peek [268]. The results are summarised in Figure A.25.

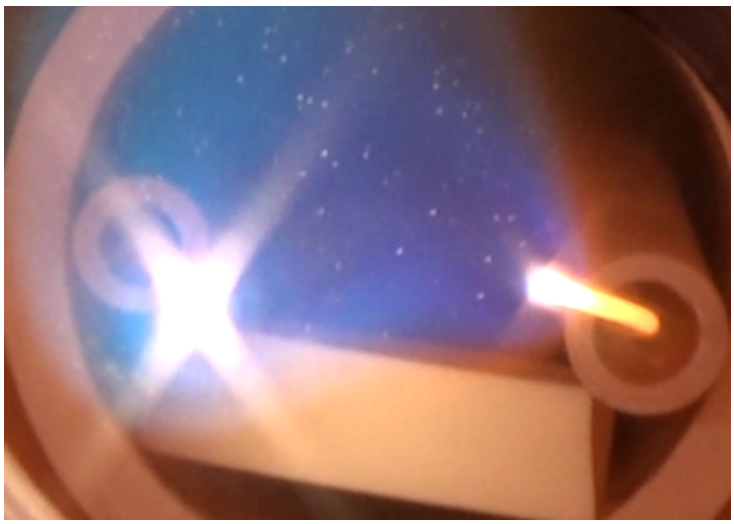


Figure A.24: Experimental setup for measuring the atmospheric breakdown voltage without a sample mounted between electrodes.

$$V_B = \frac{BPd}{\ln(P \cdot d \cdot A) - \ln\left(\ln\left(1+\frac{1}{\gamma}\right)\right)} \cdot \frac{T_0}{T}$$

Where:

VB breakdown voltage,

A (11.5 $cm^{-1}Torr^{-1}$, [318]),

B (176 $Vcm^{-1}Torr^{-1}$, [318]),

γ Townsend's second ionization coefficient (2.5 * 10^{-2}, [318])

P pressure (760 Torr),

d electrode distance (variable),

T is temperature,

T_0 room temperature (25 °C).

A and B are related to the ionisation cross section of the gas particles but were considered as being constant for a given atmosphere, Ar in this case.

For a furnace temperature of 1500 °C, as used in this work, VB-values of ≈ 2.9 kV and ≈ 5.5 kV are calculated for electrode distances of 1 and 2 cm respectively.

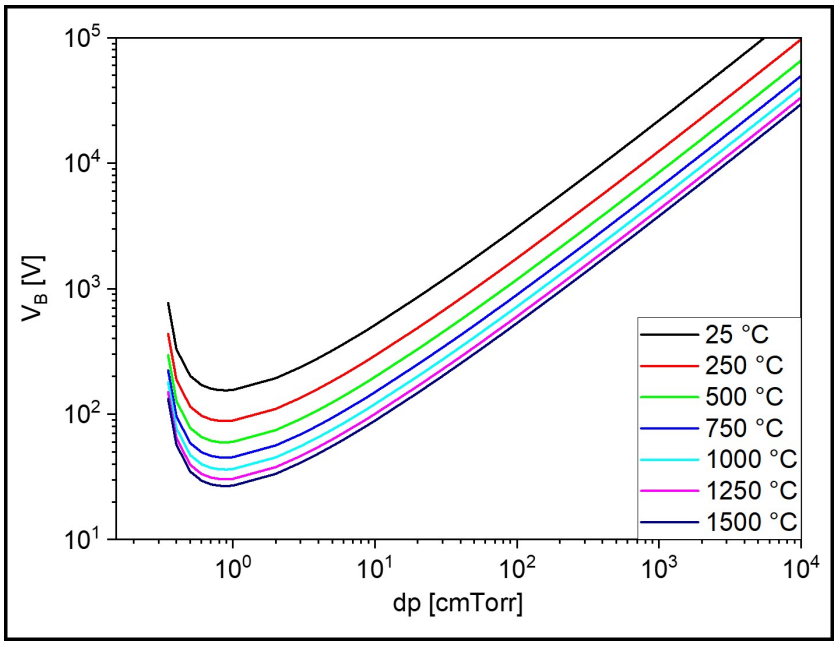


Figure A.25: Calculated Paschen Curve for Ar-atmosphere including temperature correction for various temperatures between 25 °C and 1500 °C.

Figure A.26, which is comparable to Figure 4.9 a), shows the spectra emitted from a horizontal alumina tube furnace at various temperatures showing the emergence of three distinct peaks at temperatures exceeding 1200 °C. All that matters for the present investigation is that they are emitted by the furnace tube rather than the sample itself. It is suggested that these may represent photoluminescence in response to the black body radiation at high temperature. The peak at 590 nm

may be sodium d-light from impurities introduced by the Bayer process, which seems plausible to the authors. In some respects, the doublet around 770 nm resembles the R-lines caused by the Cr^{3+} impurities commonly present in alumina. At room temperature, these are at around 694 nm but their wavelengths are known to increase with temperature, and a crude extrapolation of the low temperature results of He and Clarke [319] indicates that wavelengths in excess of 700 nm are reasonable. However, He and Clarke also find that the peaks broaden with increasing temperature and both the intensity ratio and the fact that the stronger of the two peaks in our work is at the lower wavelength are not consistent with room temperature results. Further investigation would be needed to understand these peaks more fully.

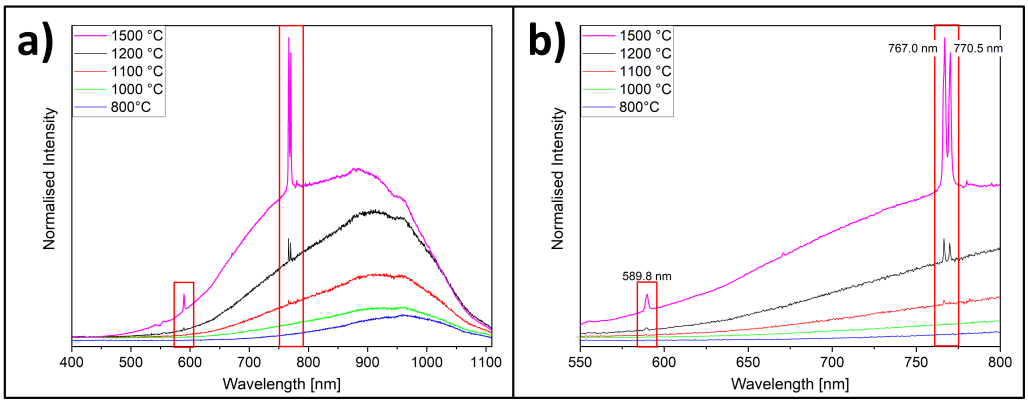


Figure A.26: Emitted spectra from a horizontal alumina tube furnace at various temperatures showing the emergence of three peaks (590, 767 and 770 nm) at temperatures exceeding 1200 °C.

Figure A.27 shows the spectrum emitted during a 400 W Ar-plasma formation in a 1500 °C hot horizontal alumina tube furnace with an Al_2O_3 sample mounted

between the electrodes. Based on this experiment and experiments with a B_4C sample, or with no sample mounted, the origin of the main peaks was determined. Peaks at 394, 396, 590, 670, 767, 770 nm can be associated with Al [320, 321], peaks located at 469, 485 and 511 nm as AlO [322], the peaks 818 and 819 nm can most likely be associated with CIII peaks according to the NIST database [283].

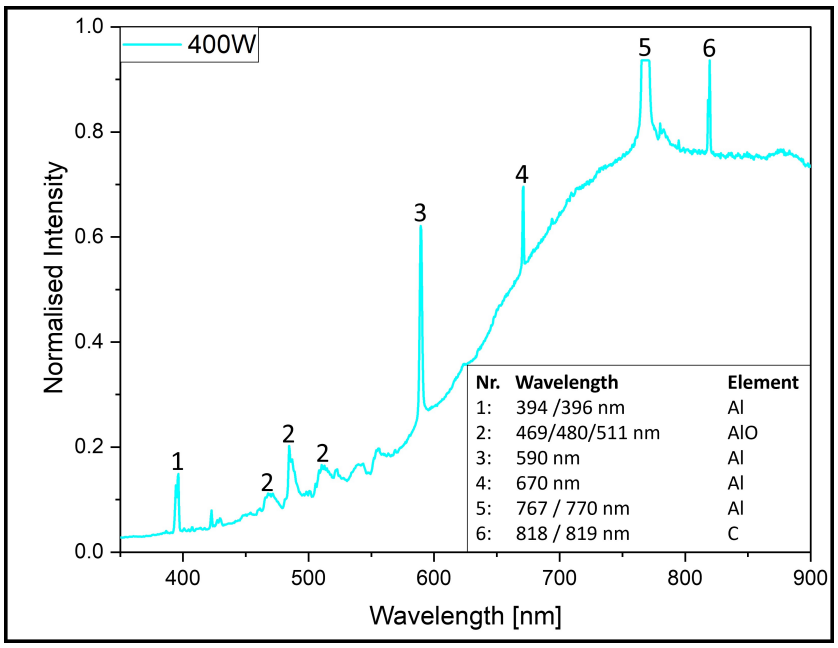


Figure A.27: Emitted spectrum during the formation of a 400 W Ar-plasma including positions of the detected peaks and labeling dependent on the element causing the emission.

Figure A.28 shows a SiC-sample surface after the plasma stage with a few cracks located on the surface where unusually big and well-structured crystals were deposited.

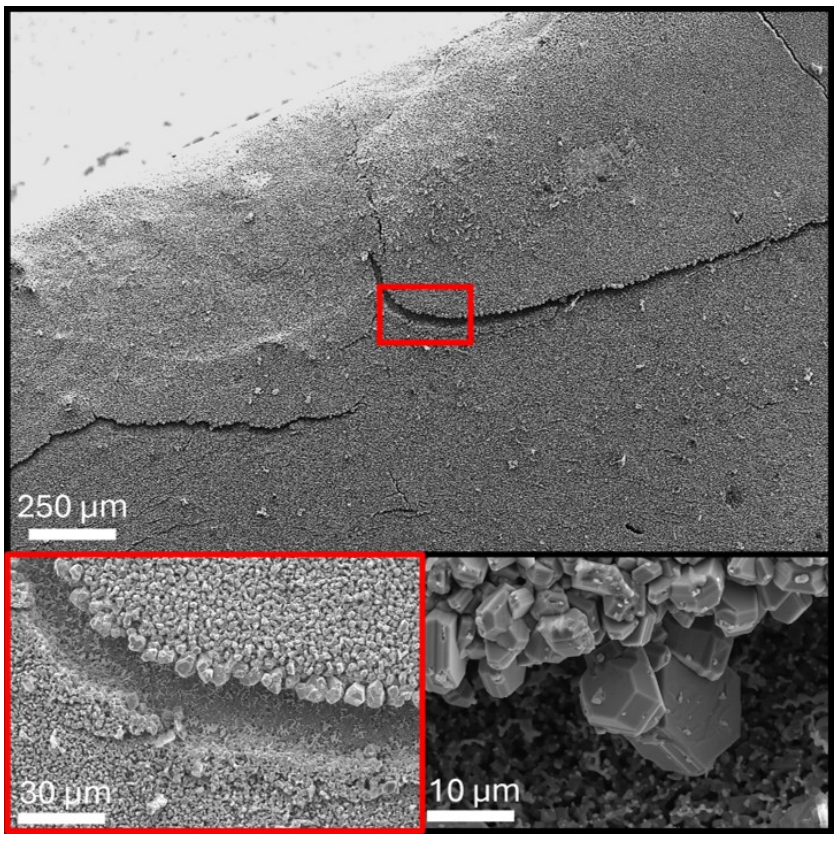


Figure A.28: SiC sample surface after the plasma formation which shows unusually big and well-structured crystals deposited along cracks. The field direction is from the bottom left (anode side) to the top right (cathode side) corner of the image.

Bibliography

[1] Walther Nernst, "Verfahren zur Erzeugung von elektrischem Glühlicht," 7 1897.

[2] C. C. Garrard, "The Nernst Lamp," *Nature*, vol. 67, pp. 67–68, 11 1902.

[3] A. L. Duval D'Adrian, "Article of fused metallic oxide and process of producing the same," 10 1922.

[4] M. Cologna, B. Rashkova, and R. Raj, "Flash Sintering of Nanograin Zirconia in 5 s at 850°C," *Journal of the American Ceramic Society*, vol. 93, no. 11, pp. 3556–3559, 2010.

[5] R. I. Todd, E. Zapata-Solvas, R. S. Bonilla, T. Sneddon, and P. R. Wilshaw, "Electrical characteristics of flash sintering: thermal runaway of Joule heating," *Journal of the European Ceramic Society*, vol. 35, no. 6, pp. 1865–1877, 2015.

[6] R. I. Todd, "Flash Sintering of Ceramics: A Short Review," in *Proceedings of the IV advanced ceramics and applications conference* (B. Lee, R. Gadow, and V. Mitic, eds.), pp. 1–12, Amsterdam and Hong Kong and Paris: Atlantis Press, 2017.

[7] E. Zapata-Solvas, S. Bonilla, P. R. Wilshaw, and R. I. Todd, "Preliminary investigation of flash sintering of SiC," *Journal of the European Ceramic Society*, vol. 33, no. 13-14, pp. 2811–2816, 2013.

[8] M. Biesuz and V. M. Sglavo, "Flash sintering of ceramics," *Journal of the European Ceramic Society*, vol. 39, pp. 115–143, 2 2019.

[9] M. Biesuz, P. Luchi, A. Quaranta, A. Martucci, and V. M. Sglavo, "Photoemission during flash sintering: An interpretation based on thermal radiation," *Journal of the European Ceramic Society*, vol. 37, pp. 3125–3130, 8 2017.

[10] S. Grasso, T. Saunders, H. Porwal, B. Milsom, A. Tudball, and M. Reece,

"Flash Spark Plasma Sintering (FSPS) of alpha and beta SiC," *Journal of the American Ceramic Society*, vol. 99, no. 5, pp. 1534–1543, 2016.

[11] M. Biesuz, R. Sedlák, T. Saunders, A. Kovalčíková, J. Dusza, M. Reece, D. Zhu, C. HU, and S. Grasso, "Flash spark plasma sintering of 3YSZ," *Journal of the European Ceramic Society*, vol. 39, no. 5, pp. 1932–1937, 2019.

[12] T. Saunders, S. Grasso, and M. J. Reece, "Ultrafast-Contactless Flash Sintering using Plasma Electrodes," *Scientific Reports*, vol. 6, no. 1, p. 27222, 2016.

[13] J. Dong, Z. Wang, X. Zhao, M. Biesuz, T. Saunders, Z. Zhang, C. Hu, and S. Grasso, "Contactless flash sintering based on cold plasma," *Scripta Materialia*, vol. 175, pp. 20–23, 1 2020.

[14] Y. V. Bykov, S. V. Egorov, A. G. Eremeev, V. V. Kholoptsev, K. I. Rybakov, and A. A. Sorokin, "Flash Microwave Sintering of Transparent Yb:(LaY)2O3 Ceramics," *Journal of the American Ceramic Society*, vol. 98, pp. 3518–3524, 11 2015.

[15] Y. V. Bykov, S. V. Egorov, A. G. Eremeev, V. V. Kholoptsev, I. V. Plotnikov, K. I. Rybakov, and A. A. Sorokin, "On the mechanism of microwave flash sintering of ceramics," *Materials*, vol. 9, 8 2016.

[16] C. Manière, G. Lee, T. Zahrah, and E. A. Olevsky, "Microwave flash sintering of metal powders: From experimental evidence to multiphysics simulation," *Acta Materialia*, vol. 147, pp. 24–34, 4 2018.

[17] M. Kermani, M. Biesuz, J. Dong, H. Deng, M. Bortolotti, A. Chiappini, M. J. Reece, V. M. Sglavo, C. Hu, and S. Grasso, "Flash cold sintering: Combining water and electricity," *Journal of the European Ceramic Society*, vol. 40, pp. 6266–6271, 12 2020.

[18] E. Gil-González, A. Perejón, P. E. Sánchez-Jiménez, M. J. Sayagués, R. Raj, and L. A. Pérez-Maqueda, "Phase-pure BiFeO3 produced by reaction flash-sintering of Bi2O3 and Fe2O3," *Journal of Materials Chemistry A*, vol. 6, pp. 5356–5366, 3 2018.

[19] E. Gil-González, L. A. Pérez-Maqueda, P. E. Sánchez-Jiménez, and A. Perejón, "Flash Sintering Research Perspective: A Bibliometric Analysis," *Materials*, vol. 15, p. 416, 1 2022.

[20] R. Raj, "Joule heating during flash-sintering," *Journal of the European Ceramic Society*, vol. 32, no. 10, pp. 2293–2301, 2012.

[21] R. Raj, M. Cologna, and J. S. C. Francis, "Influence of Externally Imposed and Internally Generated Electrical Fields on Grain Growth, Diffusional Creep, Sintering and Related Phenomena in Ceramics," *Journal of the American Ceramic Society*, vol. 94, no. 7, pp. 1941–1965, 2011.

[22] M. Cologna, A. L. G. Prette, and R. Raj, "Flash-Sintering of Cubic Yttria-Stabilized Zirconia at 750°C for Possible Use in SOFC Manufacturing," *Journal of the American Ceramic Society*, vol. 94, no. 2, pp. 316–319, 2011.

[23] Y. Zhang and J. Luo, "Promoting the flash sintering of ZnO in reduced atmospheres to achieve nearly full densities at furnace temperatures of 120 °C," *Scripta Materialia*, vol. 106, pp. 26–29, 2015.

[24] Y. Zhang, J.-I. Jung, and J. Luo, "Thermal runaway, flash sintering and asymmetrical microstructural development of ZnO and ZnO-Bi2O3 under direct currents," *Acta Materialia*, vol. 94, pp. 87–100, 2015.

[25] M. Yoshida, S. Falco, and R. I. Todd, "Measurement and modelling of electrical resistivity by four-terminal method during flash sintering of 3YSZ," *Journal of the Ceramic Society of Japan*, vol. 126, no. 7, pp. 579–590, 2018.

[26] A. Gibson, Y. Li, R. S. Bonilla, and R. I. Todd, "Pressureless flash sintering of α-SiC: Electrical characteristics and densification," *Acta Materialia*, vol. 241, p. 118362, 12 2022.

[27] C. A. Grimley, A. L. Prette, and E. C. Dickey, "Effect of boundary conditions on reduction during early stage flash sintering of YSZ," *Acta Materialia*, vol. 174, pp. 271–278, 8 2019.

[28] A. Alvarez, Y. Dong, and I. W. Chen, "DC electrical degradation of YSZ: Voltage-controlled electrical metallization of a fast ion conducting insulator," *Journal of the American Ceramic Society*, vol. 103, pp. 3178–3193, 5 2020.

[29] J. Janek and C. Korte, "Electrochemical blackening of yttria-stabilized zirconia - Morphological instability of the moving reaction front," *Solid State Ionics*, vol. 116, no. 3-4, pp. 181–195, 1999.

[30] M. Biesuz, L. Pinter, T. Saunders, M. Reece, J. Binner, V. M. Sglavo, and S. Grasso, "Investigation of Electrochemical, Optical and Thermal Effects during Flash Sintering of 8YSZ," *Materials 2018, Vol. 11, Page 1214*, vol. 11, p. 1214, 7 2018.

[31] I. Wynn Jones and L. J. Miles, "Production of Beta- Al2O3 electrolyte," *Proc Brit Ceram Soc*, no. 19, pp. 161 – 178, 1971.

[32] M. Harmer, E. W. Roberts, and R. J. Brook, "Rapid sintering of pure and doped alpha-Al2O3.," *Trans J Brit Ceram Soc*, vol. 78, pp. 22 – 25, 1 1979.

[33] M. P. Harmer and R. J. Brook, "Fast Firing - Microstructural Benefits," *Trans. J. Br. Ceram. Soc.*, vol. 80, no. 5, pp. 147–148, 1981.

[34] E. L. Kemer and D. L. Johnson, "Microwave plasma sintering of alumina," *American Ceramic Society Bulletin*, vol. 64, pp. 1132 – 1136, 8 1985.

[35] S. L. Dole, *Ph.D. Thesis*. 1985.

[36] S. L. Dole and S. Prochazka, "Densification and Microstructure Development in Boron Carbide," in *Proceedings of the 9th Annual Conference on Composites and Advanced Ceramic Materials: Ceramic Engineering and Science Proceedings, Volume 6, Issue 7/8* (W. Smothers, ed.), vol. 6 of *Ceramic Engineering and Science Proceedings*, pp. 1151–1160, Hoboken, NJ, USA: John Wiley & Sons, Inc, 1985.

[37] S. L. Dole, S. Prochazka, and R. H. Doremus, "Microstructural Coarsening During Sintering of Boron Carbide," *Journal of the American Ceramic Society*, vol. 72, no. 6, pp. 958–966, 1989.

[38] W. Ji, B. Parker, S. Falco, J. Y. Zhang, Z. Y. Fu, and R. I. Todd, "Ultra-fast firing: Effect of heating rate on sintering of 3YSZ, with and without an electric field," *Journal of the European Ceramic Society*, vol. 37, pp. 2547–2551, 6 2017.

[39] J. Lebrun and R. Raj, "A First Report of Photoemission in Experiments Related to Flash Sintering," *Journal of the American Ceramic Society*, vol. 97, pp. 2427–2430, 2014.

[40] K. Terauds, J.-M. Lebrun, H.-H. Lee, T.-Y. Jeon, S.-H. Lee, J. H. Je, and R. Raj, "Electroluminescence and the measurement of temperature during Stage III of flash sintering experiments," *Journal of the European Ceramic Society*, vol. 35, no. 11, pp. 3195–3199, 2015.

[41] E. Bichaud, J. Chaix, C. Carry, M. Kleitz, and M. Steil, "Flash sintering incubation in Al2O3/TZP composites," *Journal of the European Ceramic Society*, vol. 35, pp. 2587–2592, 9 2015.

[42] J. G. Da Pereira Silva, J. M. Lebrun, H. A. Al Qureshi, R. Janssen, and R. Raj, "Temperature Distributions During Flash Sintering of 8% Yttria-Stabilized Zirconia," *Journal of the American Ceramic Society*, vol. 98, no. 11, pp. 3525–3528, 2015.

[43] M. Biesuz and V. M. Sglavo, "Flash sintering of alumina: Effect of different operating conditions on densification," *Journal of the European Ceramic Society*, vol. 36, no. 10, pp. 2535–2542, 2016.

[44] W. Ji, J. Zhang, W. Wang, Z. Fu, and R. I. Todd, "The microstructural origin of rapid densification in 3YSZ during ultra-fast firing with or without an electric field," *Journal of the European Ceramic Society*, vol. 40, pp. 5829–5836, 12 2020.

[45] Y. Zhang, J. Nie, J. M. Chan, and J. Luo, "Probing the densification mechanisms during flash sintering of ZnO," *Acta Materialia*, vol. 125, pp. 465–475, 2 2017.

[46] M. Schie, S. Menzel, J. Robertson, R. Waser, and R. A. de Souza, "Field-

enhanced route to generating anti-Frenkel pairs in HfO2," *Physical Review Materials*, vol. 2, no. 3, 2018.

[47] K. Naik, S. K. Jha, and R. Raj, "Correlations between conductivity, electroluminescence and flash sintering," *Scripta Materialia*, vol. 118, pp. 1–4, 6 2016.

[48] R. Kirchheim, "On the mixed ionic and electronic conductivity in polarized yttria stabilized zirconia," *Solid State Ionics*, vol. 320, pp. 239–258, 7 2018.

[49] R. Muccillo and E. N. S. Muccillo, "Light emission during electric field-assisted sintering of electroceramics," *Journal of the European Ceramic Society*, vol. 35, no. 5, pp. 1653–1656, 2015.

[50] D. Yadav and R. Raj, "Two unique measurements related to flash experiments with yttria-stabilized zirconia," *Journal of the American Ceramic Society*, vol. 100, pp. 5374–5378, 12 2017.

[51] R. R. Ingraci Neto and R. Raj, "The flash effect in electronic conductors The case of amorphous carbon fibers," *Scripta Materialia*, vol. 179, pp. 20–24, 4 2020.

[52] L. Cross, R. Raj, and S. I. Jalali, "On the catalytic effect of zirconia on flash sintering of alumina," *Journal of the American Ceramic Society*, vol. 105, pp. 3746–3752, 6 2022.

[53] S. Jo, S. I. A. Jalali, and R. Raj, "Flash in argon atmosphere yields electronically conducting yttria-stabilized zirconia at ambient temperature," *Journal of the American Ceramic Society*, 5 2023.

[54] H. Okamoto, "O-Zr (Oxygen-Zirconium)," *Journal of Phase Equilibria and Diffusion*, vol. 28, pp. 498–498, 10 2007.

[55] P. Li, I. Chen, and J. E. PennerâHahn, "Effect of Dopants on Zirconia Stabilization-An X-ray Absorption Study: II, Tetravalent Dopants," *Journal of the American Ceramic Society*, vol. 77, pp. 1281–1288, 5 1994.

[56] R. Todd and M. Saran, "Transformation toughening," in *Materials Process-*

ing Handbook (J. R. Groza, ed.), vol. 20, pp. 1–20, Boca Raton, FL, USA,: CRC Press, 2007.

[57] R. A. Miller, J. L. Smialek, and R. G. Garlick, "Phase stability in plasma-sprayed, partially stabilized zirconia-yttria," *Journal of the American Ceramic Society*, vol. 3, no. 241, 1981.

[58] C. Viazzi, J. P. Bonino, F. Ansart, and A. Barnabé, "Structural study of metastable tetragonal YSZ powders produced via a sol-gel route," *Journal of Alloys and Compounds*, vol. 452, pp. 377–383, 3 2008.

[59] M. Yashima, M. Kakihana, and M. Yoshimura, "Metastable-stable phase diagrams in the zirconia-containing systems utilized in solid-oxide fuel cell application," *Solid State Ionics*, vol. 86-88, pp. 1131–1149, 7 1996.

[60] H. G. Scott, "Phase relationships in the zirconia-yttria system," *Journal of Materials Science*, vol. 10, pp. 1527–1535, 9 1975.

[61] R. C. Garvie, R. H. Hannink, and R. T. Pascore, "Ceramic steel?," *Nature*, vol. 258, pp. 703–704, 12 1975.

[62] R. H. J. Hannink, P. M. Kelly, and B. C. Muddle, "Transformation Toughening in ZirconiaâContaining Ceramics," *Journal of the American Ceramic Society*, vol. 83, pp. 461–487, 3 2000.

[63] S. Deville, J. Chevalier, G. Fantozzi, J. F. Bartolomé, J. Requena, J. S. Moya, R. Torrecillas, and L. A. DÄ±az, "$Low - temperatureageingofzirconia - toughenedaluminaceramicsanditsimpli$ $-2982, 12003$.

[64] M. Yashima, M. Kakihana, K. Ishii, Y. Ikuma, and M. Yoshimura, "Synthesis of metastable tetragonal zirconia-calcia solid solution by pyrolysis of organic precursors and coprecipitation route," *Journal of Materials Research*, vol. 11, pp. 1410–1420, 6 1996.

[65] D. G. Lamas and N. E. Walsöe De Reca, "X-ray diffraction study of compositionally homogeneous, nanocrystalline yttria-doped zirconia powders," *Journal of Materials Science*, vol. 35, no. 22, pp. 5563–5567, 2000.

[66] S. Fabris, A. T. Paxton, and M. W. Finnis, "A stabilization mechanism of zirconia based on oxygen vacancies only," *Acta Materialia*, vol. 50, pp. 5171–5178, 12 2002.

[67] K. Kobayashi, H. Kuwajima, and T. Masaki, "Phase change and mechanical properties of ZrO2-Y2O3 solid electrolyte after ageing," *Solid State Ionics*, vol. 3-4, pp. 489–493, 8 1981.

[68] T. Sato and M. Shimada, "Transformation of Yttria-Doped Tetragonal ZrO2 Polycrystals by Annealing in Water," *Journal of the American Ceramic Society*, vol. 68, pp. 356–356, 6 1985.

[69] J. Chevalier, L. Gremillard, and S. Deville, "Low-Temperature Degradation of Zirconia and Implications for Biomedical Implants," *Annual review of materials research*, vol. 37, no. 1, pp. 1–32, 2007.

[70] J. Chevalier, L. Gremillard, A. V. Virkar, and D. R. Clarke, "The Tetragonal-Monoclinic Transformation in Zirconia: Lessons Learned and Future Trends," *Journal of the American Ceramic Society*, vol. 92, pp. 1901–1920, 9 2009.

[71] J. F. Bartolome, I. Montero, M. Diaz, S. Lopez-Esteban, J. S. Moya, S. Deville, L. Gremillard, J. Chevalier, and G. Fantozzi, "Accelerated Aging in 3-mol%-Yttria-Stabilized Tetragonal Zirconia Ceramics Sintered in Reducing Conditions," *Journal of the American Ceramic Society*, vol. 87, pp. 2282–2285, 12 2004.

[72] H. Schubert and F. Frey, "Stability of Y-TZP during hydrothermal treatment: neutron experiments and stability considerations," *Journal of the European Ceramic Society*, vol. 25, pp. 1597–1602, 6 2005.

[73] M. Yoshimura, T. Noma, K. Kawabata, and S. Sōmiya, "Role of H2O on the degradation process of Y-TZP," *Journal of Materials Science Letters*, vol. 6, pp. 465–467, 4 1987.

[74] X. Guo, "Property Degradation of Tetragonal Zirconia Induced by Low-Temperature Defect Reaction with Water Molecules," *Chemistry of Materials*, vol. 16, pp. 3988–3994, 10 2004.

[75] R. De Souza and G. Harrington, "Revisiting point defects in ionic solids and semiconductors," *Nature Materials*, vol. 22, pp. 794–797, 7 2023.

[76] K. Momma and F. Izumi, "VESTA a three-dimensional visualization system for electronic and structural analysis," *Journal of Applied Crystallography*, vol. 41, pp. 653–658, 6 2008.

[77] J. M. Lebrun, S. K. Jha, S. J. McCormack, W. M. Kriven, R. Raj, and H. Chan, "Broadening of Diffraction Peak Widths and Temperature Nonuniformity During Flash Experiments," *Journal of the American Ceramic Society*, vol. 99, pp. 3429–3434, 10 2016.

[78] J. M. Lebrun, T. G. Morrissey, J. S. Francis, K. C. Seymour, W. M. Kriven, and R. Raj, "Emergence and Extinction of a New Phase During On-Off Experiments Related to Flash Sintering of 3YSZ," *Journal of the American Ceramic Society*, vol. 98, pp. 1493–1497, 5 2015.

[79] H. Charalambous, S. K. Jha, J. S. Okasinski, and T. Tsakalakos, "Generation of electric-field stabilized zirconium monoxide secondary phase within cubic zirconia," *Scripta Materialia*, vol. 190, pp. 22–26, 1 2021.

[80] N. Schönberg, G. Heimbürger, E. J. Matikkala, and N. A. Sörensen, "The Structure of the Metallic Quaternary Phase ZrTaNO.," *Acta Chemica Scandinavica*, vol. 8, pp. 627–629, 1954.

[81] R. J. Nicholls, N. Ni, S. Lozano-Perez, A. London, D. W. Mccomb, P. D. Nellist, C. R. M. Grovenor, C. J. Pickard, and J. R. Yates, "Crystal Structure of the ZrO Phase at Zirconium/Zirconium Oxide Interfaces," 2014.

[82] O. R. J. Ackermann, S. P. Garg, and E. G. Rauh, "High-Temperature Phase Diagram for the System Zr.," *Journal of the American Ceramic Society*, vol. 60, pp. 341–345, 7 1977.

[83] N. Morisaki, H. Yoshida, K. Matsui, T. Tokunaga, K. Sasaki, and T. Yamamoto, "Synthesis of zirconium oxynitride in air under DC electric fields," *Applied Physics Letters*, vol. 109, p. 083104, 8 2016.

[84] Y. Gu, F. Guo, Y. Qian, H. Zheng, and Z. Yang, "A benzene-thermal synthesis of

powdered cubic zirconium nitride," *Materials Letters*, vol. 57, pp. 1679–1682, 3 2003.

[85] A. N. Christensen, V. Romano, R. Hesse, A. F. Andresen, and P. Fischer, "A Neutron Diffraction Investigation on Single Crystals of Titanium Carbide, Titanium Nitride, and Zirconium Nitride.," *Acta Chemica Scandinavica*, vol. 29a, pp. 563–564, 1975.

[86] R. K. Kathiria, S. Jo, R. Raj, and D. Yadav, "In flash immersion and quench of yttria stabilized zirconia into liquid nitrogen yields an electronic conductor," *Journal of the American Ceramic Society*, vol. 105, pp. 1635–1639, 3 2022.

[87] J. Kilner and C. Waters, "The effects of dopant cation-oxygen vacancy complexes on the anion transport properties of non-stoichiometric fluorite oxides," *Solid State Ionics*, vol. 6, pp. 253–259, 5 1982.

[88] A. Nakamura and J. B. Wagner, "Defect Structure, Ionic Conductivity, and Diffusion in Yttria Stabilized Zirconia and Related Oxide Electrolytes with Fluorite Structure," *Journal of The Electrochemical Society*, vol. 133, pp. 1542–1548, 8 1986.

[89] O. Yamamoto, Y. Arachi, H. Sakai, Y. Takeda, N. Imanishi, Y. Mizutani, M. Kawai, and Y. Nakamura, "Zirconia based oxide ion conductors for solid oxide fuel cells," *Ionics*, vol. 4, pp. 403–408, 9 1998.

[90] Y. Arachi, H. Sakai, O. Yamamoto, Y. Takeda, and N. Imanishai, "Electrical conductivity of the ZrO2-Ln2O3 (Ln = lanthanides) system," *Solid State Ionics*, vol. 121, pp. 133–139, 1999.

[91] J. Luo, D. P. Almond, and R. Stevens, "Ionic Mobilities and Association Energies from an Analysis of Electrical Impedance of ZrO2-Y2O3 Alloys," *Journal of the American Ceramic Society*, vol. 83, pp. 1703–1708, 12 2004.

[92] D. W. Strickler and W. G. Carlson, "Ionic Conductivity of Cubic Solid Solutions in the System CaO-Y2O3-ZrO2," *Journal of the American Ceramic Society*, vol. 47, pp. 122–127, 3 1964.

[93] J. M. Dixon, L. D. LaGrange, U. Merten, C. F. Miller, and J. T. Porter, "Electri-

cal Resistivity of Stabilized Zirconia at Elevated Temperatures," *Journal of The Electrochemical Society*, vol. 110, no. 4, p. 276, 1963.

[94] R. E. Casselton, "Low field DC conduction in yttria-stabilized zirconia," *physica status solidi (a)*, vol. 2, pp. 571–585, 7 1970.

[95] R. E. Casselton, "Electrical conductivity of ceria-stabilized zirconia," *physica status solidi (a)*, vol. 1, no. 4, pp. 787–794, 1970.

[96] A. Ioffe, D. Rutman, and S. Karpachov, "On the nature of the conductivity maximum in zirconia-based solid electrolytes," *Electrochimica Acta*, vol. 23, pp. 141–142, 2 1978.

[97] C. Ahamer, A. K. Opitz, G. M. Rupp, and J. Fleig, "Revisiting the Temperature Dependent Ionic Conductivity of Yttria Stabilized Zirconia (YSZ)," *Journal of The Electrochemical Society*, vol. 164, pp. F790–F803, 5 2017.

[98] N. Masó and A. R. West, "Electronic conductivity in Yttria-stabilized zirconia under a small dc bias," *Chemistry of Materials*, vol. 27, pp. 1552–1558, 3 2015.

[99] J. Vazquez-Arce, H. Tiznado, and R. Kirchheim, "Onset of electronic conductivity in nanometer thick films of yttria stabilized zirconia (YSZ) at high electric fields," *Acta Materialia*, vol. 229, p. 117826, 5 2022.

[100] C. A. Fisher and H. Matsubara, "The influence of grain boundary misorientation on ionic conductivity in YSZ," *Journal of the European Ceramic Society*, vol. 19, pp. 703–707, 6 1999.

[101] S. J. Dillon, Y. Shen, and G. S. Rohrer, "Grain boundary energies in yttriaâstabilized zirconia," *Journal of the American Ceramic Society*, vol. 105, pp. 2925–2931, 4 2022.

[102] O. J. Durá, M. A. López de la Torre, L. Vázquez, J. Chaboy, R. Boada, A. Rivera-Calzada, J. Santamaria, and C. Leon, "Ionic conductivity of nanocrystalline yttria-stabilized zirconia: Grain boundary and size effects," *Physical Review B*, vol. 81, p. 184301, 5 2010.

[103] K. S. N. Vikrant and R. E. García, "Charged grain boundary transitions in ionic

ceramics for energy applications," *npj Computational Materials*, vol. 5, p. 24, 2 2019.

[104] A. Mitterdorfer, "Identification of the reaction mechanism of the Pt, O2(g)|yttria-stabilized zirconia system Part I: General framework, modelling, and structural investigation," *Solid State Ionics*, vol. 117, pp. 187–202, 2 1999.

[105] A. Mitterdorfer and L. Gauckler, "Reaction kinetics of the Pt, O2(g)|c-ZrO2 system: precursor-mediated adsorption," *Solid State Ionics*, vol. 120, pp. 211–225, 5 1999.

[106] R. Casselton, "Electricity from M.H.D," *Atomic Energy Agency*, vol. 4, p. 2951, 1968.

[107] R. Casselton and M. Watson, "Science of Ceramics," *British Ceramic Society*, vol. 4, p. 349, 1968.

[108] J. M. Farley, J. S. Thorp, J. S. Ross, and G. A. Saunders, "Effect of current-blackening on the elastic constants of yttria-stabilised zirconia," *Journal of Materials Science*, vol. 7, pp. 475–476, 4 1972.

[109] J. S. Thorp, A. Aypar, and J. S. Ross, "Electron spin resonance in single crystal yttria stabilized zirconia," *Journal of Materials Science*, vol. 7, pp. 729–734, 7 1972.

[110] J. S. Thorp and H. P. Buckley, "The dielectric constants of current-blackened single crystral yttria-stabilized zirconia," *Journal of Materials Science*, vol. 8, pp. 1401–1408, 10 1973.

[111] D. A. Wright, J. S. Thorp, A. Aypar, and H. P. Buckley, "Optical absorption in current-blackened yttria-stabilized zirconia," *Journal of Materials Science*, vol. 8, no. 6, pp. 876–882, 1973.

[112] R. E. Casselton, "Blackening in yttria stabilized zirconia due to cathodic processes at solid platinum electrodes," *Journal of Applied Electrochemistry*, vol. 4, pp. 25–48, 2 1974.

[113] F. K. Moghadam, T. Yamashita, and D. A. Stevenson, "Characterization of the current-blackening phenomena in scandia stabilized zirconia using transmission

electron microscopy," *Journal of Materials Science*, vol. 18, pp. 2255–2259, 8 1983.

[114] M. Caillet, C. Deportes, G. Robert, G. Vallier, and G. Vitter, "High Temperature Structure and Electric Conductibility in ZrO2-Y2O3-Ta2O5 System," *Revue Internationale des hautes Temperatures et des Refractaires*, vol. 5, no. 3, p. 173, 1968.

[115] H. Zhu and T. Hirata, "Coloration in ceria-doped zirconia induced by reduction heat treatments," *Solid State Communications*, vol. 84, pp. 527–529, 11 1992.

[116] R. F. Reidy and G. Simkovich, "Electrical conductivity and point defect behavior in ceria-stabilized zirconia," *Solid State Ionics*, vol. 62, pp. 85–97, 7 1993.

[117] C. Rodenbücher, K. Szot, D. Wrana, B. R. Jany, F. Krok, and C. Korte, "Localized electrochemical redox reactions in yttria-stabilized zirconia single crystals," *Journal of Physics: Energy*, vol. 2, p. 034008, 7 2020.

[118] Y. Yamashita, T. Kurachi, T. Tokunaga, H. Yoshida, and T. Yamamoto, "Blue photo luminescence from 3mol%Y2O3-doped ZrO2 polycrystals sintered by flash sintering under an alternating current electric field," *Journal of the European Ceramic Society*, vol. 40, pp. 2072–2076, 5 2020.

[119] Y. Yamashita, A. Itoh, T. Tokunaga, H. Yoshida, and T. Yamamoto, "Blue photoluminescence at room temperature from Y2O3-doped ZrO2 polycrystals sintered by flash sintering," *Applied Physics Express*, vol. 13, p. 035506, 2 2020.

[120] Y. Yamashita, T. Kurachi, T. Tokunaga, H. Yoshida, and T. Yamamoto, "Technique to control specimen electric current during a flash state with alternating current electric fields," *Journal of the Ceramic Society of Japan*, vol. 127, pp. 849–851, 11 2019.

[121] R. Ono, A. Kodaira, T. Tokunaga, H. Yoshida, and T. Yamamoto, "A technique to modify the photoluminescence intensity of beta-Ga2O3 polycrystals using an electric field during sintering," *Journal of Luminescence*, vol. 254, p. 119508, 2 2023.

[122] A. Itoh, T. Tokunaga, A. Kodaira, H. Yoshida, and T. Yamamoto, "Variation of

photoluminescence intensity depending on the timing of electric field application during isothermal flash sintering for 3mol%Y2O3âZrO2 polycrystal," *Ceramics International*, vol. 48, pp. 28712–28717, 10 2022.

[123] W. Qin, H. Majidi, J. Yun, and K. van Benthem, "Electrode Effects on Microstructure Formation During FLASH Sintering of Yttrium-Stabilized Zirconia," *Journal of the American Ceramic Society*, vol. 99, pp. 2253–2259, 7 2016.

[124] V. Prajzler, K. Maca, P. Stastny, and R. I. Todd, "Abnormal grain growth in DC flash sintered 3-mol% yttria-stabilized zirconia ceramics," *Journal of the American Ceramic Society*, vol. 105, pp. 5562–5568, 9 2022.

[125] M. Biesuz and V. M. Sglavo, "Current-induced abnormal and oriented grain growth in corundum upon flash sintering," *Scripta Materialia*, vol. 150, pp. 82–86, 6 2018.

[126] H. Yoshida and Y. Sasaki, "Low temperature and high strain rate superplastic flow in structural ceramics induced by strong electric-field," *Scripta Materialia*, vol. 146, pp. 173–177, 3 2018.

[127] H. Motomura, D. Tamao, K. Nambu, H. Masuda, and H. Yoshida, "Athermal effect of flash event on high-temperature plastic deformation in Y2O3-stabilized tetragonal ZrO2 polycrystal," *Journal of the European Ceramic Society*, vol. 42, pp. 5045–5052, 9 2022.

[128] K. Wang, G. Chen, Q. Wang, X. Fu, and W. Zhou, "Unusual electrode-dependent deformation of 3Y-TZP induced by weak electric current in oxygen-lean atmosphere," *Scripta Materialia*, vol. 205, p. 114220, 12 2021.

[129] K. Morita and B.-N. Kim, "Effect of electric current on high temperature flow behavior of 8Y-CSZ ceramics," *Journal of the European Ceramic Society*, vol. 42, pp. 2341–2348, 5 2022.

[130] D. Morikawa, K. Nambu, K. Morita, H. Yoshida, and K. Soga, "Effect of direct and alternating current (DC and AC) fields on creep behavior of 8 mol% Y2O3 stabilized cubic ZrO2 polycrystal," *Journal of the European Ceramic Society*, vol. 43, pp. 3498–3506, 7 2023.

[131] K. Morita, F. Naito, and D. Terada, "Microcrack healing in zirconia ceramics under a DC electric field/current," *Journal of the European Ceramic Society*, vol. 41, pp. 282–289, 12 2021.

[132] S. Kayukawa, Y. Katsuyama, A. Kodaira, T. Tokunaga, K. Morita, A. Nakamura, and T. Yamamoto, "Flash healing of Vickers microcracks formed on the (001) surface of cubic zirconia single crystals," *Journal of the European Ceramic Society*, vol. 43, pp. 6272–6278, 11 2023.

[133] V. M. Candelario, R. Moreno, R. I. Todd, and A. L. Ortiz, "Liquid-phase assisted flash sintering of SiC from powder mixtures prepared by aqueous colloidal processing," *Journal of the European Ceramic Society*, vol. 37, pp. 485–498, 2 2017.

[134] A. Rosenberger, R. E. Brennan, and A. L. Fry, "Flash sintering feasibility study and localized densification in boron carbide," *Journal of the American Ceramic Society*, vol. 104, pp. 3823–3827, 8 2021.

[135] S. Grasso, E.-Y. Kim, T. Saunders, M. Yu, A. Tudball, S.-H. Choi, and M. Reece, "Ultra-Rapid Crystal Growth of Textured SiC Using Flash Spark Plasma Sintering Route," *Crystal Growth & Design*, vol. 16, no. 4, pp. 2317–2321, 2016.

[136] E. A. Olevsky, S. M. Rolfing, and A. L. Maximenko, "Flash (Ultra-Rapid) Spark-Plasma Sintering of Silicon Carbide," *Scientific Reports*, vol. 6, p. 33408, 2016.

[137] D. Demirskyi and O. Vasylkiv, "Hot-spots generation, exaggerated grain growth and mechanical performance of silicon carbide bulks consolidated by flash spark plasma sintering," *Journal of Alloys and Compounds*, vol. 691, pp. 466–473, 2017.

[138] S. K. Sharma, M. Fides, P. Hvizdoš, M. J. Reece, and S. Grasso, "Flash Spark Plasma Sintering of SiC: Impact of Additives," *Silicon*, vol. 14, pp. 7377–7382, 8 2022.

[139] B. Niu, F. Zhang, J. Zhang, W. Ji, W. Wang, and Z. Fu, "Ultra-fast densification of boron carbide by flash spark plasma sintering," *Scripta Materialia*, vol. 116, pp. 127–130, 2016.

[140] J. Wu, B. Niu, F. Zhang, L. Lei, J. Zhang, L. Ren, W. Wang, and Z. Fu, "Effect of titanium diboride on the homogeneity of boron carbide ceramic by flash spark

plasma sintering," *Ceramics International*, vol. 44, no. 13, pp. 15323–15330, 2018.

[141] I. Mazo, A. Molinari, and V. M. Sglavo, "Electrical resistance flash sintering of tungsten carbide," *Materials & Design*, vol. 213, p. 110330, 1 2022.

[142] I. Mazo, B. Palmieri, A. Martone, M. Giordano, and V. M. Sglavo, "Flash sintering in metallic ceramics: finite element analysis of thermal runaway in tungsten carbide green bodies," *Journal of Materials Research and Technology*, vol. 23, pp. 5993–6004, 3 2023.

[143] I. Mazo, M. A. Monclus, J. M. Molina-Aldareguia, and V. M. Sglavo, "Does flash sintering alter the deformation mechanisms of tungsten carbide?," *Acta Materialia*, vol. 258, p. 119227, 10 2023.

[144] I. Mazo, L. E. Vanzetti, J. M. Molina-Aldareguia, A. Molinari, and V. M. Sglavo, "Role of surface carbon nanolayer on the activation of flash sintering in tungsten carbide," *International Journal of Refractory Metals and Hard Materials*, vol. 111, p. 106090, 2 2023.

[145] H. Li, G. He, N. Lu, and J. Li, "Flash spark plasma sintering of Zr1âxTixC solid solution," *Journal of the Ceramic Society of Japan*, vol. 129, p. 21045, 9 2021.

[146] M. Biesuz, P. Luchi, A. Quaranta, and V. M. Sglavo, "Theoretical and phenomenological analogies between flash sintering and dielectric breakdown in α-alumina," *Journal of Applied Physics*, vol. 120, p. 145107, 10 2016.

[147] J.-F. Fagnard, C. Gajdowski, L. Boilet, F. Henrotte, C. Geuzaine, B. Vertruyen, and P. Vanderbemden, "Use of partial discharge patterns to assess the quality of sample/electrode contacts in flash sintering," *Journal of the European Ceramic Society*, vol. 41, pp. 669–683, 1 2021.

[148] R. Chaim, "Particle Surface Softening as Universal Behaviour during Flash Sintering of Oxide Nano-Powders," *Materials*, vol. 10, p. 179, 2 2017.

[149] J. Liu, H. Rongxia, R. Zhang, G. Liu, X. Wang, Z. Jia, and L. Wang, "Mechanism of flash sintering with high electric field: In the view of electric discharge and breakdown," *Scripta Materialia*, vol. 187, pp. 93–96, 10 2020.

[150] M. Biesuz, T. Saunders, D. Ke, M. J. Reece, C. Hu, and S. Grasso, "A review of electromagnetic processing of materials (EPM): Heating, sintering, joining and forming," *Journal of Materials Science & Technology*, vol. 69, pp. 239–272, 4 2021.

[151] M. Rossetti, G. d. S. Falk, A. N. Klein, S. Y. Gómez González, C. Binder, and D. Hotza, "Plasma-assisted rapid sintering of nanotitania powders," *Journal of the European Ceramic Society*, vol. 42, pp. 1670–1684, 4 2022.

[152] H. Pavanati, G. Straffelini, A. Maliska, and A. Klein, "Microstructural and mechanical characterization of iron samples sintered in DC plasma," *Materials Science and Engineering: A*, vol. 474, pp. 15–23, 2 2008.

[153] A. N. Klein, R. P. Cardoso, H. C. Pavanati, C. Binder, A. M. Maliska, G. Hammes, D. Fusao, A. Seeber, S. F. Brunatto, and J. L. R. Muzart, "DC Plasma Technology Applied to Powder Metallurgy: an Overview," *Plasma Science and Technology*, vol. 15, pp. 70–81, 1 2013.

[154] T. Ishigaki, T. Sato, Y. Moriyoshi, and M. I. Boulos, "Influence of plasma modification of titanium carbide powder on its sintering properties," *Journal of Materials Science Letters*, vol. 14, no. 23, pp. 1694–1697, 1995.

[155] D. Lynn Johnson, "Microwave and plasma sintering of ceramics," *Ceramics International*, vol. 17, pp. 295–300, 1 1991.

[156] M. Y. Chen and D. L. Johnson, "Effects of additive gases on radio-frequency plasma sintering of alumina," *Journal of Materials Science*, vol. 27, no. 1, pp. 191–196, 1992.

[157] V. Pouchlý, J. Ráhel, T. Spusta, M. Ilčíková, D. Pavlinak, T. Morávek, and K. Maca, "Improved microstructure of alumina ceramics prepared from DBD plasma activated powders," *Journal of the European Ceramic Society*, vol. 39, pp. 1297–1303, 4 2019.

[158] Z. Szalay, K. Bodišová, H. Pálková, P. Švančárek, P. Dukrina, J. Ráhel, A. Zahoranová, and D. Galusek, "Atmospheric pressure air plasma treated alumina powder for ceramic sintering," *Ceramics International*, vol. 40, pp. 12737–12743, 9 2014.

[159] R. Marder, C. Estournès, G. Chevallier, and R. Chaim, "Numerical model for sparking and plasma formation during spark plasma sintering of ceramic compacts," *Journal of Materials Science*, vol. 50, pp. 4636–4645, 7 2015.

[160] T. Saunders, S. Grasso, and M. J. Reece, "Plasma formation during electric discharge (50 V) through conductive powder compacts," *Journal of the European Ceramic Society*, vol. 35, no. 3, pp. 871–877, 2015.

[161] Y. Li, Q. Chi, Z. Yan, N. Yan, J. Liu, R. Huang, and X. Wang, "Flash sintering of high-purity alumina at room temperature," *Journal of Advanced Ceramics*, vol. 12, pp. 2382–2388, 12 2023.

[162] A. Wu, Z. Zhu, X. Wang, N. Yan, H. Zhou, R. Huang, G. Ma, Z. Jia, and L. Wang, "Highâperformance ZnO varistor ceramics prepared by arcâinduced flash sintering with low energy consumption at room temperature," *High Voltage*, vol. 7, pp. 222–232, 4 2022.

[163] Y. Zhu, H. Zhou, R. Huang, N. Yan, X. Wang, G. Liu, and Z. Jia, "Gas-discharge induced flash sintering of YSZ ceramics at room temperature," *Journal of Advanced Ceramics*, vol. 11, pp. 603–614, 4 2022.

[164] Y. Li, C. Xu, R. Huang, X. Zhao, X. Wang, and Z. Jia, "Mechanism analysis of arc-induced flash sintering of 3YSZ at room temperature," *Journal of the European Ceramic Society*, vol. 43, pp. 7033–7040, 12 2023.

[165] D. Yan, J. H. Sherman, and M. Keidar, "Cold atmospheric plasma, a novel promising anti-cancer treatment modality," *Oncotarget*, vol. 8, pp. 15977–15995, 2 2017.

[166] F. L. Tabares and I. Junkar, "Cold Plasma Systems and Their Application in Surface Treatments for Medicine," *Molecules*, vol. 26, p. 1903, 3 2021.

[167] J. R. Roth, *Industrial Plasma Engineering: Volume 2 - Applications to Nonthermal Plasma Processing*. London: CRC Press, 1st ed. ed., 2001.

[168] J. Townsend, "The Theory of Ionisation of Gases by Collision," *Nature*, vol. 85, pp. 400–401, 1 1911.

[169] J. R. Roth, *Industrial plasma engineering: Volume 1 - Principles*. Bristol: Inst. of Physics Publ, repr ed., 2000.

[170] H. Tanaka, S. Sawai, K. Morimoto, and K. Hisano, "Measurement of Spectral Emissivity and Thermal Conductivity of Zirconia by Thermal Radiation Calorimetry," *Journal of Thermal Analysis and Calorimetry*, vol. 64, pp. 867–872, 11 2004.

[171] F. Kaminga, S. Sato, and Y. Okamoto, "Evaluation of Gap Heat Transfer between Boron Carbide Pellet and Cladding in Control Rod of FBR," *Journal of Nuclear Science and Technology*, vol. 29, no. 2, pp. 121–130, 1992.

[172] H. Abrams, "Grain size measurement by the intercept method," *Metallography*, vol. 4, pp. 59–78, 2 1971.

[173] N. Doebelin and R. Kleeberg, "Profex: a graphical user interface for the Rietveld refinement program BGMN," *Journal of Applied Crystallography*, vol. 48, pp. 1573–1580, 10 2015.

[174] C. Wagner, A. Naumkin, A. Kraut-Vass, J. Allison, C. Powell, and J. Rumble, "NIST Standard Reference Database 20Version 3.4 (web version) (http:/srdata.nist.gov/xps/) 2003."

[175] P. Gang Ding, *Handbook of Optical Fibers*. Singapore: Springer Singapore, 2019.

[176] Y. Li, R. Torchio, S. Falco, P. Alotto, Z. Huang, and R. I. Todd, "Promoting core/surface homogeneity during flash sintering of 3YSZ ceramic by current path management: experimental and modelling studies," *Journal of the European Ceramic Society*, vol. 41, pp. 6649–6659, 10 2021.

[177] S. M. Avdoshenko and A. Strachan, "High-temperature emissivity of silica, zirconia and samaria from ab initio simulations: role of defects and disorder," *Modelling and Simulation in Materials Science and Engineering*, vol. 22, p. 075004, 10 2014.

[178] W. W. Coblentz, "Selective Radiation from the Nernst Glower," *Bulletin of the Bureau of Standards*, vol. 4, no. 4, pp. 533–551, 1908.

[179] J. M. Costantini, F. Beuneu, M. Fasoli, A. Galli, A. Vedda, and M. Martini, "Thermo-stimulated luminescence of ion-irradiated yttria-stabilized zirconia," *Journal of Physics: Condensed Matter*, vol. 23, p. 115901, 2 2011.

[180] K. Wang, L. Ma, X. Xu, S. Wen, and Y. Zhang, "Enhancement of Triboluminescence in the Presence of CO2 by Sliding between Silica and Yttria-Stabilized Zirconia," *Langmuir*, vol. 31, pp. 8224–8227, 8 2015.

[181] D. Liu, Y. Cao, J. Liu, Y. Gao, and Y. Wang, "Effect of oxygen partial pressure on temperature for onset of flash sintering 3YSZ," *Journal of the European Ceramic Society*, vol. 38, pp. 817–820, 2 2018.

[182] I. J. Hewitt, A. A. Lacey, and R. I. Todd, "A Mathematical Model for Flash Sintering," *Mathematical Modelling of Natural Phenomena*, vol. 10, no. 6, pp. 77–89, 2015.

[183] C. Moura, P. Carvalho, F. Vaz, L. Cunha, and E. Alves, "Raman spectra and structural analysis in ZrOxNy thin films," *Thin Solid Films*, vol. 515, pp. 1132–1137, 11 2006.

[184] W. Spengler and R. Kaiser, "First and second order Raman scattering in transition metal compounds," *Solid State Communications*, vol. 18, pp. 881–884, 1 1976.

[185] W. Spengler, R. Kaiser, A. N. Christensen, and G. Müller-Vogt, "Raman scattering, superconductivity, and phonon density of states of stoichiometric and nonstoichiometric TiN," *Physical Review B*, vol. 17, pp. 1095–1101, 2 1978.

[186] M. Stoehr, H.-S. Seo, I. Petrov, and J. E. Greene, "Raman scattering from epitaxial HfN layers grown on MgO(001)," *Journal of Applied Physics*, vol. 99, 2 2006.

[187] A. Selcuk and A. Atkinson, "Analysis of the Cr3+ luminescence spectra from thermally grown oxide in thermal barrier coatings," *Materials Science and Engineering: A*, vol. 335, pp. 147–156, 9 2002.

[188] G. Gouadec, P. Colomban, N. Piquet, M. Trichet, and L. Mazerolles, "Raman/Cr3+ fluorescence mapping of a melt-grown Al2O3/GdAlO3 eutectic," *Journal of the European Ceramic Society*, vol. 25, pp. 1447–1453, 1 2005.

[189] P. Lackner, Z. Zou, S. Mayr, U. Diebold, and M. Schmid, "Using photoelectron spectroscopy to observe oxygen spillover to zirconia," *Physical Chemistry Chemical Physics*, vol. 21, pp. 17613–17620, 8 2019.

[190] M. Putkonen, T. Sajavaara, J. Niinistö, L.-S. Johansson, and L. Niinistö, "De-

position of yttria-stabilized zirconia thin films by atomic layer epitaxy from β-diketonate and organometallic precursors," *Journal of Materials Chemistry*, vol. 12, pp. 442–448, 2 2002.

[191] T. Gross, M. Ramm, H. Sonntag, W. Unger, H. M. Weijers, and E. H. Adem, "An XPS analysis of different SiO2 modifications employing a C 1s as well as an Au 4f7/2 static charge reference," *Surface and Interface Analysis*, vol. 18, pp. 59–64, 1 1992.

[192] D. Majumdar and D. Chatterjee, "X-ray photoelectron spectroscopic studies on yttria, zirconia, and yttria-stabilized zirconia," *Journal of Applied Physics*, vol. 70, pp. 988–992, 7 1991.

[193] W. Ma, F. W. Herbert, S. D. Senanayake, and B. Yildiz, "Non-equilibrium oxidation states of zirconium during early stages of metal oxidation," *Applied Physics Letters*, vol. 106, p. 101603, 3 2015.

[194] I. Bespalov, M. Datler, S. Buhr, W. Drachsel, G. Rupprechter, and Y. Suchorski, "Initial stages of oxide formation on the Zr surface at low oxygen pressure: An in situ FIM and XPS study," *Ultramicroscopy*, vol. 159, pp. 147–151, 12 2015.

[195] G. H. Major, N. Fairley, P. M. A. Sherwood, M. R. Linford, J. Terry, V. Fernandez, and K. Artyushkova, "Practical guide for curve fitting in x-ray photoelectron spectroscopy," *Journal of Vacuum Science & Technology A*, vol. 38, 12 2020.

[196] I. Milošev, H.-H. Strehblow, B. Navinšek, and P. Panjan, "Zirconium Nitride by XPS," *Surface Science Spectra*, vol. 5, pp. 152–158, 4 1998.

[197] T. Muneshwar and K. Cadien, "Comparing XPS on bare and capped ZrN films grown by plasma enhanced ALD: Effect of ambient oxidation," *Applied Surface Science*, vol. 435, pp. 367–376, 3 2018.

[198] W. De La Cruz, J. A. DÌaz, L. Mancera, N. Takeuchi, and G. Soto, "Yttrium nitride thin films grown by reactive laser ablation," *Journal of Physics and Chemistry of Solids*, vol. 64, pp. 2273–2279, 11 2003.

[199] C. Azzoni, P. Camagni, G. Samoggia, and A. Paleari, "Defect structures and elec-

tronic properties in cubic stabilized zirconia," *Solid state ionics*, vol. 60, no. 4, pp. 223–226, 1993.

[200] A. M. Slipenyuk, M. D. Glinchuk, I. P. Bykov, A. V. Ragulya, V. P. Klimenko, T. E. Konstantinova, and I. A. Danilenko, "ESR Investigation of Yttria Stabilized Zirconia Powders with Nanosize Particles," *Ferroelectrics*, vol. 298, pp. 289–296, 1 2004.

[201] F. Tietz, W. Jungen, P. Lersch, M. Figaj, K. D. Becker, and D. Skarmoutsos, "X-ray Diffraction and Electron Paramagnetic Resonance Investigations of the Fluorite Material Y0.25Ti0.15Zr0.6O2-x," *Chemistry of Materials*, vol. 14, pp. 2252–2257, 5 2002.

[202] J. C. Evans, C. R. Owen, and C. C. Rowlands, "Electron paramagnetic resonance study of monoclinic zirconium dioxide polycrystalline powders doped with paramagnetic transition-metal ions," *Journal of the Chemical Society, Faraday Transactions 1: Physical Chemistry in Condensed Phases*, vol. 85, no. 12, p. 4039, 1989.

[203] M. Labaki, S. Siffert, J.-F. Lamonier, E. A. Zhilinskaya, and A. Aboukais, "Total oxidation of propene and toluene in the presence of zirconia doped by copper and yttrium," *Applied Catalysis B: Environmental*, vol. 43, pp. 261–271, 7 2003.

[204] J. Matta, J.-F. Lamonier, E. Abi-Aad, E. A. Zhilinskaya, and A. Aboukais, "Transformation of tetragonal zirconia phase to monoclinic phase in the presence of Fe3+ ions as probes : an EPR study," *Physical chemistry chemical physics : PCCP*, vol. 1, no. 21, pp. 4975–4980, 1999.

[205] N. Sergent, J.-F. Lamonier, and A. Aboukaïs, "Electron Paramagnetic Resonance in Combination with the Thermal Analysis, X-ray Diffraction, and Raman Spectroscopy to Follow the Structural Properties of ZrxCe1-xO2 Solid Systems and Precursors," *Chemistry of Materials*, vol. 12, pp. 3830–3835, 12 2000.

[206] B. A. Goodman and P. L. Hall, "Electron paramagnetic resonance spectroscopy," in *Clay Mineralogy: Spectroscopic and Chemical Determinative Methods*, pp. 173–225, Dordrecht: Springer Netherlands, 1994.

[207] J. M. Costantini, F. Beuneu, D. Gourier, C. Trautmann, G. Calas, and M. Toule-

monde, “Colour centre production in yttria-stabilized zirconia by swift charged particle
}irradiations,” *Journal of Physics: Condensed Matter*, vol. 16, p. 3957, 5 2004.

[208] V. M. Orera, R. I. Merino, Y. Chen, R. Cases, and P. J. Alonso, “Intrinsic electron and hole defects in stabilized zirconia single crystals,” *Physical Review B*, vol. 42, pp. 9782 – 9789, 1 1990.

[209] C. B. Azzoni and A. Paleari, “Sevenfold- and sixfold-coordinated Zr3+ ions in cubic stabilized zirconia : crystal-field approach,” *Physical review. B, Condensed matter*, vol. 44, no. 13, pp. 6858–6863, 1991.

[210] C. Gionco, M. C. Paganini, E. Giamello, R. Burgess, C. Di Valentin, and G. Pacchioni, “Paramagnetic Defects in Polycrystalline Zirconia: An EPR and DFT Study,” *Chemistry of Materials*, vol. 25, pp. 2243–2253, 6 2013.

[211] Y. Dong, L. Qi, A. Alvarez, J. Li, and I.-W. Chen, “Enhanced mobility of cations and anions in the redox state: The polaronium mechanism,” *Acta Materialia*, vol. 232, p. 117941, 6 2022.

[212] S. B. Ogale, “Dilute Doping, Defects, and Ferromagnetism in Metal Oxide Systems,” *Advanced Materials*, vol. 22, pp. 3125–3155, 8 2010.

[213] N. H. Hong, J. Sakai, N. Poirot, and V. Brizé, “Room-temperature ferromagnetism observed in undoped semiconducting and insulating oxide thin films,” *Physical Review B*, vol. 73, p. 132404, 4 2006.

[214] P. Zhan, W. Wang, Z. Xie, Z. Li, Z. Zhang, P. Zhang, B. Wang, and X. Cao, “Substrate effect on the room-temperature ferromagnetism in un-doped ZnO films,” *Applied Physics Letters*, vol. 101, 7 2012.

[215] H. Peng, J. Li, S.-S. Li, and J.-B. Xia, “Possible origin of ferromagnetism in undoped anataseTiO2,” *Physical Review B*, vol. 79, p. 092411, 3 2009.

[216] J. Zippel, M. Lorenz, A. Setzer, G. Wagner, N. Sobolev, P. Esquinazi, and M. Grundmann, “Defect-induced ferromagnetism in undoped and Mn-doped zirconia thin films,” *Physical Review B*, vol. 82, p. 125209, 9 2010.

[217] S. Ryu, D. Cho, J. K. Park, J. S. Lee, T. E. Hong, M. Byeon, and H. Jeen,

"Ferromagnetism in defective yttria-stabilized zirconia," *Current Applied Physics*, vol. 43, pp. 66–71, 11 2022.

[218] S. Ostanin, A. Ernst, L. M. Sandratskii, P. Bruno, M. Däne, I. D. Hughes, J. B. Staunton, W. Hergert, I. Mertig, and J. Kudrnovský, "Mn-Stabilized Zirconia: From Imitation Diamonds to a New Potential High- Tc Ferromagnetic Spintronics Material," *Physical Review Letters*, vol. 98, p. 016101, 1 2007.

[219] S. Ning, P. Zhan, Q. Xie, Z. Li, and Z. Zhang, "Room-temperature ferromagnetism in un-doped ZrO2 thin films," *Journal of Physics D: Applied Physics*, vol. 46, p. 445004, 11 2013.

[220] E. Albanese, A. Ruiz Puigdollers, and G. Pacchioni, "Theory of Ferromagnetism in Reduced ZrO2-X Nanoparticles," *ACS Omega*, vol. 3, pp. 5301–5307, 5 2018.

[221] M. Venkatesan, C. B. Fitzgerald, and J. M. D. Coey, "Unexpected magnetism in a dielectric oxide," *Nature*, vol. 430, pp. 630–630, 8 2004.

[222] J. M. D. Coey, M. Venkatesan, P. Stamenov, C. B. Fitzgerald, and L. S. Dorneles, "Magnetism in hafnium dioxide," *Physical Review B*, vol. 72, p. 024450, 7 2005.

[223] T. Dietl, H. Ohno, F. Matsukura, J. Cibert, and D. Ferrand, "Zener Model Description of Ferromagnetism in Zinc-Blende Magnetic Semiconductors," *Science*, vol. 287, pp. 1019–1022, 2 2000.

[224] M. Yashima, S. Sasaki, M. Kakihana, Y. Yamaguchi, H. Arashi, and M. Yoshimura, "Oxygen-induced structural change of the tetragonal phase around the tetragonal-cubic phase boundary in ZrO2-YO1.5 solid solutions," *Acta Crystallographica Section B Structural Science*, vol. 50, pp. 663–672, 12 1994.

[225] N. Shibata, J. Katamura, A. Kuwabara, Y. Ikuhara, and T. Sakuma, "The instability and resulting phase transition of cubic zirconia," *Materials Science and Engineering: A*, vol. 312, pp. 90–98, 8 2001.

[226] A. Kuwabara, J. Katamura, Y. Ikuhara, and T. Sakuma, "Influence of Interaction between Neighboring Oxygen Ions on Phase Stability in Cubic Zirconia," *Journal of the American Ceramic Society*, vol. 85, pp. 2557–2561, 10 2002.

[227] L. Song, Q. Zhang, J. Ma, C. Chen, B. Xu, M. Zhu, X. Xu, C. Nan, and Z. Shen,

"Vacancy-ordered yttria stabilized zirconia as a low-temperature electronic conductor achieved by laser melting," *Journal of the European Ceramic Society*, vol. 39, pp. 1374–1380, 4 2019.

[228] S. Banerjee and P. Mukhopadhyay, *Phase Transformations Examples from Titanium and Zirconium Alloys-Chapter 1 Phases and Crystal Structures*, vol. 12. Elsevier Ltd, 2007.

[229] M. Hillert, "Thermodynamic Model of the Cubic to Tetragonal Transition in Nonstoichiometric Zirconia," *Journal of the American Ceramic Society*, vol. 74, pp. 2005–2006, 8 1991.

[230] J. M. Lebrun, C. S. Hellberg, S. K. Jha, W. M. Kriven, A. Steveson, K. C. Seymour, N. Bernstein, S. C. Erwin, and R. Raj, "In-situ measurements of lattice expansion related to defect generation during flash sintering," *Journal of the American Ceramic Society*, vol. 100, pp. 4965–4970, 11 2017.

[231] A. S. Foster, V. B. Sulimov, F. Lopez Gejo, A. L. Shluger, and R. M. Nieminen, "Structure and electrical levels of point defects in monoclinic zirconia," *Physical Review B*, vol. 64, p. 224108, 11 2001.

[232] C. Bonola, P. Camagni, P. Chiodelli, and G. Samoggia, "Study of Defects Introduced by Electroreduction in YSZ," *Radiation Effects and Defects in Solids*, vol. 119-121, no. 1, pp. 457–462, 1991.

[233] M. Youssef and B. Yildiz, "Intrinsic point-defect equilibria in tetragonal ZrO2: Density functional theory analysis with finite-temperature effects," *Physical Review B*, vol. 86, p. 144109, 10 2012.

[234] T. P. Mishra, R. R. I. Neto, G. Speranza, A. Quaranta, V. M. Sglavo, R. Raj, O. Guillon, M. Bram, and M. Biesuz, "Electronic conductivity in gadolinium doped ceria under direct current as a trigger for flash sintering," *Scripta Materialia*, vol. 179, pp. 55–60, 4 2020.

[235] R. W. Harrison and W. E. Lee, "Processing and properties of ZrC, ZrN and ZrCN ceramics: a review," *Advances in Applied Ceramics*, vol. 115, pp. 294–307, 7 2016.

[236] W. S. Williams, "Physics of transition metal carbides," *Materials Science and Engineering: A*, vol. 105-106, pp. 1–10, 11 1988.

[237] C. D. Gelatt, A. R. Williams, and V. L. Moruzzi, "Theory of bonding of transition metals to nontransition metals," *Physical Review B*, vol. 27, pp. 2005–2013, 2 1983.

[238] H. Okamoto, "Hf-O (Hafnium-Oxygen)," *Journal of Phase Equilibria and Diffusion*, vol. 29, pp. 124–124, 2 2008.

[239] S. Andersson, B. Collén, U. Kuylenstierna, A. Magnéli, A. Magnéli, H. Pestmalis, and S. Åsbrink, "Phase Analysis Studies on the Titanium-Oxygen System.," *Acta Chemica Scandinavica*, vol. 11, pp. 1641–1652, 1957.

[240] H. Wang, Q. Chao, X. Y. Cui, Z. B. Chen, A. J. Breen, M. Cabral, N. Haghdadi, Q. W. Huang, R. M. Niu, H. S. Chen, B. Lim, S. Primig, M. Brandt, W. Xu, S. P. Ringer, and X. Z. Liao, "Introducing C phase in additively manufactured Ti-6Al-4V: A new oxygen-stabilized face-centred cubic solid solution with improved mechanical properties," *Materials Today*, vol. 61, pp. 11–21, 12 2022.

[241] C. Bechteler and R. I. Todd, "Lattice modification of ZrO2-δ and formation of rocksalt structure ZrO and Zr(O,N) after DC electrical loading of 3YSZ," *Journal of the European Ceramic Society*, 9 2023.

[242] Emsley John, *The Elements*. Oxford: Clarendon Press, 3 ed., 1998.

[243] N. J. Ashley, D. Parfitt, A. Chroneos, and R. W. Grimes, "Mechanisms of nonstoichiometry in HfN1-x," *Journal of Applied Physics*, vol. 106, 10 2009.

[244] D. N. Miller, A. K. Azad, H. Delpouve, L. Quazuguel, J. Zhou, A. Sinha, P. Wormald, and J. T. S. Irvine, "Studies on the crystal structure, magnetic and conductivity properties of titanium oxycarbide solid solution (TiO1-xCx)," *Journal of Materials Chemistry A*, vol. 4, no. 15, pp. 5730–5736, 2016.

[245] Y. Zhou, J. Watts, C. Li, W. G. Fahrenholtz, and G. E. Hilmas, "Vacancy ordering in zirconium carbide with different carbon contents," *Journal of the European Ceramic Society*, vol. 43, pp. 5814–5821, 11 2023.

[246] M. M. Opeka, I. G. Talmy, E. J. Wuchina, J. A. Zaykoski, and S. J. Causey, "Me-

chanical, Thermal, and Oxidation Properties of Refractory Hafnium and zirconium Compounds," *Journal of the European Ceramic Society*, vol. 19, pp. 2405–2414, 10 1999.

[247] W. Lengauer, "Properties of bulk δ-TiN1-x prepared by nitrogen diffusion into titanium metal," *Journal of Alloys and Compounds*, vol. 186, pp. 293–307, 8 1992.

[248] A. N. Christensen, E. K. Andersen, I. G. K. Andersen, O. Dahl, M. Nielsen, M. S. Lehmann, and T. Tokii, "A Neutron Diffraction Investigation on Single Crystals of Titanium Oxide, Zirconium Carbide, and Hafnium Nitride.," *Acta Chemica Scandinavica*, vol. 44, pp. 851–852, 1990.

[249] A. R. West, *Basic solid state chemistry*. Chichester: Wiley, 2nd ed. ed., 1999.

[250] W. Lengauer, "Transition Metal Carbides, Nitrides, and Carbonitrides," in *Handbook of Ceramic Hard Materials*, pp. 202–252, Wiley, 4 2000.

[251] D. A. Tenne, I. E. Gonenli, A. Soukiassian, D. G. Schlom, S. M. Nakhmanson, K. M. Rabe, and X. X. Xi, "Raman study of oxygen reduced and re-oxidized strontium titanate," *Physical Review B*, vol. 76, p. 024303, 7 2007.

[252] T. S. Bjørheim, M. Arrigoni, D. Gryaznov, E. Kotomin, and J. Maier, "Thermodynamic properties of neutral and charged oxygen vacancies in BaZrO3 based on first principles phonon calculations," *Physical Chemistry Chemical Physics*, vol. 17, no. 32, pp. 20765–20774, 2015.

[253] R. Evarestov, E. Blokhin, D. Gryaznov, E. A. Kotomin, R. Merkle, and J. Maier, "Jahn-Teller effect in the phonon properties of defective SrTiO3 from first principles," *Physical Review B*, vol. 85, p. 174303, 5 2012.

[254] S. Jo, M. Kindelmann, D. Jennings, L. Balice, Y. J. Sohn, W. S. Scheld, M. Bram, O. Guillon, J. Mayer, and R. Raj, "Flash-induced defects in single-crystal 8YSZ characterized by TEM, XRD, and Raman spectroscopy," *Journal of the American Ceramic Society*, vol. 107, pp. 5786–5800, 9 2024.

[255] A. Eqbal, K. S. Arya, and T. Chakrabarti, "In-depth study of the evolving thermal runaway and thermal gradient in the dog bone sample during flash sintering us-

ing finite element analysis," *Ceramics International*, vol. 46, pp. 10370–10378, 6 2020.

[256] S. Grasso, Y. Sakka, N. Rendtorff, C. Hu, G. Maizza, H. Borodianska, and O. Vasylkiv, "Modeling of the temperature distribution of flash sintered zirconia," *Journal of the Ceramic Society of Japan*, vol. 119, no. 1386, pp. 144–146, 2011.

[257] R. J. Ackermann, S. P. Garg, and E. G. Rauh, "The Lower Phase Boundary of ZrO2-x," *Journal of the American Ceramic Society*, vol. 61, pp. 275–276, 5 1978.

[258] S.-W. Kim, S. G. Kim, J.-I. Jung, S.-J. L. Kang, and I.-W. Chen, "Enhanced Grain Boundary Mobility in Yttria-Stabilized Cubic Zirconia under an Electric Current," *Journal of the American Ceramic Society*, vol. 94, pp. 4231–4238, 12 2011.

[259] Y. Dong, H. Wang, and I.-W. Chen, "Electrical and hydrogen reduction enhances kinetics in doped zirconia and ceria: I. grain growth study," *Journal of the American Ceramic Society*, vol. 100, pp. 876–886, 3 2017.

[260] Y. Dong and I. Chen, "Electrical and hydrogen reduction enhances kinetics in doped zirconia and ceria: II . Mapping electrode polarization and vacancy condensation in YSZ," *Journal of the American Ceramic Society*, vol. 101, pp. 1058–1073, 3 2018.

[261] Y. Sasaki, K. Morita, T. Yamamoto, K. Soga, H. Masuda, and H. Yoshida, "Electric current dependence of plastic flow behavior with large tensile elongation in tetragonal zirconia polycrystal under a DC field," *Scripta Materialia*, vol. 194, p. 113659, 3 2021.

[262] S. Pan, G. Shao, H. He, R. Zhao, C. Ma, H. Lu, H. Xu, H. Wang, R. Zhang, and L. An, "Effects of strain rate and current density on plastic deformation of zirconia ceramics under a high electric field," *Ceramics International*, vol. 49, pp. 27758–27763, 9 2023.

[263] D. M. Hulbert, D. Jiang, J. D. Kuntz, Y. Kodera, and A. K. Mukherjee, "A low temperature high strain rate formable nanocrystalline superplastic ceramic," *Scripta Materialia*, vol. 56, pp. 1103–1106, 6 2007.

[264] H. C. Back, J. Gibmeier, and R. Vaßen, "Phase Transformation-Induced Changes

in Microstructure and Residual Stresses in Thermally Sprayed MnCoFeO4 Protective Coatings," *Journal of Thermal Spray Technology*, vol. 29, pp. 1242–1255, 8 2020.

[265] Q. Fang, L. Blum, and D. Stolten, "Electrochemical Performance and Degradation Analysis of an SOFC Short Stack Following Operation of More than 100,000 Hours," *Journal of The Electrochemical Society*, vol. 166, pp. F1320–F1325, 1 2019.

[266] B. Luerßen, J. Janek, S. Günther, M. Kiskinova, and R. Imbihl, "Microspectroscopy at a moving reduction front in zirconia solid electrolyte," *Physical Chemistry Chemical Physics*, vol. 4, pp. 2673–2679, 5 2002.

[267] D. Eder and R. Kramer, "Impedance spectroscopy of reduced monoclinic zirconia," *Physical Chemistry Chemical Physics*, vol. 8, no. 38, p. 4476, 2006.

[268] F. W. Peek, *Dielectric phenomena in high-voltage engineering*. New York: McGraw-Hill Book Company, inc., 1929.

[269] V. A. Lisovskiy, S. D. Yakovin, and V. D. Yegorenkov, "Low-pressure gas breakdown in uniform dc electric field," *Journal of Physics D: Applied Physics*, vol. 33, pp. 2722–2730, 11 2000.

[270] M. E. Abdel-kader, W. H. Gaber, F. A. Ebrahim, and M. A. Abd Al-Halim, "Characterization of the electrical breakdown for DC discharge in Ar-He gas mixture," *Vacuum*, vol. 169, p. 108922, 11 2019.

[271] A. Vijh, "Electric strenght and molecular properties of gaseous dielectrics," *IEEE Transactions on Electrical Insulation*, vol. EI-12, pp. 313–315, 8 1977.

[272] S. Li, Y. Huang, D. Min, G. Qu, H. Niu, Z. Li, W. Wang, J. Li, and W. Liu, "Synergic effect of adsorbed gas and charging on surface flashover," *Scientific Reports*, vol. 9, p. 5464, 4 2019.

[273] E. L. Gurevich, A. W. Liehr, S. Amiranashvili, and H.-G. Purwins, "Role of surface charges in dc gas-discharge systems with high-ohmic electrodes," *Physical Review E*, vol. 69, p. 036211, 3 2004.

[274] H. Miller, "Surface flashover of insulators," *IEEE Transactions on Electrical Insulation*, vol. 24, no. 5, pp. 765–786, 1989.

[275] H. C. Miller, "Flashover of insulators in vacuum: the last twenty years," *IEEE Transactions on Dielectrics and Electrical Insulation*, vol. 22, pp. 3641–3657, 12 2015.

[276] T. B. Holland, U. Anselmi-Tamburini, D. V. Quach, T. B. Tran, and A. K. Mukherjee, "Local field strengths during early stage field assisted sintering (FAST) of dielectric materials," *Journal of the European Ceramic Society*, vol. 32, pp. 3659–3666, 11 2012.

[277] S. C. Brown, *Basic Data of Plasma Physics* . 1967.

[278] A. F. Ismail, K. Chandra Khulbe, and T. Matsuura, *Gas Separation Membranes*. Cham: Springer International Publishing, 2015.

[279] D. W. Breck, *Zeolite Molecular Sieves: Structure, Chemistry, and Use*. New York: Wiley, 1974.

[280] R. C. Wetzel, F. A. Baiocchi, T. R. Hayes, and R. S. Freund, "Absolute cross sections for electron-impact ionization of the rare-gas atoms by the fast-neutral-beam method," *Physical Review A*, vol. 35, pp. 559–577, 1 1987.

[281] B. Freiser, "Electron impact ionization of argon ions by trapped ion cyclotron resonance spectroscopy," *International Journal of Mass Spectrometry and Ion Physics*, vol. 33, pp. 263–267, 4 1980.

[282] F. Rezaei, Y. Gorbanev, M. Chys, A. Nikiforov, S. W. H. Van Hulle, P. Cos, A. Bogaerts, and N. De Geyter, "Investigation of plasmaâinduced chemistry in organic solutions for enhanced electrospun PLA nanofibers," *Plasma Processes and Polymers*, vol. 15, 6 2018.

[283] A. Kramida, Y. Ralchenko, J. Reader, and NIST ASD Team, "NIST Atomic Spectra Database (version 5.11)," 3 2024.

[284] F. Thévenot, "Boron carbide - A comprehensive review," *Journal of the European Ceramic Society*, vol. 6, no. 4, pp. 205–225, 1990.

[285] V. Domnich, S. Reynaud, R. A. Haber, and M. Chhowalla, "Boron Carbide: Structure, Properties, and Stability under Stress," *Journal of the American Ceramic Society*, vol. 94, no. 11, pp. 3605–3628, 2011.

[286] D. R. Tallant, T. L. Aselage, A. N. Campbell, and D. Emin, "Boron carbide structure by Raman spectroscopy," *Physical Review B*, vol. 40, pp. 5649–5656, 9 1989.

[287] H. Werheit, "On excitons and other gap states in boron carbide," *Journal of Physics: Condensed Matter*, vol. 18, pp. 10655–10662, 11 2006.

[288] H. Werheit, V. Filipov, U. Schwarz, M. Armbrüster, A. Leithe-Jasper, T. Tanaka, and S. O. Shalamberidze, "On surface Raman scattering and luminescence radiation in boron carbide," *Journal of Physics: Condensed Matter*, vol. 22, p. 045401, 2 2010.

[289] H. Werheit, H. W. Rotter, S. Shalamberidze, A. Leithe-Jasper, and T. Tanaka, "Gap-state related photoluminescence in boron carbide," *physica status solidi (b)*, vol. 248, pp. 1275–1279, 5 2011.

[290] K. Takahashi, *Wide Bandgap Semiconductors*. Berlin, Heidelberg: Springer Berlin Heidelberg, 2007.

[291] C. Persson and U. Lindefelt, "Detailed band structure for 3C-, 2H-, 4H-, 6H-SiC, and Si around the fundamental band gap," *Physical Review B*, vol. 54, pp. 10257–10260, 10 1996.

[292] M. Biesuz, J. Dong, S. Fu, Y. Liu, H. Zhang, D. Zhu, C. Hu, and S. Grasso, "Thermally-insulated flash sintering," *Scripta Materialia*, vol. 162, pp. 99–102, 3 2019.

[293] H. Lee and R. F. Speyer, "Hardness and Fracture Toughness of Pressureless-Sintered Boron Carbide (B4C)," *Journal of the American Ceramic Society*, vol. 85, no. 5, pp. 1291–1293, 2002.

[294] H. Lee and R. F. Speyer, "Pressureless Sintering of Boron Carbide," *Journal of the American Ceramic Society*, vol. 86, no. 9, pp. 1468–1473, 2003.

[295] K. A. Schwetz and G. Vogt, "Process for the production of dense sintered shaped

articles of polycrystalline boron carbide by pressureless sintering: United States Patent."

[296] K. A. Schwetz and W. Grellner, "The influence of carbon on the microstructure and mechanical properties of sintered boron carbide," *Journal of the Less Common Metals*, vol. 82, pp. 37–47, 1981.

[297] L. S. Sigl, "Processing and mechanical properties of boron carbide sintered with TiC," *Journal of the European Ceramic Society*, vol. 18, no. 11, pp. 1521–1529, 1998.

[298] H. Suzuki, T. Hase, and T. Maruyama, "Effect of carbon on sintering of boron carbide: (Japanese)," *Ceram Soc Jpn.*, vol. 87, no. 8, pp. 430–433, 1979.

[299] A. K. Suri, C. Subramanian, J. K. Sonber, and T. S. R. C. Murthy, "Synthesis and consolidation of boron carbide: a review," *International Materials Reviews*, vol. 55, no. 1, pp. 4–40, 2010.

[300] J. Zorzi, C. Perottoni, and J. da Jornada, "Hardness and wear resistance of B4C ceramics prepared with several additives," *Materials Letters*, vol. 59, pp. 2932–2935, 10 2005.

[301] T. K. Roy, C. Subramanian, and A. K. Suri, "Pressureless sintering of boron carbide," *Ceramics International*, vol. 32, no. 3, pp. 227–233, 2006.

[302] A. V. Gubarevich, G. Homma, and K. Yoshida, "Boron carbide with improved mechanical properties fabricated via rapid pressureless densification with electromagnetic induction assistance," *Scripta Materialia*, vol. 238, p. 115731, 1 2024.

[303] H. Martin, B. Feng, and A. Michaelis, "Pressureless sintering and properties of boron carbide composite materials," *International Journal of Applied Ceramic Technology*, vol. 17, pp. 407–412, 3 2020.

[304] W. Zhang, S. Yamashita, and H. Kita, "Progress in pressureless sintering of boron carbide ceramics - a review," *Advances in Applied Ceramics*, vol. 118, no. 4, pp. 222–239, 2019.

[305] G. Liu, S. Chen, Y. Zhao, Y. Fu, and Y. Wang, "The effect of transition metal carbides MeC (Me = Ti, Zr, Nb, Ta, and W) on mechanical properties of B4C

ceramics fabricated via pressureless sintering," *Ceramics International*, vol. 46, no. 17, pp. 27283–27291, 2020.

[306] Y. Zhu, F. Wang, Y. Wang, H. Cheng, D. Luo, and Y. Zhao, "Mechanical properties and microstructure evolution of pressureless-sintered B4C-SiC ceramic composite with CeO2 additive," *Ceramics International*, vol. 45, pp. 15108–15115, 8 2019.

[307] B. M. Moshtaghioun, D. Gomez-Garcia, A. Dominguez-Rodriguez, and R. I. Todd, "Grain size dependence of hardness and fracture toughness in pure near fully-dense boron carbide ceramics," *Journal of the European Ceramic Society*, vol. 36, pp. 1829–1834, 6 2016.

[308] U. Anselmi-Tamburini, Z. A. Munir, Y. Kodera, T. Imai, and M. Ohyanagi, "Influence of Synthesis Temperature on the Defect Structure of Boron Carbide: Experimental and Modeling Studies," *Journal of the American Ceramic Society*, vol. 88, pp. 1382–1387, 6 2005.

[309] K. Ashbee, "Defects in boron carbide before and after neutron irradiation," *Acta Metallurgica*, vol. 19, pp. 1079–1085, 10 1971.

[310] T. Sano and C. L. Randow, "The Effect of Twins on the Mechanical Behavior of Boron Carbide," *Metallurgical and Materials Transactions A*, vol. 42, pp. 570–574, 3 2011.

[311] X. Du, Z. Zhang, Y. Wang, J. Wang, W. Wang, H. Wang, and Z. Fu, "HotâPressing Kinetics and Densification Mechanisms of Boron Carbide," *Journal of the American Ceramic Society*, vol. 98, pp. 1400–1406, 5 2015.

[312] B. M. Moshtaghioun, D. G. García, A. D. Rodríguez, and N. P. Padture, "High-temperature creep deformation of coarse-grained boron carbide ceramics," *Journal of the European Ceramic Society*, vol. 35, pp. 1423–1429, 5 2015.

[313] C. W. Li, M. M. McKerns, and B. Fultz, "Raman spectrometry study of phonon anharmonicity of hafnia at elevated temperatures," *Physical Review B - Condensed Matter and Materials Physics*, vol. 80, p. 054304, 8 2009.

[314] B.-K. Kim and H.-o. Hamaguchi, "Raman spectrum of 18O-labelled Hafnia," *Materials Research Bulletin*, vol. 32, pp. 1367–1370, 10 1997.

[315] M. Alotaibi, L. Li, and A. R. West, "Electrical properties of yttria-stabilised hafnia ceramics," *Physical Chemistry Chemical Physics*, vol. 23, no. 45, pp. 25951–25960, 2021.

[316] M. Alotaibi, F. Almutairi, and A. R. West, "Resistive-switching in yttria-stabilized hafnia ceramics," *Journal of the American Ceramic Society*, vol. 106, pp. 822–828, 2 2023.

[317] J. Lee, K. Yang, J. Y. Kwon, J. E. Kim, D. I. Han, D. H. Lee, J. H. Yoon, and M. H. Park, "Role of oxygen vacancies in ferroelectric or resistive switching hafnium oxide," *Nano Convergence*, vol. 10, p. 55, 12 2023.

[318] M. A. Lieberman and A. J. Lichtenberg, *Principles of Plasma Discharges and Materials Processing*. Wiley, 4 2005.

[319] J. He and D. R. Clarke, "Determination of the Piezospectroscopic Coefficients for ChromiumâDoped Sapphire," *Journal of the American Ceramic Society*, vol. 78, pp. 1347–1353, 5 1995.

[320] M. A. Baig, M. A. Fareed, B. Rashid, and R. Ali, "On the Rydberg transitions and elemental compositions in the laser produced Al (6063) plasma," *Physics of Plasmas*, vol. 18, 8 2011.

[321] M. M. Suliyanti, M. Pardede, T. J. Lie, K. H. Kurniawan, A. Khumaeni, K. Kagawa, M. O. Tjia, and Y. I. Lee, "Direct Powder Analysis by Laser-Induced Breakdown Spectroscopy Utilizing Laser-controlled Dust Production in a Small Chamber," *Journal of the Korean Physical Society*, vol. 58, pp. 1129–1134, 5 2011.

[322] B. Koroglu, M. Mehl, M. R. Armstrong, J. C. Crowhurst, D. G. Weisz, J. M. Zaug, Z. Dai, H. B. Radousky, A. Chernov, E. Ramon, E. Stavrou, K. Knight, A. L. Fabris, M. A. Cappelli, and T. P. Rose, "Plasma flow reactor for steady state monitoring of physical and chemical processes at high temperatures," *Review of Scientific Instruments*, vol. 88, 9 2017.